

**Changes in Some of the Physical and
Chemical Properties of Amorphous
 $\text{Fe}_{68}\text{Ni}_{14}\text{Si}_2\text{B}_{16}$ Alloy due to Molybdenum
Substitution for Ni**

A Thesis submitted
for the award of the Degree of
Doctor of Philosophy

By

Bhamidipati Seshu



**School of Physics
University of Hyderabad
Hyderabad 500 046, India**

April 1998

*... to those who have the thrust for knowledge
and urge for learning*

CONTENTS

CERTIFICATE	i
DECLARTION	ii
ACKNOWLEDGEMENTS	iii
PREFACE	iv

CHAPTER - 1 Introduction

Introduction	1
1.1 Glass formation	2
1.2 Classification of metallic glasses	4
1.3 Preparation techniques	5
1.4 Characterization	6
1.5 Atomic structure	7
1.5.1 Structural models	7
1.5.2 Short range order	8
1.5.3 Types of disorder in glasses	9
1.6 Electronic structure and transport properties	10
1.7 Magnetic properties	12
1.8 Crystallisation	15
1.9 Corrosion	15
1.10 Applications	17
1.11 Aim and scope of the thesis	17
Motivation	17
Objectives	19
1.12 References	21

CHAPTER-2 Electrical Transport Measurements

2.1 Introduction	27
2.2 Theoretical models	30

2 2.1	Ziman-Faber diffraction model	30
2 2.2	Mott s-d scattering model	33
2 2.3	Two level tunneling model	34
2 2.4	Weak localisation (or) Quantum interference effects	35
2 2.5	Magnetic contribution to resistivity	38
2 3	Experimental details	40
2 4	Results and discussion	42
2 4.1	Behaviour of RR for $T > 150\text{ K}$	43
2 4.2	Behaviour of RR for $T_{\text{min}} < T < 150\text{ K}$	45
2.4.3	Behaviour of RR for $T < T_{\text{min}}$	47
2.5	Summary	51
2.6	References	53

CHAPTER - 3 Mossbauer and Magnetization Studies

3 1	Introduction	57
3 2	Mossbauer effect	58
3 2.1	Principle	58
3 2.2	The ^{57}Fe decay scheme	60
3 3	Hyperfine interactions	61
3.3.1	Isomer shift	62
3 3.2	Electric quadrupole interaction	64
33.3	Magnetic hyperfine interaction	64
3 3.4	Combined magnetic and electric hyperfine coupling	66
33.5	Intensity ratios	66
3 4	Experimental details	67
3.4.1	Mossbauer measurements	67
3 4.2	Bulk magnetization measurements	68
	Principle	68
	Experimental setup	69
3 5	Results and discussion	70
35.1	Mossbauer spectra of metallic glasses	70

3 5 2	Analysis of ⁵⁷Fe Mossbauer spectra of amorphous alloys	71
3 5 3	Room temepature Mossbauer spectra of Fe-Ni-Mo-Si-B alloys	73
3 5 4	Magnetization axis	75
3 5 5	Temperaure dependence studies studies of Mossbauer spectra of Fe-Ni-Mo-Si-B alloys	77
	Temperature dependence of linewidths	77
	Temperature dependence of Isomer shift	78
	Temperature dependence of H_{eff}(T) and spin wave excitations	79
	Spin wave excitations	80
3 5 6	Hyperfine field distribution	84
	The Window method	85
3 5 7	Bulk magnetization measurements	90
	Temperature dependence of magnetization	90
3 6	Summary	91
3 7	References	93

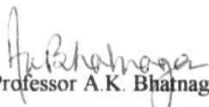
CHAPTER - 4 Crystallisation Studies


•1 1	Introduction	99
4 2	The technique Differential Scanning Calorimetry (DSC)	103
4 2 1	Introduction	103
4 2 2	Description of the setup	104
4 2 3	Experimental procedure	105
4 3	Methodology	106
4 3 1	Kissinger's method of analysis of non-isothermal transformation	107
4 3 2	Determination of the Avrami exponent, n	109
4 4	Results	MO
	Composition dependence of crystallisation temperatures and activation energies	112
4 5	Discussion	113
4 6	Summary	117

4 7	References	119
 CHAPTER - 5	 Corrosion Studies	
5 1	Introduction	124
5 2	Corrosion principles	127
5 2 1	Corrosion rate	128
5 2 1(a)	Non-electrochemical method	129
5 2 1(b)	Electrochemical theory of corrosion	130
(a)	Polarisation method	131
	Tafel's extrapolation method	133
	1 linear polarisation method	134
(b)	ac impedance spectroscopy method	135
	The Nyquist plot	136
	The Bode plot	137
5 3	Materials and specimen preparation	137
5 4	Experimental techniques	138
5 5	Results and Discussion	139
5 6	Conclusions	143
5 7	References	144
 CHAPTER - 6	 Conclusions	 146
	Suggestion for future work	152
	List of Publications	154
	Curriculum vitae	156

CERTIFICATE


This is to certify that Ms Bhamidipati Seshu has submitted the Doctoral Thesis entitled "Changes in Some of the Physical and Chemical Properties of Amorphous $\text{Fe}_{68}\text{Ni}_{14}\text{Si}_2\text{B}_{16}$ alloy due to Molybdenum Substitution for Ni" to the School of Physics, University of Hyderabad, India on the 16th of April, 1998.


(Professor A.K. Bhattacharya) 16.4.98
Thesis Supervisor


Dean
School of Physics
UNIVERSITY OF HYDERABAD
HYDERABAD, INDIA

DECLARATION

I hereby declare that the work reported in this thesis has been carried out by me in the School of Physics, University of Hyderabad under the supervision of Professor A.K Bhatnagar. This work is original and has not formed the basis for the award of any degree, diploma, fellowship, associateship or similar title of any University or Institution.


(Bhamidipati Seshu)

Date 16-04-1998

Place Hyderabad

ACKNOWLEDGEMENTS

The arduous task of submission of this thesis is the result of untiring, **effective**, affectionate and professional guidance by my supervisor **Prof. A. K. Bhatnagar**

I extend my profound thanks to Prof **D. G** Naugle and his group, Texas A&M University, USA, Dr V S Raja, IIT, Bombay, **Dr A K Nigam**, LTP division, TIFR and Prof S N **Kaul** for providing experimental facilities for Crystallisation (DSC) & Low temperature **magnetization**, Corrosion, Mossbauer and RT magnetization (VSM) measurements

I sincerely thank **the** Dean, School of Physics, for extending the facilities in the school in completing this work My thanks are also due to all teaching and non-teaching **staff of the** school and to the **staff of CII**. for their kind cooperation

I wish to express my deep sense of gratitude to Dr L Raghavendra Rao for his constant encouragement and inspiration which prompted me to pursue this **research**

I am indebted to all **of** my colleagues in the university as well as in the institutions elsewhere who have provided insightful suggestions My warmest thanks are specially due to my labmates who stood by me in my hours **of** need and made my stay a memorable one with their association

It is the support, guidance and encouragement *of so many people* because **of** which I am able to complete this piece of work

My sincere thanks to Special Assistance Programme (SAP) funded by **UGC**, Department of Atomic **Energy** (DAE) and Council of Scientific and Industrial Research (CSIR) for their financial assistance in the form of predoctoral fellowships to complete this project I also wish to thank CSIR and Department **of** Science and Technology (DST) for providing me the Partial **Travel** Grant to attend an international conference held in SLOVAKIA

My overriding debt is to my *parents*, who provided me with time, support and inspiration needed for my research **work**

Preface

This thesis presents the effect of Molybdenum (Mo) substitution in the **Fe₆₈Ni₁₃B₂Si₁₆ metallic** glass system through a study of electrical transport, magnetic, thermal and chemical properties. In the present work a **series** of amorphous alloys **Fe₆₈Ni_{14-x}Mo_xSi₂B₁₆** (x = 0,1,2,3 and 4) are systematically **investigated**. Because of the unusual combination of various physical and chemical properties associated with these Fe-rich metallic glasses, they have become potential materials for **scientific** investigations and technological **applications**.

This thesis is essentially divided into six chapters.

Chapter I gives a brief introduction to the field of metallic glasses and a discussion on glass formation, preparation techniques and disorder in the **glasses**. An overall review of the important physical and chemical properties of these glasses and their applications in this context are discussed. A brief review of the work reported on this system is also given.

Chapter II describes the measurement of electrical transport properties through electrical resistivity measurements of the samples under study. The chapter begins with a brief introduction of electrical transport phenomena in metallic glasses. Various theoretical models are given and analysis of the results based on more recent theoretical concepts is **presented**. Analysis of results in terms of composition and temperature variation is clearly presented.

Chapter III deals with Mossbauer measurements on the samples used in the present work. A brief introduction to the Mossbauer Effect and **hyperfine** interactions is given which are relevant to the work done. A brief review of various Mossbauer parameters and their physical interpretation is **given**. Details of analysis are presented and information about hyperfine fields, hyperfine field distribution, **isomer** shift etc., as a function of Mo concentration and temperature is obtained and the results are **discussed**. Magnetization studies at room temperature using VSM and at low temperatures in the range 10-100 K using **Lakeshore** ac **Susceptometer** are also presented towards the end of the chapter.

Chapter IV presents details of crystallisation studies on the samples chosen for the present investigation, using Differential Scanning **Calorimetry, (DSC)**. A brief

introduction to DSC technique and its importance in understanding **thermal** stability and crystallization of **metallic** glasses is given. Crystallization temperatures and the related kinetics are studied as a function of Mo content and a discussion with respect to the thermal stability of these samples is presented. Though measurements are mainly restricted to the non-isothermal **method**, the isothermal kinetic parameter, the **Avrami** exponent is also deduced along with the activation **energies**.

Chapter V gives a detailed study of chemical stability against corrosion resistance of the samples under consideration. Measurements in different acidic media are made by electrochemical methods using potentiodynamic polarisation and ac impedance spectroscopic techniques. These techniques are emphasized with the necessary basic theory in this subject area. Data is analysed using the latest software techniques available and results are discussed in **detail**.

Chapter VI gives overall conclusions of the present studies, emphasizing certain unresolved problems and work which can be taken up in future with further experimentation.

CHAPTER I

Introduction

Introduction

A solid with **liquid-like** atomic arrangement is called **glass**, or alternatively an amorphous (non-crystalline) solid. Though glassy solids are known since long time, their preparation and characterization with desirable physical and chemical properties has been the subject of relatively recent studies [1-4]. Glasses do not exhibit long range periodicity of atomic arrangements found in crystalline materials. They are '**amorphous**', or have liquid-like atomic structure and over distances of more than 5 atomic spacings, the correlation between the positions of the atoms is completely **lost**. **Thus**, amorphous alloys are characterized by structurally disordered networks in which each atom constitutes a structural unit. In crystalline material lattice periodicity and crystal structure play a decisive role in determining the basic properties whereas in amorphous alloys structural disorder leads to changes in their physical and chemical

properties. In order to freeze a liquid-like structure while solidification process is taking place, it is **necessary** that the quenching rate must be high enough to arrest the atomic movement suddenly and restrict nucleation and growth **of microcrystallites**. Metallic glasses which are stable at room temperature and above could not be prepared until 1960. Around this time, **Klement**, Willens and Duwez [5] discovered accidentally that the melt of an alloy of gold and silicon (**Au₈₀Si₂₀**) when rapidly quenched, at a rate **of $\sim 10^6$ K/s**, was amorphous and showed glassy or liquid-like structure when examined by X-ray diffraction and was stable at room temperature too. The discovery of glassy metals which can be prepared by rapid quenching **of** certain alloys and are stable at room temperature started a **new** era of research and development in this area. In particular, metallic glasses exhibiting ferromagnetic behaviour have attracted a great deal of attention by way of understanding the fundamental properties that govern their behaviour and looking into the possibilities of using them with numerous advantages from technological point of view [1,2]. Metallic glasses have contributed a great deal in enhancing our knowledge **of** the solid state and they have also been exploited **for** potential applications. Variation in composition of the metallic glasses is used as a means to vary their physical and chemical properties of interests to physicists, chemists and technologists. The growth of interest on the subject **of amorphous** alloys since its discovery is indeed phenomenal. The explosive literature on the subject in general, and amorphous ferromagnetic alloys in particular, **is** an indication of the importance gained by the subject [6-12].

In this chapter, we provide a brief introduction to glass formation, classification, preparation and characterization **of** metallic glasses with some of their important properties and applications which lay the foundation for our motivation to take up the present investigations.

1.1 Glass Formation

The basic criterion for the preparation of glasses is that the cooling process should be fast enough that the crystallization is by passed quickly. This is best illustrated in the Time-Temperature-Transformation (**TTT**) diagram [13], shown in **Fig 1.1**, in which the time for the onset of crystallization in an undercooled melt (i.e., at a temperature below the equilibrium melting point, **T_m**) is plotted against the

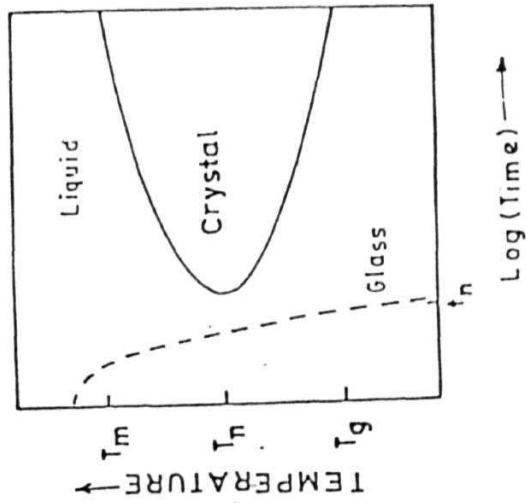


Fig. 1.1 Schematic time-temperature-transformation (TTT) diagram for the onset of crystal growth in an undercooled melt.

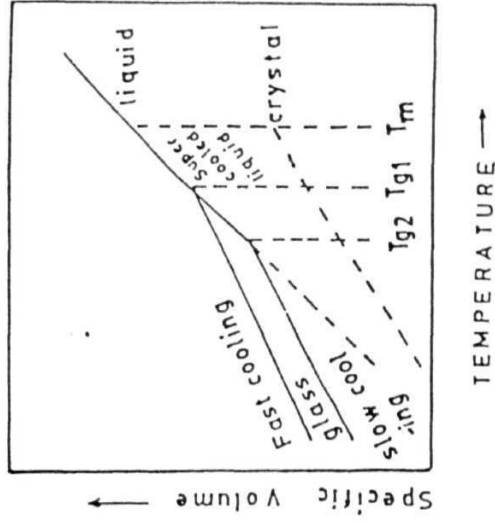


Fig. 1.2 Schematic illustration of the change of specific volume of a liquid with temperature by fast and slow cooling.

temperature. An essential feature of this (TTT) diagram is that as the liquid is undercooled below the equilibrium melting point, the crystallization rate does not continue to rise indefinitely but reaches a maximum at a temperature T_n . Consequently if the liquid is quenched from above T_m to well below T_n in a time less than the minimum time for crystallization, t_{min} , the undercooled liquid is retained and, at T_g , the glass transition temperature, the configuration is frozen to form a **glass**. As the temperature is lowered further and further below T_m , the difference in free energy between the liquid and crystalline phases increases and hence the time for crystallization **decreases**. At the glass transition temperature, T_g , (typically defined by viscosity $> 10^{13}$ Poise), crystal growth becomes almost impossible and the liquid remains frozen in a single **configuration**. At sufficiently large cooling rates even the nucleation can be eliminated.

When a liquid is cooled from a high temperature, its specific volume (V) changes discontinuously at or below the melting temperature T_m . This is illustrated in Fig. 1.2 [14]. If the growth of the nuclei is absent or low, the volume of the supercooled liquid continues to decrease till T_g , where a remarkable change in the slope of the V vs T plot occurs. The glass transition depends upon the cooling rate as shown in Fig. 1.2. T_g increases with the cooling rate and so does the specific volume of the glass **formed**. **Differences** in volume are typically only a few percent but these have enormous effect on the properties of the **material**. A sample in the glassy state is in a **thermodynamically metastable** state, and therefore with time its configuration tends to change towards the equilibrium state of lowest free **energy**. Therefore, the structure of a glass is dependent on its thermal history.

Marcus and Tunbull [15] have proposed an empirical criterion for the formation of metallic **glasses**. They have suggested that the glass forming ability may be related to the depression of the melt temperature, T_m below a certain average temperature, T_a of ideal solution liquidus. The criterion for the formation is that $(T_a - T_m)/T_a > 0.15$ to 0.2 . A typical example is shown in Fig. 1.3 where the dotted line represents temperature T_a . Another criterion for the ease of metallic glass formation is that if a liquid has reduced glass transition temperature $T_{gr}, (=T_g/T_m) > 0.7$ then the

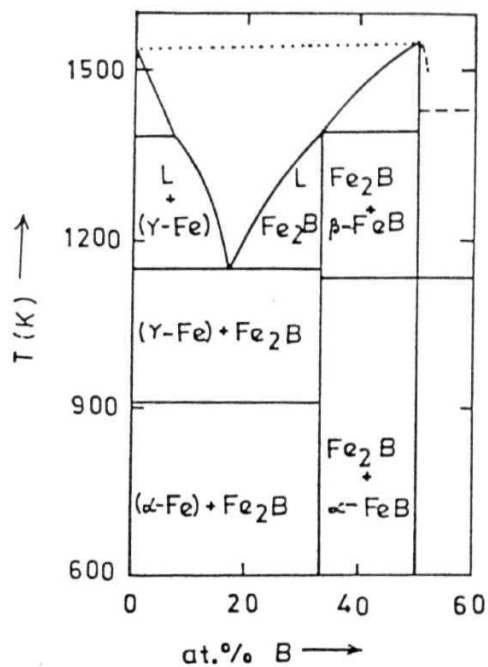


Fig. 1.3 Phase diagram of the $\text{Fe}_{100-x}\text{B}_x$ alloy.

liquid can be rapidly cooled (cooling rate $\sim 10^6$ K/s) to prepare glass without much difficulty [16]. On the other hand, if $T_{gr} < 0.5$ then it is very difficult to cool the liquid into a glassy state. This criterion is related to the one previously given by Rawson [17] based on the ratio of bond strength to T_m . Glass formation is easier in a multicomponent system compared to a single component system, since the ratio of the bond strength to liquidus temperature will be greater for all intermediate compositions, and largest at the eutectic composition (the composition at which the system is invariant with all the phases in equilibrium and has its lowest melting point).

1.2 Classification of Metallic Glasses

The two important classifications of metallic glasses are made either by their composition or by some chosen property, e.g., magnetic properties of these glasses. The first classification [18] has four categories:

1. The first category consists of transition metal - metalloid (TM - M) glasses. This group combines one or more of the late 3d - transition metals (Fe, Co, Ni) with one or more of the metalloids (B, C, Si, P) in an atomic ratio $TM : M = 80 : 20$. A typical and important example of this group is the $Fe_{80}B_{20}$ metallic glass.
2. In the second category of metallic glasses an early transition metal combines with a late transition metal (TE - TL), e.g., $Nb_{40}Ni_{60}$.
3. The third category of metallic glasses are made up of simple metals like Ca - Al.
4. The fourth category of metallic glasses are of rare earth - transition metal (RE - TM) combination e.g., Gd - Co alloys.

Alloys cannot be formed in the amorphous state over the entire concentration range using liquid quenching techniques but are formed within a narrow concentration range generally centered around the deep eutectic points in the alloy phase diagrams. The width of the concentration range over which a particular alloy series can be formed in the amorphous state also depends on the type of preparation technique used.

Based on the magnetic state of metallic glasses (on which the electronic state and electron transport property depend heavily) another classification has been proposed by Mizutani [18]. According to this classification these metallic glasses are then categorised as

- 1 Ferromagnetic (**e.g.**, $\text{Fe}_{80}\text{B}_{20}$, $\text{Fe}_{40}\text{Ni}_{40}\text{B}_{20}$ etc)
- 2 Weak ferromagnetic (**e.g.**, NiY and FeZr systems)
- 3 Spin glass (**e.g.** $\text{Fe}_{100-x}\text{P}_{10}\text{B}_4$)
- 4 Paramagnetic (e.g., **Cu-Zr**, Nb - Ni) and
- 5 Weak paramagnetic or **diamagnetic** (**e.g.**, Mg - Zn, Pd - Si)

1.3 Preparation Techniques

Amorphous alloys can be prepared by a number of techniques. The basic procedure is to rapidly quench the metallic system either from its vapour phase or liquid phase on a heat sink so as to bypass the crystallization quickly to produce noncrystalline structure akin to frozen **liquid**. These techniques are broadly classified into two **categories**: (i) melt-quenching and (ii) deposition techniques. Melt-quenching methods include, (i) splat-cooling, (ii) roller-quenching, (iii) spark erosion and (iv) laser glazing [19-24]. Fabrication of amorphous alloys in a concentration range away from the eutectic point is facilitated by the deposition techniques which include **vacuum** thermal evaporation [25] and sputter deposition [26]. Other occasionally used techniques are **electrodeposition** [27], ion-implantation [28] and solid-state diffusion [29].

Splat quenching is the simplest form of melt-quenching. In this **method**, a liquid alloy droplet is squeezed between a rapidly moving piston and a fixed anvil. Alloys obtained by this method are in the form of thin discs (1-3 cm in diameter and 20-60 μm in thickness). Laser quenching [30] is another form of melt quenching **technique**. In this method, a short and highly intense laser beam is used to melt a portion of a thin metallic surface, which is then cooled rapidly by the surrounding crystal. The cooling rates achieved in this way are in the range of 10^{10} to 10^{12} K/s. Another simple and popular technique is **melt-spinning**. This method employs a jet from which alloy melt is dropped onto a rapidly moving wheel made of a material with high thermal conductivity such as copper, shown in **Fig 1.4**. Continuous ribbons of amorphous alloys are obtained by this method and higher cooling rates (10^6 K/s) are achieved compared to splat-quenching.

The above mentioned melt-quenching techniques are useful to prepare

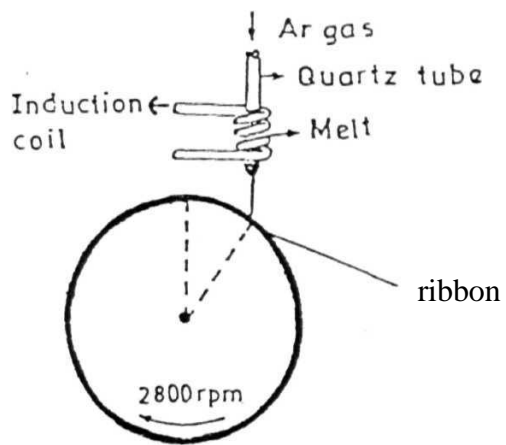


Fig. 1.4 Schematic diagram of single roller quenching technique.

amorphous alloys in a narrow concentration range around the eutectic **point**. Preparation of amorphous alloys in the concentration range away from the eutectic point requires techniques such as thermal evaporation [25], in which metals constituting the alloy are evaporated in vacuum and condensed on a substrate by removing them from the source under bombardment with energetic inert gas atoms. When very high cooling rates of the order of 10^{14} K/s are required, ion-implantation technique [28] is used. It should be noted that all the present methods produce metallic glasses which are very thin, a drawback for many practical **applications**. A new technique of solid state diffusion by Johnson et al [29] to produce thicker metallic glasses is found to be very promising.

Most of the metallic glasses prepared earlier were binary and ternary alloys. Later, metallic glasses with four to six constituents have been prepared for commercial usage, as well as for research purposes to **investigate** the effects of additional components as the alloy shows improved thermal stability and other **properties**.

1.4 Characterization

Metallic glasses are characterized through a study of their structural, physical, chemical and other properties. Techniques such as X-ray, electron and neutron diffraction are mostly used to characterize **them**. The simplest way of determining whether the atomic structure confirms the amorphous state or not is to take an X-ray **diffraction pattern**. The X-ray diffraction pattern of an amorphous solid typically consists of diffuse rings or a broad peak at low scattering angles (**20 values**). It is not possible at once to distinguish between a **microcrystalline** structure and a homogeneous random distribution of atoms on the basis of diffraction patterns **alone**. A more refined X-ray technique, known as Extended X-ray Absorption Fine Structure, (**EXAFS**), is particularly useful to probe local atomic structure of amorphous alloys [31]. Another extremely powerful technique for probing short range atomic order of amorphous alloys is neutron **scattering**. Since neutron scattering amplitude of an individual nucleus varies with different isotopes and their spin states, coherent and incoherent **scatterings** take place depending on whether the neutron waves scattered by different nuclei interfere with one another or **not**. While coherent neutron scattering provides useful information about the collective structure and atomic pair correlation

function, the incoherent neutron scattering gives important clues about localised vibration and atomic **diffusion**. Techniques such as nuclear magnetic resonance (NMR) and Mossbauer spectroscopy are useful in probing nearest-neighbour environments and magnetic **hyperfine** fields as they are more sensitive to variations in the local **environment**. Various techniques such as atomic absorption spectroscopy, X-ray fluorescence, electron **microprobe analysis**, Auger spectroscopy and secondary-ion mass spectroscopy are available for analysing the **chemical** composition of metallic **glasses**.

1.5 Atomic Structure

1.5.1 Structural Models

A number of theoretical models have been proposed to describe the atomic arrangement in amorphous **alloys**. Bernal [32] introduced the idea of dense random packing of hard spheres (DRPHS) to simulate the structure of mono-atomic liquid metals. In this picture there exists a random distribution of atoms such that only weak correlations exist between spheres separated by **five** or more sphere diameters. This work was followed up by Scott [33] and **Finney** [34], who concluded that the maximum density of a hard sphere non-crystalline packing was 0.6366 ± 0.0004 . With this model it was possible to calculate an accurate radial distribution function, which reproduced the split second **peak**. But this model was not entirely successful as no real amorphous alloy can be thought of as an experimental realisation of the hard-sphere model or consisting of only one species of **atoms**.

Subsequent models improved on the DRPHS model by considering realistic softer potentials and observing structural changes when two (or more) components and their chemistry are **considered**. One such model is due to Gaskell [35] who first built the required chemical ordering and then allowed relaxation processes to bring in the dense packing constraints. He used trigonal prismatic units as basic building blocks as compared to the tetrahedral structures of Bernal. This type of chemical ordering is at the expense of packing constraints like large **cavities**. These constraints are then **manipulated** by computer-relaxing the whole **assembly**. Gaskell successfully applied this model to **a-Pd₄₀Si₂₀** and related TM - M **alloys**.

Besides these models, several other models [36,37,38] which involve computer simulation and allow for the interplay between local chemical ordering and overall packing constraints of high density **structures**, have been put **forward**

1.5.2 Short Range Order

Fig 1.5 shows the difference in behaviour of structure factor $S(q)$ vs q for a liquid, a glass and a crystal from diffraction **experiments**. From this figure, it is seen that a crystalline solid is characterized by sharp **peaks**. These sharp peaks are replaced by a broad peak followed by smaller broad peaks, in glass or liquid indicating that the long range order present in crystalline solids is absent in glass or liquid. It is interesting to note that the broad peaks in $S(q)$ behaviour of a glass which are similar to that of a liquid, clearly bring out the **similarities** between glassy and liquid structures at the atomic level, although there are subtle differences **present**. The atomic order in glasses seems to extend only **for** two or three nearest neighbour distances and is classified as short range order (**SRO**).

In amorphous solids, atomic positions are strongly correlated in the nearest-neighbour shell but are uncorrelated beyond a few interatomic **spacings**. In other words, glassy alloys possess short-range atomic order but no long range atomic order and the structure of these solids resembles that of liquids from which they have been obtained by **quenching**. Short-range atomic order or simply short -range order (SRO) varies from one amorphous material to the other and is of two **types**: compositional or chemical short- range order (CSRO) and geometrical short- range order (GSRO). In many glassy alloys, the chemical composition on a local scale is different from the macroscopic average and this deviation is called CSRO. The CSRO is confined to the first nearest-neighbours and hence can be described in terms of the deviation of the nearest-neighbour composition from the **average**. The topological short-range order (TSRO) describes the short-range order in the atomic positions regardless of the chemical activity of individual **atoms**. This type of SRO is present in all the glassy alloys including the single-component glasses made up of one kind of atoms only. In addition, geometrical distortions, which are independent of topology, can also occur in such elementary glasses and the corresponding short-range order is known as **distortional** short-range order (DSRO). Therefore, the geometrical short-range order

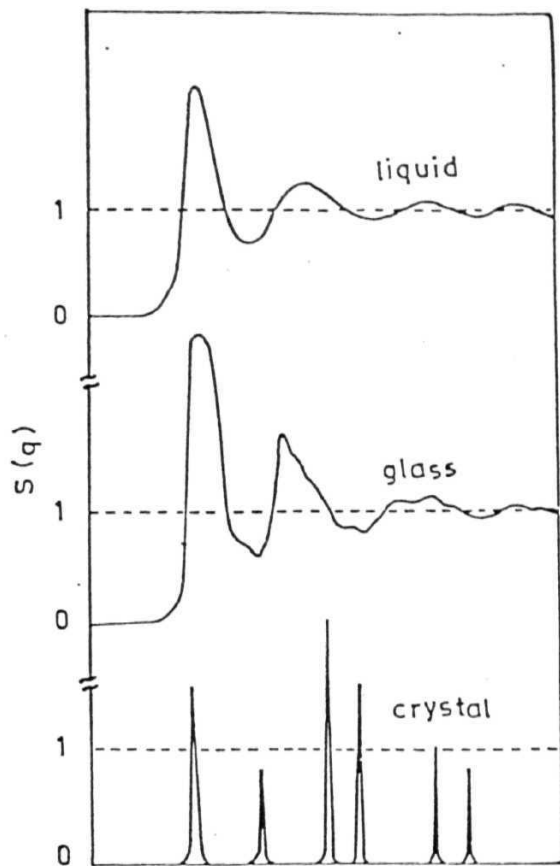


Fig. 1.5 Schematic plot illustrating the difference between x-ray structure factor of a liquid, a glass and a crystal.

(GSRO), which characterizes local atomic structure includes both TSRO and **DSRO**

1.5.3 Types of Disorder in Glasses

All glassy or amorphous materials are characterized by a complete lack of translational symmetry but the degree and type of short-range order or **local** order varies from glass to **glass**. Different types of short-range order give rise to various kinds of disorder that have a direct bearing on the magnetic properties of these alloys [2,39] and generally a glass is characterized by the presence of all types of disorders.

(i) **Topological Disorder**

Topological disorder is intrinsic to the amorphous structure and it results when translational symmetry in the positions of atoms is completely absent and the nearest, next-nearest neighbour coordination number varies from site to site. A topologically disordered structure cannot be ordered back into a **crystal**.

(ii) **Chemical Disorder**

When different types of atoms or molecules occupy the lattice sites without disturbing the periodicity of an ordered structure, chemical disorder results. In such cases, the translational symmetry of the atoms or molecules is broken by the chemical identity of the objects that occupy the lattice sites. If the concentration of one species of atoms is increased at the expense of the other in a binary or quasi-binary alloy further complication can arise. The disorder that results by changing the composition is known as compositional **disorder**. Compositional disorder includes substitutional **disorder**. A similar situation can also occur in a structurally disordered lattice. Thus, chemical and compositional disorder can occur in both crystalline and amorphous **solids**.

(iii) **Site-Disorder**

The fluctuation in the coordination number arising from the random occupation of sites in a regular crystalline lattice or an aperiodic amorphous network constitutes site disorder.

(iv) **Bond Disorder**

Bond disorder results when wild variation in the bond lengths and bond angles

destroy the periodicity of the lattice or long- range atomic order The bond-disordered network remains topologically equivalent to the **crystal**

From the above description, it is clear that the site- and bond-disorder are included in topological and chemical/compositional disorder, and the terms "amorphous" and "**disordered**" cannot be used interchangeably All amorphous solids are disordered but all disordered systems need not be **amorphous** While the topological disorder alone is specific to amorphous solids, the other types, i.e., site-, bond-, chemical- and compositional disorder are found in both crystalline and amorphous **materials**

1.6 Electronic Structure and Transport Properties

To understand the physics and chemistry of metallic glasses, it is necessary to obtain information about their electronic band structure and transport properties (electrical resistivity etc) The ideas of **Bloch's** theorem and reciprocal space breakdown **for** glasses since there is no long range lattice **periodicity** Hence it is of interest to study the effect of lack of crystalline periodicity on the band structure **of** these materials Since a number of physical properties **of** solids like electronic specific heat, superconductivity, magnetic susceptibility, **ferromagnetism** etc, are directly **related** to their electronic structure, the usual experimental methods, *viz.*, ultraviolet and X-ray **photoemission** spectroscopy, Auger electron spectroscopy, soft X-ray spectroscopy and optical reflectivity which have been applied to study the band structure of crystalline solids have also been applied to glasses to study the **same** These studies have shown that the valence bands show distinct bonding effects which are directly observable in the valence band **spectra** **Besides** this information on the valence bands in many metallic glasses, information on the density of states near Fermi energy, E_F , has also been **obtained** It may be noted that the density of states at E_F is a very important parameter for solids to understand many of their electronic properties including specific **heat** Detailed survey on the electron spectroscopy of metallic glasses has been given by Oelhafen [40]

Electronic transport properties, like, electrical resistivity (ρ) Hall coefficient (R_H) and thermoelectric power (S) provide valuable information about electronic transport and electronic scattering mechanisms in solids and particularly metallic

systems Electrical resistivity has been the most investigated electrical property of metallic glasses since their discovery [18,40,41] Data on Hall effect and thermoelectric power in metallic glasses is not of the same magnitude as in the case of electrical resistivity

The electrical resistivity, ρ , of metallic glasses at room temperature is of the order of 80-420 $\mu\Omega\text{-cm}$, which is high in comparison with that of their crystalline counter **parts** The resistivity varies by less than 7% in the whole temperature range between 4.2-300 K. A sudden drop in resistivity will be observed at the crystallization temperature, usually much higher than room temperature in most **cases** Furthermore, on heating, the resistivity of the crystalline sample increases more rapidly and changes at the melting point, T_m Temperature coefficient of resistivity (**TCR**), α , defined as

$\rho^{-1} \left(\frac{d\rho}{dT} \right)$, is typically of the order of 10^{-4} K^{-1} and it can be positive, zero or negative

depending upon the glass composition and the temperature **interval** It has been possible to change the sign of **TCR** by continuously changing the composition of many metallic glasses [42,43] The resistivity values in the liquid state lie in a region which can be obtained from a rough extrapolation of the glassy state data, with the difference that the magnitude of α in the liquid state is lightly greater than that in the glassy **state** This point suggests that the theories developed for explaining the electrical resistivity of liquid metals can just as well be applied to metallic glasses Also, the magnitude and composition dependence of ρ of metallic glasses and its temperature dependence above Debye **temperature**, θ_D , have been found comparable to liquid metal data [44] Therefore, theoretical models which have been earlier used to explain liquid metal data on electronic transport properties have also been applied to metallic glasses with reasonable **success**

One of the important features of $\rho(T)$ behaviour in metallic glasses is that many of these materials show a resistivity minimum at low temperatures ($T < 25 \text{ K}$) and some even at higher **temperatures** Attempts to explain this widely observed effect have been made either by invoking Kondo effect mechanism [45,46], the existence of two level system (TLS) [47] or spin fluctuations [48]. However, there are difficulties associated with these theoretical models which have been discussed in detail by Harris and **Strom-Olsen** [49] Later, it was recognised that disorder plays an important role

and electron-electron interaction and quantum interference effects do appear in these materials modifying the resistivity behaviour at low temperatures [49-52]

1.7 Magnetic Properties

In the recent years, magnetic properties of amorphous alloys have been a subject of intense **experimental** and theoretical **interest**. In the initial stages, scientific interest in such non-crystalline systems was mainly because of the attractive technological prospects that these alloys were supposed to **offer**. A complete success in the realisation of the envisaged technological applications has, in turn, triggered off intensive research activity regarding the fundamental properties of amorphous **alloys**. When viewed in retrospect, a study of the magnetic properties of amorphous materials was, initially not given serious consideration due to the belief that magnetic ordering and structural disorder are incompatible with each **other**. The possible existence of amorphous magnetism was first explored theoretically by Gubanov [53], who predicted that amorphous solids would be ferromagnetic on the grounds that the electronic band structure of crystalline solids does not change in any **fundamental** way upon transition to the liquid or amorphous state (implying thereby that the band structure is basically controlled by the short-range **order**). **Ferromagnetism**, which is sustained by direct exchange interactions between the nearest-neighbour spins, should not, therefore, be destroyed in the corresponding amorphous solid. The predictions of Gubanov were experimentally verified only after the first amorphous alloy, stable at room temperature, was prepared by Duwez and coworkers [5] by rapid quenching of the melt of Cu-Ag **alloy**. Of particular significance was the work of Duwez and Lin [54] on liquid-quenched amorphous Fe-P-C alloy, which exhibited properties like high saturation magnetisation, low coercive field, high Curie temperature and good stability at room temperature against **crystallization**. This theoretical prediction was also confirmed experimentally when metallic amorphous **ferromagnets** were obtained by vapour deposition of Co-Au [55], by splat quenching from the melt of $\text{Pd}_{80}\text{Si}_{20}$ [56] alloys containing ferromagnetic impurities and by the electrodeposition of Co-P [57]. The discovery of ferromagnetism in amorphous solids led to large scale scientific and engineering investigations. Since then numerous iron-rich metallic glasses, which are ferromagnetic at room temperature and above, and which show excellent soft

ferromagnetic properties [58,59] **i.e.**, high saturation induction (~ 10 T), low coercivity (< 3 Oe) and hysteresis losses **etc** have been produced and they seem to be very good for a large number of applications

For magnetic order to exist in a solid there must be magnetic moments associated with unpaired electrons in the atoms and an interaction to couple them **together**. Except for so called weak itinerant ferromagnets, the above conditions remain valid for magnetic order to exist in a vast majority of metallic and **nonmetallic solids**. For ferromagnetic order to exist, the exchange interaction, to couple the moments together, must be positive and in principle, there are no **fundamental** differences between glassy and crystalline **ferromagnets**. However, disorder in amorphous solids leads to smearing effects in some of the properties, and in the ferromagnetic state, magnetic and non-magnetic atoms can coexist. Besides this, the chemical and bond disorders in amorphous solids lead **to** a distribution both in magnetic moments and the exchange interaction, thereby affecting the magnetic properties of metallic glasses. This is in contrast to the crystalline solids which show unique values for these parameters. Differences in Curie temperature etc., are also there even when one considers an alloy with the same composition, in crystalline and glassy states. On the other hand, **anti** ferromagnetic interactions in a disorder lattice produce quite a different and novel result and it has led to **discovery** of **non-collinear magnetic** structures, classified as speromagnetic, sperimagnetic and **asperomagnetic** structures [2].

The structure of glasses is normally considered to be isotropic on a long range scale, and therefore, the magnetisation vector in ferromagnetic glasses should, in general, be free from special magnetic **anisotropy**. The random electrostatic fields, due to random atomic **arrangements**, create local anisotropies via spin-orbit coupling, giving rise to a variation in the orientation of magnetic **moments**. However, in practice, thus most amorphous ferromagnets behave **anisotropically** [1]. Certain mechanical treatments like cold rolling, magnetic field cooling and stress annealing can induce additional **anisotropy**. Similarly, relaxation due to annealing or by some other method as well as crystallization result in changes of magnetic properties and therefore one has to be **careful** and certain about the thermal history of magnetic glasses before interpreting **results** or considering **applications**.

Choosing the basic binary Fe-B alloy system, which was found to have excellent soft magnetic properties, it has been possible to prepare metallic glasses having different magnetic and other physical and chemical properties by partially substituting Ni, Co, **Mn**, Cr and Mo for Fe **and/or** C, Si, P, **Al** and **Ge** for B [60-65] Glasses of suitable composition and method of preparation exhibit different types of magnetism observed in crystalline materials dia-, para-, ferro-, antiferro- and ferrimagnetism and the more exotic types of magnetic order discovered in recent years For example, **Pd₈₀Si₂₀** is a paramagnet, **Pd₇₈Si₁₆Cr₆** a **diamagnet**, while **Mn₇₅P₁₅C₁₀** is an **antiferromagnet** However, they are soft **ferromagnets**, such as some transition metal-metalloid alloys, which are of great interest, because of their potential **applications**

The structural and chemical disorder present in amorphous/glassy alloys give rise to a large number of nonequivalent atomic sites in the material As a result, all microscopic directions become nonequivalent, although the overall effect is such that **the** material behaves in an isotropic manner, in the sense that the response of the material to a small applied field is **isotropic** In these glasses, the random atomic arrangement also modifies various characteristic magnetic parameters such as the exchange interaction, the magnetic moments, the orientation of the electric field, the hyperfine field **etc** These parameters exhibit a distribution of values rather than the unique values observed in the case of crystalline ferromagnetic **materials** This has led to the current research effort, aimed at investigating the magnetic properties of these **materials** at the atomic level The experimental techniques suitable for the study of magnetic properties of a **ferromagnet** are (a) magnetization [1,66,67], (b) ferromagnetic resonance [68], (c) low field susceptibility [1], (d) Mossbauer spectroscopy [69,4] and (e) nuclear magnetic resonance [70,71]

The first three techniques give information on average bulk properties and are applicable to all **materials** The other two techniques provide information at the atomic level and are applicable only when nuclei of one of the elements in the composition are appropriate probes for the technique These two techniques probe the individual moment carried by the magnetic atom Since most of the ferromagnetic metallic glasses are iron rich in composition, the well celebrated ⁵⁷Fe Mossbauer spectroscopy has been extensively used to study magnetic interactions in iron rich metallic **glasses**

Several excellent reviews have appeared in literature on the magnetic properties

and the process of magnetization in amorphous alloys and of potential applications of these alloys [9,66,72-74] Since then, a huge amount of data on the **fundamental** as well as applied properties of amorphous alloys has accumulated and their physical implications have formed the subject of several books and review articles [1,2,59,75-78] A complete bibliography about amorphous magnetism and magnetic **materials** has been compiled by **Ferchmin** and Kobe [79,80]

1.8 Crystallization

The glassy state is essentially a metastable state. Hence it inherently possesses the possibility of transformation into a more stable crystalline state Depending upon the external conditions like heating, stress **etc** the system (glass) tends to relax towards a more stable state which either could be another metastable state of lower energy or an equilibrium crystalline state [66] Such external influences can change the magnetic, **electrical** and mechanical properties of these glasses, depending upon the intensity of the influence and the duration for which it is applied However, during crystallization the most promising properties of metallic glasses e.g., excellent magnetic behaviour of the high hardness and strength, combined with ductility and high corrosion resistance, have been found to deteriorate drastically Therefore, understanding the **micromechanisms** of crystallization, to impede or control crystallization, is a prerequisite for most applications, as the stability against crystallization determines their effective working **limits** There have been enormous effects to improve thermal stability of metallic glasses by changing their composition i.e., from binary to ternary, ternary to quaternary etc., and by substituting different transition metals and metalloids to the basic iron-boron **system**

The work on crystallization behaviour of metallic glasses has contributed to enhance our understanding of glass formation, factors affecting thermal stability and nucleation and growth process during **crystallization** Excellent reviews have appeared in this area which cover a wide variety of research topics and results obtained [81-83]

1.9 Corrosion

During the last two decades a great deal of effort has been made to characterize and understand the general corrosion behaviour of metallic glasses, in

particular **TM-Metalloid** metallic glasses [84,85] It has been found that glasses of certain compositions of Fe-rich metallic glasses have, far **superior** corrosion resistance compared to their crystalline counterparts [85,86] Because of the high corrosion resistance, in addition to the unusual combination of various advantageous physical properties, these glasses become potential candidates for technological applications However, the application of these alloys is viable only when their chemical stability is **guaranteed** So, in order to improve the chemical stability against corrosion, corrosion behaviour of these glasses has been studied extensively by adding metalloid elements like P, Cr which act as strong passivators [87-91] Although strong influence on the corrosion behaviour has been noted, it is still not clear as to whether such effects are results of their amorphous nature or chemical homogeneity It will be generally difficult to dissociate these two aspects The experimental results have indicated that high degree of homogeneity, both compositional and structural, confer greatly improved corrosion resistance on the glassy **alloys** However, composition also plays an important role in the determination of their corrosion behaviour [92,93]. Thus, further understanding of the relative importance of the amorphous structure and elemental composition in the corrosion resistance of amorphous metallic alloys will be **useful**

Much interest has been centered on the effects of different alloying elements **like** metalloids P, B, Si, C and metals like Cr, Mo, W, Nb etc, on the corrosion resistance of Fe-based metallic glasses, due to their good soft magnetic properties In particular, the effects of Phosphorous, P and Molybdenum, Mo (with or without Cr) on the promotion of stable passive films have been investigated by several authors [87-91]

It is well known that P offers excellent corrosion resistance to glasses [92] and the addition of Ni is considered to promote the formation of a passive film in the presence of Cr, thus providing good corrosion resistance [89] Already much work has been reported on the effect of addition of P and Cr and in the absence of both these elements the corrosion resistance of these glasses significantly **decreases** Hence it is thought worthwhile to examine the corrosion behaviour of Fe based metallic glasses free from P and Cr and having low Ni content, which are generally preferred for magnetic **applications**

1.10 Applications

Metallic glasses exhibit **excellent** mechanical and **soft** magnetic properties and offer tremendous potential for industrial exploitation [2,9,16,40,94,95] They have potential application in power distribution transformers, magnetic shielding, transducers, magnetic heads for audio, video and data recording and magnetic **sensors**. The large variation in the saturation magnetostriction constant, λ_s , as a function of annealing treatment can be exploited by metallic glasses as electronically controllable acoustic delay lines which are important components in radar, computers and all signal processing equipment [96,97] With Nd-Fe-B metallic glasses there is a possible replacement for the costly **Sm-Co**s permanent magnets [94] Their mechanical properties are being utilized in applications for brazing filler materials, strengthening fibers in composite materials etc [40] While possessing the most attractive soft magnetic properties and highest mechanical strengths, Fe-B based glasses easily rust even in air at room **temperature** By the addition of **Cr** they can be made corrosion resistant without much degradation of their magnetic properties [98] Metallic glasses with good corrosion resistance are used in applications, such as magnetic separators, chemical and mechanical filters, marine cables etc Extremely high hardness and chemical inertness make glassy alloys possible candidates for surgical implants, razor blades and cutlery [9] Addition of Mo to iron rich metallic glasses has been reported [99] to be of great use in high frequency **applications** The limitations in the production of thick metallic glasses has been overcome to some extent by optimising certain parameters with utmost care while producing them [100]

Thus the excellent soft magnetic properties combined with the high strength, bond ductility, toughness and corrosion resistance, make metallic glasses attractive materials for several applications [101-103]

1.11 Aim and Scope of the Thesis

Motivation

In Fe-based metallic glasses, a number of substitutions by Ni and other metals have been made to change their magnetic properties. Some of the earlier reports suggest that the substitution of a non-magnetic element, in Fe-rich metallic glasses

shows a similar behaviour of transport and magnetic properties as observed with that of Cr substitution, an anti-ferromagnetic **element**. For **comparison** here we show the resistivity behaviour with temperature and Mossbauer spectra of similar alloys containing Mo and Cr separately in **Figs 1.6 and 1.7**. Only limited work has been reported on substitution of the non-magnetic metal Molybdenum (Mo) in such systems. As such, with a view to **find** out the changes in the physical and chemical properties of amorphous $\text{Fe}_{64}\text{Ni}_{14-x}\text{Mo}_x\text{Si}_2\text{B}_{16}$ alloy series ($x=0,1,2,3$ and 4) in which Ni has already been replaced partially for Fe, due to the effect of substitution of Mo, a non-magnetic metal a systematic study was **undertaken**. Also, the effect of Ni or Mo substitution on magnetic properties of Fe-B and Fe-B-Si glasses is found to be quite drastic in the sense that the Curie temperature and other magnetic hyperfine parameters decrease drastically. It has been pointed out that Fe-based alloys with less Ni content and without phosphorous, P are preferred for magnetic applications. However, application of these glassy materials for practical purposes is viable only when their thermal and chemical stabilities are **guaranteed**. It is well known that addition of P to Fe-rich metallic glasses results in very good corrosion resistance and a high content of Ni can also promote corrosion **resistance**. In the absence of both these elements, corrosion resistance of these glasses significantly decreases. **Hence** it is thought worthwhile to examine the corrosion behaviour of the metallic glass system which is free from elements like P and Cr and having low Ni **content**. Also not much work has been reported in such **systems**. For any long term practical application, which is based on the glassy state of Fe-rich metallic glass, it requires a very stable glassy **state**. As many of the promising physical and chemical properties of these materials deteriorate due to crystallization, understanding of the crystallization behaviour and the thermal stability against crystallization of these materials is of importance both from fundamental and technical point of **view**. Understanding the mechanisms involved in the crystallization is therefore valuable in controlling crystallization, as the thermal stability against crystallization determines their effective working limits for technological applications. Some of the earlier reports indicate that Mo seems to enhance the thermal stability of these glasses. Another important factor is that it has been reported by Hasegawa et al [99] that in addition to their use in transformer cores, tape heads and magnetic shielding commercially, Mo substituted Fe-

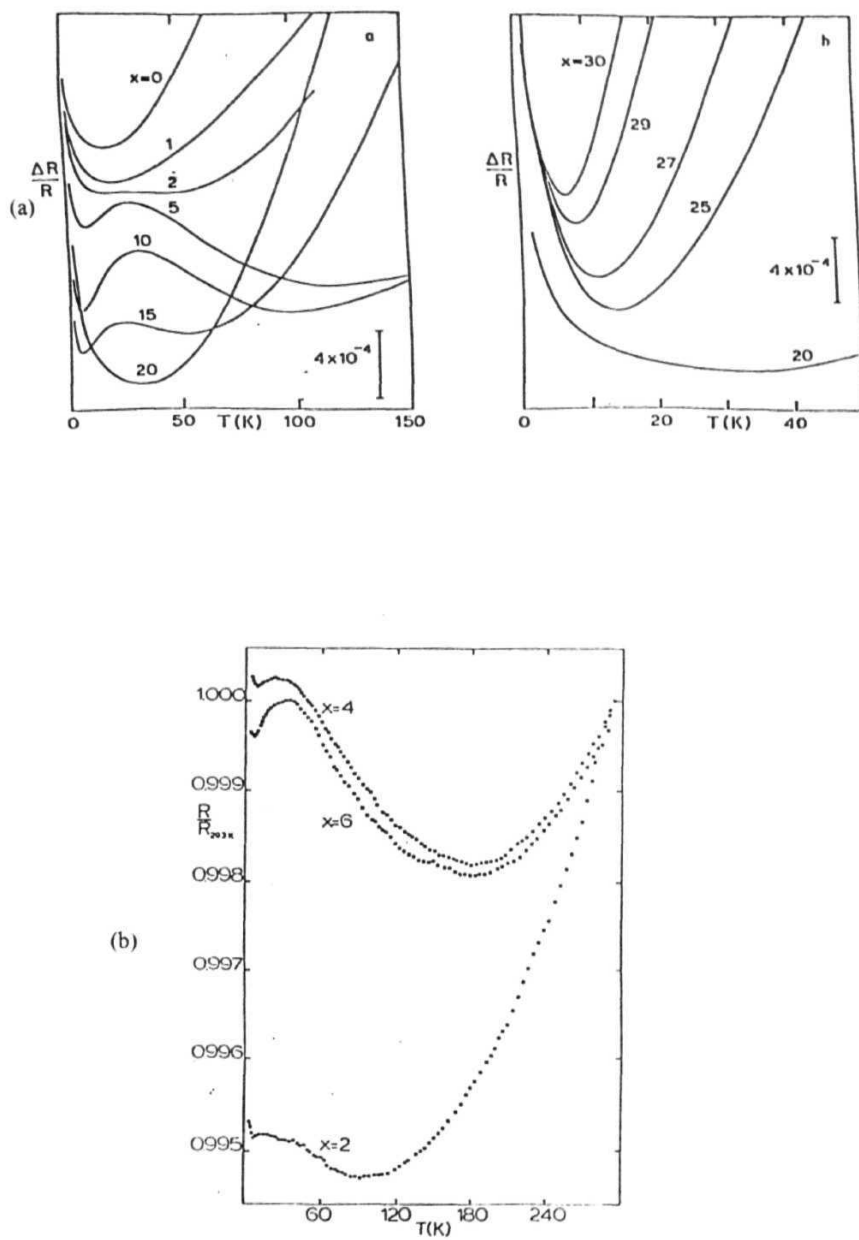


Fig. 1 (a) & (b) Temperature dependence of normalised resistivity of $\text{Fe}_{90-x}\text{Cr}_x\text{B}_{20}$ and $\text{Fe}_{90-x}\text{Mo}_x\text{B}_{20}$ alloys respectively.

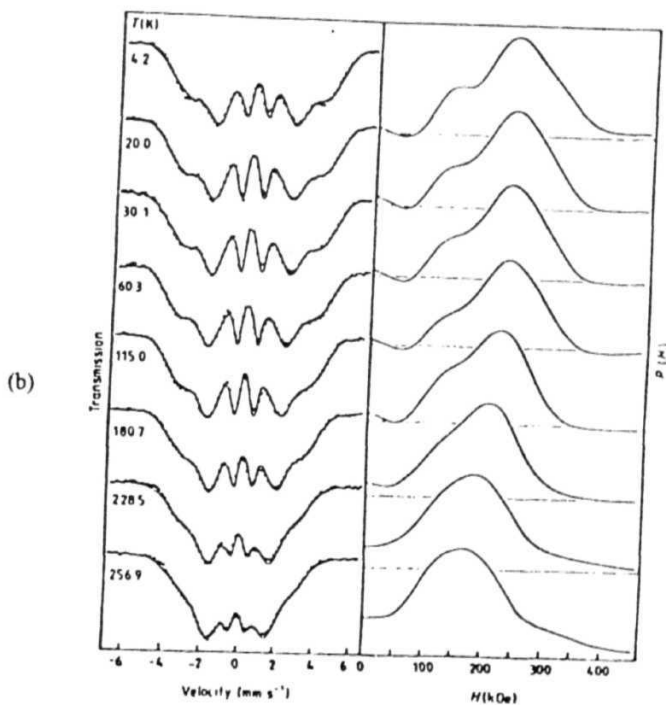
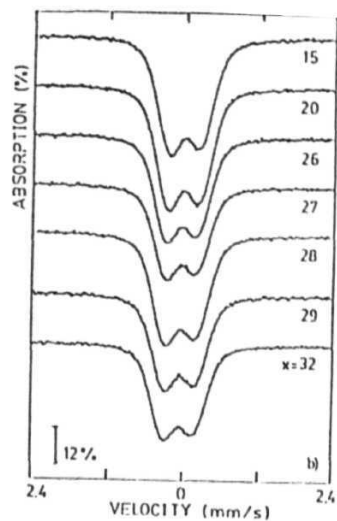
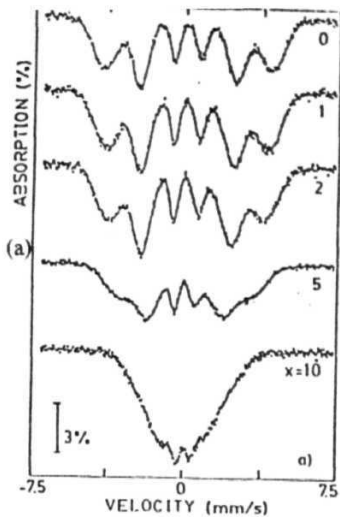


Fig 1.1 (a) & (b) Mössbauer spectra at RT of $\text{Fe}_{80-x}\text{Cr}_x\text{B}_{20}$ alloy and the corresponding spectra at different temperatures for the alloy $\text{Fe}_{73}\text{Mo}_7\text{B}_{20}$ with their $P(H)$ distribution curves respectively.

based glasses having remarkable soft magnetic properties combined with high resistivity and improved thermal stability are quite useful in high frequency electromagnetic applications (≥ 100 kHz) where conventional magnetic alloys cannot be used due to excessive eddy current losses. With the above factors in mind, it is therefore considered to be interesting to choose this particular system for the study of effect of Mo substitution on the various properties mentioned above

Objectives

The main objectives of the present work are as follows

- To verify the amorphous nature of the samples using X-ray diffraction (XRD) technique and a typical diffractogram for one such sample is shown in Fig. I 8
- To study the changes in electrical resistivity and its temperature dependence as a function of Mo concentration in the system chosen, in the temperature range 10-300 K using dc four probe method
- To study the changes in the magnetic properties as a function of Mo and to find out different magnetic hyperfine parameters and their temperature dependence, using magnetization and Mossbauer effect measurements The experimental setups used are VSM and Lakeshore ac susceptometer for magnetization at room temperature and low temperatures respectively and Mossbauer spectroscopy
- To investigate the crystallization behaviour of the samples chosen using the well known DSC technique, which gives quantitative information about the heat changes occurring, thus enabling us to determine the crystallization kinetic parameters precisely
- To study the corrosion behaviour of the samples chosen through electrochemical corrosion methods, using potentiodynamic polarisation and ac impedance spectroscopic techniques

In all the above, results have been analysed mainly as a function of composition and temperature and the effect of the substitution of Mo is discussed A discussion of the results is presented in the light of the current theoretical models

The results of the present work include

- i Determination of (1) Absolute resistivity at RT, $\rho(RT)$, (2) Temperature

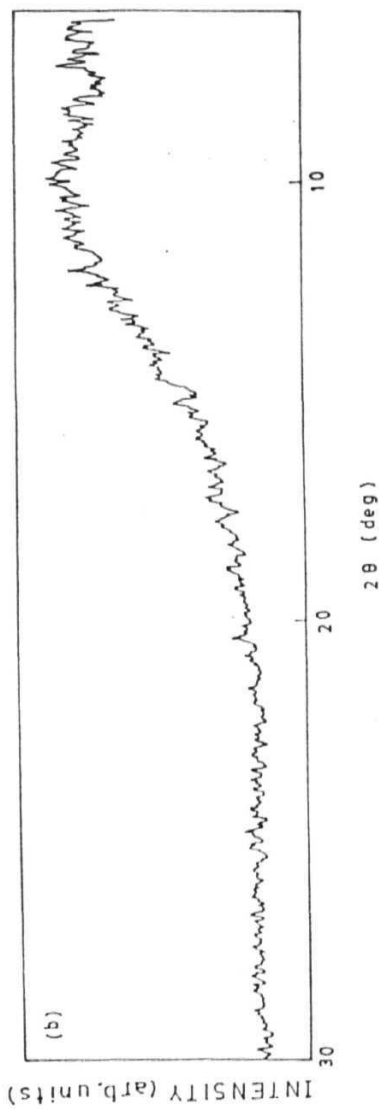
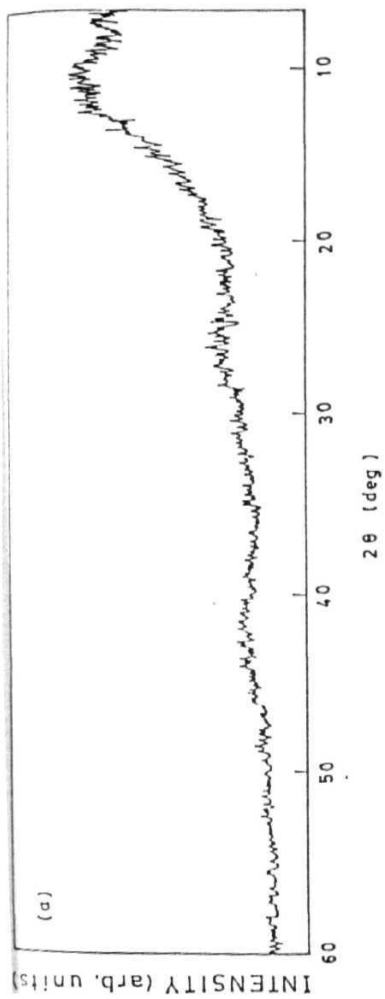


Fig. 1.8 XRD pattern of sample $\text{Fe}_{0.8}\text{Ni}_{1+x}\text{Mo}_x\text{Si}_2\text{B}_{16}$ ($x=2$) (a) shiny side (b) dull side.

- coefficient of resistivity (TCR), α at RT, (3) Temperature corresponding to minimum resistivity, T_{\min} ; (4) Debye **temperature**, Θ_D , (5) ρ_{mag} , magnetic contribution to resistivity, and the dependence of the above parameters on Mo concentration
- ii Determination of various **hyperfine** parameters viz., effective magnetic **hyperfine** field, H_{eff} , average and peak fields, H_{av} and H_p , and the hyperfine field distribution, $P(H)$, **isomer** shift, δ , and magnetization axis as a function of temperature and other Mossbauer **parameters**
 - iii Determination of room temperature magnetization, $M_s(\text{RT})$ and spontaneous magnetization $M_s(0)$ and their dependence on composition and the existence of the spin wave excitations through bulk magnetization **measurements**
 - iv Determination of various crystallization kinetic parameters viz., onset and crystallization temperatures, activation energies, as a function of Mo concentration and heating rate and an estimation of **Avrami exponent**, n
 - v Determination of polarisation resistance, R_p , and other related corrosion kinetic parameters, like corrosion potential, E_{corr} , corrosion current density, i_{corr} , Tafel slopes β_a and β_c . A correlation is made between the values of α'' polarisation resistance obtained from **potentiodynamic** polarisation and ac impedance spectroscopic **measurements**

Apart from the introduction chapter, the thesis contains five chapters. The second to the fifth chapters describe the results of the present work and discuss them under the headings of electrical resistivity, Mossbauer and magnetization, crystallization and corrosion **respectively**. The thesis presents the details of experimental arrangements and related details wherever necessary in the respective **chapters**. At the beginning of each chapter a brief discussion of theoretical background and important models widely used to interpret the data obtained is **included**. Each of these chapters includes a thorough discussion of the relevant experimental results and the conclusions are summarized. References are listed at the end of each **chapter**.

The last chapter contains the summary of the results of the present investigations with overall conclusions and towards the end some suggestions for further work are also indicated.

1.12 References

- 1 F E. **Luborsky** (ed) "*Amorphous Metallic Alloys*", **Butterworths and Co Ltd.**, London (1983) Chap 6, 451, 257, **372**
2. K Moorjani and J.M.D. Coey, "*Magnetic Glasses*", Elsevier, Amsterdam (1984)
- 3 **R** Hasegawa (ed) "*Glassy Metals: Chemical and Structural Properties*", CRC Press, Florida, USA (1983)
- 4 TR, **Anantharaman** (ed) "*Metallic glasses: Production, Properties, Applications*", Trans **Tech** Publications, Switzerland (1984) **81**
- 5 **W** Klement Jr., **R H** Willens and **P** Duwez, *Nature* **187** (1960) 869
- 6 **R** Jagannathan, *Proc. Indian Natn. Sci.Acad.*, 52 (1986) 192
- 7 **S.J** Campbell, **J.D** Cashion, **P.E** Clark, **R.J** Pollard and **IF** Smith (eds) "*Proc. of Int. (Conf. on the Applications of Mössbauer Effect*", Melbourne, Australia, (1987) {*Hyper Int.*, 42 (1988)).
- 8 **A.K** Bhatnagar (ed) "*Proc. of Int. Conf. on Metallic and Semiconducting Glasses*", Hyderabad, India, (1986) {*Key Engg. Mater.*, **B-15** (1985)
- 9, **T** Masumoto and **K** Suzuki (ed.), "*Proc. of 4th Int. Conf. on Rapidly Quenched Metals*", The Japan Institute of Metals, Sandai, Japan (1982) **Vol I and II**
- 10 **T** Kaneyoshi, "*Amorphous Magnetism*", CRC Press, Florida, **USA** (1984)
- 11 **S** Steeb and **H** Warlimont (eds) "*Proc. 5th Int. Conf. on Rapidly Quenched Metals*", Wurzbue, Germany (1984)
- 12 **B** Cantor (ed) "*Proc. 3rd Int. Conf. on Rapidly Quenched Metals*", Metal Society, London (1978) **Vol I** and **II**.
13. **M.G** Scott, "*Amorphous Metallic Alloys*", edited by F.E. Luborsky, Butterworths & Co , Ltd , London (1983) **144**
- 14 **G.O** Jones, "*Glass*", Chapman and Hall, London (1971) **57**
- 15 **MM.** Marcus and **D** Turnbull, *Mat. Sci. Engg.*, 23 (1976) 211
- 16 **H.A** Davies, "*Amorphous Metallic Alloys*", edited by F.E. Luborsky, Butterworths & Co., Ltd., London (1983) **8**
- 17 **H.** Rawson, "*Inorganic Glass-Forming Systems*", Academic Press, London

- (1967)
- 18 U Mizutani., *Prog. Mat. Sci.* **28** (1983) 97
 - 19 P Petrokovsky, *Rev. Sci. Instrum.*, **34** (1963) 445
 - 20 H S Chen and C E Miller, *Rev. Sci. Instrum.* **41** (1970) 1237
 - 21 H.H. Libermann and C.D Graham, Jr., *IEEE Trans. Mag.* **MAG-12** (1976) 921
 - 22 S. Kavesh, in '*Metallic Glasses*', edited by J J Gilman and H J Leamy, ASM, Metal Park, 36
 - 23 T Yamaguchi and K Narita, *IEEE Trans. Mag.*, **MAG-13** (1977) 1621
 - 24 B H Kear, J.W Mayer, J M Poate and P R Struti, "*Metallurgical Treatises*", edited by J K Tien and J F Elliot, AIME, Warrendale, Phoenix (1981) 321
 - 25 R Glang, "*Handbook of Thin Film Technology*", edited by L.I Maissel and R Glang, McGraw Hill, New York (1970)
 - 26 J L Vossen and W Kern, (eds) "*Thin Film Processes*", Part **II**, Academic Press, New York (1978)
 - 27 A Brenner, D.E. Couch and E K Williams, *J. Res. Nat. Bur. Std.*, **109** (1950)
 - 28 A Ali, W A Grant and P J Grundy, *Phil. Mag.* **B 37** (1978) 353
 - 29 W L Johnson, M Atzmon, M Van Rossum, B.P Dolgin and X L Yeh, "*Proc. 5th Int. Conf. on Rapidly Quenched Metals*", edited by S Steeb and H Warlimont Wurzbue, Germany (1984) 1515
 - 30 M Von Allmen, "*Glassy Metals II*", edited by H -J Guntherodt and H Beck, Springer Verlag (1983) 261
 - 31 J Wong, "*Glassy Metals I*", edited by H -J Guntherodt and H Beck, Springer Verlag, Berlin (1981) Chap 4.
 - 32 J D Bernal, *Nature*, **188** (1960) 910
 - 33 C J D scott, *Nature*, **194** (1962) 956
 - 34 J L. Finney, *Proc. Roy. Soc. London*, **A 319** (1970) 479.
 - 35 P.H. Gaskell, *J. Non-Cryst. Solids*, **32** (1979) 207
 - 36 L V Woodcock, *J. Chem. Soc. Faraday II*, **72** (1976) 1667

- 37 D S Boudreaux and J M Gregor,/. *Appl. Phys.*, 48 (1977) **5057**
- 38 L Von Heimendahl and J Hafner, *Phys. Rev. Lett.*, 42 (1979) **386**
- 39 S.N. Kaul, "Lecture Notes", workshop on Glassy materials held at IUC-DAEF, Indore, India (1994)
- 40 Oelhafen, "Glassy Metals I", edited by H.-J. Guntherodt and H Beck, Springer-Verlag (1981), H Beck and H -J Guntherodt, "Glassy Metals I", edited by H.-J. Guntherodt and H. Beck, Springer-Verlag (1981)15
- 41 "Glassy metals II", edited by H Beck and H.J Guntherodt, Springer-Verlag (1983)
- 42 Z Altounian, C L Foiles, W B Muir and J O Strom-Olsen, *Phys. Rev. B*, 27 (1983) 1955
- 43 J P Carini, S R Nagel, L K Varga and T Schmidt, *Phys. Rev. B*, 27 (1983) 7589
- 44 H -J Guntherodt and H U Kunzi, "Metallic Glasses", edited by O Parks, American Society of Metals, New York (1978) 247
- 45 R Hasegawa and C C Tsuei, *Phys. Rev. B*, 2(1970) 1631, 3 (1971) 214.
- 46 G S. Grest and S R Nagel, *Phys. Rev. B*, 19 (1979) 3571
- 47 R W Cochrane, R Harris, J O Strom-Olsen and M J Zuckerman, *Phys. Rev. Lett.*, 35 (1975) 676
- 48 R Aromoza, A Fert, I A Campbell and R Mayer,/. *Phys. F*, 7 (1977) L327
- 49 R Harris, and O J Strom-Olsen, "Glassy Metals II: Atomic Structure and Dynamics, Electronic Structure, Magnetic Properties", edited by H Beck and H.-J. Guntherodt, Springer-Verlag, Berlin (1983) 325
- 50 D G. Naugle,/. *Phys. (hem. Solids*, 45 (1984) 367
- 51 M A Howson and B L Gallagher, *Phys. Rep.*, 170 (1988) **265**
- 52 U Mizutani, *Prog. Mat. Sci.*, 28 (1983) 2, *Phys. Stat. Solidi. (B)*, 176 (1993) 9
- 53 A I Gubanov, *Sov. Phys. Solid State*, 2 (1960) 468
- 54 P Duwez and S.C.H Lin,/. *Appl. Phys.*, 38 (1967) 4096
- 55 S Mader and A.S Nowick, *Appl. Phys. Lett.*, 7 (1965) **57**

- 56 C C Tsuei and P Duwez, *J. Appl. Phys.*, 37 (1966) 43 5
- 57 B G Bagley and D Turnbull, *Hull. of Amer. Phys. Soc.*, 10 (1965) 1101
- 58 J.M.D. Coey, *J. Appl. Phys.*, 49 (1978) 1646
- 59 F E Luborsky, "*Ferromagnetic Materials*", edited by E.P Wohlfarth, North-Holland, Amsterdam (1980) Vol 1 451
- 60 H.O Hooper and A.M deGraaf, (eds) "*Amorphous Magnetism I*", Plenum Press, New York
- 61 R A. Levy and R Hasegawa, (eds) "*Amorphous Magnetism II*", Plenum Press, New York
- 62 R W Cahn, *Contemp. Phys.*, 21 (1980) 43
- 63 H S Chen, *Rep. Prog. Phys.*, 43 (1980) 353
- 64 R Boll and H Warlimont, *IEEE Trans. on Mag.*, **MAG-17** (1981) 3053
- 65 C Hargital, I Bakonyi and T Kemeny, (eds) "*Metallic Glasses: Sciences and Technology*", Central Research Institute of Physics, Budapest, Hungary (1980).
- 66 E M Gyorgy, "*Metallic Glasses*", edited by J J Oilman and H.J. Leamy, American Society of Metals, USA, 275, D R Uhlman and R W Hooper, "*Metallic Glasses*", edited by J J Oilman and H J Leamy, American Society of Metals, USA, 129
- 67 R Krishnan, "*Recent Advances in Materials Research*", edited by C M Srivastava, Oxford and IBM Publishing Co, New Delhi, India, 65
- 68 ML Spano and SM Bhagat, *J. Magn. & Magn. Mater.*, **24** (1981) 143
- 69 R W Grant, "*Mossbauer Spectroscopy*", edited by U Gonser, Springer-Verlag, Heidelberg, 77
- 70 J Durand, *J. de physique*, 41 (1980) C8-609
- 71 J Durand and P Pannisod, *IEEE Trans. Mag.*, **MAG-17** (1981) 2595
- 72 F E Luborsky, *IEEE Trans. Mag.*, **MAG-14** (1978) 1008
- 73 F.E Luborsky, J J Becker, P G Frischmann and L A Johnson, *J. Appl. Phys.*, **49** (1978) 1769.
- 74 C.D Graham and T Egami, *J. Magn. & Magn. Mater.*, 15-18 (1980) 1325

- 75 T Mizoguchi, A.I P., *Conf. Proc.*, **34** (1976) **286**
- 76 T Egami, *Rep. Prog. Phys.*, **47** (1984) **160**
- 77 K Handrich and S Kobe, (eds) *"Amorphous Ferro- and Ferrimagnetika"*, Akademic Verlag, Berlin, (1980)
- 78 R Hasegawa, (ed) *"Glassy Metals: Magnetic. Chemical and Structural Properties"*, CRC, Boca Raton, Florida (1983)
- 79 A.R Ferchmin and S Kobe, (eds.) *"Amorphous Magnetism and Metallic Magnetic Materials - Digest"*, selected topics in Solid State Physics, Vol. 17 North-Holland, Amsterdam (1983)
- 80 S. Kobe, A R Ferchmin, H Nose and F Stobiecki, *J. Magn. & Magn. Mater.*, 60(1986) **1**
- 81 U Koster and U Herold, *"Glassy Metals II"*, edited by H -J Guntherodt and H. Beck, Springer Verlag, (1983) **225**
- 82 M G Scott, *Appl. Phys.*, 38 (1967) **144**
- 83 U Koster, *Key Engg. Mat.*, 13-15(1987)**281**
- 84 K Hashimoto, *"Amorphous Metallic Alloys"*, edited by F.E Luborsky, Butterworth & Co., London, (1983)**Chap 24**
- 85 R B Diegle, N.R Sorensen, T Tsuru and R M Latanision, *"Treatise of Material Science and Technology, Vol 23, Corrosion : Aqueous Processes and Passive Films"*, edited by J Scully, Academic Press, New York (1983) **59**
- 86 K Hashimoto and T Masumoto, *"Ultra Rapid Quenching of Liquid Alloys", "Treatise of Material Science and Technology", Vol 20*, edited by H Herman, Academic Press, New York (1981)**291**
- 87 M Naka, K Hashimoto K Asami and T Masumoto, *Physique*. 41 (1980) **862**
- 88 K Hashimoto, K Asami, M. Naka and T Masumoto, *Corrsion Sci.*, 19 (1979) **857**.
- 89 K Asami, K Hashimoto, T Masumoto and S Shimodaira, *Corrosion Sci.*, 16 (1976) **71, 909**
90. M Naka, K Hashimoto and T Masumoto, *J. Non-Cryst. Solids*, 29 (1978) **61**
- 91 K Hashimoto, M. Naka, K Asami and T Masumoto, *Corrsion Sci.*, 19 (1979) **165**

- 92 M Naka, K Hashimoto and T Masumoto, *J. Non-Cryst. Solids*, 28 (1978) 403
- 93 M Naka, K Hashimoto and T Masumoto, *J. Non-Cryst. Solids*, 31 (1979) 355
- 94 J S Dugdale, D Pavuna and P Rhodes, *Endeavour, New Series*, 9 (1985) 62
- 95 T R. Anantharaman and C Suryanarayana, (eds) "*Rapidly Solidified Metals*", Trans Tech Publications, Switzerland
- 96 K.I Arai, N Tsuya, M Yadama and T Masumoto, *IEEE Trans. Mag.*, **MAG-12** (1976) 936
- 97 N Tsuya, K.I. Arai and T. Oshaka, *IEEE Trans. Mag.*, **MAG-14** (1978) 948
- 98 M Kikuchi, K Fukamichi and T Masumoto, *Science Reports of the Research Institute of Thoku University*, A 27 (1979) 210
- 99 R Hasegawa, G.E. Fish and V R V Ramanan, "*Proc. of the 4th Int. Conf. on Rapidly Quenched Metals*", Vol II edited by T Masumoto and K Suzuki, The Japan Institute of Metals, Japan (1981) 929.
- 100 A.K. Das, "*Proc. of the 9th Int. Conf. on Rapidly Quenched & Metastable Materials*", Bratislava, Slovakia (1996) 3
- 101 J.J Gilman, *Metal Progress*. **116** (1979) 42
- 102 J J Oilman, *Science* **208** (1980) 856
- 103 F.E Luborsky and L. A Johnson, *J. de Physique-C olloques*, **C 8** (1980) 820

Electrical Transport Measurements

2.1 Introduction

Detailed investigations on transport properties of solids provide valuable information about the electronic structure and various scattering processes that are responsible for the electronic transport. Glasses, produced by rapid quenching, also show a full spectrum of electronic behaviour similar to that of crystalline **solids**. That is, glasses show properties, which range from those of a superconductor, normal metallic conductor, semiconductor to that of an **insulator**. Theoretical interpretation of the **electronic** transport in glasses has been a difficult problem due to the lack of translational invariance in their atomic arrangement. Another difficulty arises from the fact that the electron mean free path is very small in highly disordered glassy alloys. Studies on the transport properties of metallic glasses have shown some peculiar and

interesting features which seem to be **characteristic** of the glassy state [1-4] Among various transport coefficients, electrical resistivity is the one which is simpler in measurement and provides bulk of valuable information on the electronic transport. It is a sensitive probe to study structural disorders and various scattering processes that occur in a given material and to study phase transformations as well as phase **transitions**. However, it is by no means trivial to interpret the observed magnitude of resistivity and its temperature dependence in amorphous/highly disordered **metals**. This is because, in addition to the dependence on the intrinsic mechanisms involved, the electrical resistance is also sensitive to factors like possible differences in the free volume in an amorphous solid, as a consequence of different rates at which a melt has been rapidly quenched [5], structural relaxation [6], changes in local atomic arrangement [7], remnant crystallinity [8] and electron mean free path of the order of interatomic spacing in the solid [9], to name a **few**.

Resistivity studies on metallic glasses as a function of composition, temperature, magnetic field and other parameters have been reported extensively to understand their electronic transport **behaviour**. In particular, resistivities of iron-rich metallic glasses which are based on a composition $\text{Fe}_{80}\text{M}_{20}$ or close to it, where **M** is a single metalloid or a combination of metalloids like B, Si, P and C have been extensively reported in literature, in which element like Ni, **Cr** and Co have been partially substituted for Fe [10-17].

The behaviour of electrical resistivity of amorphous metallic alloys, is in general, quite different from that of the corresponding crystalline **systems**. First it is possible to produce metallic glasses for a given system like Fe-B, Fe-Si-B, Ni-Zr, Ni-P etc with a continuous range of room temperature resistivity values by changing composition within the range in which the amorphous nature is **preserved**.

A few of the salient features of the electrical resistivity data taken on a large number of metallic glasses with regard to the variation of electrical resistivity (ρ) with temperature can be summarized as below [2,18-21]

- (a) The room temperature resistivities, $\rho(\text{RT})$, and residual resistivities, ρ_0 , of amorphous alloys are considerably larger than those of their crystalline counterparts, but are of similar magnitude as that of the corresponding **liquids**.

This is because the dominant scattering mechanism responsible for resistivity is scattering from the structural disorder [2,18-21]

- (b) The overall change in the resistivity of a metallic glass from low temperature (-4 K) to that **near** at its **crystallisation temperature** is usually less than 10% [1]
- (c) The temperature coefficient of resistivity (**TCR**) in **some** metallic glasses can be changed continuously from positive to negative by changing **its** composition continuously like in Ni-P system [21-a] The temperature coefficient of resistivity, (TCR), defined as $\alpha = \rho^{-1}(d\rho/dT)$, is **small** and usually positive **for** alloys with $\rho_0 < 150 \mu\Omega\text{-cm}$ and negative for alloys with $\rho_0 > 150 \mu\Omega\text{-cm}$, over a wide range of temperature [3,4,17,22] Such a relation between the magnitude of ρ_0 and TCR has **come** to be known as **the** Mooij correlation [23]
- (c) In a number of alloys containing large amounts of ferromagnetic and antiferromagnetic elements, resistivity as a function of temperature goes through a minimum (ρ_{\min}), **at** a temperature T_{\min} in the temperature range 4-300 K, below which ρ shows either **ln T** or **T^{-1}** dependence with temperature [24-27] and at higher temperatures resistivity saturates to a value $\approx 150 \mu\Omega\text{-cm}$

The resistivity minimum in most of the 3d transition metal-metalloid alloys occur at temperatures as low as 20 K [2,19-21,28,29], but in some transition metal based alloys containing Cr, Mn, Mo, V, W, **etc** the resistivity minimum can occur at temperature $T > 250$ K [2,19-21,30] A number of theoretical models have been proposed to explain the resistivity minimum, and the corresponding low temperature resistivity anomaly and other characteristic features of resistivity behaviour in amorphous materials, but none of these models, on its own, can describe the variation of resistivity in the entire temperature **range** **Matheissen**'s rule which states that the contributions to total resistivity of a solid arising from different scattering mechanisms are additive, is also considered to be valid in amorphous solids Therefore, one needs to take into account of all possible known scattering mechanisms to explain the observed resistivity behaviour as a function of temperature, magnetic field **etc**

In this chapter we present the results of resistivity measurements on a-

Fe₆₈Ni_{14-x}Mo_xSi₂B₁₆ (**x=0,1,2** and 3) as a function of Mo concentration and temperature and try to interpret these within the framework of current theoretical models **available**

2.2 Theoretical Models

Over the years a number of theories have been proposed to interpret the experimentally observed anomalous resistivity behaviour in amorphous metallic alloys, magnetic as well as non-magnetic, as a function **of** composition and to predict the exact form of its temperature **dependence**. These include

- i) **Ziman-Faber** diffraction model
- ii) Mott s-d scattering model
- iii) Two level tunneling model
- iv) Localisation and electron interaction/Quantum interference **effects**.

2.2.1 Ziman-Faber Diffraction Model

This model considers the effect of scattering **of** conduction electrons from the potential of the disordered **lattice**. Originally proposed by **Ziman** [31] for simple liquid metals, this theory is based on the following assumptions [2,21,31]

- a) The electronic transport properties can be described by the **Boltzmann** transport **equation**
- b) The interaction between the conduction electrons and ions can be described by a pseudo potential.
- c) The conduction electrons are assumed to be nearly free (i.e , $k_F \gg 1/\lambda$, k_F is the Fermi wave vector, λ is the electron mean free path) and the scattering potential is weak enough to be treated by first-order perturbation theory (Born approximation is **valid**)

Evans et al [32] extended the Ziman **theory** to include liquid transition metals in the transport properties of metallic glasses by using the **muffin-tin** potential and arrived at the following expression for resistivity [2,19,21,32,33]

$$\rho = \frac{30\pi \hbar^3}{m e^2 k_F^2 E_F \Omega} \sin^2[\eta_2(E_F)] S_T(2k_F) \quad (21)$$

where \mathbf{k}_F and E_F are the Fermi wave vector and Fermi energy respectively Ω is the atomic volume, $\eta_2(E_F)$ is the d partial-wave phase shift, describing the scattering of the conduction electrons by the ion-cores which carry a muffin-tin potential centered around each ion position and $S_T(2k_F)$ is the structure factor, at $\mathbf{k}=2\mathbf{k}_F$. The temperature dependence of ρ comes from the temperature dependence of $S_T(2k_F)$. Within the framework of the diffraction model, there are several ways [33] of calculating the $S_T(\mathbf{k})$. However, the one using a Debye Spectrum due to Nagel [33] yields the expression

$$S_T(\mathbf{k}) \simeq 1 + [S_0(\mathbf{k}) - 1] e^{-2W_{\mathbf{k}}(T)} \quad (22)$$

where $S_0(\mathbf{k})$ is the static (equilibrium) structure factor and $e^{-2W_{\mathbf{k}}(T)}$ is the Debye-Waller factor, with $W_{\mathbf{k}}(T)$ in the Debye approximation given by [28,34]

$$W_{\mathbf{k}}(T) = W_{\mathbf{k}}(0) + 4W_{\mathbf{k}}(0) \left(\frac{T}{\theta_D} \right)^2 \int_0^{\theta_D/T} \frac{z dz}{e^z - 1} \quad (23)a$$

where

$$W_{\mathbf{k}}(0) = \frac{3\hbar^2 k^2}{2M k_B \theta_D} \quad (2.3)b$$

where M is the atomic mass, θ_D is the Debye temperature, k is the wave vector and k_B is the Boltzmann constant. Substituting Eq (2.3) in Eq. (2.2), one obtains [28]

$$\rho_{str}(T) = \frac{30\pi \hbar^3}{m e^2 k_F^2 E_F \Omega} \sin^2[\eta_2(E_F)] [1 + S_0(2k_F) - 1] e^{-2[W(T) - W(0)]} \quad (2.4)$$

where ρ_{str} is the structural contribution to ρ and $W(T) = W_{2k_F}(T)$ and $W(0) = W_{2k_F}(0)$ are the values of $W_{\mathbf{k}}(T)$ and $W_{\mathbf{k}}(0)$ at $k = 2k_F$, respectively, i.e.,

$$W(0) = W_{2k_F}(0) = \frac{3\hbar^2 k_F^2}{2M k_B \theta_D} \quad (2.5)$$

dropping the subscripts $2k_F$ and str for simplicity, the temperature coefficient of resistivity (TCR), α , can be calculated from Eq (2.4) as [28]

$$\alpha = \frac{1}{\rho} \left(\frac{d\rho}{dT} \right) = 2 \left[\frac{1 - S_T(2k_F)}{S_T(2k_F)} \right] \frac{\partial W(T)}{\partial T}$$

$$= 8 \left[\frac{1 - S_T(2k_F)}{S_T(2k_F)} \right] \frac{W(0)}{T} \times \left\{ 2 \left(\frac{T}{\theta_D} \right)^2 \int_0^{\theta_D/T} \frac{z dz}{e^z - 1} - \frac{1}{e^{\theta_D/T} - 1} \right\}$$

Since $\frac{\partial W(T)}{\partial T} > 0$ for all temperatures, Eq (2.6) demonstrates that α is negative if

$S_T(2k_F) > 1$ and positive if $S_T(2k_F) < 1$. The relative positions of $2k_F$ and k_p , the wave vector at which the first peak in $S(k)$ appears, determines the sign of α . In other words, negative TCR is expected only when $2k_F$ lies close to k_p whereas a positive TCR is expected when $2k_F$ is far away from k_p .

In low and high temperature asymptotic limits, Eq (2.4) simplifies to:

$$\rho(T) \sim C + BT^2 \quad \text{for } T < \theta_D \quad (2.7a)$$

$$\rho(T) \sim C' + B'T \quad \text{for } T > \theta_D \quad (2.7b)$$

where the constants C , B , C' and B' are related to various parameters in Eq (2.4). Thus, according to the diffraction model, resistivity varies as T^2 at low temperatures and linearly at high temperatures. In order to facilitate a direct comparison with experiments, Eq. (2.4) is written in a different form [28] as

$$\begin{aligned} r(T) &= \frac{\rho(T)}{\rho(0)} = a_1 + a_2 e^{-2[W(T) - W(0)]} \\ &= a_1 + a_2 \exp \left\{ -8W(0) \left(\frac{T}{\theta_D} \right)^2 \int_0^{\theta_D/T} \frac{z dz}{e^z - 1} \right\} \end{aligned} \quad (2.8a)$$

$$\text{with} \quad a_1 = \left\{ 1 + [S_0(2k_F) - 1] e^{-2[W(T_0) - W(0)]} \right\}^{-1} \quad (2.8b)$$

$$\text{and} \quad a_2 = a_1 [S_0(2k_F) - 1] \quad (2.8c)$$

where $T_0 = 273.15$ K is the ice temperature

$$\text{or} \quad S_0(2k_F) = 1 + \frac{a_2}{a_1} \quad (2.9)$$

One can also estimate θ_D , for a given glass from the Eqs. (2.7)a and (2.7)b, since

$$\alpha = \frac{1}{\rho_{RT}} \left[\frac{d\rho}{dT} \right] = \frac{C}{\theta_D} \quad T \geq \theta_D \quad (2.10)$$

$$\beta = \frac{1}{\rho_{RT}} \left[\frac{d\rho}{dT^2} \right] = \frac{\pi^2}{6} \left(\frac{C}{\theta_D^2} \right) \quad T < \theta_D \quad (2.11)$$

where C is a constant. From Eqs. (2.10) and (2.11), we get

$$\theta_D = \frac{\pi^2}{6} \left(\frac{\alpha}{\beta} \right)$$

The **diffraction** model has been **successful** in describing the electrical resistivity behaviour of a large number of low resistivity ($\rho < 150 \mu\Omega\text{-cm}$) amorphous alloys. However, the model does not give an adequate description in the case of high resistivity glassy materials.

2.2.2 Mott **s-d** Scattering **Model**

This model, originally proposed by Mott [9] for transition metals and alloys, assumes that the current is carried by nearly free s electrons which are scattered from fluctuations in the local environment (arising from structural disorder) into the vacant states above the Fermi level in the d-band, resulting in high resistivities. In the case of transition metal alloys the electrical resistivity, ρ is composed of two parts, $\rho = (\rho_s + \rho_d)$, where ρ_s is the contribution from the sp-band and ρ_d is that from **d-band**. The basic assumption is that the **effective** mass of the **d-electrons** is too large for them to contribute significantly to the conduction process [22].

Since the number of vacant states in a d band is proportional to the d-density of states (DOS), $N_d(E_F)$, the electrical resistivity is proportional to $N_d(E_F)$. The temperature dependence of resistivity arises because of the shift in Fermi energy level, E_F , with increasing temperature. The expression for resistivity, given by this model is [2,9,21]

$$\rho_{\text{mott}}(T) = \rho(0) \left\{ 1 - \frac{\pi^2}{6} (k_B T)^2 \left[3 \left(\frac{N'(E_F)}{N_d(E_F)} - \frac{N''(E_F)}{N_d(E_F)} \right) \right] \right\}$$

$$\text{or} \quad \left\{ \frac{1}{N_d} \frac{dN_d}{dE} - \frac{1}{N_d} \frac{d^2 N_d}{dE^2} \right\}_{E_F} \quad (2.13)$$

where $N'(E_F)$ and $N''(E_F)$ are the first and second energy derivatives of DOS at $E = E_F$ respectively.

If one assumes that d band is nearly full, and that $N_d(E) = C(E_0 - E_F)^{1/2}$, where $E_F < E_0$, then Eq (2.13) reduces to

$$\rho(T) = \rho(0) \left[1 - \frac{\pi^2}{6} (k_B T)^2 (E_0 - E_F)^{-2} \right] \quad (2.14)$$

where E_0 is the energy of the filled d-band **level**

Thus, $\rho(T)$ should decrease as T^2 with increasing T . **If** one includes the effect of temperature dependence and smearing of the d band density of states [35] one finds that it leads to a contribution of $\rho(T)$ which can either increase or decrease with T in a manner consistent with Mooij **correlation**

This model gives rise to a large negative value of TCR if the Fermi level lies in a region where the d band is rapidly varying. However, such a model would be applicable only to those systems where there is a significant difference in the mobilities of the s and d **electrons**. For very high resistivity materials, where all mobilities are very low, this model breaks down. The energy derivatives of $N_d(E)$ at E_F for amorphous metals are expected to be extremely small, and hence, the Mott model when applied to amorphous materials gives a weak temperature dependence of resistivity [21]

2.2.3 Two Level Tunneling Model

The observation of resistivity minimum in a large number of amorphous alloys, regardless of whether they are magnetic or non-magnetic, has prompted some workers to propose scattering mechanisms, which are inherent to the amorphous structure itself. One such model is the two level tunneling model [25], which is the structural analogue of the Kondo model [36]. The amorphous state is a highly **metastable** state and there exists a number of local atomic configurations which are energetically equivalent leading to significant number of atoms or group of atoms which can tunnel between the states of equivalent **energy**. In the simplest form they constitute the two level systems (TLS) [2,20,21,24]. The TLS model due to Cochrane et al [25] considers a potential well with two minima of equal energy and asserts that the electron scattering by such two level states is analogous to Kondo scattering, giving rise to a contribution to the resistivity, which increases with decreasing **temperature**. This approach leads to the following expression for the contribution to the total resistivity arising from electron-TLS scattering [2,20,21,25]

$$\rho_{\text{TLS}}(T) = -C \ln(k_B^2 T^2 + A^2) \quad (2.15)$$

where C is a constant, whose magnitude depends only on the number of sites and the strength of Coulomb interaction, $2k_B\Delta$ is the energy splitting between the tunneling states. If Δ is small, then $p(T)$ will vary as $-\ln T$, C being a new constant. Tsuei [27] has suggested that this mechanism is most probably responsible for producing a $\text{TCR} < 0$, i.e., negative over a wide temperature range in high resistivity metals. He found that a better fit to the resistivity data of amorphous $(\text{Ni}_{50}\text{Pd}_{50})_{73.5}\text{P}_{26.5}$ is given by the resistivity contribution of the form,

$$p(T) = \rho_0 \ln(k_B T^2 + \Delta^2) \quad (2.16)$$

rather than $p(T)$ proportional to T at higher temperatures as predicted by the Ziman theory.

Thus, this model predicts that resistivity increases as the temperature is lowered and finally saturates at low temperatures.

2.2.4 Weak Localisation and Quantum Interference Effects

In highly disordered systems in which the electron mean free path is of the order of atomic spacing, motion of electrons at low temperatures is diffusive rather than ballistic [21] and this realization has prompted many workers [37-40] to propose quantum corrections to the normal Boltzmann conductivity, arising from enhanced electron-electron interaction (EEI) effects and quantum interference (QI or weak localisation (WL)) effects. The conduction electrons in disordered systems with high values of resistivity undergo more frequent collisions than in crystalline systems. Such an increased scattering reduces the effective electronic screening and thus enhances the electron-electron interactions. The enhanced electron-electron interaction gives rise to an additional contribution to conductivity, which can be expressed as [38]

$$\Delta\sigma_{\text{EEI}}(T) = [\sigma(T) - \sigma(0)]_{\text{EEI}} = \frac{e^2}{4\pi^2\hbar} \left(\frac{1.294}{\sqrt{2}} \right) \left(\frac{4}{3} - \frac{3}{2} \bar{F}_\sigma \right) \left(\frac{k_B T}{\hbar D} \right)^{1/2} \quad (2.17)\text{a}$$

$$\bar{F}_\sigma = \frac{32}{3F} \left[\left(1 + \frac{1}{2} F \right)^{3/2} - \frac{3}{4} F - 1 \right] \quad (2.17)\text{b}$$

where F is the average static screened Coulomb interaction potential, over the Fermi surface and D is the diffusion constant. Eq. (2.17)a rewritten in the following form represents the EEI contribution to resistivity,

$$\frac{\rho_{\text{EEH}}(T)}{\rho_{\text{EEH}}(0)} = 1 - \rho_{\text{EEH}}(0) \left(\frac{1294}{\sqrt{2}} \right) \left(\frac{4}{3} - \frac{3}{2} \bar{F}_\sigma \right) \left(\frac{k_B T}{\hbar D} \right)^{1/2} \quad (2.18)$$

The contribution of electron-electron interaction to total resistivity is thus proportional to \sqrt{T} . It turns out that the effect of this Coulomb anomaly is an additional contribution to the resistivity, which varies as $-T^{1/2}$ at low temperatures (below 20 K). This effect was first noticed by Rapp et al [41] in magnetic metallic glasses. Since then it has been found in a number of metallic glasses, magnetic and non-magnetic type.

In addition, electrons in disordered systems undergo multiple scattering when the electron mean free path is of the order of the interatomic spacing. At low temperatures, these collisions are elastic, and hence the electron wavefunctions retain their phase over large distances. Therefore, there exists a finite probability for the two partial waves of the electron, originating from a point (origin) and propagating in opposite directions on a given path, to return to the origin in phase and interfere constructively. In other words, multiple elastic scattering leads to phase coherence between the partial waves scattered from nearby ions and hence enhances the probability for an electron to return to its origin, hence of localisation [21]. The result of this electron localisation process is that the electrical resistivity in the presence of such scattering in disordered materials is higher than would be calculated from the quasi-classical Boltzmann approach. If the disorder is strong enough, the electrons can get completely localised leading to a transition from metallic to the insulating state. However, if the disorder is not sufficiently strong, the weak localisation or quantum interference effects leads to relatively higher resistivity. Since phase coherence is responsible for the weak localisation, this also means that any process, which destroys the phase coherence of the two electron partial waves will reduce the additional resistivity (due to localisation). A process, which is known to destroy the phase-coherence, is inelastic scattering. As the temperature is increased from absolute zero, the inelastic electron-phonon scattering sets in at finite temperatures which tends to destroy the phase coherence and thereby leads to an increase in conductivity or a decrease in the resistivity, a result opposite to the normally observed behaviour in metals in which the resistivity should increase with rise in temperature due to electron-phonon scattering.

Mott and **Kavesh** [42] and later Howson [43] made suggestions that the resistivity minimum in metallic glasses may be due to a competition between a negative TCR due to QIE. mentioned above, and a positive TCR due to the normal Boltzmann conductivity. Whether the conductivity is due to the QIE will dominate or the Boltzmann conductivity will dominate is determined by the ratio of inelastic scattering time to elastic scattering time (τ_i/τ_e). At low temperatures, τ_i is always greater than τ_e so **QIEs** may determine the behaviour of $\sigma(T)$. Mott and Kavesh [42] have predicted that $T_m \propto \rho^{5/2}$, where T_m is the temperature at which minimum resistivity is **observed**. Mickey et al [44] have shown that QIEs are not likely to be responsible for a low **temperature** resistivity minimum except in alloys with a very weak spin-orbit **coupling**.

A number of other scattering processes, such as inelastic **electron-magnon** scattering, external magnetic field and **Zeeman** splitting of spin sub-bands, can also destroy the phase coherence and delocalise the **electrons**. The final expression for the contribution to total resistivity arising from weak localisation in the presence of spin-orbit and inelastic scattering and including the splitting of spin sub-bands, is given by [39,40,45],

$$\rho_{WL}(T) = \rho_{WL}(0) \left[1 - \rho_{WL}(0) \left(\frac{e^2}{2\pi^2 \hbar} \right) \left(\frac{e}{\hbar} \right)^{1/2} (3\sqrt{B_2} - \sqrt{B_\phi}) \right] \quad (2.19a)$$

$$\text{with} \quad B_2 = B_{ie} + \frac{4}{3} B_{so} + \frac{2}{3} B_s \quad (2.19b)$$

$$B_\phi = B_{ie} + 2B_s \quad (2.19c)$$

where $B_j = \left(\frac{\hbar}{4eD\Gamma_j} \right)$; $j \equiv ie, so, s, \phi$ and $\Gamma_\phi, \Gamma_{ie}, \Gamma_{so}, \Gamma_s$ are the phase coherence, inelastic scattering, spin-orbit scattering and spin scattering times, **respectively**. If

$B_{so} \ll B \ll B_{ie}$, Eq (2.19a) reduces to

$$\rho_{WL}(T) = \rho_{WL}(0) \left[1 - \rho_{WL}(0) \left[\frac{e^2}{2\pi^2 \hbar} \right] (D\Gamma_{ie})^{-1/2} \right] \quad (220)$$

In the case of inelastic electron-phonon interaction, the relaxation time τ_{ep} varies as

$\tau_{ep}^{-1} \propto T^p$ (where p ranges from 2 to 4) for $T < \theta_D$ and

$$\tau_{\text{ep}} \propto T \text{ for } T > \theta_D$$

Thus, the resistivity due to weak localisation effects is of the form,

$$\rho_{\text{wl}}(T) \propto T^2 \quad \text{for } T < \theta_D \quad (2.21)\text{a}$$

$$\rho_{\text{wl}}(T) \propto T \quad \text{for } T > \theta_D \quad (2.21)\text{b}$$

The temperature dependence of $\rho_{\text{wl}}(T)$ and $\rho_{\text{int}}(T)$ due to weak localisation and electron-electron interaction effects predicted by Eqs (2.21) and (2.18), respectively, have been found in a number of metallic glasses [21,46]

2.2.5 Magnetic Contribution to Resistivity

The existence of significant magnetic contribution to the electrical resistivity in magnetically concentrated amorphous alloys like $\text{Fe}_{80}\text{B}_{20}$, though expected, has been ignored earlier [47]. Earlier workers [8,17] tried to explain the intermediate and high temperature dependence of resistivity in terms of the diffraction model [33], which takes into account not only the scattering of conduction electrons by the ion-cores that carry a muffin-tin potential but also the change in the shape of the structure factor, $S(k)$, with temperature. The reasons for this appear to be twofold: firstly in both magnetic and non-magnetic glasses, the resistivity shows same temperature dependence in the intermediate and high temperature regions. Secondly, the diffraction model yields quadratic and linear temperature dependence of ρ at low ($T \ll \theta_D$) and high ($T > \theta_D$) temperature, respectively. There are several works, which contradicted the simple T^2 dependence of resistivity for ferromagnetic alloys at intermediate temperature [32,48]. A sharp anomaly in the temperature derivative of resistivity at the Curie temperature, reminiscent of the critical resistivity behaviour, normally found in crystalline ferromagnets, has been observed in such glasses [49]. These observations assert that in addition to a contribution due to scattering of conduction electrons from the structural disorder, electron magnon scattering (which at low temperatures gives rise to a quadratic temperature dependence for crystalline ferromagnetic 3d transition metals) should also give a contribution to ρ in magnetic glasses and hence the approach of completely neglecting the magnetic contribution to resistivity, $\rho_{\text{mag}}(T)$, while analyzing the resistivity data on FM glasses is not exactly correct. Theoretical investigations [50,51] that pursue this line of thinking and use

spin-wave approximation to calculate $\rho_{\text{mag}}(\mathbf{T})$ for amorphous **ferromagnets** is given below

The spin-disorder model, applicable to **FM materials**, deals with the scattering of conduction electrons by spin **waves**. The spin-disorder model for amorphous ferromagnets developed by Richter et al [51], considers a **Heisenberg** spin system in which spins are localised at the sites of an amorphous network and conduction electrons get scattered from these localised spins (moments) through the s-d exchange **interaction**. Using the nearly free electron concept, the magnetic part of resistivity in the spin-wave approximation is given by [28,51]

$$\rho_{\text{SD}}(\mathbf{T}) = \rho_{\text{SD}}(0) \left\{ 1 + \frac{\Omega_c}{(2\pi)^2 S} \Gamma\left(\frac{3}{2}\right) \zeta\left(\frac{3}{2}\right) \left(\frac{k_B T}{D_{\text{sw}}}\right)^{3/2} + \frac{1}{J_s(2k_F)} \left[\frac{\pi^2}{3S} \left(\frac{k_B T}{D_{\text{sw}}}\right)^2 - F(\mathbf{T}) \right] \right\} \quad (2.22)\text{a}$$

with

$$\rho_{\text{SD}}(0) = \left(\frac{2\Omega_c}{3h^3} \right) \left[\left(\frac{\Omega}{N_e} \right) m S J_{\text{sd}} \right]^2 J_s(2k_F) \quad (222)\text{b}$$

where N_e is the number of electrons, Ω_c and Ω are the atomic and sample volumes, respectively. S is the spin of the local atomic magnetic moment, D_{sw} is the spin wave stiffness coefficient, Γ and ζ are the gamma and **Riemann Zeta** functions, respectively,

J_{sd} is the exchange coupling constant and $J_s(2k_F) = \int_0^{2k_F} k^3 S_m(k) dk$, $S_m(\mathbf{k})$ is the static

magnetic structure **factor**. The $T^{3/2}$ term in the **Eq** (2.22)a is the net result of a partial cancellation of two competing $T^{3/2}$ terms, one arising from incoherent (momentum non-conserving) **electron-magnon** scattering and increasing with increasing temperature, and the other originating from the elastic scattering of conduction electrons from randomly oriented temperature dependant local moments decreasing with increasing temperature, whereas the T^2 term in **Eq** (2.22)a is the coherent **electron-magnon** scattering **term**. The function $F(\mathbf{T})$, arising because of structural disorder, constitutes only a minute correction to the T^2 term indicating thereby that the coherent electron-magnon scattering is not significantly altered by the presence of quenched disorder. Both $\rho_{\text{SD}}(0)$ and the $T^{3/2}$ term are zero for crystalline **ferromagnets**

but possess finite values in the case of amorphous ferromagnets. In addition, the coefficient of T^3 term in amorphous magnets is expected to be roughly two orders of magnitude [51] larger than that of T^2 term. Thus, the spin-disorder model predicts that at low temperatures, $\rho_{SD}(T)$ should vary as T^3 in amorphous ferromagnets in contrast with the T^2 variation in crystalline systems [28,51]. However, measurements on some magnetic metallic glasses reveal that the competing contributions to $\rho_{mag}(T)$ due to the incoherent and elastic components of electron-magnon scattering almost balance each other so that at low temperatures the T^3 term is negligibly small compared to the T^2 term [28].

In addition to the above models, other theoretical works, viz the Kondo-Spin Flip model [36], the coherent exchange scattering model [52] have also been proposed which calculate the magnetic contribution to ρ in dilute magnetic alloys and rare earth based alloys respectively.

2.3 Experimental Details

Electrical resistivity measurements for $a\text{-Fe}_{68}\text{Ni}_{14-x}\text{Mo}_x\text{Si}_2\text{B}_{16}$ ($x=0,1,2$ and 3) have been carried out in the temperature range 10-300 K using a API closed cycle refrigerator [53], the schematic diagram of which is shown in Fig 2.1. Samples were in thin ribbon form of ~25-30 μm thickness and ~5 mm width obtained from Allied Signals, (USA), prepared by melt spinning technique.

The closed cycle refrigerator works on the principle of Joule-Thomson effect. The cryogenic system is formed from basic modules which, include compressor modules, expander modules, inter-connecting hoses and interfaces. The high pressure helium gas from the compressor enters the refrigerator (expander) and the low pressure helium gas returns to the compressor. The inter-connecting hoses carry the refrigerant between the compressor module and the expander module. Together they form a closed-loop system.

The expansion of helium gas in the refrigerator has two stages one which cools the lower section of the sample well to 10 K and the other which cools the upper section of the sample well to 40 K.

The temperature of the sample area is controlled by using a resistance heater on

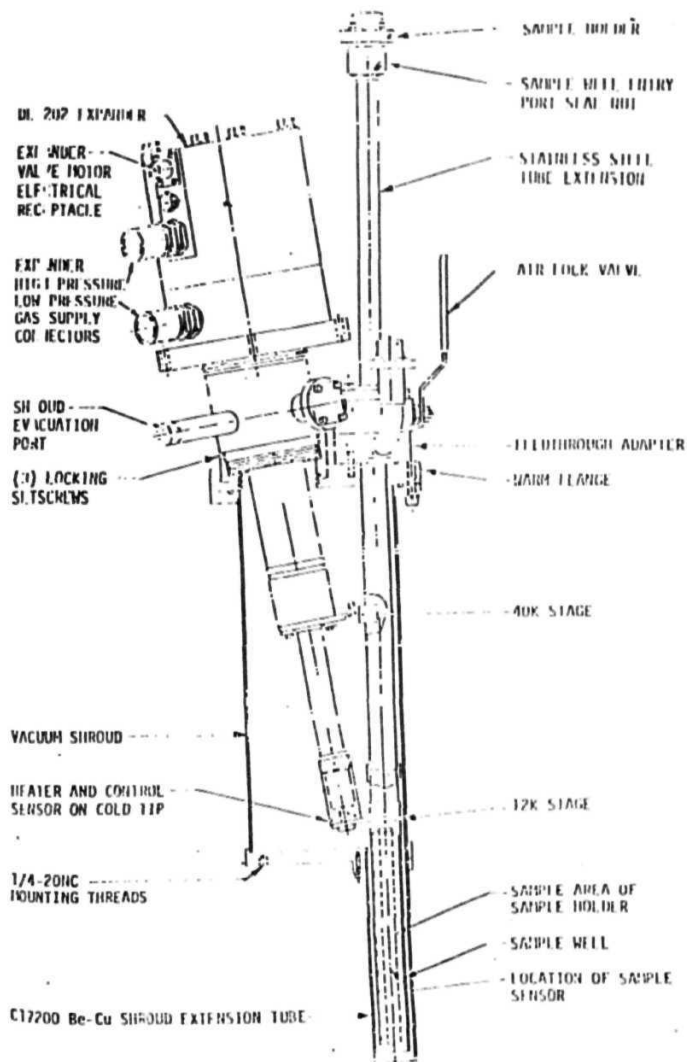


Fig. 2.1 Schematic diagram of closed cycle refrigerator.

the expander cold tip. Silicon diode is used as a temperature **sensor**. One sensor is located at the expander cold tip and the other is on the sample holder in the sample area.

A four probe **dc-method** was employed for the measurements. Amorphous ribbons of length 2-3 cm and 1-2 mm width were cut and to avoid local crystallisation and for better stability, current and voltage contacts were made on the sample with 42 gauge copper wire, using a silver **epoxy**. The sample is fixed to a sample holder using a scotch masking which can withstand low **temperatures**. The sample mounting permits changes in the sample dimensions during thermal cycling and thereby avoids stress-induced effects, which could otherwise affect the results in stress sensitive materials like metallic **glasses**. The sample space is filled with 99.99% pure helium as an exchange **gas**.

A schematic of the four terminal setup for electrical resistance measurements is shown in Fig. 2.2. The linearity of **I** vs **V** was checked for the contacts to be **ohmic**. The resistance was measured using a constant current programmable source (Keithley Model No 224) and a **nanovoltmeter** (Keithley Model No 181). The current during the measurement is kept constant (3 **mA**) up to one part in 10^4 and the voltage is measured to an accuracy of 0.01 μV and relative accuracy of 1 to 5 parts in 10^4 . Parasitic thermoelectric voltages are **eliminated** by reversing the polarity of current at a given temperature. The relative accuracy of resistance measurement is about a **few** parts per **million**. The temperature is monitored using a microprocessor-based temperature controller (Model 5500-1-25) to an accuracy of ± 0.5 **K**.

In all the cases, the width of the sample and the length between the voltage leads for each measurement were measured using a travelling microscope with an accuracy of 0.01 **mm**. A number of readings were taken over the whole dimensions of the sample to get a good accuracy in these measurements. The measurement of thickness posed a problem because of thin **samples**. A sensitive screw gauge was used to measure thickness at various positions over the whole length in order to get a reasonably accurate average value of **thickness**. A better method would have been to measure the density and then to find out the **thickness**. However, since we are more interested in the temperature dependence of p , we did not follow the density method to find out the thickness due to small amount of the sample at our disposal. The error in

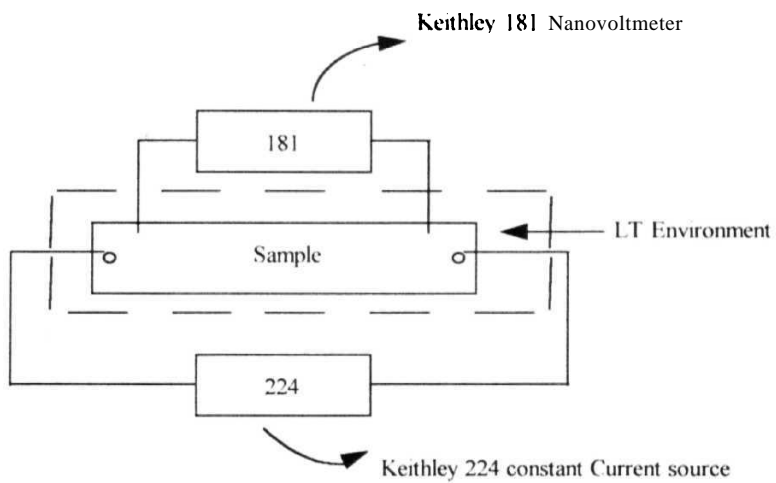


Fig 2 2 Four terminal setup to measure electrical resistance

the measurement of the absolute value of $\rho(RT)$ mainly determined by the error in the thickness measurement. The estimated error in the absolute value of ρ is $\pm 10\%$. However, the relative resistivity ratios are much more accurate and the error in these measurements is better than 1% neglecting any effects due to thermal expansion or contraction.

2.4 Results and Discussion

The resistance measurements of $\text{Fe}_{0.8}\text{Ni}_{1.4-x}\text{Mo}_x\text{Si}_2\text{B}_{16}$ alloys have been carried out in the temperature 10-300 K. A sample with x at% of Mo will be referred as **S_x**, sample **hereafter**. $\rho(RT)$ vs x is shown in **Fig. 2.3(a)** and are listed in Table (2.1). It is observed that an increase in Mo concentration increases $\rho(RT)$ as found earlier in similar Mo substituted **systems**. Since the values of $\rho(RT)$ are less than 150

one expects from Mooij correlation $\frac{1}{\rho} \frac{d\rho}{dT}$, the temperature coefficient of resistivity

(TCR), to be positive near RT, Table (2.1) lists $\frac{1}{\rho} \frac{d\rho}{dT}$ for all the samples. It is seen

that for all the samples $\text{TCR} > 0$ as expected from Mooij's correlation. As can be seen from **Fig. 2.3(a)** one also notes that as Mo concentration x increases, which leads to increase in $\rho(RT)$, the corresponding TCR decreases which is also consistent with Mooij's correlation. The $\rho(RT)$ vs TCR is also shown in **Fig. 2.3(b)**. **Fig. 2.4** shows the resistivity ratio $\text{RR} = \rho(T)/\rho(300)$ vs T in the temperature range 10-300 K for $x = 0, 1, 2$ and **3**. $x=4$ did not give repeatable results, hence data on this sample is not **discussed**. This was most probably the result of some crack developing along the length of the sample since the sample was a wide one and was prepared by a two nozzle **method**.

Fig. 2.4 clearly shows that in most of the higher temperature region (200-300 K) RR is almost linear with small **scatter**. **Lower** the value of x , larger is the 'almost' linear region in **temperature**. RR shows a minimum in RR vs T data, and the **temperature** at which this minimum is observed, depends upon the Mo concentration x . This temperature shall be referred as **T_{min} hereafter**. Since the lowest temperature was limited to ~ 10 K, a larger amount of data could not be collected below **T_{min}** for $x=0, 1$

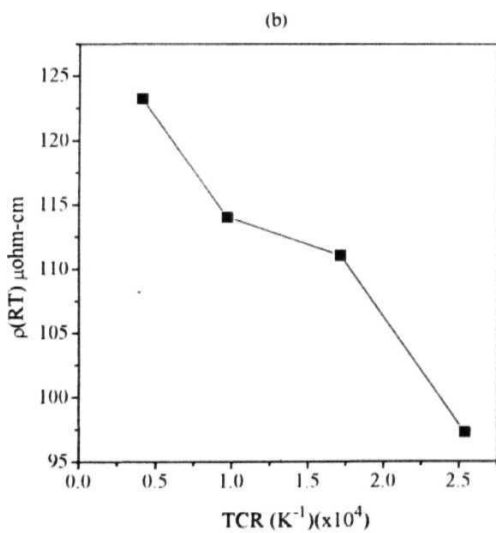
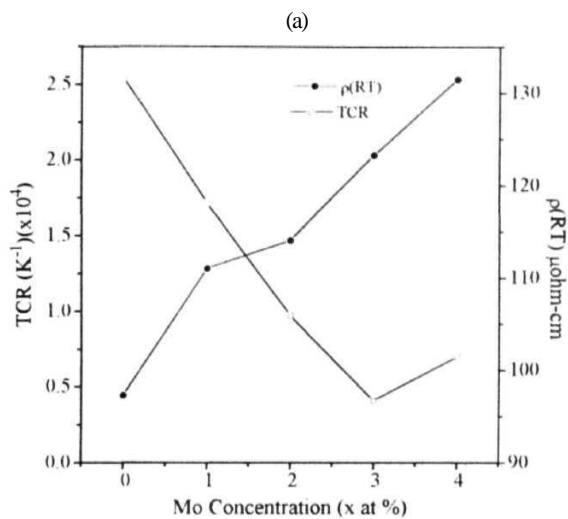


Fig 2 3(a) TCR at RT, (a) and Room temperature resistivity, $\rho(RT)$ as a function of Mo concentration, x

Fig 2 3(b) The plot of $\rho(RT)$ vs TCR

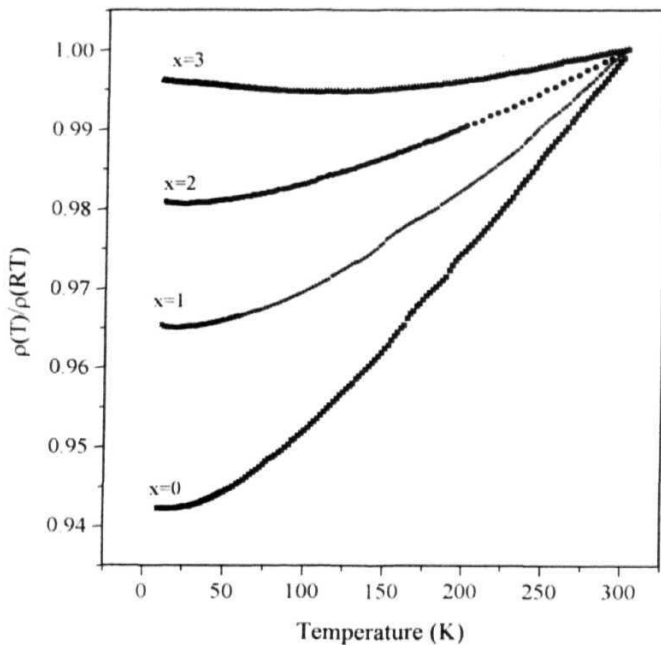


Fig 2.4 The resistivity ratio $RR = \rho(T)/\rho(RT)$ vs T in the temperature range 10-300 K for $\text{Fe}_{68}\text{Ni}_{14-x}\text{Mo}_x\text{Si}_2\text{B}_{16}$ ($x = 0-3$) alloys

Table 2.1 Different parameters calculated from resistivity data

Sample (x)	T_{\min} (K)	TCR(α) at RT (K^{-1})	$\rho(RT)$ $\mu\Omega\text{-cm}$	T_0 (K)	D (cm^2/s)
0	15	$2.538\text{e-}4$	97.3	332	$7.3\text{e-}4$
1	21	$1.724\text{e-}4$	111.0	390	$1.858\text{e-}4$
2	25	$0.9715\text{e-}4$	114.0	350	$3.8\text{e-}4$
3	•12	$0.4107\text{e-}4$	1233		$*5.15\text{e-}4$
4	110	$0.6962\text{e-}4$	131.5		$1.83\text{e-}4$

* represents for the first minimum of $x=3$ sample

and 2 samples. For $x=3$ sample, one seems to observe two minima, one at **110 K** and another a very weak one at about **12 K** as shown in Figs. 2.5(a) & (b) in which the curves drawn show for the smoothened data ρ vs T at higher temperatures becomes smaller as Mo concentration value x increases. The temperature dependence of ρ of the sample S_0 ($Fe_{0.8}Ni_{1.4}Si_2B_{16}$; $x=0$) is similar to that of other iron rich metallic glasses like $Fe_{80}B_{20}$ or $Fe-B-Si$. As x increases the resistivity minimum becomes flatter/shallower, and for the sample S_1 ($Fe_{0.8}Ni_{1.1}Mo_1Si_2B_{16}$; $x=3$), it is comparatively much flatter. To show this clearly ρ vs T data for S_1 is shown separately in Fig. 2.6 where the flat portion of the low temperature region where minimum is observed is indicated by dashed curve and the observed weak minimum at ~ 10 K with the minimum at **110 K** are indicated by the **arrows**. Similar observation has been reported in literature for Mo containing Fe-B glasses [11,54,55]. We analyse the temperature dependence of ρ of these samples using the theoretical ideas discussed earlier. For this we separate the temperature region in **three** (1) $T > 150$ K, (2) $T_{min} < T < 150$ K and (3) $T < T_{min}$.

2.4.1 Behaviour of ρ for $T \geq 150$ K

Figs. 2.7 and 2.8 show ρ vs T for $100 \text{ K} < T < 300 \text{ K}$ and $200 \text{ K} < T < 300 \text{ K}$ regions for the four samples **respectively**. One can easily see that while S_0 sample has ρ vs T linear region between 100 and 300 K, as x increases data starts to show departure from this linear behaviour more and more as one goes down in temperature from 300 K. This is clearly visible for S_1 sample. In the temperature region 200-300 K almost linear behaviour is observed for all the samples, although one observes a very small hump at ~ 250 K for S_1 sample. Since θ_D , the Debye temperatures for these samples are expected to be between 300-400 K as reported in literature [56,57], one may consider applying the **Ziman** theory in the temperature region $200 \text{ K} < T < 300 \text{ K}$ where $\rho \propto T$ may be expected although it should be strictly valid only in the region $T > \theta_D$. Since these glasses are highly magnetic there may be some contribution of the magnetic scattering to the total ρ . Hence, both contributions must be considered in analysing resistivity data as a **function of temperature**.

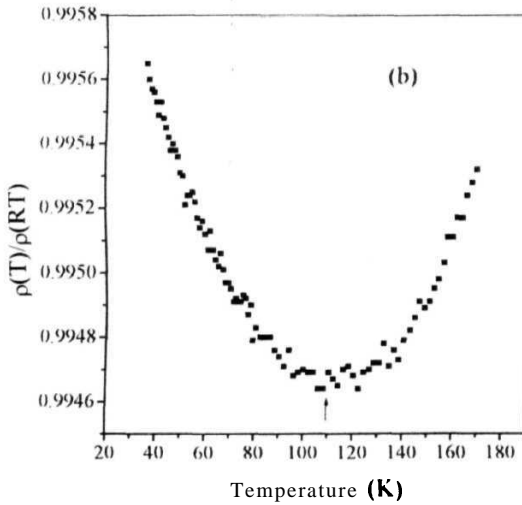
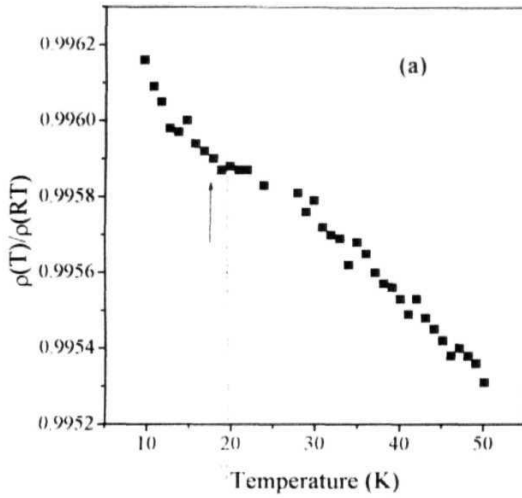


Fig 2 5(a) The resistivity ratio $RR = \rho(T)/\rho(RT)$ vs T in the temperature range 10-50 K showing the first T_{\min} for $\text{Fe}_{68}\text{Ni}_{14-x}\text{Mo}_3\text{Si}_2\text{B}_{16}$ ($x=3$) alloy

Fig 2 5(b) The resistivity ratio $RR = \rho(T)/\rho(RT)$ vs T in the temperature range 35-120 K showing the second T_{\min} for $\text{Fe}_{68}\text{Ni}_{14-x}\text{Mo}_3\text{Si}_2\text{B}_{16}$ ($x=3$) alloy

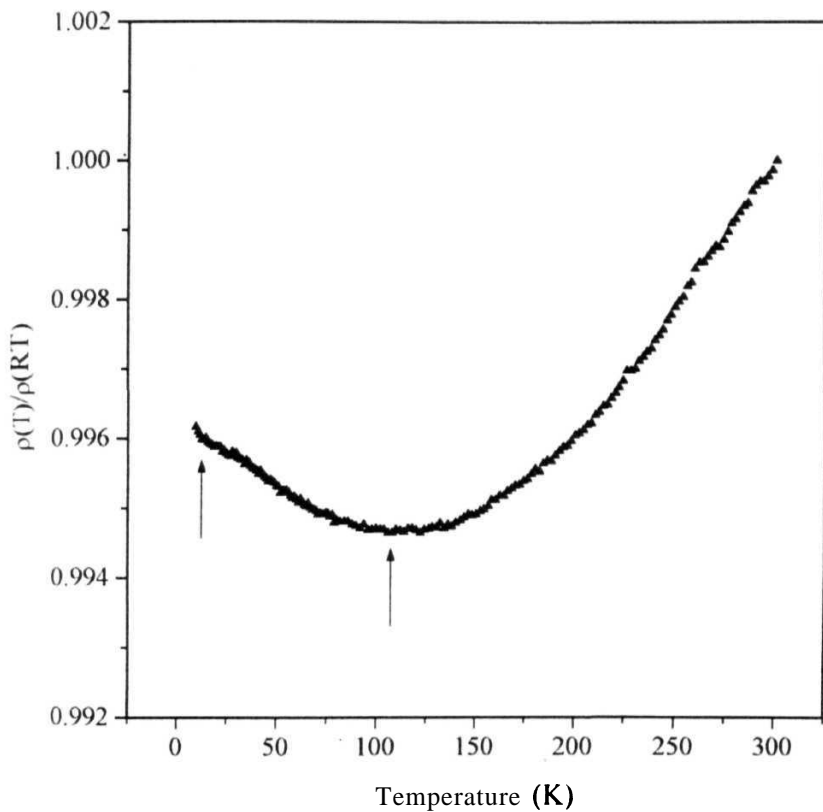


Fig 2.6 The resistivity ratio $RR = \rho(T)/\rho(RT)$ vs T in the temperature range 10-300 K for $\text{Fe}_{68}\text{Ni}_{14-x}\text{Mo}_3\text{Si}_2\text{B}_{16}$ ($x=3$) alloy with the minima indicated by the arrows in the respective regions

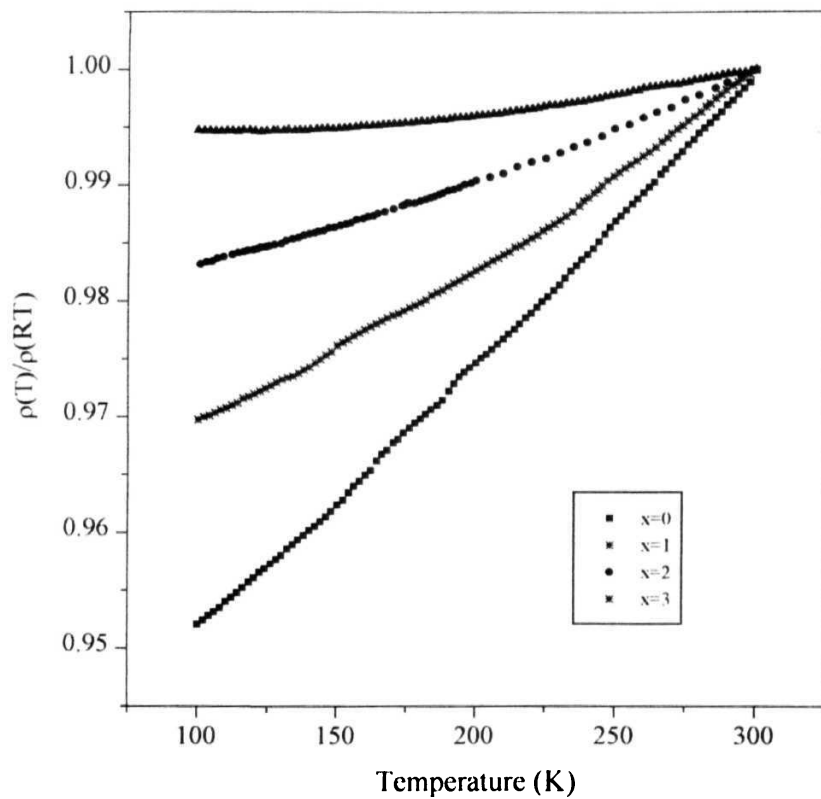
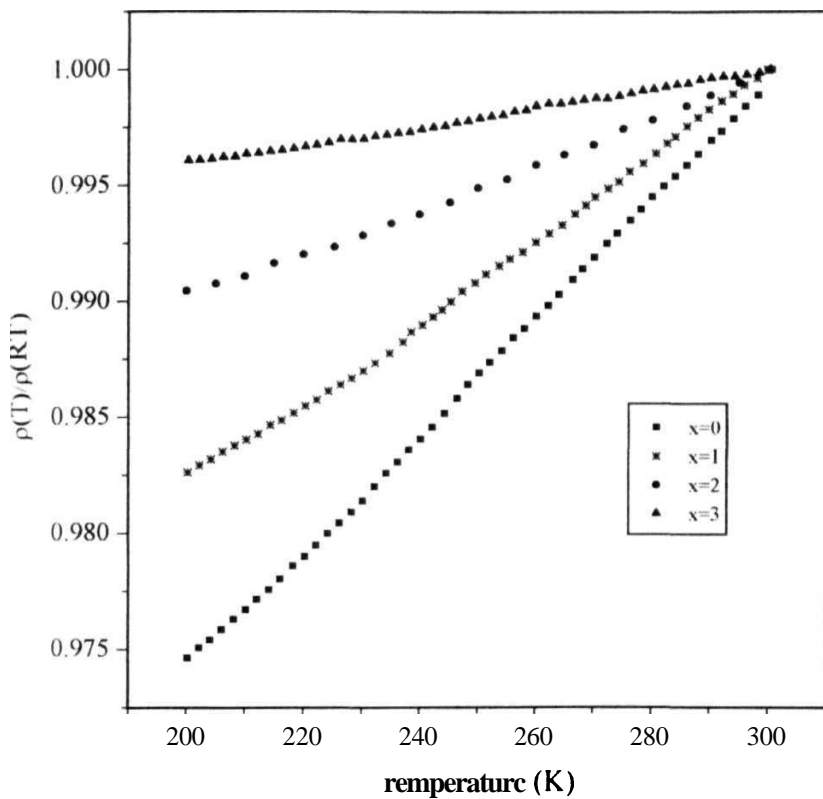


Fig 2 7 The resistivity ratio $RR=\rho(T)/\rho(300\text{ K})$ vs T in the temperature range 100-300 K for $\text{Fe}_{68}\text{Ni}_{14-x}\text{Mo}_x\text{Si}_2\text{B}_{16}$ ($x=0-3$) alloys



2 8 The resistivity ratio $RR=\rho(T)/\rho(RT)$ vs T in the temperature range 200-300 K for $\text{Fe}_{68}\text{Ni}_{14-x}\text{Mo}_x\text{Si}_2\text{B}_{16}$ ($x=0-3$) alloys

Experiments which claim to have observed a magnetic **contribution** to ρ fall under two categories

- (a) A magnetic contribution proportional to T^2 . Thummes et al [46] found qualitative evidence of a T^2 magnetic term in $\text{Ni}_{100-x}\text{Fe}_x\text{Si}_8\text{B}_{12}$ ($2.4 \leq x \leq 16$) metallic **glasses** Kaul et al [28] quantitatively found the same on FeBC **alloys** Bhatnagar et al [54] found T^2 term in FeNiMoSiB **alloys**
- (b) A magnetic contribution proportional to $T^{3/2}$. In Fe-Ni-P-B glasses Babic et al [48] obtained a $T^{3/2}$ term for $T < T_c/3$ Kettler and Rosenberg [58] found a $T^{3/2}$ term in Ni-based $\text{Ni}_{100-x}\text{Fe}_x\text{B}_{16}\text{Si}_4$ ($x=0-19$) and in $\text{Ni}_{77-x}\text{Fe}_x\text{B}_{13}\text{Si}_{10}$ ($x=0-15$) **systems** Also Das et al [46] and Rita Singhal et al [59] have discussed in detail about the T^2 and $T^{3/2}$ contribution to magnetic resistivity of Co-rich alloys and $\text{Fe}_{80}\text{B}_{20-x}\text{Si}_x$ alloys **respectively** The contribution of $T^{3/2}$ term to resistivity [$\rho_{\text{mag}}(T)$] is at least two orders of magnitude greater than the one arising from T term These theories predict $T^{3/2}$ power law for $\rho(T)$ at low temperatures in amorphous transition metal alloys which contrasts the T^2 dependence found in these **materials**

Thus, it is quite clear that a controversy still exists in deciding the relative weights of the magnetic contributions of the $T^{3/2}$ and T^2 terms to the total resistivity in ferromagnetic metallic **glasses** Although in our data, number of points are not very large we have still tried to fit our data to the combined contributions arising from the diffraction model and from the magnetic scattering.

According to Matheissen's rule

$$\rho(T) = \rho_{\text{str}}(T) + \rho_{\text{mag}}(T) \quad (2.23)$$

where $\rho_{\text{str}}(T)$ is the structural contribution and $\rho_{\text{mag}}(T)$ is the magnetic contribution to the electrical **resistivity** Since

$$\rho_{\text{str}}(T) \propto T \quad \text{Near RT} \quad (2.24a)$$

$$\rho_{\text{str}}(T) \propto T^2 \quad T < \theta_D \quad (2.24b)$$

$$\text{while} \quad \rho_{\text{mag}}(T) = aT^{3/2} + bT^2 \quad T < T_c \text{ (Curie temperature)} \quad (2.25)$$

Thus, total resistivity ratio, RR_1 can be written as

$$RR_T = \frac{\rho_{Total}(T)}{\rho_{Total}(300)} = A + BT + CT^2 + DT^{3/2} \quad T \geq \theta_D \quad (2.26)$$

Resistivity data for $200 \text{ K} < T < 300 \text{ K}$ has been fitted to $RR_T = A + BT$, $RR_T = A + BT + CT^2$ and $RR_T = A + BT + DT^{3/2}$ to see which expression gives lower χ^2 value. The fitted parameters are given in Table (2.2). The coefficient B of T in Eq (2.26) is of the order of 10^{-4} K^{-1} which also agrees well with earlier reported results [54]. It is seen that inclusion of either CT^2 or $DT^{3/2}$ term to $A + BT$ does improve χ^2 but very little, not by an order of magnitude. There does not seem to be much difference in fitting whether one chooses $T^{3/2}$ and T^2 term for ρ_{mag} . Thus our data is not able to distinguish between these two dependences of $\rho_{mag}(T)$. When we used $RR_T = A + BT + CT^2 + DT^{3/2}$ to fit the data unphysical results (negative coefficients) were obtained. Hence, both T^2 and $T^{3/2}$ contributions cannot be present in $\rho_{mag}(T)$ together. It is also seen from Table (2.2) that D, the coefficient of $T^{3/2}$ is about 3 orders of magnitude smaller than C, the coefficient of T^2 in the fitting for $T \geq \theta_D$. Hence, T^2 term is dominant in $\rho_{mag}(T)$. It should be pointed out that any quantitative data analysis involving more terms (here four) demands more resolution of the data.

2.4.2 Behaviour of RR for $T_{min} < T < 150 \text{ K}$

Fig. 2.9 shows the RR vs T in this region, i.e., $10\text{-}120 \text{ K}$ for all the samples.

Total resistivity ratio, RR_T can be written as

$$RR_T = \frac{\rho_{Total}(T)}{\rho_{Total}(300)} = A + FT^2 + CT^2 + DT^{3/2} \\ = A + GT^2 + DT^{3/2} \quad T < \theta_D \quad (2.27)$$

where FT^2 term comes from $\rho_{structure}$. Again, it was found that fitting to the above expression for $T_{min} < T < 150 \text{ K}$, the fit was not good and D came out to be negative which is not acceptable since T increases spin disorder and hence ρ_{mag} must increase with increase in T. Thus, the assumption that T^2 term is the really dominant term in $\rho_{mag}(T)$ as reported by Kaul et al [28] is quite good. Fig. 2.10 displays RR vs T which shows that RR does vary as T^2 well for all the samples from $50 \text{ K} < T < 150 \text{ K}$ except for So sample for which T^2 variation seems to be good only for $70 \text{ K} < T < 150 \text{ K}$. The

Table 2.2 Fitting parameters for different expressions in 200-300 K range for resistivity variation.

(i) $A+BT$

Sample (x)	A	B (K^{-1})	χ^2
0	09232	2 539e-4	3 227e-8
1	0 9600	1 719e-4	6 606e-8
2	0 9706	9.715e-5	2 059e-8
3	09876	4 107e-5	4 678e-9

(ii) $A+BT+CT^2$

Sample (x)	A	B(10^{14}) (K^{-1})	C(10^{-7}) (K^{-2})	$\chi^2(10^{-8})$
0	0 9300	1 984	1.108	2 468
1	0 9629	1 485	0.4702	5613
2	0 9800	0 2102	1.521	0 5067
3	0 9902	0 1980	0 4247	0 3595

(iii) $A+BT+DT^3$

Sample (x)	A	B(10^{14}) (K^{-1})	D(10^{-10})	$\chi^2(10^{-8})$
0	0 9276	2.272	2 820	2 485
1	0 9619	1 599	1 327	5630
2	09768	0 5924	4 004	0 543
3	09893	0 3081	1 082	0 369

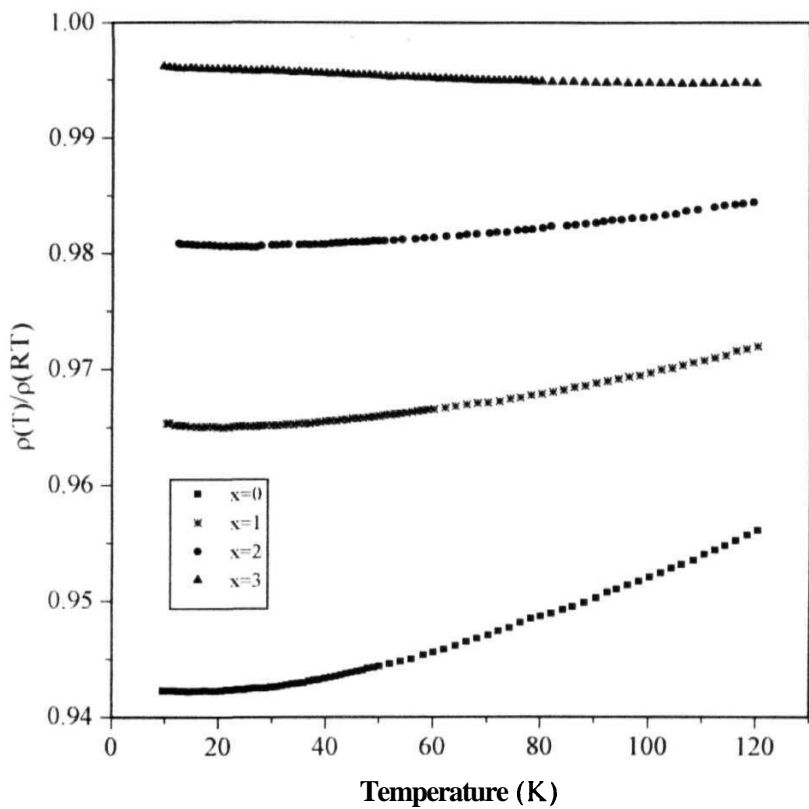


Fig 2.9 The resistivity ratio $RR = \rho(T)/\rho(RT)$ vs T in the temperature range 10-120 K for $\text{Fe}_{68}\text{Ni}_{14-x}\text{Mo}_x\text{Si}_2\text{B}_{16}$ ($x=0-3$) alloys.

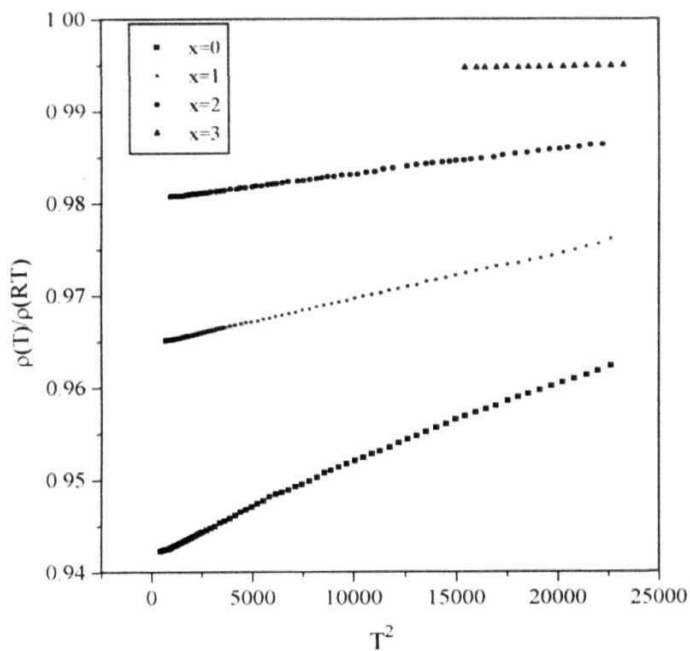


Fig. 2.10 The resistivity ratio $\rho(T)/\rho(RT)$ vs T^2 in the temperature range 10-150 K for $\text{Fe}_{6x}\text{Ni}_{14-x}\text{Mo}_x\text{Si}_2\text{B}_{16}$ ($x = 0-3$) alloys

Table 2.3 Fitting parameters to $\mathbf{A+GT^2}$ above $\mathbf{T_{min}}$ to 150 K.

Sample (x)	A	G	χ^2	Fit Range AT (K)
0	0.9420	$9.416\text{e-}7$	$1.556\text{e-}7$	20-150
1	0.9769	$5.001\text{e-}7$	$.1783\text{e-}9$	25-150
2	0.9804	$2.760\text{e-}7$	$3.596\text{e-}9$	30-150
3	0.9942	$3.142\text{e-}8$	$7.971\text{e-}10$	125-150

corresponding **fit** coefficients are listed in Table (2.3)

The coefficient of T^2 term $\sim 10^{-7} K^{-2}$ (coefficient G) agrees well with that reported by **Kaul** et al [28] except for $x=1$ & 3, where the coefficient is lower than the reported, by an order magnitude i e , $(3.0-5.5 \times 10^{-8} K^{-2})$ **Thummes** et al [46] obtain a T term coefficient of this order $(\approx 3.0 \times 10^{-8} K^{-2})$ in a series of Ni-rich samples

Thus our analysis of RR vs T seems to disagree with the results of Kettler et al [58] and Singhal et al [59] who found that their results are better described by a positive $T^{3/2}$ magnetic term over and above the structural T^2 term. However, this result is in agreement with that of Kaul et al [28] and Bhatnagar et al [54], who observed that the low temperature resistivity in amorphous magnetic materials could be described by a T^2 term alone, which includes both the magnetic and structural contributions

As we do not see much improvement in the χ^2 values, from the fits of data of high temperature to $A+BT$ and $A+BT+CT^2$, due to additional T^3 term, we conclude that $\rho_{str}(T)$ dominates $\rho_{mag}(T)$ in the entire temperature range above T_m , but one should not ignore magnetic contribution completely

From these results we can calculate θ_D , using the diffraction model which is given by Eq (2.12) as

$$\theta_D = \frac{\pi^2}{6} \left(\frac{\alpha}{\beta} \right)$$

$$\text{where } \alpha = \frac{1}{\rho_{(300)}} \left(\frac{d\rho}{dT} \right) \quad (2.28a)$$

$$\text{and } \beta = \frac{1}{\rho_{(300)}} \left(\frac{d\rho}{dT^2} \right) \quad (228)b$$

From above fitting Eq (2.26) & (2.27)

$$\theta_D = \frac{\pi^2}{6} \left(\frac{B}{F} \right) \quad (2.29)$$

But fitting RR vs T^2 for $T < \theta_D$ includes both contributions structural and magnetic. From **Fig 2.10** one determines G (Eq. (2.27)). Fitting data RR vs T to $A+BT+CT^2$ for $T \geq \theta_D$ gives C

$$\text{hence } F = G - C \quad \text{or}$$

$$\theta_D = \frac{\pi^2}{6} \left(\frac{B}{G-C} \right) \quad (2 \ 30)$$

Using this expression θ_D has been calculated for S_0 , S_1 and S_2 only. Since S_2 shows a resistance minimum at higher temperatures (~ 110 K) hence it is not possible to fit low T ($T < \theta_D$) data to T^2 . Values of θ_D vs x are listed in Table (2-1). It is seen that these do lie between 300 to 400 K as reported for other iron-rich metallic glasses in which similar analysis has been performed [56,57].

2.4.3 Behaviour of RR for $T < T_{min}$

In the study of $Fe_{68}Ni_{14-x}Mo_xSi_2B_{16}$ alloys all the samples show a minimum in resistivity at a characteristic temperature T_{min} , which are listed in Table (2-1). T_{min} is found by noting the value of T at which dp/dT becomes zero. The values of T_{min} for these samples increase from 15-25 K as x varies from 0-2. Smoothed RR data vs T in the range 10-50 K are shown in Fig. 2-11(a)-(c) for S_0 , S_1 and S_2 samples respectively. This behaviour is similar to that of the Cr containing alloys and other Mo containing alloys [11,14,55]. For $x=3$, T_{min} drastically increased to 110 K. The resistivity data for this sample also seems to show an additional minimum, although a very weak one occurring around 10-15 K, as shown in Fig. 2-5(a) & (b). (All the samples show a negative TCR below T_{min}). Fig. 2-12 shows T_{min} vs $\rho(RT)$. For the first three samples $T_{min} \propto \rho$. Errors in the values of T_{min} are determined by the flatness of the resistivity variation near these temperatures. Similar results have been reported for glassy alloys $Fe_{80-x}Cr_xB_{20}$ [14], and $Fe_{80-x}Mo_xB_{20}$ [55] although it has been reported that T_{min} in glassy $Fe_{80-x}Mo_xB_{20}$ [11] alloy increases up to $x=4$ then reduces for $x=6$. Before resistivity results are analyzed for $T > T_{min}$, a brief description of resistivity behaviour around T_{min} in other iron rich metallic glasses as reported in the literature is given below.

Almost all iron-rich metallic glasses show a resistance minimum in R vs T data if one reaches low enough temperatures. The behaviour of T_{min} varies with the type of the elements that constitute the alloy, their composition and thermal treatment. For instance, in $(Fe_{80}B_{20-x}C_x)$ alloy [28], T_{min} increases with increasing carbon content.

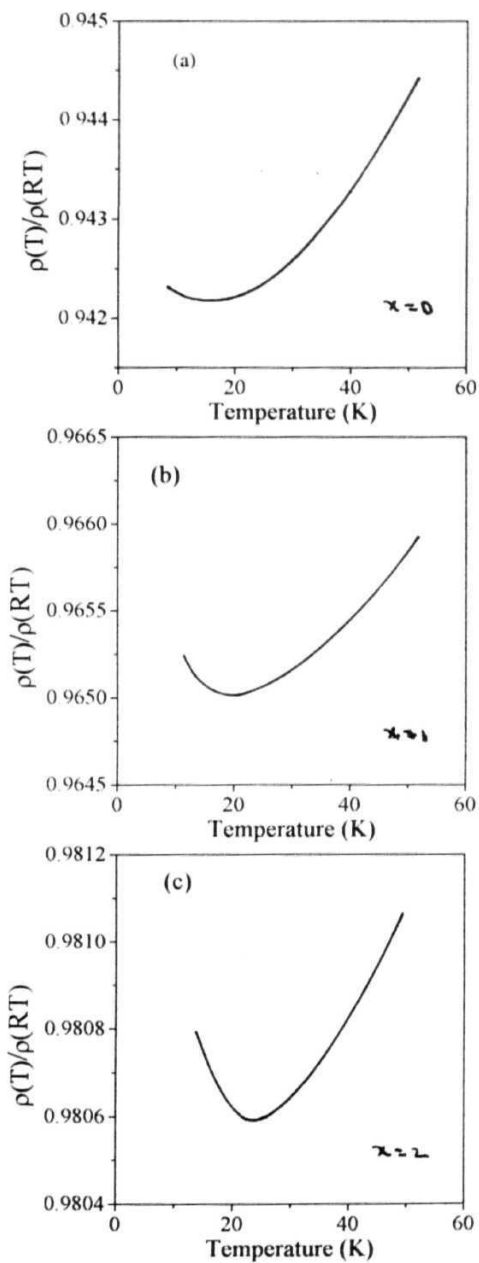


Fig 2 1 (a)-(c) The resistivity ratio $RR = \rho(T)/\rho(RT)$ vs T in the temperature range 10-50 K for $\text{Fe}_{68}\text{Ni}_{14-x}\text{Mo}_x\text{Si}_2\text{B}_{16}$ ($x=0-2$) alloys.

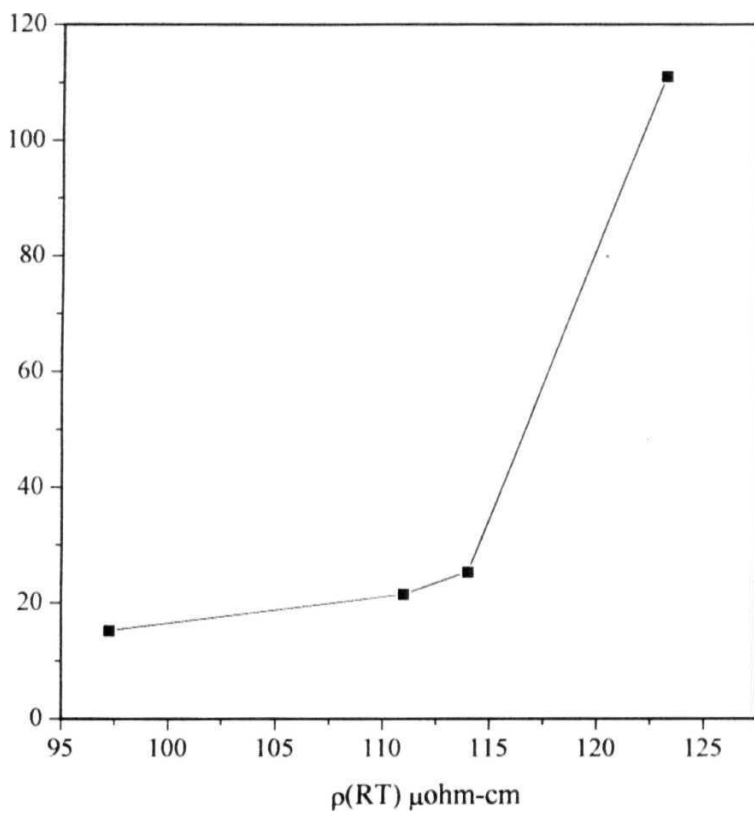


Fig 2 12 The plot of $\rho(RT)$ vs T_{\min} .

Fig 2 13 shows the T_{\min} vs Fe at% and Ni at% of various metallic glasses. The values of T_{\min} of $\text{Fe}_{80-x}\text{B}_{20}$ ($T=\text{Co, Ni}$) alloys fall between 10-25 K where as for Fe-(Cr/W)-B alloys the T_{\min} is increasing drastically with increase in Cr or W concentration. Similar observation can be seen in $\text{Fe}_{40-x}\text{Ni}_{40}\text{Cr}_x\text{B}_{20}$ [60]. In $\text{Fe}_x\text{Ni}_{80-x}\text{B}_{20}$ alloy [29] it increases with iron composition till 55 at% and decreases thereafter. In $\text{Au}_{1-x}\text{Ni}_x$ alloy [61], T_{\min} increases with Ni concentration. Addition of Ni or Co for Fe in metallic glasses with Fe-rich composition based on $\text{Fe}_{80}\text{B}_{20}$ and $\text{Fe}_{80}\text{B}_{20-x}\text{Si}_x$ does not shift T_{\min} very much, but addition of Cr [14,62] or Mn [63] shifts T_{\min} substantially. It has been observed that in the absence of Ni, the addition of Cr and V leads to double minimum in resistivity, one at low temperature ~ 20 K and the other at higher temperature, above 100 K [14,62]. Sas et al [30] have shown that in case of $\text{Fe}_{80}\text{T}_{18}\text{B}_{17}$ alloys (where $T=\text{Pd, Pt, Fe, Ni, Rh, Co}$ and Cu) the T_{\min} does not shift significantly, where as for $T=\text{Ir, Mn, Ta, W, Ru, V, Cr, Os}$ and Nb , T_{\min} is shifted towards higher temperatures. By observing the overall results in these alloys, it may be noted that the addition of elements of the groups VB, VIB and VIIB, i.e., for the elements, which are located to the left of iron in the periodic table, shifts the T_{\min} towards higher temperatures. Whereas addition of the elements in the groups VIII and IB, that is to the right of Fe, does not change T_{\min} significantly.

Since a resistivity minimum in ρ vs T data at low temperatures in pure metals with a few parts per million magnetic impurities (like Mn in Cu), has been associated with the Kondo type s-d exchange scattering [64], one is tempted to claim that the observed resistivity minima in iron-rich metallic glasses may be due to Kondo type scattering. High purity Pd-Si and Pd-Si-Cu glasses show no ρ_{\min} [1], however, an addition of controlled quantities of Co, Fe, Cr and Mn to amorphous $\text{Pd}_{80}\text{Si}_{20}$ resulted in a ρ_{\min} and the T_{\min} increased with the magnetic impurity [65,66]. Thus, ρ_{\min} in this system has been explained on the basis of Kondo type s-d exchange scattering [65]. Thus, below $T < T_{\min}$, $\rho(T)$ is expected too be proportional to $\ln T$ with a negative slope. $\rho(T)$ should eventually saturate at very low temperatures. If Kondo type scattering is considered responsible for ρ_{\min} , then the application of magnetic field

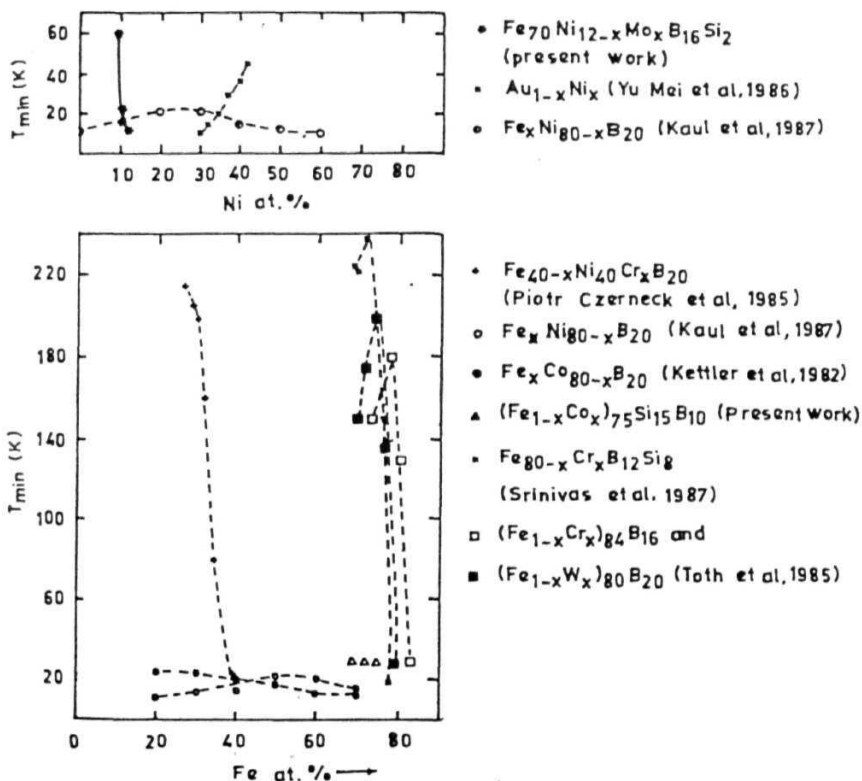


Fig. 2.13 T_{min} vs Fe and Ni at% for different amorphous alloys

should change $\rho(T)$ behaviour. However, Cochrane et al [25] observed that $\ln T$ dependence of resistivity is unaltered by an applied magnetic field of 45 kOe. It was therefore, suggested by them that the resistivity minimum may not have its origin in the Kondo effect. It may not be due to magnetic impurities alone, it must also be related to the amorphous structure of these materials. They explained ρ_{\min} using two-level tunneling model described in Sec. 2.2.3.

In order to look for possible explanation of the temperature dependence of resistivity behaviour of these alloys, near and below T_{\min} , we consider the predictions of various theories, which were outlined briefly earlier in this chapter. The resistivity minimum and negative TCR at low temperature have been observed in a number of metallic glasses whether ferromagnetic or not. The resistivity minimum cannot be explained using the Ziman diffraction model, and hence one has to look for an alternate explanation.

Earlier analysis of ρ vs T data for such glasses in the temperature region $T > T_{\min}$ has been usually carried out using $\ln T$ dependence of ρ [66,67]. This $\ln T$ behaviour also comes from the scattering from two level states as suggested by Cochrane et al [25]. On the otherhand Tsuei [26] has shown that this anomalous electron transport is due to an attractive interaction between conduction electrons and localised excitations arising from a structural disorder in the atomic arrangement in a glass. He found that the resistivity can be expressed as

$$\rho(T) = A + B\rho(N) + C \ln[T^2 + \Delta^2] \quad (2.31)$$

where A , B and C are constants and $\rho(N)$ is the resistivity due to other scattering mechanisms. The coefficient C is a measure of the abundance of the effective tunneling configurations. If A is zero or $\Delta \ll T$, then one would see a simple $\ln T$ behaviour. Inclusion of A^2 in the logarithmic term leads to flattening of the resistivity, the strength of which depends upon the ratio of T and A .

More recently, theories based on quantum interference effects arising due to extremely small electron mean free path are being used to explain ρ vs T behaviour of high $\rho(RT)$ metallic glasses as described in Sec. 2.2.4. In particular, the electron interaction effects consider the modification of the effective Coulomb interaction in the presence of high degree of structural disorder which leads to $T^{1/2}$ dependence of ρ .

below T_{\min} with a negative slope **Rapp et al [41]** reanalyzed earlier ρ vs T data on a number of **iron-rich** metallic glasses and have shown that the resistivity for temperature below T_{\min} can be fitted to $a_2\sqrt{T}$, where a_2 is a constant. Numerous reports indicate that the temperature dependence of resistivity of many magnetic and non-magnetic metallic glasses can be fitted to $T^{1/2}$ reasonably well below T_{\min} , at which minimum in resistivity is **observed**, with negative slope as predicted by Coulomb interaction theories [68]

While nowadays, there is a preference to fit ρ vs T data on metallic glasses using the interaction **effects**, here, we present both the fits, i.e., $(\rho - \rho_{\min})/\rho_{\min}$ vs $\ln T$ as well as $T^{1/2}$ in Figs. 2.14(a) & (b) and 2.15(a) & (b) for all the samples where the respective figures “(b)” are separately shown for the second minimum of S_1 . It is noted that it is hard to say whether one is a better fit over other given the constraint that data here is only limited to 10 K and above

The slopes of $\ln T$ fits for different samples are given in Table (2.4). These have similar magnitude as found for other iron-rich metallic glasses with low T_{\min} (<30 K). For example, **Kaul et al [28]** have reported values of B ranging from $(1.81 \text{ to } -4.32) \times 10^{-4} (\text{K}^{-1})$ for $\text{Fe}_{80}\text{B}_{20-x}\text{C}_x$.

Since $x=3$ sample has two minima, Fig. 2.15(b) shows $(\rho - \rho_{\min})/\rho_{\min}$ vs $T^{1/2}$ in the region 36 K to 100 K. It is seen that, $(\rho - \rho_{\min})/\rho_{\min}$ vs $T^{1/2}$ data exhibit a **linear** behaviour for all the samples, but the slopes which are also shown in Table (2.4) are smaller $(-1.0 \times 10^{-4} \text{ to } -2.5 \times 10^{-4}) \text{ K}^{-1/2}$ than those obtained by **Rapp et al [41]** and **Bhatnagar et al [54]** on iron-rich glasses by a factor of 2 to 3. This may be since our data points below T_{\min} are less in number and are not closely spaced and hence deviation (Scatter in the data) is more.

According to the Coulomb or electron-electron interaction theory [68] the major contribution to the resistivity arises from the diffusion channel, which predicts an additional term to the conductivity, which, in absence of spin-orbit interaction theory is given by [14]

$$\sigma_D(H, T) = \frac{13}{\sqrt{2}} \frac{e^2}{4\pi^2\hbar} \left(\frac{k_B T}{\hbar D} \right)^{1/2} \left\{ \frac{4}{3} + \lambda^{i=1}(F) \left[\frac{3}{2} + \frac{g_3(h)^2}{1.3} \right] \right\} \quad (2.32)$$

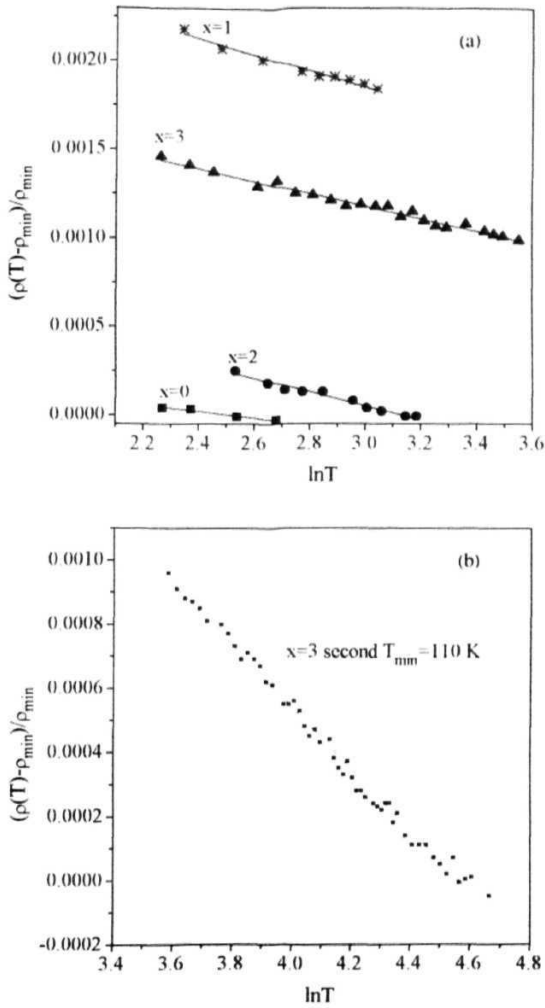


Fig 2 14(a) The plots of $(\rho - \rho_{\min}) / \rho_{\min}$ vs $\ln T$ for amorphous $\text{Fe}_{68}\text{Ni}_{14-x}\text{Mo}_x\text{Si}_2\text{B}_{10}$ ($x = 0-3$) alloys where for $x = 3$ data represents for its first minimum

Fig 2 14(b) The plot of $(\rho - \rho_{\min}) / \rho_{\min}$ vs $\ln T$ for amorphous $\text{Fe}_{68}\text{Ni}_{14-x}\text{Mo}_x\text{Si}_2\text{B}_{10}$ ($x = 3$) alloy representing data for its **second** minimum

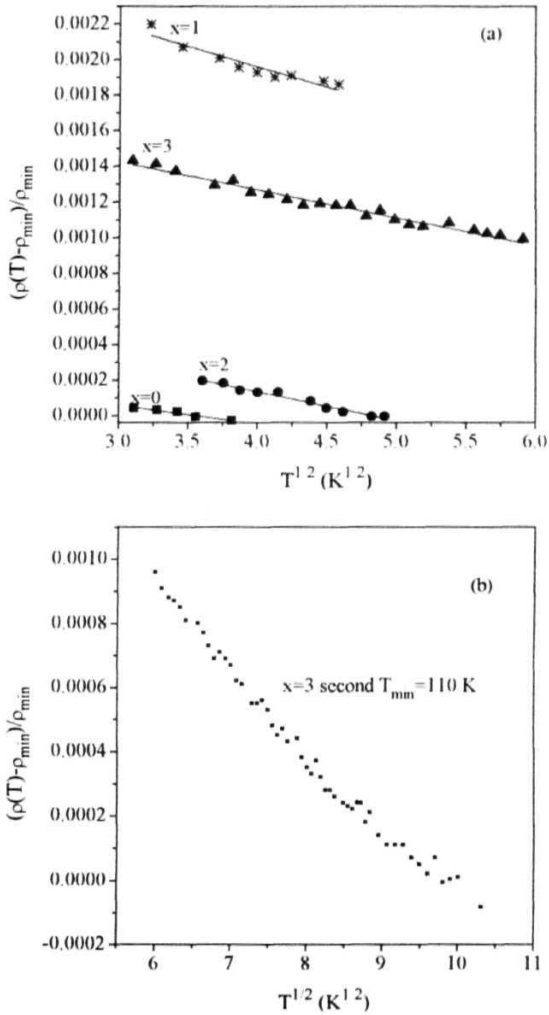


Fig 2 15(a) The plots of $(\rho - \rho_{\min}) / \rho_{\min}$ vs $T^{1/2}$ for amorphous $\text{Fe}_{68}\text{Ni}_{14-x}\text{Mo}_x\text{Si}_7\text{B}_{16}$ ($x=0-3$) alloys where for $x=3$ data represents for its first minimum
 fig 2 15(b) The plots of $(\rho - \rho_{\min}) / \rho_{\min}$ vs $T^{1/2}$ for amorphous $\text{Fe}_{68}\text{Ni}_{14-x}\text{Mo}_x\text{Si}_7\text{B}_{16}$ ($x=3$) alloy representing data for its second minimum

Table 2.4 Fitting parameters to $A+B\ln T$ and $a_1+a_2T^{1/2}$ below T_{\min}

Sample (x)	A	B (10^{-4}) (ln K)	ΔT (K)	χ^2	a_1	a_2 ($K^{-1/2}$)	ΔT (K)	χ^2
0	4.553e-4	-1.815	10-14	1.569e-11	3.727e-4	-1.054e-4	10-14	3.168e-11
1	0.0032	-4.598	10-20	3.700e-10	0.0029	-2.305e-4	10-20	1.039e-9
2	0.0013	-3.913	10-24	2.229e-10	7.869e-4	-1.634e-4	10-24	1.230e-10
3	0.0022	-3.486	10-35	3.130e-10	0.0018	-1.559e-4	10-35	4.983e-10
	0.0044	-9.618	35-110	6.986e-10	0.0023	-2.410e-4	35-110	1.864e-9

$$\lambda^{-1}(F) = \frac{32}{3F} \left[1 + \frac{3F}{4} \left(1 + \frac{F}{2} \right)^{1/2} \right]$$

is a **measure** of the electron-phonon interaction. The function $g(h)$ has the asymptotic form $0.056h^{-1}$ for $h \rightarrow 1$ and $(h^{-1} - 1/3)$ for $h \rightarrow \infty$ where $h = g\mu_B H/k_B T$ and the other constants have their usual meaning.

From Eq. (2.32), an upper limit for D , the diffusion constant has been calculated by assuming $\lambda^{-1} = 0$. These are listed in Table (2.1). These values are **higher** than the reported values of $(3.5-7.8 \times 10^{-5})$ cm²/s for similar glasses using the similar analysis [54] by an order of magnitude. Further confirmation of the results reported here **below** T_{min} can only be done if additional measurements like magnetic field dependence of resistivity are performed at **low temperatures**.

2.5 Summary

- (1) In these alloys, a resistivity minimum is observed at around 15 K for $x = 0$ and it increases drastically to 110 K for $x=3$. The alloy with $x=3$ **Mo-at%** shows a double minimum with the first minimum occurring around 10-15 K, and second minimum at about 110 K.
- (2) As $\rho(RT)$ increases, TCR, $\alpha(RT)$ decreases. The values of T_{min} , $\rho(RT)$ increase with increase of Mo content. The values of Debye temperature, θ_D , for these alloys lie in **between** 300-400 K. Table (2.1) lists the values of $\rho(RT)$, T_{min} , $\alpha(RT)$, θ_D for each sample.
- (3) At higher temperatures, i.e., $(200-RT)$ the temperature dependence of resistivity is found to be nearly linear and follows an equation of the type $A+BT$, the values of the coefficient B are presented in Table (2.2). This region has also been fitted to an equation of the form $A+BT+CT^2$ in which the T^2 term gives magnetic contribution to resistivity and the linear term T comes from the structural contribution to resistivity and the **fit** parameters are **tabulated** in Table (2.2). Data in this region is also fitted to an expression $A + BT + D/T^{1/2}$ in which the $T^{-1/2}$ term gives magnetic contribution. The coefficients are **listed** in Table (2.2). There is not much difference in the **fits** with either of these terms and hence our data is not able to distinguish between these two T^2 and $T^{-1/2}$.

dependences of $\rho_{\text{mag}}(T)$. Also since the coefficient of $T^{1/2}$ is about 3 orders of magnitude smaller than that of T^2 term, T^2 term is dominant in $\rho_{\text{mag}}(T)$

- (4) Above T_{min} up to **150 K**, a quadratic temperature dependence of resistivity is observed and the data in this region has been fitted to an equation of the form $A+GT^2$ and the values are tabulated in Table (2.3). The **Fig 2 10** shows the plot of $\rho(T)/\rho(RT)$ vs T^2 . The samples show T^2 dependence in the range **50-150 K** except for the sample **S₀**, for which T^2 variation seems to be good only in the range **70-150 K**. The coefficient of T^2 is $\sim 10^{-7} \text{ K}^{-2}$
- (5) Below T_{min} a logarithmic behaviour of resistivity with temperature as shown in Fig. 2 14(a & b) is **observed**. The data in this region has been fitted to an empirical relation of the form **$A+B\ln T$** . This **$\ln T$** behaviour comes from two level **states**. The values are tabulated in Table (2 4). The data is also fitted to an expression of the form **$a_1+a_2\sqrt{T}$** , represented in **Fig 2 15(a & b)**, and the values are tabulated in **Table (2 4)** where $T^{1/2}$ dependence is due to electron interaction **effects**. Both the **fits** are reasonably good and it is hard to say which one is better over the other given the constraint that data here is limited only **10 K** and **above**

2.6 References

- 1 C Suryanarayana, "Metallic glasses: Production, Properties and Applications", edited by TR Anantharaman, *Trans. Tech. Publications*, Switzerland (1984) 249
- K V Rao, "Amorphous Metallic Alloys", edited by F E Luborsky, Butterworth and Co Ltd (1983) 401 and references therein.
- U Mizutani, *Prog. Mat. Sci.*, 28 (1983) 97
- 4 S R Nagel, "Advances in Chemical Physics", Vol 51, edited by I Prigogine and S A Rice, John Wiley and Sons, New York (1982) 227
- 5 A Mogro-Campero and F.E Luborsky, *Phys. Appl. Phys*, 52 (1981) 515
- 6 S.H Lin, K J Bev and D Turnbull, *Solid State Commun.*, 29(1979)641
- 7 M Balanzat, *Scripta Met.*, 14 (1973)
- 8 A Mogro-Campero, *Phys. Lett.*, 76A (1980) 315; A Mogro-Campero and J L Walter, *Phys. (Paris) Colloque*, 41 (1980) C8-497
- 9 N.F Mott, *Phil. Mag.*, 26 (1972) 1249
- 10 K V Rao, H Gudmundsson, H V Astrom and H S Chen, *Appl. Phys.*, 50 (1979) 1592
- 11 D F Jones, G Stroink, Z.M Stadnik, and R A Dunlap, *Mater. Sci. & Engg.*, 99 (1988) 208
- 12 B Sas, T Kemeny, J Joth and F.I.B Williams, *Mat. Sci. & Engg.*, 99 (1988) 223.
- 13 H Gudmundsson, H.J Hannesson and H V Astrom, *Appl. Phys.*, 57 (1985) 3523
- 14 M Olivier, J.O Strom-Olsen and Z Altounian, *Phys. Rev. B*, 35 (1977) 333
- 15 J O Strom-Olsen, Z Altounian, R.W Cochrane and A B Kaiser, *Phys. Rev. B*, 31 (1985) 6116.
- 16 G V Rao and A K. Bhatnagar, "Proc. of the Indo-US workshop", edited by Vipin Srivastava, A.K Bhatnagar and D G Naugle, American Inst of Physics, AIP Conf. Science No. 286 (1993) Hyderabad, India.
- N Banerjee, Ratnamala Roy, A.K Majumdar and R. Hasegawa, *Phys. Rev. B*, 24(1981)6801.

- 18 W Teoh, N Teoh and S Arjas, "*Amorphous magnetism II*", edited by R Levy and R Hasegawa, Plenum Press. New York 327
- 19 P J Cote and L V Meissel, "*Glassy Metals I*", edited by H -J Guntherodt and H Beck, Springer-Verlag, Berlin (1983) 141
- 20 R Harris and J O Strom-Olsen, "*Glassy Metals II*", edited by H-J Guntherodt and H Beck, Springer-Verlag, Berlin (1983) 325.
- 21 J S Dugdale, *Contemp. Phys.*, 28 (1987) 547; M.A Howson and B.L Gallagher, *Phys. Rep.*, 170(1988)265
- 21-a P J Cote, *Solid State Commun.*, 18 (1976) 1311, J P Carini, S R Nagel, L K Varga and T Schmidt, *Phys. Rev. B*, 27 (1983) 7589
- 22 D G Naugle, *J. Phys. Chem. Solids*, 45 (1984) 367
- 23 J H Mooij, *Phys. Stat. Sol. A*, 17 (1973) 321
- 24 R W Cochrane, R Harris, J O Strom-Olsen and M.J Zuckerman, *Phys. Rev. Lett.*, 35(1975)676.
- 25 R.W. Cochrane and J.O Strom-Olsen, *J. Phys. F*, 7 (1977) 1799
- 26 C C Tsuei, *Hull. Amer. Phys. Soc*, 22 (1977) 322
- 27 C C Tsuei, *Hull. Amer. Phys. Soc*, 23 (1978) 359 and 406
- 28 S.N Kaul, W.H. Kettler and M Rosenberg, *Phys. Rev. B*, 33 (1986) 4987, S.N Kaul, W.H. Kettler and M Rosenberg, *Phys. Rev. B*, 35 (1987) 7153
- 29 S.N. Kaul and M Rosenberg, *Key Engg. Mater.*, 13-15 (1987) 475
- 30 B. Sas, J Toth, A Lovas and G Konczos, *Key Engg. Mater.*, 13-15 (1987) 493
- 31 J M Ziman, *PhilMag.*, 6 (1961) 1013
- 32 R Evans, DA. Greenwood and P Lloyd, *Phys. Lett. A*, 35 (1971) 57, 38 (1972) 151
- 33 S R Nagel, *Phys. Rev. H*, 16 (1977) 1694, P J Cote and L.V Meissel, *Phys. Rev. Lett.*, 39(1977) 102, K Frobose and J Jackie, *J. Phys. A*, 7 (1977) 2331
- 34 J M. Ziman, "*Principles of Theory of Solids*", Cambridge Univ., England (1972)64.

- 35 F Brouers and M Brauwiers, *J. Phys. (Paris) Lett.*, 36 (1975) L17
- 36 J Kondo, *Solid State Phys.*, 23, edited by F Seitz, D Turnbull and H Ehrenreich, Academic Press, New York (1969) 184. A Heeger, *Solid State Phys.*, 23, edited by F Seitz, D Turnbull and H Ehrenreich, Academic Press, New York (1969) 284
- 37 E Abrahams, P.W. Anderson, D C Licciardello and T V Ramakrishnan, *Phys. Rev. Lett.*, 42(1979)673
- 38 B.L. Altshuler and A.G Aronov, "Electron-Electron Interactions in Disordered Systems" edited by F L Efros and M Pollak, Elsevier, New York (1985) 1
- 39 P.A. Lee and T.V Ramakrishnan, *Rev. Mod. Phys.*, 57 (1985) 287
- 40 G Bergmann, *Phys. Rep.*, 107 (1984) 1
- 41 O Rapp, S.M. Bhagat and H Gudmundsson, *Solid State Commun.*, 42 (1982) 741
- 42 N.F Mott and M Kavesh, *J. Phys. C*, 15 (1982) L707.
- 43 M.A Howson, *J. Phys. F*, 14 (1985) L25
- 44 B.J. Hickey, D. Greij and M A Howson, *J. Phys. F*, 16 (1986) L13
- 45 H. Fukuyama and K Hoshimo, *J. Phys. Soc. Jpn*, 50(1981) 2131.
- 46 G. Thummes, J Kotzler, R Ranganathan and R Krishnan, *Z. Phys. B*, 69 (1988) 489; A Das and A K Majumdar, *Phys. Rev. B*, 43 (1991) 6042
- 47 S.N Kaul, "Proc. of the Int. Conf. on Metallic and Semiconducting Glasses, edited by A K Bhatnagar, Trans Tech Publications, Switzerland (1987) 475
- 48 E Babic, Z. Marohnic, M. Ocko, A Hamzic, K. Saub and B. Pivac, *J. Magn. & Magn. Mater.*, 15-18 (1980) 934
- 49 G Bohnke, S.N Kaul, W.H. Kettler and M Rosenberg, *Solid State Commun.*, 48(1983)743.
- 50 G. Bergmann and F Marquardt, *Phys. Rev. B*, 17 (1978) 1355.
- 51 R Richter, M Wolf and F Goedsche, *Phys. Stat. Solidi B*, 95 (1975) 473, R Richter and F. Goedsche, *Phys. Stat. Solidi B*, 123 (1984) 143.
- R. Asomoza, I A Campbell, A Fert, A Leinard and J P. Rebouillat, *J. Phys. F*, 9 (1979) 349.

- 53 APD Cryogenics, **Inc** , Superconductor Characterisation Cryostat Technical **Manual - P/N 257171A**
- 54 **A K Bhatnagar, B Seshu, C D D Rathnayaka and D G Naugle, *J. Appl. Phys.*, 76 (1994) 6 107**
- 55 H J V Nielsen, *Solid State Commun.*, **30** (1979) 239
- 56 **N.R Muniratnam, *Ph.D Thesis*, University of Hyderabad, Hyderabad, India, 1989**
- 57 G V Rao, *Ph.D Thesis*, University of Hyderabad, Hyderabad, India, **1989**
- 58 **W.H Kettler and M Rosenberg, *Phys. Rev. B*, 39 (1989) 12142**
- 59 Rita Singhal and **A K Majumdar, *Phys. Rev. B*, 44 (1991) 2673**
- 60 Piotr **czernecki** and Aiojzy wrzeciono, "*Proc. of 5th Int. Conf. on Rapidly Quenched Metals*", Vol I, edited by **S Steeb** and H Warlimont, Wurzburg, Germany, (1984) **1067**
- 61 Yu **Mei** and H L Luo, *Phys. Rev. B*, **34** (1986) **509**
- 62 V. Srinivas, G Rajaram, Shiva Prasad, **Girish Chandra**, S N Shringi and **R Krishnan, *Key Engg. Mater.*, 13-15 (1987) 481**
- 63 **A K Nigam, Nirupama Sharma**, Shiva Prasad, Girish Chandra, S N Shringi, R Krishnan and P Rougier, *J. Magn. rt Magn. Mater.*, **103** (1991) 297
- 64 **S C.H Lin, *J. Appl. Phys.*, 40 (1969) 2173**
- 65 **C.C. Tsuei and R Hasegawa, *Solid State Commun.*, 7 (1969) 1581**
- 66 **R Hasegawa and C C Tsuei, *Phys. Rev. B*, 2(1970) 1631,3(1971)214.**
- 67 G.S. Grest and **S R Nagel, *Phys. Rev. B*, 19 (1979) 3571**
- 68 Y **Imry, *Phys. Rev. Lett.*, 44 (1980) 469**

CHAPTER III

Mossbauer and Magnetization Studies

3.1 Introduction

Among the metallic glasses, iron-based amorphous alloys have been found to be quite important both by way of understanding magnetic properties in amorphous systems as well as for a wide range of their applications [1-4] due to the existence of **ferromagnetism**, where they can replace conventional **alloys**. One aspect that can systematically be studied in these alloys, is the compositional dependence of physical properties of these amorphous alloys in general and magnetism in particular due to their potential applications in electronic devices. This aspect can be investigated by systematically replacing iron by another transition metal and/or one metalloid by another [1,5-7]. Extensive studies on substitution of Cr, Co and Ni for Fe in binary, ternary and quaternary glassy alloys have been reported in the literature [8-14]. Mo

substitution effects for Fe in binary and ternary glassy alloys have been investigated **somewhat** but there is hardly any systematic investigation of Mo substitution in **quaternary** glassy alloys although molybdenum containing quaternary alloys have been shown to be particularly important in high frequency transformer applications [1,15-17] From the applications point of view as well as to understand the role of composition, detailed investigations on the magnetic properties of these alloys are required The magnetic properties of these amorphous alloys can be studied at bulk level by magnetization and magnetic susceptibility measurements [18,19] or at **microlevel** by **Mössbauer** spectroscopy [20] and Nuclear magnetic resonance [21] In this chapter we present detailed Mössbauer studies of the magnetic interactions at microlevel of a family of amorphous alloys of nominal compositions, **Fe₈₈Ni_{12-x}Mo_xSi₂B₁₆** ($x=0,1,2,3$ and 4) over a temperature range varying from room temperature (RT)-80 K An attempt has been made to cover all the aspects, such as temperature and composition dependence of hyperfine parameters and distribution of **hyperfine** fields, spin wave behaviour etc In order to understand the bulk magnetic properties, RT magnetization measurements on these samples have been made using Vibrating Sample Magnetometer (VSM) while low temperature (10-100 K) magnetization measurements have been performed using a **Lakeshore** ac **Susceptometer/dc** Magnetometer The applicability of spin wave theory to these amorphous alloys is also discussed

3.2 Mossbauer Effect

3.2.1 Principle

Since its discovery in 1957, **Mössbauer** effect [22] has been studied extensively and is recognised as a **powerful** microscopic probe to study the local environments of certain **nuclei** The theory of Mössbauer Effect Spectroscopy (MES) has been extensively dealt in several text books and review articles [23-27] and hence, only some important aspects of the theory are presented **here**

When a γ -ray is emitted by the nucleus in a free atom, the energy of the γ -ray, E_γ is reduced by an amount equal to the recoil energy that is imparted to the nucleus, in accordance with the momentum conservation laws. The same occurs in the case of

absorption **also** Due to this recoil, the emission line is shifted towards longer wavelength region and the absorption line towards smaller wavelength region and there is no overlap between the two This recoil energy is very high for γ -rays due to their high energy (keV-MeV range) in comparison with photons of, say, 1 eV On the otherhand, the natural **linewidth** for γ -rays used in the popular Mossbauer source, Fe^{57} is much smaller than that of infrared radiation In γ -ray spectroscopy usually energy of γ -rays is modulated using Doppler effect which leads to thermal broadening of the **line** This results in overlapping of the emission and absorption curves to a certain degree, solely determined by the thermal **broadening** When thermal broadening is more, larger **overlap** is expected, however, too high a velocity of a source is required to obtain sufficient overlap which are not easily accessible in **laboratories**

Mossbauer, while doing experiment on Ir^{191} , found that the resonant effect increased on cooling the sample while the expectation was that the effect will decrease since lower temperature will reduce thermal broadening which should reduce the **overlap** of **lines** Mossbauer postulated that a significant fraction of γ -rays were emitted without recoil in a solid This discovery and **Mössbauer's** explanation gave rise to an extremely important experimental tool to investigate solids.

If an excited nuclei is rigidly held in a solid, γ -emission cannot eject the emitting atom from its fixed position in the lattice since the recoil energy E_R (10^{-2} eV) is much less than chemical binding **energies** The recoiling mass, therefore, will be that of whole of the crystal ($\sim 10^{17}$ atoms) and recoil energy becomes negligibly small. Similarly since the atom cannot undergo random thermal motion, since it is rigidly held, thermal broadening also becomes negligible compared to the natural **linewidth** Thus for a rigidly held atom the source and absorber energy profiles will completely overlap and therefore γ -ray resonance becomes **observable**

However, the approximation that the emitting atom/nucleus is rigidly held is not strictly valid but it does **vibrate** The recoil energy E_R could then be transferred to exciting a lattice vibration, whose energies might be comparable to E_R . On a simple **I** nstein model of a solid, an energy $n\hbar\omega_L$ where n is an integer and ω_L is the Einstein frequency, is required for the **excitation/deexcitation** of the lattice. This is only possible if $E_R \geq \hbar\omega_L$ If $E_R < \hbar\omega_L$, then the lattice will not be excited and the emitting nuclei effectively do not recoil and the whole crystal mass takes up the recoil. This is

called the zero-phonon **process** Thus E_R and thermal broadening effects become negligibly small and therefore resonance becomes easily observable

It turns out that if E_R and lattice excitation energies are comparable in magnitude, then only a fraction of the emission and absorption occurs without recoil This fraction denoted as f , **varies** from solid to solid, temperature and E_γ This fraction f is given by

$$f = \exp\left(-k^2 \langle x^2 \rangle\right) \quad (3.1)$$

where k is the wave vector of γ -ray, $\langle x^2 \rangle$ is the mean square vibrational amplitude of the emitting/absorbing nucleus in the solid It may be noted that the bound state recoil free process is solely determined by $\langle x^2 \rangle$ No further specification of the solid state is necessary, i.e., the solid can be crystalline or amorphous The only requirement is that $\langle x^2 \rangle$ should not become infinite in which case f becomes zero and therefore Mossbauer **effect** cannot be **observed**

In a more realistic mode of lattice vibrations, namely, the Debye approximation, the Mossbauer fraction is given by

$$f = \exp\left[-\frac{6E_R}{k_B\theta_D}\left\{\frac{1}{4} + \left(\frac{T}{\theta_D}\right)^2 \int_0^{\theta_D/T} \frac{x dx}{e^x - 1}\right\}\right]$$

where E_R is the recoil energy and θ_D is the Debye temperature of the host **lattice** At low temperatures, i.e., $T \ll \theta_D$, Eq (3.2) reduces to

$$f = \exp\left[-\frac{E_R}{k_B\theta_D}\left\{\frac{3}{2} + \frac{\pi^2 T^2}{\theta_D^2}\right\}\right] \quad T \ll \theta_D \quad (3.3)$$

whereas in the high temperature limit, it takes the form

$$f = \exp\left[\frac{-6E_R T}{k_B\theta_D^2}\right] \quad T > \theta_D/2 \quad (3.4)$$

3.2.2 The ^{57}Fe Decay Scheme

To date, Mossbauer effect has been observed in a number of nuclei, but the most widely used one has been that of iron, ^{57}Fe , as Fe occurs naturally in many solids and Fe containing materials have always been considered important for various

scientific/technical reasons The present work also utilised ^{57}Fe to investigate magnetic and other hyperfine interactions in iron-rich metallic **glasses**

The decay scheme for ^{57}Fe Mossbauer effect is shown in Fig 3.1. ^{57}Co , having a half life of 270 days, in the state $I = 7/2$ decays through electron capture into the $I = 5/2$ state of ^{57}Fe . Eleven percent of the decays from this state result in a 136.32 keV γ -ray and 85%, in a 121.9 keV γ -ray. The $I = 3/2$ state then decays to the ground ($I = 1/2$) state through emission of 14.41 keV γ -rays. The lifetime, τ , of this energy state is 0.781 ns, corresponding to a natural linewidth of about $\sim 5 \times 10^{-9}$ eV obtained from the Heisenberg uncertainty relation $\Delta E = \Gamma = \hbar/\tau = 0.693 \hbar/t_{1/2}$, where Γ is the full linewidth at half maximum and $t_{1/2}$ is the half-lifetime of ^{57}Fe . The linewidth, when converted into velocity unit, it is 0.194 mm/s. The ratio Γ/E_γ is a measure of the accuracy in the determination of relative energy changes which for ^{57}Fe is $\sim 10^{-13}$. The power of Mossbauer spectrometer (MS) lies in the narrow linewidth and the extremely small relative energy change which can be measured. Small line shifts can be easily measured to a fraction of 1% of the linewidth, thus, this technique allows determination of the relative line position on the ^{57}Fe line to one part in 10^{14} .

Intensity, width, position and splitting are the parameters which characterize a Mossbauer line. A physical interpretation of these parameters yield information on various interactions that play in the solid affecting nuclear levels.

3.3 Hyperfine Interactions

The narrow linewidth of the Mossbauer line and the possibility of determining the energy positions of the emitted γ -rays from a source relative to an absorber with a high degree of accuracy is the most important feature of Mossbauer **spectroscopy**. Various interactions can change the energy levels of a **nucleus**. The ones which are important in MS are (1) The hyperfine interactions and (2) Relativistic **effects**. The hyperfine interactions are the results of interaction between a nuclear (moment) property and an appropriate atomic or electronic **property**. There are three main **hyperfine** interactions investigated by MS

- 1 **Isomer** shift due to electric **monopole** interaction.
- 2 Nuclear **Zeeman** effect due to magnetic dipole interaction.

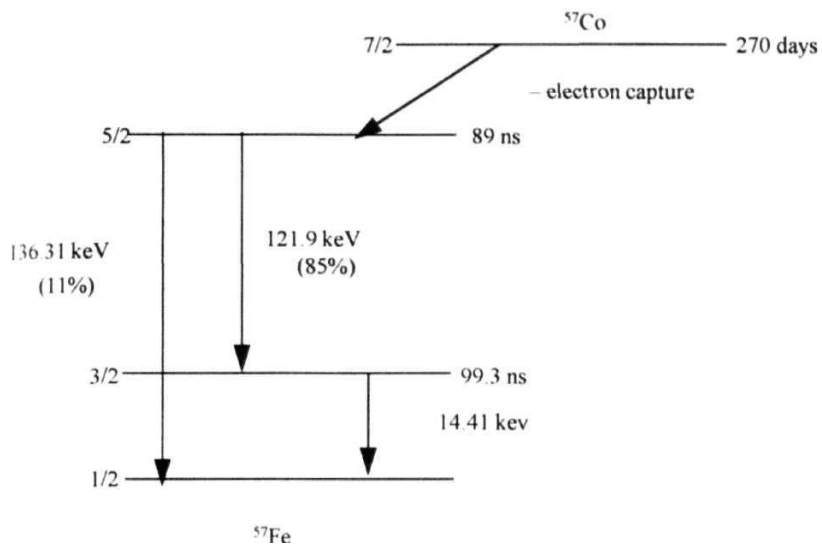


Fig 3.1 Decay scheme for ^{57}Fe .

3 Electric quadrupole splitting due to electric quadrupole **interaction**

The relativistic effect causes a shift of the resonance line by a second order **Doppler** effect

In the following text a brief **description** of these interactions/effects is given

3.3.1 Isomer Shift

The electrostatic interaction between the charge distribution of the nucleus and those electrons, which have a finite probability of being found in the regions of nucleus, results in what is known as **Isomer Shift (IS)**. This interaction leads to only a slight shift of the energy levels in a compound relative to those in the free **atom**. The shift, in general, will be different in source and **absorber**. **Fig 3 2(a)** shows the nuclear energy levels and the resulting isomer shift.

The IS can be calculated easily by assuming a nucleus to be uniformly charged sphere of radius R , and the **s-electron** density at the nucleus $|\psi_s(0)|$ to be constant over the nuclear **dimensions**. The energy difference of electrostatic interaction of a point nucleus and a nucleus having a radius, R , with $|\psi_s(0)|$

$$\delta E = K |\psi_s(0)|^2 R^2 \quad (3.5)$$

where K is a **constant**. Since R is generally different in the ground and excited nuclear states, δE will be different for both and

$$\delta E_e - \delta E_g = K |\psi_s(0)|^2 (R_e^2 - R_g^2) \quad (3.6)$$

where the subscripts e and g refer to excited and ground **states**. The R values are nuclear constants but $|\psi_s(0)|$ will vary from compound to **compound**. This energy difference becomes measurable by a **Mössbauer** experiment by comparing the nuclear transition energy in a source (E_γ^s) and that in an absorber (E_γ^a). The isomer shift, **IS** is then given by

$$IS = K (R_e^2 - R_g^2) \left[|\psi_s(0)|_A^2 - |\psi_s(0)|_S^2 \right] \quad (37)$$

Since $\delta R = R_e - R_g$ is very small, IS can be written as

$$IS = K R^2 \frac{\delta R}{R} \left[|\psi_s(0)|_A^2 - C \right] \quad (38)$$

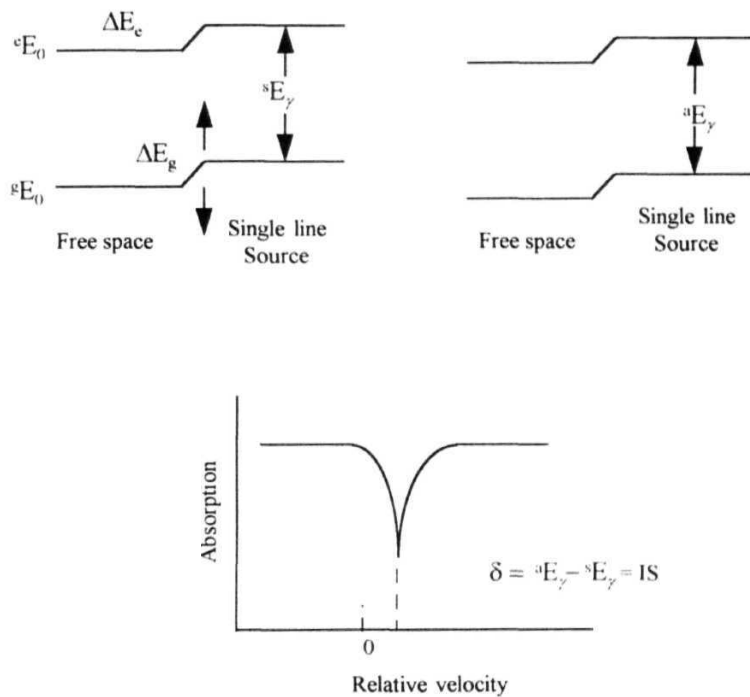


Fig 3 2(a) Nuclear energy levels and the resulting isomer **shift**.

where C is a constant characteristic of the **source**. For a given nucleus δR and R are constant so that **IS** is directly proportional to the **s-electron** density at the nucleus. δR is negative for Fe^{57} , therefore, an increase in the s-electron density at the absorber nucleus will result in a more negative **IS**. Although electrons other than **s-electrons** have a density zero at the nucleus, the s-electron density is often found to be sensitive to the p- and d- electron **density**. If the sign of $\delta R/R$ is known for a **Mossbauer** nucleus, IS provides a method of examining the covalent character of a bond and a potential method to determine the valency and oxidation state of the Mossbauer **atom**.

Relativistic Effects

The vibrating atoms in a solid make large number of oscillations ($\approx 10^{11}/\text{s}$) during the lifetime of the excited nuclear states ($\sim 10^{-5}$ - 10^{-10} sec), thus the average velocity, $\langle v^2 \rangle$ is zero and the first order Doppler effect cannot be **observed**. However, the $\langle v^2 \rangle$ is nonzero and causes a shift of the resonance by a second order Doppler **effect**. It is a relativistic temperature-dependant contribution to the **isomer** shift which is caused by time dilations resulting from the thermal motions of the γ -ray emitting and absorbing **nuclei**. This shift is proportional to the mean square velocity of the nucleus and is given by

$$\frac{\delta E_\gamma}{E_\gamma} = - \frac{\langle v^2 \rangle}{2c^2} \quad (3.0)$$

where E_γ is the recoilless γ -ray energy, δE_γ is its shift, V is the velocity of the emitting nuclei and c is the velocity of **light**. In the harmonic approximation, the temperature **dependence** of the centroid of the Mossbauer spectrum is given by (in velocity units)

$$\delta v_T = - \frac{C_L}{2Mc} (T_a - T_s) \quad (3.10)$$

where M is the atomic mass, C_L is the lattice specific heat, and T_a and T_s denote the temperatures of the absorber and source, **respectively**. In the high temperature limit ($T_a, T_s \gg \theta_D$), $C_L \approx 3k_B$ and δv_T is a linear function of temperature with a slope equal to $3k_B/2Mc$. For Fe^{57} ($E_\gamma = 14.4$ keV) a temperature shift of $\delta v_T \approx 7 \times 10^{-4}$ mm/s-K is observed [28].

3.3.2 Electric Quadrupole Interaction

When a nucleus has a spin quantum number, $I, I > 1$, the nucleus no longer has spherical symmetry and the higher order terms in the **multipole** expansion of the electrostatic interaction between nuclear and electronic charges come into **being**. The deviation of the charge distribution of the nucleus from spherical symmetry is described by the nuclear quadrupole moment, given by

$$eQ = \int \rho r^2 (3 \cos^2 \theta - 1) d\tau \quad (3.11)$$

where e is the charge of the proton, Q is the nuclear quadrupole moment, ρ is the charge density in a volume element dx , which is at a distance r from the center of nucleus and at an angle θ with the nuclear spin quantization **axis**. The interaction of the nuclear quadrupole moment eQ with the principal component of the diagonalised electric field gradient (EFG) tensor, $V_{zz} = \partial^2 V / \partial z^2$, at the nucleus splits the nuclear state into sublevels with the eigen values

$$E_Q = \frac{eQq}{4I(2I-1)} \left[3m_I^2 - I(I+1) \right] \left(1 + \frac{\eta^2}{3} \right)^{1/2} \quad (3.12)$$

The asymmetry parameter, η , is given by

$$\eta = \frac{V_{xx} - V_{yy}}{V_{zz}} \quad (3.13)$$

with $|V_{zz}| \geq |V_{yy}| \geq |V_{xx}|, V_{zz} + V_{yy} + V_{xx} = 0$ thus $0 \leq \eta \leq 1$.

The electric quadrupole interaction splits the first excited nuclear state of ^{57}Fe ($I = 3/2$) as shown in **Fig 3.2(b)** with eigen values

$$E_Q = \pm \frac{1}{4} eQq \left(1 + \frac{\eta^2}{3} \right)^{1/2} \quad (3.14)$$

This leads to a **Mössbauer** spectrum consisting of a pair of absorption lines separated by an energy ΔE_Q , called the quadrupole splitting **energy**.

3.3.3 Magnetic Hyperfine Interaction

In the presence of a magnetic field at the nuclear site, nuclear **Zeeman** splitting of the energy levels **occurs**. The **Hamiltonian** that describes the hyperfine interaction is given by

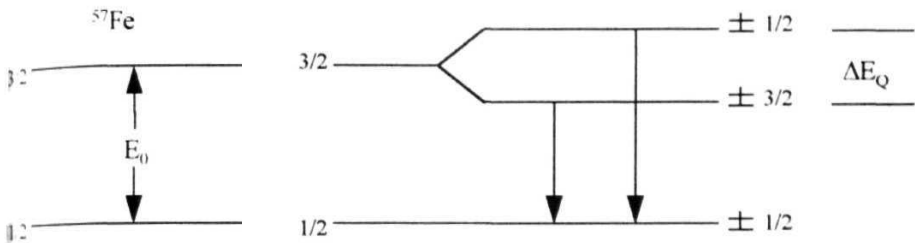


Fig 3 2(b) Nuclear energy levels for ^{57}Fe and the resulting quadrupole interaction

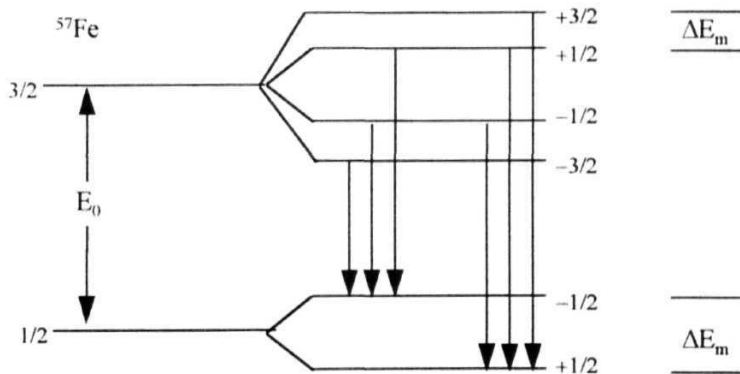


Fig 3 2(c) Nuclear energy levels for ^{57}Fe and the resulting magnetic hyperfine interaction.

$$\mathcal{H} = -g_N \mu_N \hat{\mathbf{I}} \cdot \mathbf{H} \quad (3.15)$$

where g_N is the nuclear **Lande** factor, μ_N is the nuclear magneton, $\hat{\mathbf{I}}$ is the nuclear spin and \mathbf{H} is the magnetic **field**. This interaction splits the nuclear state with spin \mathbf{I} into $(2I+1)$ sublevels whose energy eigen values are given by,

$$E_m = -g_N \mu_N H m_I \quad (3.16)$$

where m_I ($m_I = I, I-1, \dots, -I$) is the magnetic quantum number representing the z component of \mathbf{I} , if \mathbf{H} is oriented along the **z -axis**. For the isotope **^{57}Fe** , the ground state $I=1/2$ and the excited state $I=3/2$ split into 2 and 4 sublevels, as shown in **Fig 3.2(c)**, if a magnetic field is present at the nucleus and if no quadrupole interaction is present. The ordering of the sublevels m_I indicates the fact that the ground state magnetic moment is positive, while that of the excited state is **negative**. Since the **multipolarity** of the 14.4 keV **γ -rays** transition is almost exclusively a magnetic dipole in nature, the transitions between various levels are governed by the selection rules $\Delta m_I = 0, \pm 1$ and there can only be six allowed transitions in **^{57}Fe** . These six allowed transitions lead to the six lines in the Mossbauer spectrum of **^{57}Fe** . A **Mössbauer** spectrum of iron foil with an effective magnetic field of $H=330$ kOe is shown in **Fig 3.3**. The separation between the two outermost lines is proportional to the effective magnetic field, H_{eff} , seen by the Mossbauer nucleus from which magnetic behaviour of solids can be deduced.

In general this magnetic field can be written as

$$H_{\text{eff}} = H_0 - DM + \frac{4}{3} \pi M + H_s + H_l + H_p \quad (3.17)$$

H_0 is an externally applied field, DM is the demagnetizing field, $\frac{4}{3} \pi M$ is the Lorentz field for cubic **symmetry**. H_s , called the Fermi contact term, arises from the interaction of nuclear spin with the unpaired **s -electron** spin density at the nucleus and is written as

$$H_s = - \left(\frac{16\pi}{3} \right) \mu_B \left\langle \sum_i s_i^z \delta(r_i) \right\rangle \quad (3.18)$$

where the term in angular brackets is the expectation value of the local spin density, r_i is the radial coordinate of the i -th **electron**. This field is the dominant contribution to the hyperfine field in the case of transition **metals**. The last two terms in Eq. (3.17),

$$H_l = -2\mu_B \langle 1/r^3 \rangle \langle L_z \rangle = -2\mu_B \langle 1/r^3 \rangle (g-2) \langle S_z \rangle \quad (3.19)$$

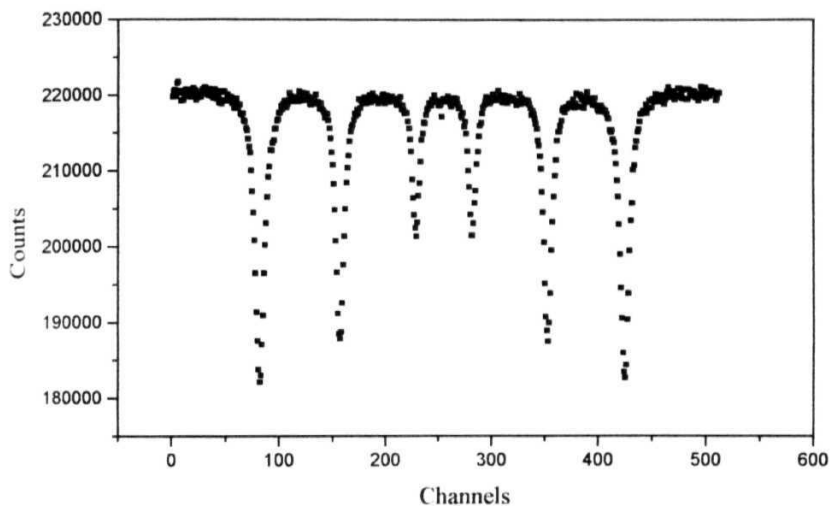


Fig 3.3 Mossbauer spectrum of thin Fe-foil at room temperature

and

$$H_{dd} = -2\mu_B \langle 3r(s \cdot r)/r^3 - s/r^3 \rangle \quad (3.20)$$

arise from a non-zero orbital angular momentum and the dipolar interaction of the nucleus with the neighbouring spins, respectively. Both the terms are either zero or negligible for transition elements, but can be larger for rare earth elements because the orbital angular momentum is not quenched in rare earth elements.

3.3.4 Combined Magnetic and Electric Hyperfine Coupling

Under the combined action of magnetic hyperfine and electric quadrupole interactions, an additional shift in the excited state energy levels (**Fig 3 2(c)**) occurs. If the EFG tensor is axially symmetric with its principal axis making an angle θ with the magnetic axis, the quadrupole interaction may be treated as a first order perturbation to the magnetic interaction, provided that $eQq \ll \mu H$. Then, the energy eigen values for $I = 3/2$ are given by

$$E = -g_N \mu_N H m_I + (-1)^{m_I+1/2} \frac{eqQ}{4} \left[\frac{3\cos^2\theta - 1}{2} \right] \quad (3.21)$$

When the quadrupole interaction is no longer a small perturbation on the hyperfine field, it becomes difficult to predict or interpret the splittings and the intensities when observed and usually recourse has to be taken to analyze by computer simulation [29]

3.3.5 Intensity Ratios

The angular dependence of the allowed transitions in the Nuclear Zeeman pattern is, in general, a function of the angle θ between the direction of the effective magnetic field at the nucleus and the direction of propagation of the γ -ray. This can be calculated using standard quantum mechanics techniques and are given below

Intensities	Transitions	Δm_I	Angular dependence
$I_{1,6}$	$\pm 3/2$ to $\pm 1/2$	± 1	$(3/4)(1+\cos^2\theta)$
$I_{2,5}$	$\pm 1/2$ to $\pm 1/2$	0	$\sin^2\theta$
$I_{3,4}$	$\pm 1/2$ to $\pm 1/2$	± 1	$(1/4)(1+\cos^2\theta)$

For a thin, polycrystalline/amorphous absorber, the angular term can be

integrated over all orientations to give an average value. In such a **case**, the average value of $\cos^2\theta$, denoted by $\langle \cos^2\theta \rangle$, turns out to be $1/3$ and $\langle \sin^2\theta \rangle = 2/3$. The ratio of line intensities can be written as $3b/1+b$ where

$$b = \frac{I_{2,5}}{I_{3,4}} = \frac{4\sin^2\theta}{1 + \cos^2\theta} \quad (322)$$

According to this **equation**, b assumes the value 0 when all the moments are aligned parallel ($\theta=0^\circ$) to the γ -ray direction, ∞ when aligned perpendicular ($\theta=90^\circ$) and for a **perfectly** random alignment of the local moments, $b=2$.

3.4 Experimental Details

3.4.1 Mossbauer Measurements

All the Mossbauer **experiments** on samples $\text{Fe}_{0.8}\text{Ni}_{1-x}\text{Mo}_x\text{Si}_2\text{B}_{16}$ ($x=0, 1, 2, 3$ and 4) which are of ~ 5 mm width and 25-30 μm thickness, obtained from Allied Signals, U.S.A. prepared by melt spinning technique, were carried out in the standard transmission geometry in a zero external field and in the temperature range from RT-80 K. The spectra were taken with the Mossbauer spectrometer facility using $^{57}\text{CoRh}$ radioactive **source**, operating in the conventional constant acceleration mode, available with the Low Temperature Physics (LTP) section, at Tata Institute of **Fundamental** Research, (TIFR) **Mumbai**. The sample was sandwiched between two copper rings of about 2 cm outer **diameter**. Spectra were collected over 512 channels. Typically 10^5 counts were collected per channel and the time taken to acquire this for **each** spectrum was of the order of 24-36 hours.

A schematic diagram of the Mossbauer spectrometer is shown in Fig. 3.4. It consists of a source, the drive system to impart an additional Doppler energy to the emitted γ -ray and the detector along with the data acquisition system. The detector, the source and the absorber (sample) were clamped to an optical bench for maintaining co-linearity. Folding of the spectra was obviated by driving the velocity transducer by a linear ramp waveform, the end of which is returned to the starting point by two parabolas. These parabolas are such that the velocity and acceleration are continuous functions of time to avoid 'ringing'.¹ A high efficiency scintillation counter with 0.2 mm thick **NaI (Tl)** scintillator stage was used for detection. The multichannel analyzer

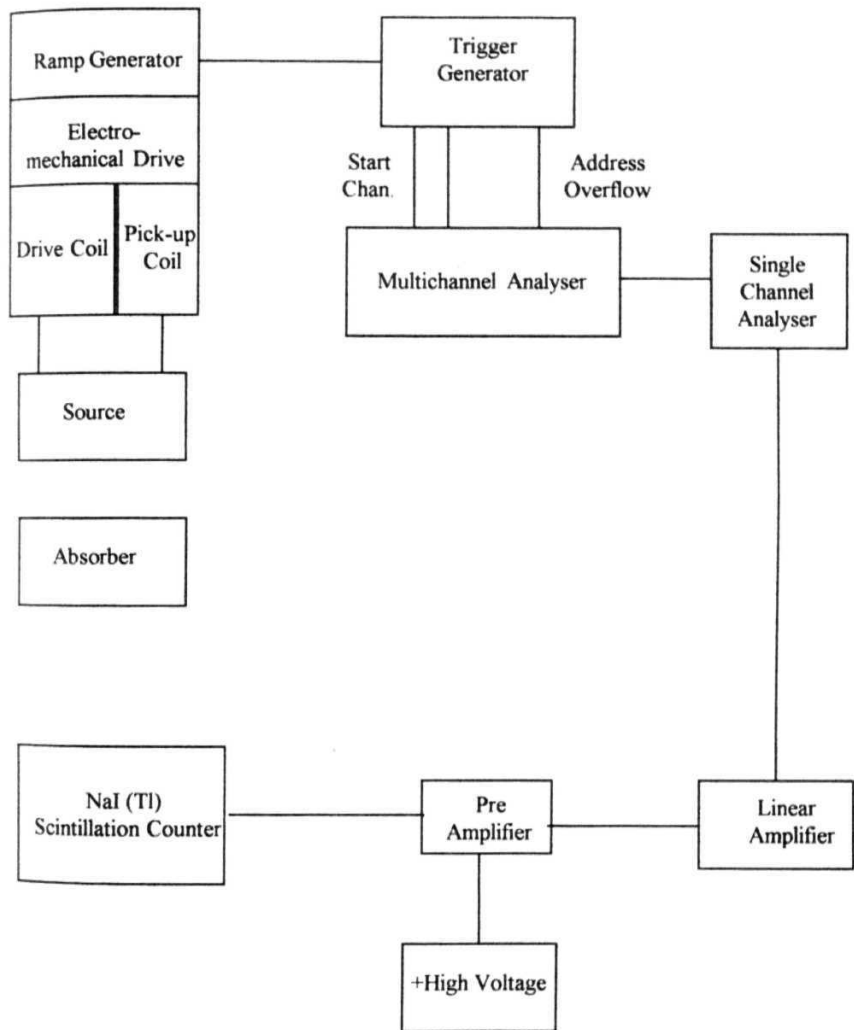


Fig 3 4 Block diagram of the Mossbauer spectrometer.

was provided with a serial port through which data collected over **512** channels, could be transferred directly to a **computer**. For calibration, natural iron foil was **used**. **Typical** intrinsic linewidths for the innermost lines were 0.24 ± 0.01 **mm/s** and the separation between the outermost lines was **9.9-10.5 mm/s**, for the Mossbauer spectrum at **RT**. This essentially determines the resolution of the Mossbauer spectrometer.

Mossbauer measurements at low temperatures were carried out using a low temperature continuous flow type cryostat (Lakeshore, Model **310**) the schematic of which is shown in **Fig 3.5**. The samples, which were sandwiched between the copper rings with one end fixed, were clamped to the cold finger. The temperature was measured using a calibrated Si-diode and controlled by a **PI D** temperature controller to a stability better than **50 mK**. The diffusion pump was required to operate for long times to collect a set of spectra at different **temperatures**. The vacuum system arrangement is shown in **Fig 3.6**. The sorption pump was used as backing for the diffusion **pump**. The reasons for this **are** (i) to reduce the vibrations created by rotary pump motor which would result in line broadening of Mossbauer spectrum and (ii) to reduce wear and tear of the rotary pump. The sorption pump consisted of a brass can (**500 cc**) brazed to a thin walled (**0.5 mm**) stainless steel (SS) tube (**2-2.5 cm** diameter and **50 cm length**). It was filled with **300 cc** of molecular sieve (**Zeolite**). The rotary pump was used for fore pumping as well as backing whenever the cryostat was being evacuated or when the temperature of the sample was **raised**. During the Mossbauer run the sorption pump was used for backing by cooling it down with **LN₂**.

3.4.2 Bulk Magnetization Measurements

The magnetization measurements at room temperature were done using Vibrating Sample Magnetometer model 4500 [30], the principle of operation and the details of the experimental setup of which are given below.

Principle

The Vibrating Sample Magnetometer (VSM) was first developed by Simon Foner [31] and independently by Van Oosterhout [32]. The underlying principle [31-34] of VSM is that a magnetic dipole placed in an external static magnetic field and

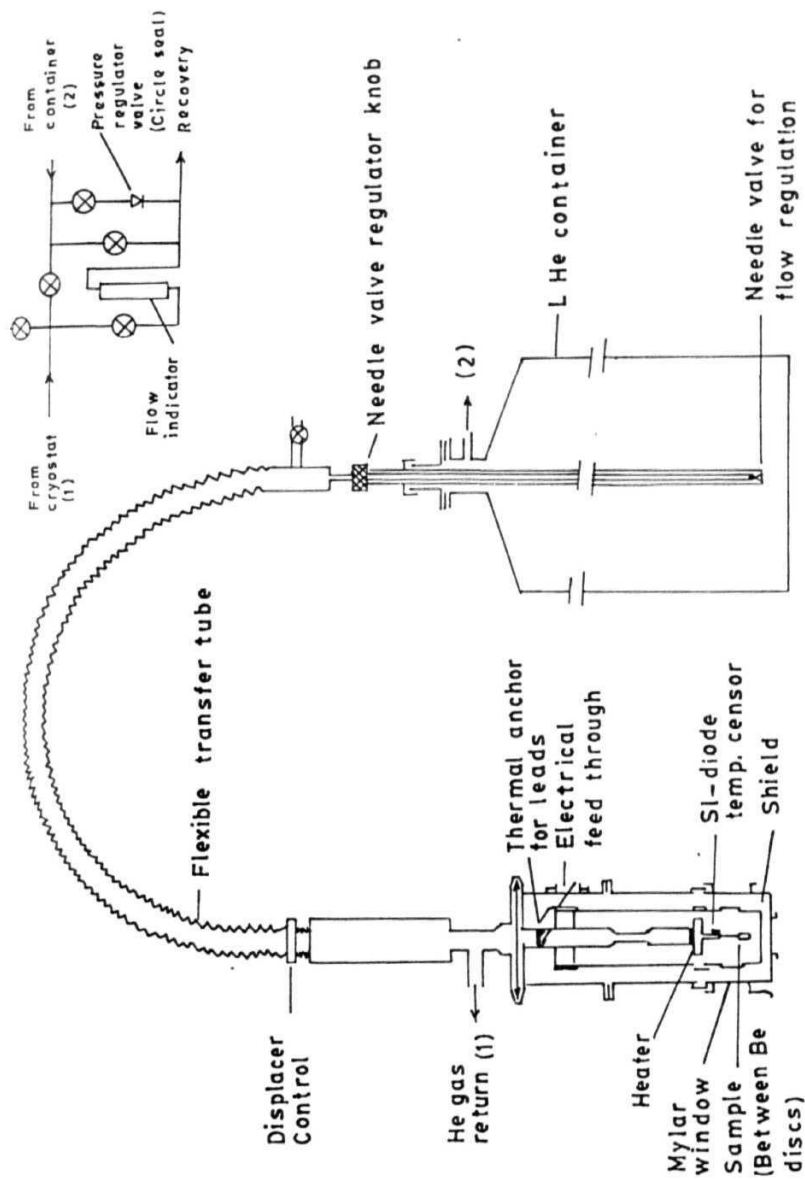


Fig. 3.5 Mössbauer low temperature setup.

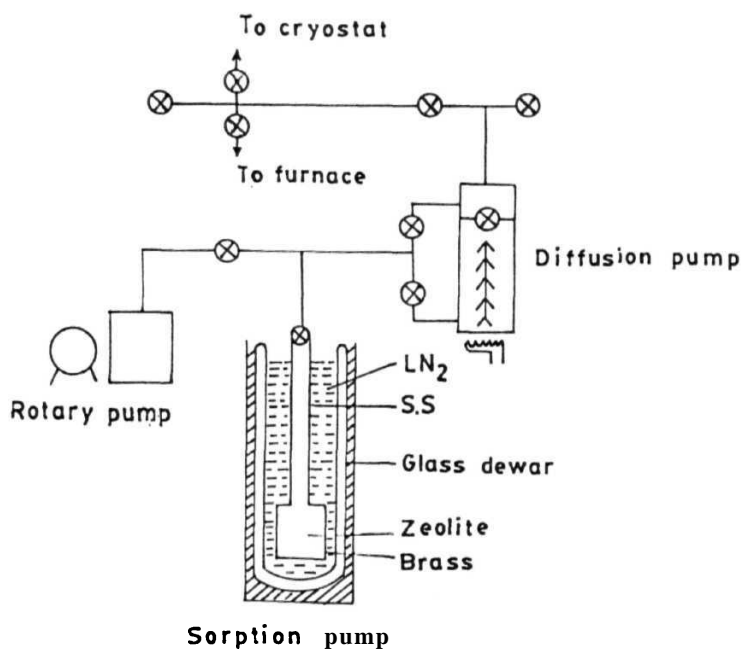


Fig. 3.6 Vacuum system arrangement for cryostat.

undergoing sinusoidal oscillation induces an electrical signal in suitably located pickup coils. The induced signal, which is at the frequency of dipole oscillation, is proportional to the magnetic moment, amplitude and frequency of oscillation. If the amplitude and frequency of oscillation are kept constant, the induced signal is proportional to the magnetic moment alone.

Experimental Setup

The block diagram of EG & G Princeton Applied Research, VSM Model 4500 system used in the present work is shown in Fig. 3.7. The VSM system consists of a microprocessor based VSM controller unit, temperature controller, electromagnet capable of producing magnetic fields up to ± 15 kOe and a bipolar dc power supply (maximum current ± 65 A dc, at 130 V). The drive signal from VSM controller drives the transducer located above the magnet, which in turn transmits vibrations to the sample through the sample holder assembly. That the amplitude and frequency of vibration remain constant is ensured by means of a feedback mechanism involving a vibrating capacitor arrangement. The vibrating capacitor located just beneath the transducer generates an ac signal that depends solely on the amplitude and frequency of vibration and fed back to the VSM controller where it is compared with the drive signal so as to maintain a constant drive output. This ac control signal is also phase-adjusted and routed to the signal demodulator in which it serves as reference drive signal. Thus, the feedback mechanism ensures that both the amplitude and frequency of vibration remain constant. The output signal due to the magnetic moment of the specimen induced in the pickup coils (located at the center of the pole pieces) is detected by means of lock-in phase detector housed in the VSM controller. The Hall probe placed between the pole pieces of the electromagnet forms a part of the Gaussmeter, which measures the external magnetic field strength at the sample site. The VSM controller which has a provision to control the bipolar dc power supply, can either sweep the field at constant rate or maintain it stable at any given value.

The system is calibrated using high purity Nickel. Small amount of ~ 10 mg of the sample is taken in several strips of alloy ribbons, all of 2.5 cm length and 1-2 mm width stacked one above the other after a thin layer of Silicone high vacuum grease was applied in between them to ensure a good thermal contact between the ribbon

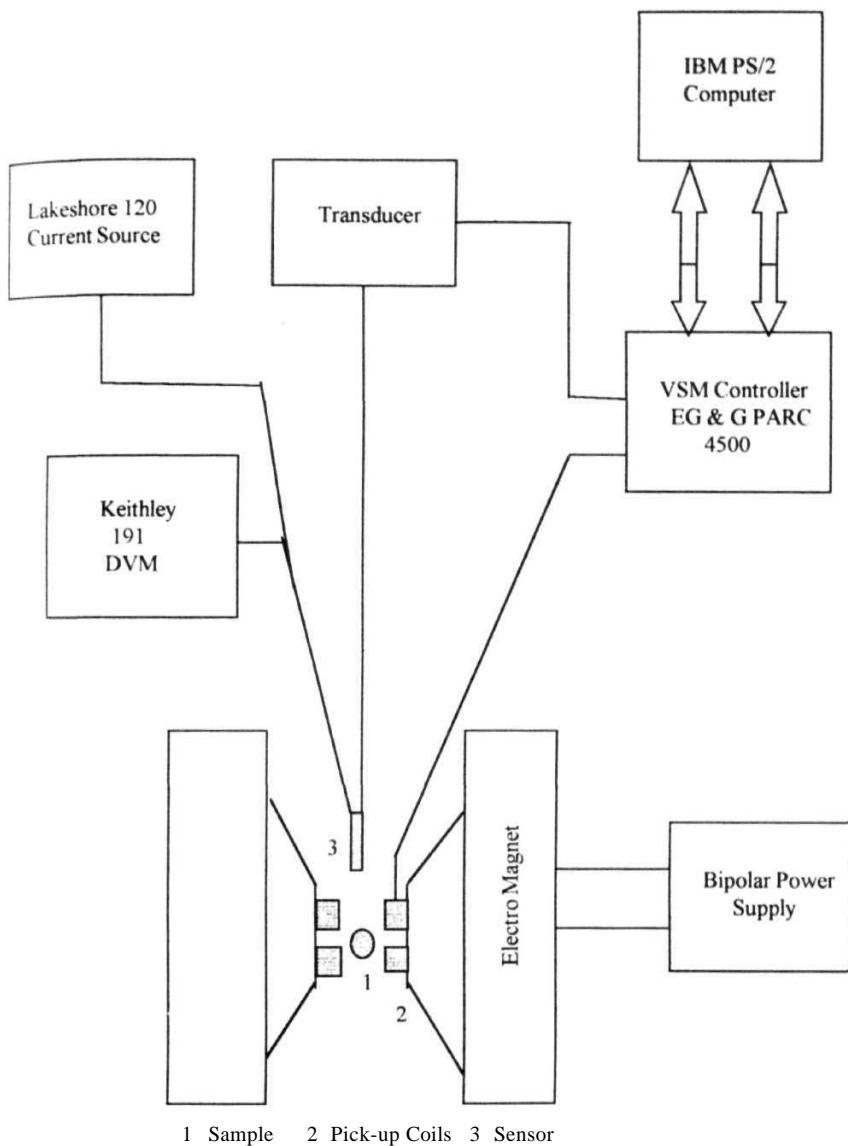


Fig 3 7 Block diagram of the Vibrating Sample Magnetometer.

strips. The sample in the form of a stable bundle was placed in the sample holder assembly and rotated such that the field lies within the ribbon plane and is directed along the length of the ribbons. This arrangement minimizes the demagnetizing effects. A microbalance is used to weigh the samples used.

Fig. 3.8 shows the schematic diagram of **VSM Model 4500**. Using the X, Y and Z position adjustments the sample is located symmetrically with respect to the detection coils, thus minimizing the effects of geometry on the results of measurements with this **system**. By increasing the current through the coils, the applied magnetic field is varied from 0 to **15 kOe** and the total magnetic moment of the sample is recorded in **emu**. The stability of the output signal is better than $\pm 0.05\%$ of **full scale** and the sensitivity of the VSM is 5×10^{-5} **emu**.

Magnetization measurements at low temperatures in the range (10-100 K) were carried out in Texas A&M University, USA, using a Series 7000 **Lakeshore** ac Susceptometer/dc Magnetometer [35] which measures magnetic moment as a function of temperature and applied dc fields of ± 1 , ± 5 and ± 9 **kOe**. Samples of ~ 10 **mg** were used with a constant applied magnetic field of 1 kOe, up to a resolution of 9×10^{-5} **emu**. The block diagram of the experimental setup is shown in Fig. 3.9.

3.5 Results and Discussion

3.5.1 Mossbauer Spectra of Metallic Glasses

In pure crystalline iron, all the iron atoms occupy crystallographically equivalent positions and therefore a single set of hyperfine interaction parameters, H_{eff} , IS and ΔE_Q characterize the Mossbauer spectrum. In crystalline compounds and dilute iron alloys, each Mossbauer spectrum consists of reasonably sharp absorption lines. Since the number of different neighbourhoods is small in such cases, it is usually not difficult to establish a correspondence between the different sets of H_{eff} , IS and ΔE_Q and the atomic arrangements in such alloys or compounds. However, the situation is quite different in metallic glasses. The Mossbauer spectra of iron-rich ferromagnetic metallic glasses show six broad overlapping line-patterns, characteristic of the ferromagnetic state of amorphous ferromagnetic glasses [2,36-41]. The absorption

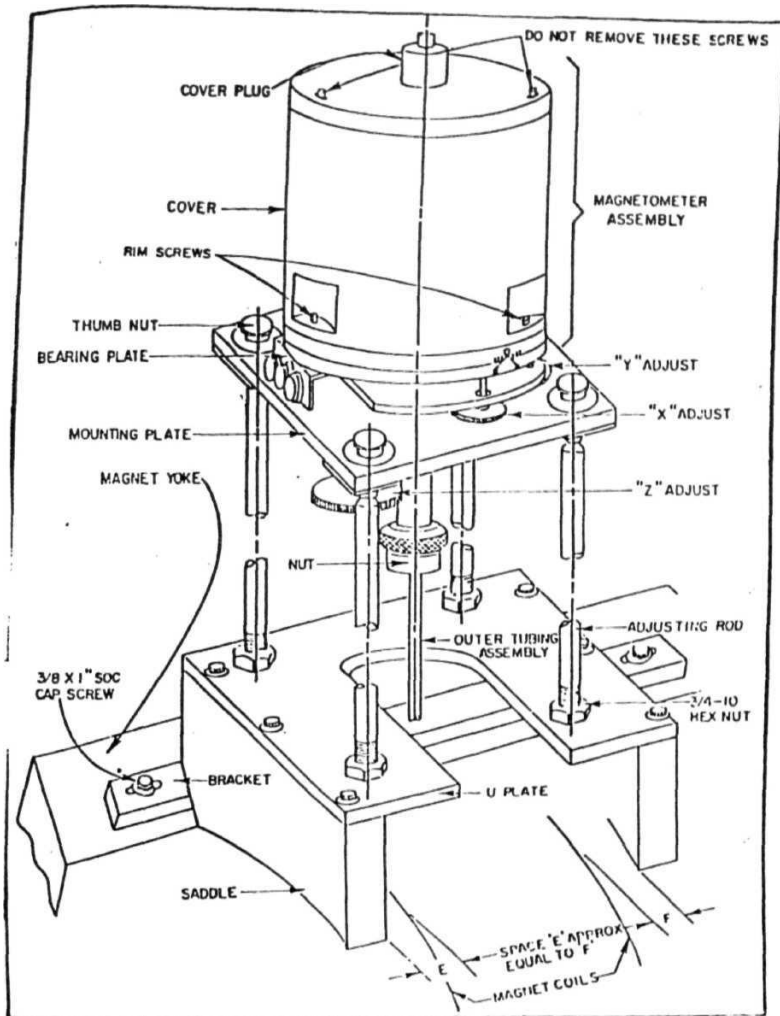


Fig. 3.8 Schematic diagram of Vibrating Sample Magnetometer Model 4500

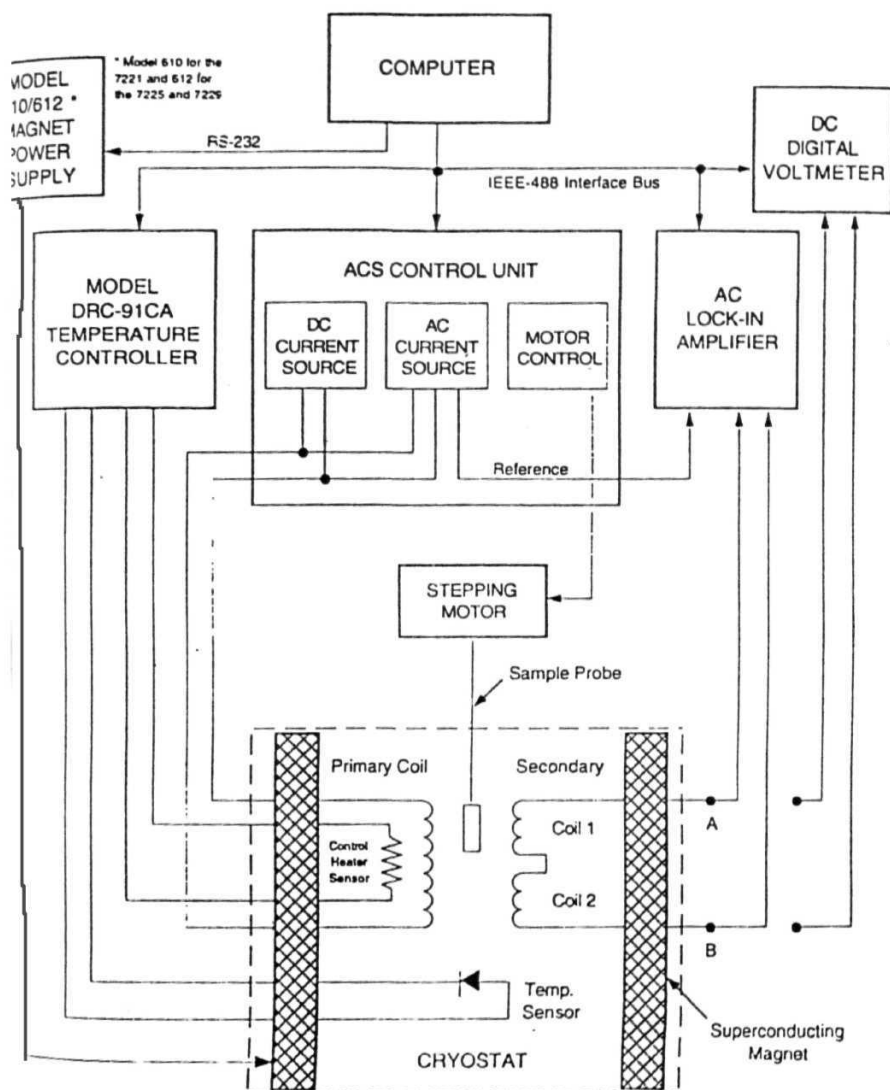


Fig 3 9 Block diagram of Lakeshore Series 7000 ac Susceptometer/dc Magnetometer

lines have rather large linewidths (0.5-2.0 mm/s), which are about **five** to six times the linewidth of the absorption lines in the Mossbauer spectrum of a thin **Fe-foil**

The large linewidths in six line Mossbauer spectra of metallic glasses are explained by invoking the distribution of magnetic **hyperfine fields**, electric field gradients of the Mossbauer probe atom and **isomer** shifts, which are consequences of the amorphous nature of the solid, which in turn is responsible for a wide distribution in the neighbours of any given iron atom in the solid i.e., all iron atom sites are not crystallographically equivalent in an amorphous **solid**. However, it is observed that the broadening is not the same for all the **lines**, and the linewidth increases from the central to the outermost line of the spectrum, i.e., $\Gamma_{1,6} > \Gamma_{2,5} > \Gamma_{3,4}$ where $\Gamma_{1,6}$, $\Gamma_{2,5}$ and $\Gamma_{3,4}$ are **FWHM** of lines 1 & 6, 2 & 5 and 3 & 4 in Mossbauer spectrum where numbering of lines, i.e., 1 to 6 is done from left to right in Fig. 3.10. This suggests that the major broadening of lines is caused by magnetic hyperfine field distribution and the effect of the distribution of other **hyperfine** parameters is comparatively **less**. From the observed Mossbauer spectrum it is not easy to extract information about the local surroundings of the iron atom as the differences between the various local neighbourhoods of the iron atom are too small to be resolved separately in the **spectrum**. However, since the Mossbauer spectrum still shows well resolved six lines, below Curie temperature, T_c , it is possible to get information about the average **magnetic** behaviour of the sample directly from the **spectrum**. The characteristic features of the Mossbauer spectrum of the metallic glass system Fe-Ni-Mo-B-Si with respect to composition and temperature dependence are discussed in the following **sections**.

3.5.2 Analysis of Fe^{57} Mossbauer Spectra of Amorphous Alloys

Fe^{57} Mossbauer spectrum of crystalline materials containing six lines only indicates that the iron Mossbauer probe finds itself in a unique environment thus having unique hyperfine magnetic field at the probe **site**. **Lineshapes** in **α -Fe** Mossbauer spectra are expected to be **Lorentzian**. Hence, one can fit the spectrum using six Lorentzian lines with a parabolic background to obtain the line positions, linewidths, intensities **etc.**, from which hyperfine interaction parameters like hyperfine magnetic **field**, quadrupole splitting, isomer shift **etc.**, can be determined [42].

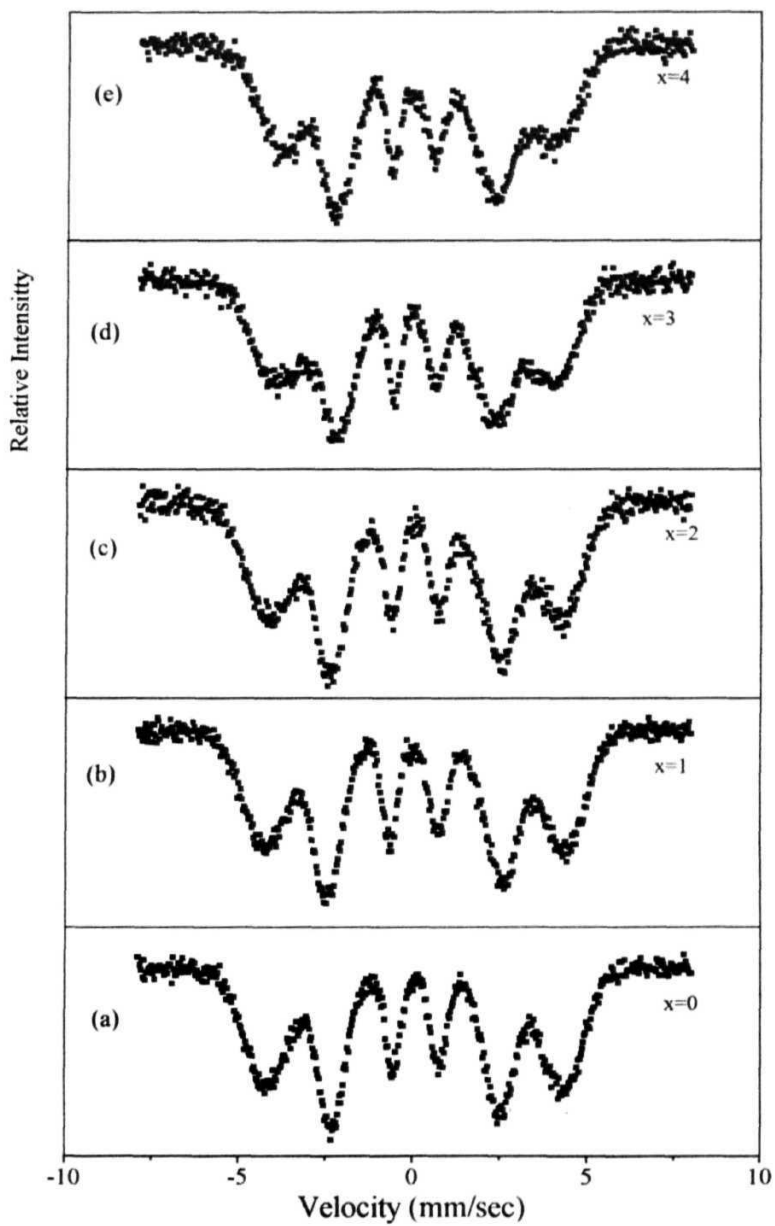


Fig 3 10 Mossbauer spectra of all the samples $\text{Fe}_{68}\text{Ni}_{14-x}\text{Mo}_x\text{Si}_2\text{B}_{16}$ ($x=0-4$) at RT

However, the situation is quite different in amorphous iron-rich alloys in which crystal type long-range order of atomic sites is not present

Mossbauer nuclei, being local probes, are extremely sensitive to small changes in the local environments of atoms, i.e., when two Mossbauer atoms in the same sample have different local environments, their individual Mossbauer spectra will also be different, each having its own set of Mossbauer parameters. In amorphous alloys, there exists a wide distribution in local environments of the Mossbauer atoms due to chemical and topological disorder. As a result of this, the hyperfine field, isomer shift, and the electric field gradient (EFG) vary from one iron nuclear site to the other and this variation, in turn, gives rise to broad overlapping of Mossbauer lines. Hence the interpretation of Mossbauer effect (ME) spectra in these materials is often difficult and judicious choice of the method of analysis has to be made in order to arrive at the correct values for the hyperfine interaction parameters.

Although Mossbauer spectrum of an iron-rich metallic glass consists of six broad overlapping lines, yet these are reasonably resolved and one can easily identify the six lines. Therefore, as a first approximation, one can still fit the spectrum using six overlapping Lorentzian lines to obtain H_{eff} , IS, ΔE_Q , linewidths etc. Therefore, a least square fit method has been used to fit each Mossbauer spectrum of a sample to a sum of six Lorentzian lineshapes with a parabolic background. The equation for one or more Lorentzians plus a parabola [43] is given by

$$Y = \sum_{i=1}^n \frac{A_i}{1 + \left[\frac{X - P_i}{\Gamma_i/2} \right]^2} + E + FX + GX^2 \quad (323)$$

where A_j is the amplitude of the i^{th} peak (counts), X is the number in the i^{th} channel, P_j is the position of the i^{th} peak (channel), Γ_i is Full Width at Half Maximum (FWHM) of the i peak (channels) and E , F and G are constants of the parabolic background.

Initially, the program uses estimated values of the parameters to solve the equation of the curve for each X to obtain a calculated value for each Y . This calculated Y is subtracted from the observed value of Y for the corresponding X to

give the residual, ΔY . The residual for each value of X is squared and summed over all values and this sum of squared residuals is **minimized**. The observed Y values that lie sufficiently below the other Y values are to be rejected and set equal to zero. These values are ignored in fitting the curve by giving them a weight (W) of **zero**. Each other Y value has a weight 1.

Most of the Mossbauer data on metallic glasses have been fitted using a Lorentzian lineshape [44-46] though, the glassy nature of metallic glasses produces Mossbauer lines, which are not strictly Lorentzian. The fit of **Mossbauer** data of metallic glasses using non-Lorentzian lineshape [28,47] gives only a slight improvement in fitting the data in comparison with the fit using Lorentzian lineshape. In addition not much difference in the hyperfine interaction parameters is found by fitting Mossbauer data by using either Lorentzian or non-Lorentzian lineshapes, i.e., Gaussian or Pseudo Lorentzian. Hence we have used Lorentzian lineshape to fit our data.

For each Mossbauer spectrum of a sample, the output of the LSF program using **Eq (3.23)** gives information about the amplitude, **position**, Half Width at Half Maximum (HWHM) and peak area of each **peak**. The parabolic constants E, F and G are also obtained from which the three hyperfine parameters can be **calculated**.

Later, we have used another method to analyze the Mossbauer data to take into account of the distributions in hyperfine magnetic field. This is described later in Sec **3.5.6**.

3.5.3 Room Temperature Mossbauer Spectra of Fe-Ni-Mo-B-Si Alloys

The room temperature Mossbauer spectra of **Fe₆₈Ni_{14-x}Mo_xSi₂B₁₆** (**x=0,1,2,3** and 4) alloys are shown in Fig. **3.10(a)-(e)**. As usual all the samples show six broad peaks, which is a characteristic feature of amorphous alloys due to random distribution of **atoms**. The asymmetries in the lines are evident from the **Fig 3.10** which is an observed feature in similar FM metallic glasses [41]. One also observes that as Mo concentration increases, data for first and sixth lines **become** relatively **noisy**. This may be indicative of small inhomogeneity of the sample, especially for **x=4** sample, but no evidence of crystallites in the sample was observed by X-rays. The data was fitted using May's program to obtain **Isomer Shift (IS), H_{eff}(RT), ΔE_Q and Γ** for the six **lines**.

ΔE_Q is found to be nearly zero as expected in an amorphous solid. The values of parameters IS and H_{eff} at RT thus obtained from these fittings are listed in Table (3.1). There does not seem to be any systematic variation of IS with Mo concentration. $H_{eff}(RT)$ values for these samples show that for $x=1$, $H_{eff}(RT)$ increase a little bit. This was not expected, hence, the RT Mossbauer spectrum was taken again and the results were found to be exactly similar. Samples were X-rayed and found to be amorphous. For $x>1$ there is a decrease in $H_{eff}(RT)$ as Mo concentration is further increased, an expected result. The average decrease in $H_{eff}(RT)$ comes out to be ~ 5 kOe/Mo-at% in $Fe_{68}Ni_{14-x}Mo_xSi_2B_{16}$. Values of Curie temperature, T_c determined by low field dc magnetization method, are also listed Table (3.1) for all the samples. These values show decrease with addition of Mo upto $x=3$ but no further decrease for $x=4$ is noted, it rather shows some increase although within error it is difficult to conclude. T_c also decreases with Mo concentration at a rate of ~ 40 K/at% upto $x=3$. However, T_c for $x=4$ does not decrease further but shows slight increase. For $Fe_{70}Ni_{12-x}Mo_xSi_2B_{16}$ a similar observation has been recorded i.e., for $x>3$ at%, T_c does not decrease with the same rate. This may indicate a possibility that Mo beyond $x=3$ at% may not be getting into the alloy $Fe_{68}Ni_{14}Si_2B_{16}$ homogeneously which is also reflected in $H_{eff}(RT)$ vs x results i.e., the rate of decrease in $H_{eff}(RT)$ from $x=3$ to $x=4$ samples is smaller compared to the decrease of $H_{eff}(RT)$ for $x=2$ to $x=3$ samples. Overall average behaviour of $H_{eff}(RT)$ and T_c is to decrease with Mo concentration shown in Fig 3.11(a)&(b). This is not surprising as cooperative magnetism with exchange and dipolar interactions contribute to T_c and H_{eff} . Such systematics may arise either due to magnetic dilution effect of molybdenum or due to Fe-Mo antiferromagnetic exchange interactions as suggested for analogous alloys containing Cr, Mn and Mo [39,40,48-54]. This decrease is ~ 8.5 kOe/Mo-at% for $a-Fe_{72}Ni_{10-x}Mo_xB_{16}Si_2$ alloys [55] and ~ 7.9 kOe/Mo-at% for $a-Fe_{70}Ni_{12-x}Mo_xSi_2B_{16}$ alloys [56] while Sostarich et al [49] observed a decrease of 12 kOe/Mo-at%. The observed fall of ~ 30 K/Mo-at% in T_c for the present family of alloys (except for $x=4$) may be compared with 32 K/Mo-at% in the case of $a-Fe_{72}Ni_{10-x}Mo_xB_{16}Si_2$ [55], 50 K/Mo-at%

Table 3.1 The values of Isomer shift (δ), effective hyperfine field $H_{\text{eff}}(\text{RT})$ at RT and Curie temperature (T_c).

Sample (x)	IS, δ mm/s	$H_{\text{eff}}(\text{RT})$ (kOe)	T_c (K)
0	0.099	264	711
1	0.065	268	652
2	0.081	262	623
3	0.050	251	592
4	0.053	248	594

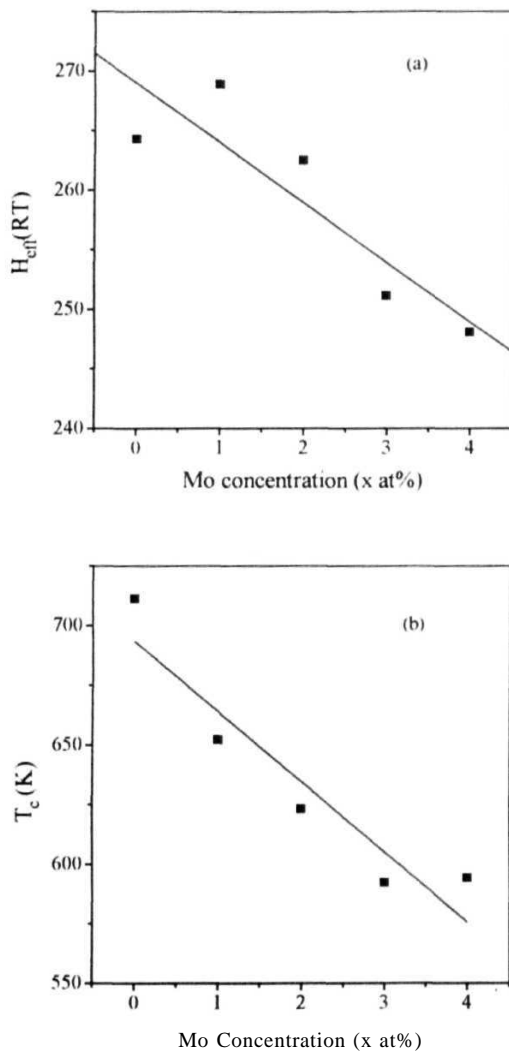


Fig. 3 1 (a) The plot of effective **hyperfine** field at **RT**, ($H_{\text{eff}}(\text{RT})$) as a function of Mo concentration, **x**
 (b) The plot of Curie temperature, T_c as a function of Mo concentration, **x**

in the case of a-Fe₇₄Mo_{80-y}B₂₀ [57] and 40 K/Mo-at% in the case of a-Fe_{80-x}Mo_xB₂₀ [49]

It is interesting to compare this value with the value of 30 K/Cr-at%, observed for the family of a-Fe₇₄Co_{10-x}Cr_xB₁₆ and 2.1 K/Cr-at% for a-Fe_{85-x}Cr_xB₁₅ family [49]. Thus, it seems that although Mo is a non-magnetic metal, its behaviour, when added to iron rich metallic glasses Fe/Si/B etc., is similar to that of Cr which is antiferromagnetic material. These observations are also consistent with the results reported by Nielsen [49]. Thus it seems that a substitution of Mo in the present alloys, in which Ni has already been substituted for Fe by 14%, degrades magnetic properties of these samples at a slightly smaller rate in comparison with the changes observed in the magnetic properties of Fe₈₀B₂₀ or a-FeBSi alloys when only Mo is substituted. This effect is possible if most of the Fe atoms are shielded from Mo atoms by Ni atoms. Thus Mo atoms avoid a direct interaction with Fe atoms but have it through Ni atoms in these alloys, while for a-Fe_{80-x}Mo_xB₂₀ or a-(Fe_xMo_{1-x})₇₅P₁₆B₆Al₁, Mo atoms have a direct interaction with Fe atoms, leading to a larger decrease in effective magnetic interaction between Fe atoms. In addition because Mo is larger in size, it is possible that beyond a certain at%, Mo atoms may not be able to occupy nearest neighbour positions to Fe when Ni, a smaller atom, is also there in larger concentration. This may be the reason why going for x=3 to x=4 Mo concentration, magnetic properties do not seem to change at the same rate as they do when x is small.

3.5.4 Magnetization Axis

The direction of saturation magnetization M_s of an iron-rich FM alloy is inferred from the ratio of intensities of the second (fifth) line to the first (sixth) line in the ⁵⁷Fe Mossbauer spectrum. The ratio is given by

$$\frac{I_{2,5}}{I_{1,6}} = \frac{4\sin^2\theta}{3(1 + \cos^2\theta)} \quad (3.24)$$

where, θ is the angle between the direction of emission of the 14.4 keV gamma rays and the direction of the magnetization. The values of $I_{2,5}/I_{1,6}$ vary from 0 to 4/3 as θ changes from 0 to 90 degrees. If a sample contains more than one magnetization direction then the values of $I_{2,5}/I_{1,6}$ have to be averaged suitably. It is therefore

possible to derive information about the direction of the magnetization axis from the Mossbauer **spectrum**. For a glassy sample, since the six Mossbauer lines do not have the same linewidth, because of a **hyperfine** field distribution, it is more appropriate to compare area ratios instead of line intensity ratios. For the same reason we have chosen to compare area ratios $A_{2,5} = (A_2 + A_5)/(A_1 + A_6)$ and $A_{3,4} = (A_3 + A_4)/(A_1 + A_6)$ rather than A_2/A_1 or A_5/A_6 due to the observed asymmetry of the lines (1,6), (2,5) and (3,4). The areas and area ratios of Mossbauer lines at RT are given in Table (3.2). It is observed that the values of $A_{2,5}$ lie between 0.8 and 1.3 depending upon the sample. Table (3.2) shows that $A_{2,5}$ increases with Mo concentration, x .

Thus, it seems that the magnetization axis, which is out of plane of the ribbon for $x=0$ sample, tilts towards the ribbon plane as x increases. For the $x=4$ sample, it lies in the plane of the ribbon since $A_{2,5}$ is ~ 1.33 . Since samples are clamped between two copper rings, there could be some stress due to this which shall effect these results since magnetization axis in these samples is stress **sensitive**. However, the effect at RT should be minimal since reasonable care was taken not to either stretch or compress the samples lengthwise.

However, the situation becomes quite different at lower **temperatures**. The difference in thermal expansions of the copper ring and the sample would induce a stress in the sample, which would change the magnetization axis in the **sample**. The lower the temperature, the larger is the stress expected to be generated in the sample. Thus, the results obtained on the temperature dependence of $A_{2,5}$ and $A_{3,4}$ are really not meaningful under the said **conditions**. However, for the sake of completeness, we present the results in Fig. 3.12. There does not seem to be any systematic behaviour of $A_{2,5}$ of a given sample with T . $A_{3,4}$ for a given sample, specially for $x=3$ and $x=4$ shows a decreasing trend with T . The induced stress should affect $A_{2,5}$ much more than $A_{3,4}$, hence much more unsystematic behaviour is seen for $A_{2,5}$ in Fig. 3.12. Similar behaviour of the direction of the magnetization axis has been observed for clamped iron-rich metallic glasses [58]. The **unclamped** samples seem to show that the magnetization axis nearly lies in the plane [28]. However, the direction of magnetization axis varies from sample to sample studied and may be due to the effect of **'quenching'** conditions in preparing iron rich metallic glasses.

Table 3.2 The area values of the six individual absorption peaks in the spectra and the area ratios $A_{2,5}$ and $A_{3,4}$ at KT for all the samples.

Sample (x)	$A_1(10^4)$	$A_2(10^5)$	$A_3(10^4)$	$A_4(10^5)$	$A_5(10^5)$	$A_6(10^4)$		$A_3 + A_4$
							$A_1 + A_6$	$A_1 + A_6$
0	5.60	424	1.72	1.76	451	508	0.82	0.33
1	7.18	6.24	2.44	2.89	704	650	0.97	0.34
2	447	3.82	1.27	1.57	4.48	3.30	1.07	0.37
3	5.17	5.55	1.21	1.64	588	432	1.20	0.30
4	3.33	3.94	0.84	1.54	4.57	2.97	1.35	0.38

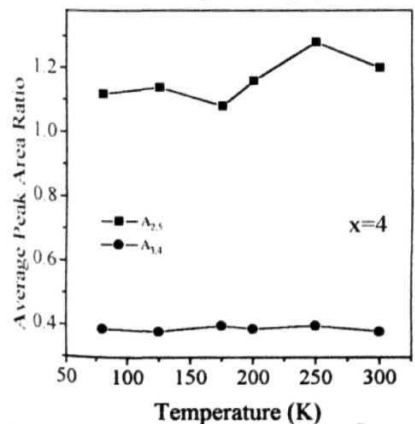
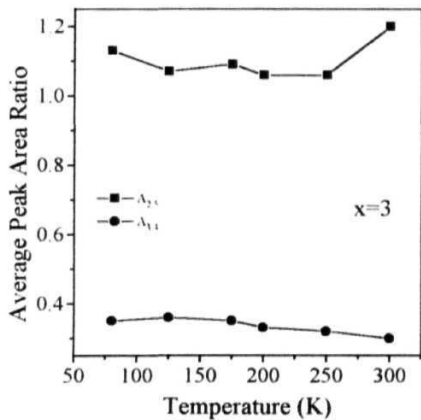
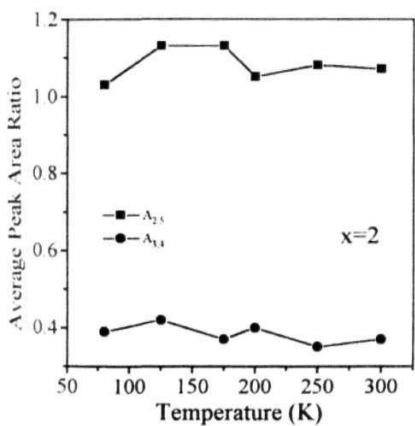
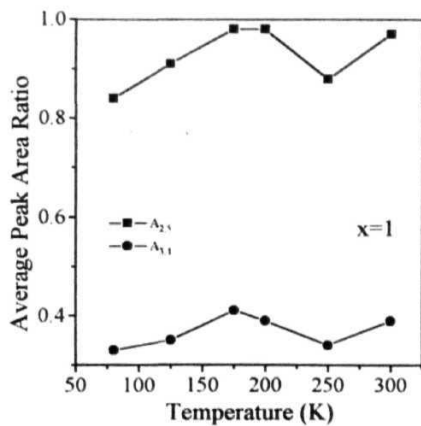
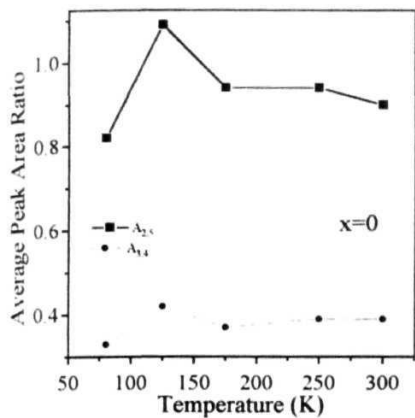


Fig. 3.12 Average peak area ratios of spectral lines of amorphous $\text{Fe}_{68}\text{Ni}_{14-x}\text{Mo}_x\text{Si}_2\text{B}_{16}$ ($x=0-4$) alloys as a function of temperature where A_1 , A_2 , A_3 , A_4 , A_5 and A_6 are the areas of the peaks 1, 2, 3, 4, 5 and 6 respectively.

3.5.5 Temperature Dependence Studies of Mossbauer Spectra of Fe-Ni-Mo-Bi-Si Alloys

The Mossbauer studies on $\text{Fe}_{68}\text{Ni}_{14-x}\text{Mo}_x\text{Si}_2\text{B}_{16}$ ($x=0,1,2,3$ and 4) alloys in the temperature range 80 K-RT below T_c , have been carried out and the Mossbauer spectra are shown respectively in Figs 3 13, 3 14, 3 15, 3 16 and 3 17 for $x=0$ to 4. All the samples show six broad peaks, which is a typical observation for ferromagnetic metallic glasses. Here, the linewidths at room temperature for all the compositions for x varying from 0 to 4 are $\Gamma_1 > \Gamma_2$, $\Gamma_2 < \Gamma_3$, $\Gamma_3 < \Gamma_4$ shown in Table (3.3), indicating significant asymmetry in the linewidths. The values of IS at different temperatures are tabulated in Table (3 4)(a) and in Table (3 4)(b) the corresponding values of slopes ($=d(\text{IS})/dT$) for the respective samples are given. In the following sections the temperature dependence of magnetic hyperfine fields, isomer shifts and linewidths of these glasses is discussed.

Temperature Dependence of Linewidths

As per our earlier discussions, the first and sixth lines of Mossbauer spectrum show large linewidths, which are due to a distribution in hyperfine fields present in the Mossbauer probe. Therefore, they are a measure of distribution in hyperfine magnetic fields at the Mossbauer probe. A study of temperature dependence of the linewidths of the outermost lines provides information regarding the short-range or long-range magnetic interactions present in the sample. As the temperature is increased the linewidth of the outermost lines may vary in one of the following ways:

- If $H_{\text{eff}}(T)$ has similar temperature dependence for all possible sites, then the line width will decrease monotonically.
- For small values of H_{eff} , the decrease of $H_{\text{eff}}(T)$ is faster and in this situation, the linewidth increases first and as T approaches T_c it decreases.
- For small values of H_{eff} , the decrease of $H_{\text{eff}}(T)$ is slower and this results in decrease of the linewidth initially followed by an increase before finally decreasing as T tends to T_c .

Balogh & Vincze [59] analyzed the behaviour of magnetic moment versus

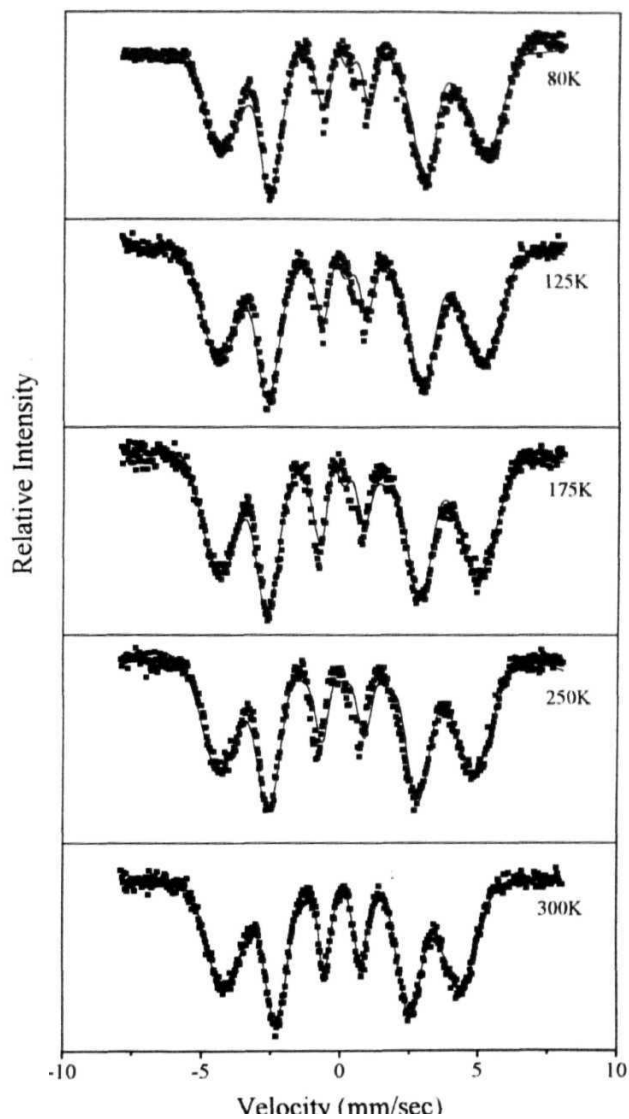


Fig 3 13 Mossbauer spectra of the sample $x=0$ at different temperatures 80 K-RT

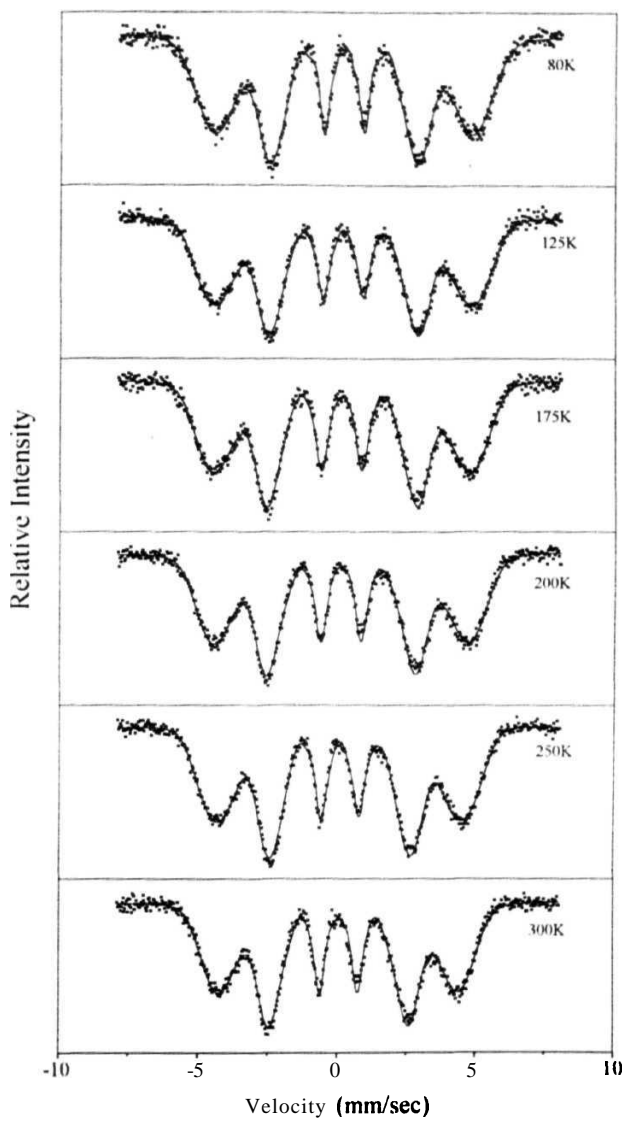


Fig 3 **14** Mossbauer spectra of the sample $x=1$ at different temperatures 80 K-RT with the line showing the fitted **data**

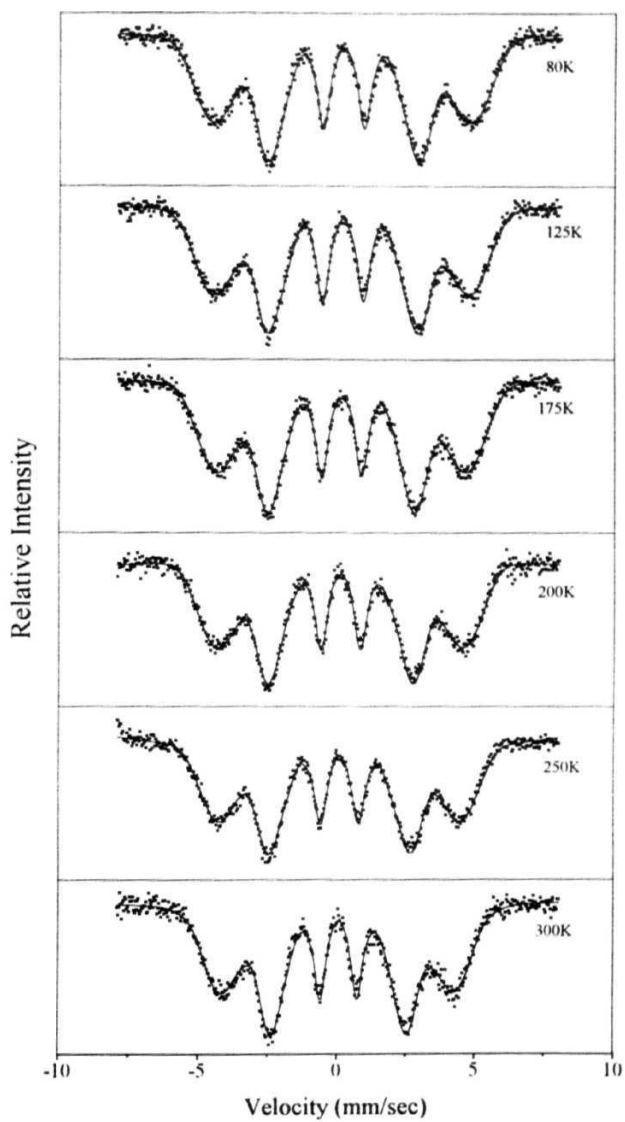


Fig 3 15 Mossbauer spectra of the sample $x=2$ at different temperatures 80 K-RT with the line showing the fitted **data**

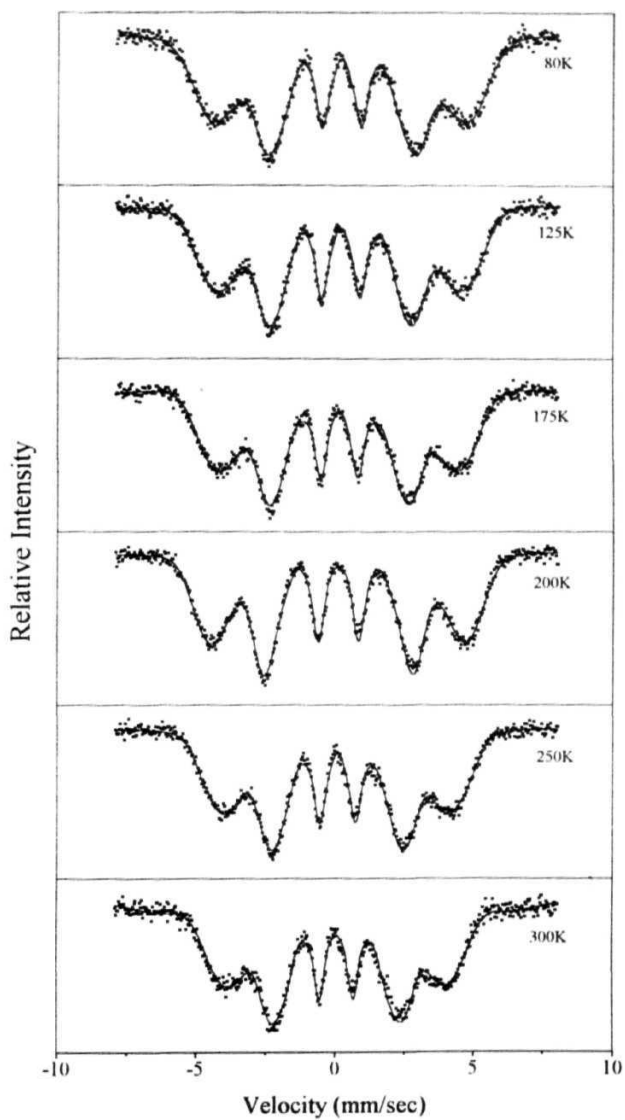
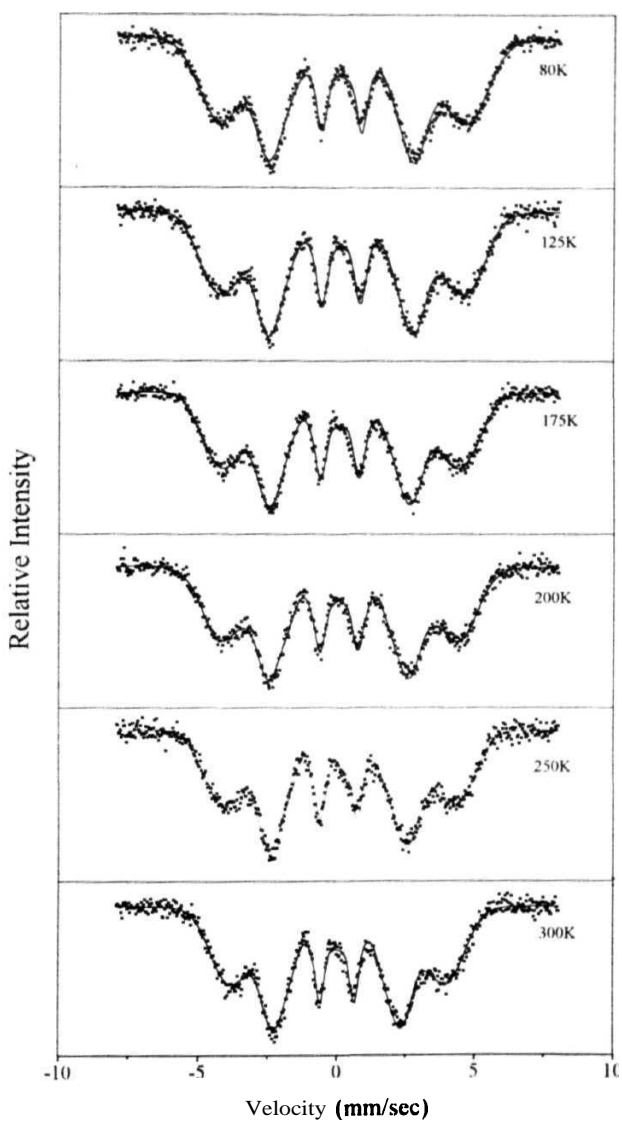


Fig. 3 16 Mossbauer spectra of the sample x-3 at different temperatures 80 K-RT with the line showing the fitted **data**



3 17 Mossbauer spectra of the sample $x=4$ at different temperatures 80 K-RT with the line showing the fitted **data**

Table 3.3 The Mossbauer linewidths in mm/s of all the six lines for each sample at RT.

Sample (x)	Γ_1	Γ_2	Γ_3	Γ_4	Γ_5	Γ_6
0	1.66	1.00	0.61	0.63	1.15	1.47
1	1.74	1.15	0.62	0.81	1.37	1.58
2	1.95	1.20	0.59	0.78	1.48	1.52
3	1.93	1.43	0.45	0.71	1.62	1.72
4	1.74	1.34	0.45	0.85	1.65	1.72

Table 3.4(a) The values of isomer shift (δ) at different temperatures for all the samples.

Temperature (K)	Isomer shift, δ (mm/s)				
	$x=0$	$x=1$	$x=2$	$x=3$	$x=4$
80	0.229	0.189	0.185	0.213	0.168
125	0.136	0.177	0.183	0.168	0.159
175	0.099	0.150	0.155	0.141	0.141
200		0.139	0.136	0.123	0.101
250	0.065	0.106	0.112	0.098	0.099
300	0.099	0.065	0.081	0.050	0.053

Table 3.4(b) The values of slopes of Isomer shift vs T plots.

Sample (x)	$d(\delta)/dT(10^{-4})$ mm/s-K
0	-5.661
1	-5.650
2	-4.998
3	-6.969
4	-5.242

temperature Case (a) is the narrow **distribution** of exchange interactions and the distribution falls monotonically, as the values fall **monotonically** and converges at T_c . This is the case where all the magnetic moments have the same temperature **dependence**. Cases (b) and (c) are similar, the field corresponding to long-range order follow the Brillouin behaviour, whereas the field corresponding to short-range order does **not**. Consequently, the systematic variation in the magnetic moment distribution **is lost**. The corresponding picture in Mossbauer spectroscopy will be dependant on the temperature effect of linewidth assuming that the linewidth corresponding to the distribution of the magnetic moment or a quantity proportional to it which is the **hyperfine** field in this **case**. The systematic fall in linewidth due to temperature will imply case (a), and any other behaviour will imply cases (b) and (c) indicating that both short-range and long-range interactions are **important**. This behaviour of magnetic moment vs temperature is shown in Fig. 3.18.

Fig 3.19 shows the temperature dependence of the average linewidth of lines 1 and 6, 2 and 5, and 3 and 4 of six line Mossbauer spectra, respectively $\Gamma_{1,6}$, $\Gamma_{2,5}$ and $\Gamma_{3,4}$, for our samples, where $\Gamma_{x,y}$ is the average of widths of lines x and y. Fig. 3.19 shows that while there is quite a bit of scatter for $\Gamma_{1,6}$, $\Gamma_{2,5}$ and $\Gamma_{3,4}$ show a systematic decrease with temperature, even though $\Gamma_{1,6}$ does not show a decreasing trend with T. Thus the temperature dependence of the linewidths of Mossbauer line suggest that the long-range order predominates over the short-range **order**. Not so smooth behaviour of $\Gamma_{x,y}$ vs T may be due to the possibility of the presence of the bimodal distribution of hyperfine magnetic fields, to be discussed in **Sec 3.5.6**. Mo and Cr containing iron-rich metallic glasses do seem to show such a behaviour [39,40,48-54].

Temperature Dependence of Isomer Shift

The details of the isomer shift have already been discussed in **Sec 3.3.1**. This is a shift of the centroid of the spectrum of an absorber with respect to the **source**. This shift arises from the **Coulombic** interaction of the nuclear charge density and the **s-electrons** at the **nucleus**. As a **result**, the nuclear energy levels of the Mossbauer nucleus are shifted by a small but measurable amount ($\sim 10^{-4}$ eV). The isomer shift, **IS**, for a given Mossbauer nucleus is a measure of the relative **s-electron** density at the nucleus and hence provides information about the valence state of the Mossbauer

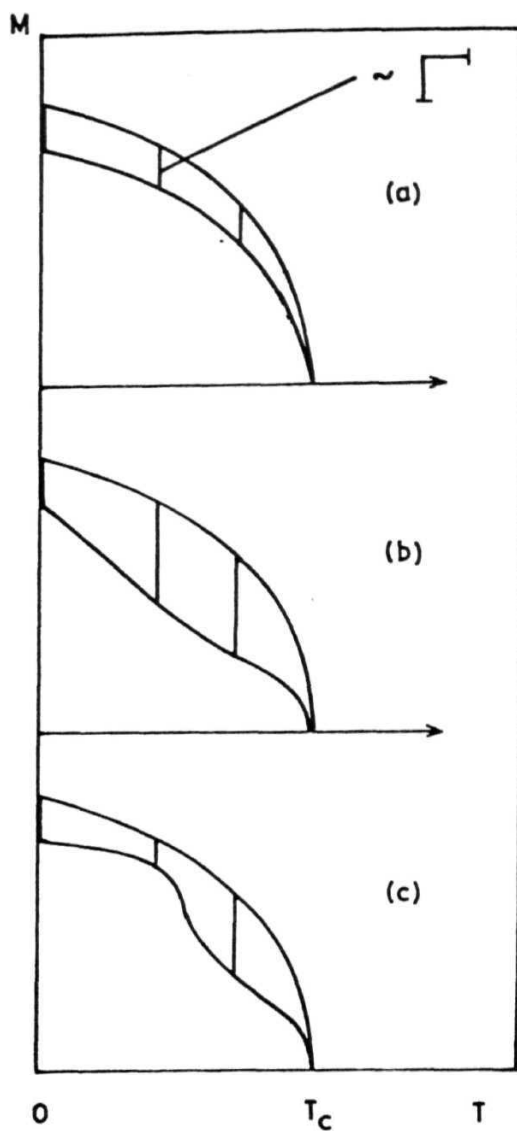


Fig 3.18 Schematic temperature behaviour of the magnetic moment distribution in the case of

- (a) narrow exchange interaction distribution indicating predominant long-range interactions,
- (b) & (c) large exchange interaction distribution, **characteristic** of predominant short-range interactions.

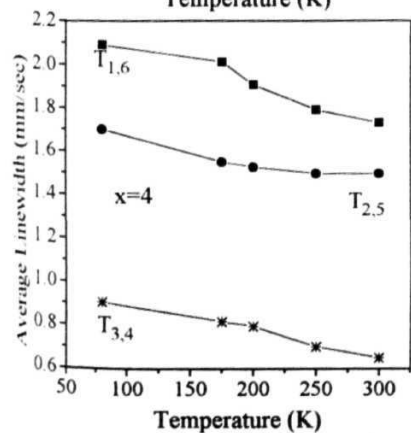
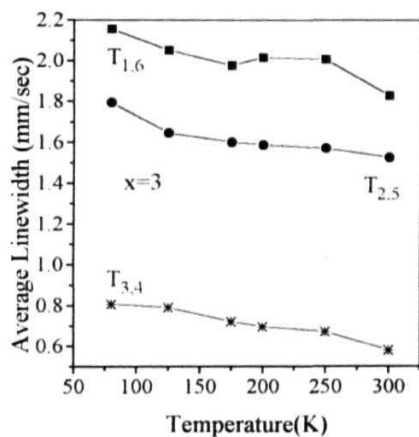
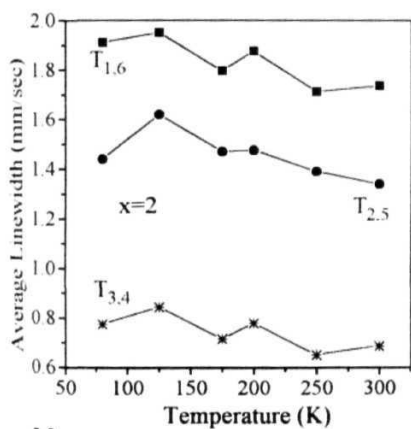
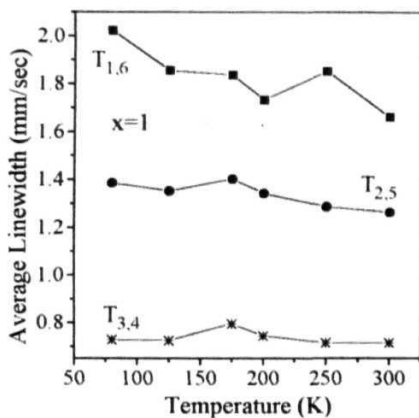
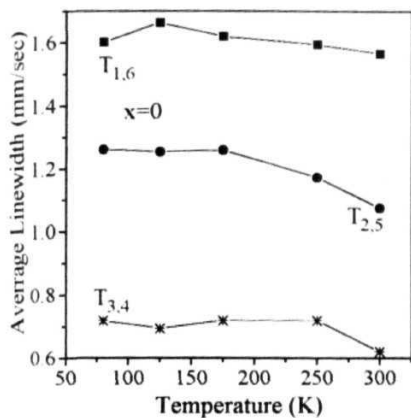


Fig 3 19 Temperature dependence of average line widths of $\text{Fe}_{68}\text{Ni}_{14-x}\text{Mo}_x\text{Si}_2\text{B}_{16}$ ($x=0-4$) alloys. $\Gamma_{1,6} = (\Gamma_1 + \Gamma_6)/2$, similarly $\Gamma_{2,5}$ and $\Gamma_{3,4}$

nuclei in the **solid** From the temperature dependence of IS an estimate of the Debye temperature of the solid can also be **obtained**

The IS of the samples ($x=0-4$) at **RT** are 0.099, 0.065, 0.081, 0.050 and 0.053 mm/s, respectively The temperature dependence of the **isomer** shift for these alloys is plotted in **Fig 3.20** from the values listed in Table (3.4)(a) This temperature dependant shift arises due to the thermal motion of the Mossbauer nuclei and is referred to as the Second Order Doppler (SOD) **effect** No doubt, in an amorphous system, there is a distribution in all the **hyperfine** parameters, including isomer shift. But, the simple LSF values should in principle correspond to isomer shift of maximum probability. So, analysis of temperature dependence of the IS data obtained should throw light on whether the amorphous solid can be approximated to a Debye model, an approximation of the harmonic force coupling between the atoms gives rise to a linear temperature dependence of IS [25] given by $d(IS)/dT = -(3k_B/2Mc^2)E_\gamma$ where k_B is the Boltzmann constant, M is the atomic mass of the nucleus and E_γ is the energy of unperturbed gamma rays [60] For ^{57}Fe Mossbauer nucleus ($E_\gamma=144$ keV), the theoretical value of the slope is -7.3×10^{-4} mm/s-K [28] A computer fit to the experimental points for our samples gives the slopes for the isomer shift vs temperature, in the range $(5-7) \times 10^{-4}$ mm/s-K, given in Table (3.4)(b), which are, within the experimental accuracy are in agreement with the value quoted above Thus one may infer that the coupling between atoms in these metallic glasses is harmonic to a good **approximation** This has been reported to be the same for all metallic glasses [61]

Temperature Dependence of H_{eff} and Spin Wave Excitations

From Mossbauer spectra for all the samples **a-Fe₈₈Ni_{14-x}Mo_xSi₂B₁₆** ($x=0-4$ in step of 1) taken at **different** temperatures are shown in Figs 3.13-3.17 By fitting these spectra to a six Lorentzian lines, as explained earlier, H_{eff} was deduced for each sample as a function of temperature The Mossbauer spectrum of a thin foil of iron was used to calibrate H_{eff} vs velocity of the source in mm/s. For each spectrum, the separation between the **first** and sixth line positions obtained from **May's** fitting is calculated and is then converted to field from **Fe-calibration** which then gives the effective hyperfine

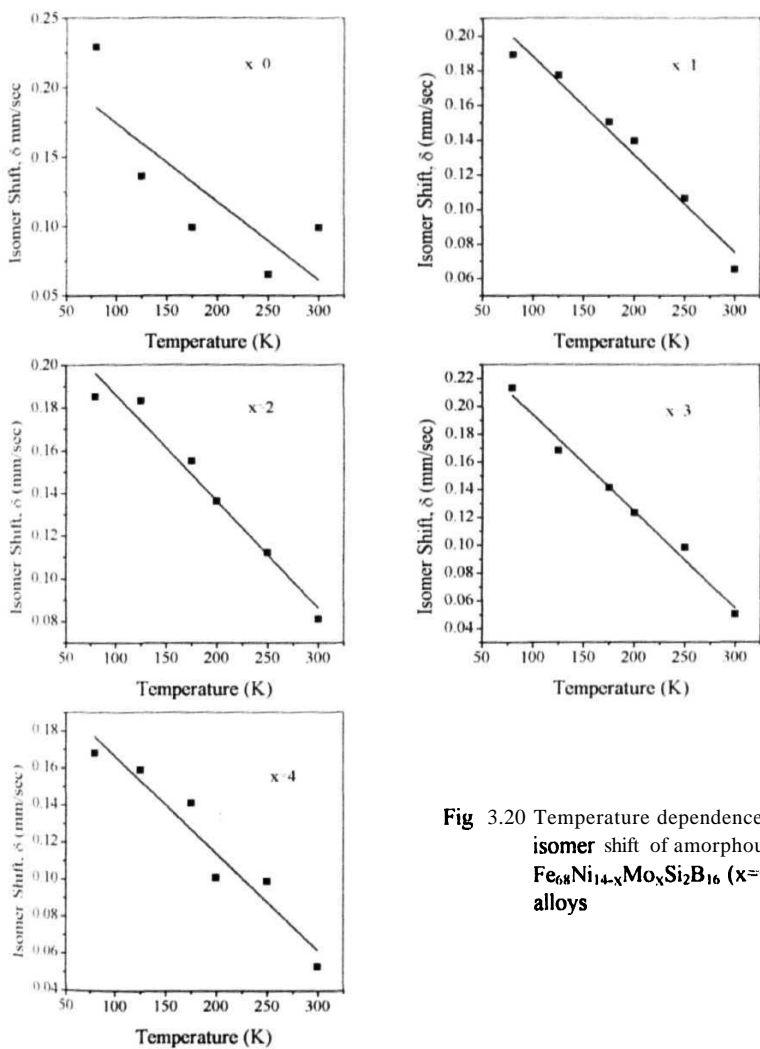


Fig 3.20 Temperature dependence of isomer shift of amorphous $\text{Fe}_{68}\text{Ni}_{14-x}\text{Mo}_x\text{Si}_2\text{B}_{16}$ ($x=0-4$) alloys

field $H_{eff}(T)$ i.e., the separation between the first and sixth line positions of **Fe-spectrum** is 330 kOe which is used for **conversion**. The values of $H_{eff}(T)$ for each sample thus obtained are given in Table (3.5) for temperatures between 80 K and **RT**. Higher temperature data was not taken since longer time required for collection of Mossbauer data invariably leads to annealing and relaxation resulting in possible changes in atomic structure, hence **H_{eff} also**. Mossbauer data taken on a number of metallic glasses **from** liquid Helium temperature to **Curie** temperature (T_c) and above have always shown that for $0.25 \leq T/T_c \leq 1$ the temperature dependence of $H_{eff}(T)$ does not follow the Standard **Brillouin** relation [38,61]. It is universally observed that $H_{eff}(T)$ values of iron-rich metallic glasses are always lower than those predicted in the temperature range mentioned [62]. Since $H_{eff}(T)$ does not vary substantially (for $T/T_c \leq 0.25$), $H_{eff}(T)$ vs T data were fitted to a straight line (as a first approximation) to obtain $H_{eff}(0)$ for each **sample**. These are listed in Table (3.6). Using these values of $H_{eff}(0)$ for different values of x and known values of T_c , $H_{eff}(T)/H_{eff}(0)$ vs T/T_c are plotted for all the samples in Fig 3.21(a)&(b). It is seen that $H_{eff}(T)/H_{eff}(0)$ for all the samples show a certain decreasing trend inspite of the **scatter**. This decreasing trend is faster than the one predicted by the Brillouin function as shown by the continuous line **drawn**. This is expected as mentioned earlier.

It is well known that the decrease in magnetization of a ferromagnet at low temperatures is more **appropriately** described by Spin wave **excitations**. The excitation of the spin waves at low temperatures in amorphous **ferromagnets** also has been firmly established by magnetization, neutron scattering and Mossbauer measurements (since $H_{eff} \propto M$, magnetization). Below, brief discussion is given for the spin wave **excitations**.

Spin-wave excitations

The decrease in magnetization of a crystalline ferromagnet at low temperatures can be explained if the low lying magnetic excitations are spin waves which obey the following dispersion relation

$$E(q) = \hbar\omega(q) = A + Dq^2 + Eq^4 \quad (3.25)$$

where $\hbar\omega(q)$ is the energy of the spin wave with propagation wave number q , and D

Table 3.5 The values of effective hyperfine fields for the spectra recorded at different temperatures for all the samples.

Temperature (K)	$H_{\text{eff}}(\text{T})$ ($\pm 5 \text{ kOe}$)				
	$x=0$	$x=1$	$x=2$	$x=3$	$x=4$
80	296	290	289	285	281
125	296	290	288	277	278
175	291	288	283	270	271
200		284	277	267	268
250	283	275	273	259	262
300	264	269	262	251	248

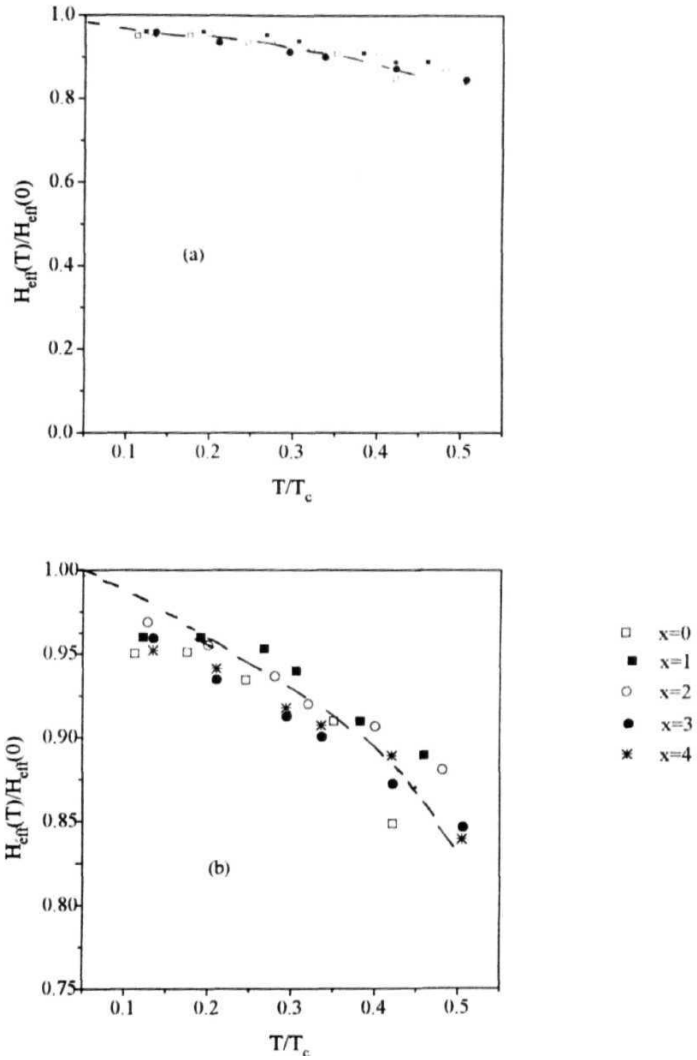


Fig 3 21 (a) & (b) Reduced effective magnetic hyperfine field, $H_{\text{eff}}(T)/H_{\text{eff}}(0)$ vs reduced temperature, (T/T_c) for the amorphous $\text{Fe}_{68}\text{Ni}_{14-x}\text{Mo}_x\text{Si}_2\text{B}_{16}$ ($x=0-4$) alloys in different scales.

and E are the stiffness constants. Usually E is much smaller than D . This dispersion relation leads to the following temperature dependence of magnetization $M(T)$ [63]

$$M(T) = M(0)(1 - BT^{3/2} - CT^{5/2}) \quad (3.26)$$

where B and C are constants and are related to D and E as given below

$$B = 2.612[g\mu_B/M(0)](k_B/4\pi D)^2 \quad (3.27)$$

$$C = 1.341[g\mu_B/M(0)](k_B/4\pi D)^{5/2}(15\pi E/D) \quad (3.28)$$

where k_B is the Boltzmann constant, μ_B is the Bohr magneton and g is the usual g -factor. Eq. (3.26) can be arranged to give

$$\frac{M(T) - M(0)}{M(0)} = -BT^{3/2} - CT^{5/2} \quad (3.29)$$

or

$$\frac{M(0) - M(T)}{M(0)} = B_{3/2}(T/T_c)^{3/2} + C_{5/2}(T/T_c)^{5/2} \quad (3.30)$$

It should be noted that the $T^{3/2}$ law is always obtained for a quadratic dispersion relation and is independent of the specific model for the magnetic interactions. In particular, it has been shown by Herring and Kittel [64] that a $T^{3/2}$ law is also expected in a macroscopic continuum model showing that lattice periodicity is not required. On the other hand, it is necessary to assume lattice periodicity in order to derive the higher order term in the expansion of $M(T)$. A contribution proportional to $T^{5/2}$ appears when cubic symmetry is assumed because the second term in Eq. (3.25), $E(q)$ is proportional to q^4 . Since $H_{\text{eff}}(T)$ for magnetic metallic glasses is approximately proportional to $M_s(T)$, the Bloch's law can also be applied to $H_{\text{eff}}(T)$. Therefore, the temperature dependence of $H_{\text{eff}}(T)$ from Eqs. (3.29) and (3.30) can be expressed as

$$\frac{H_{\text{eff}}(0) - H_{\text{eff}}(T)}{H_{\text{eff}}(0)} = BT^{3/2} + CT^{5/2} \quad (3.31)$$

$$\frac{\Delta H_{\text{eff}}(T)}{H_{\text{eff}}(0)} = \frac{H_{\text{eff}}(0) - H_{\text{eff}}(T)}{H_{\text{eff}}(0)} = B_{3/2}(T/T_c)^{3/2} + C_{5/2}(T/T_c)^{5/2} \quad (3.32)$$

where B , C , $B_{3/2}$ and $C_{5/2}$ constants remain the same as in Eqs. (3.29) and (3.30). It has been found that many amorphous ferromagnets follow Eqs. (3.31) and (3.32) over an extended temperature region [28,65-67]. In most cases $T^{3/2}$ dependence heavily dominates over $T^{5/2}$ dependence, therefore, one can neglect it ($T^{5/2}$ dependence) in Eq.

(3.32) The existence of spin wave excitations has been clearly demonstrated in amorphous **ferromagnets** using neutron **scattering** [68], ferromagnetic resonance [69] and specific heat [70] as mentioned earlier

In order to obtain $B_{3/2}$, from Eq (3.32) a knowledge of $H_{eff}(0)$ is required. Previously, $H_{eff}(T)$ vs T data was fitted to a straight line to obtain $H_{eff}(0)$. However, since $H_{eff}(T)$ should vary as $T^{3/2}$ at low temperatures ($T \ll T_c$), it is better to obtain $H_{eff}(0)$ by fitting data $H_{eff}(T)$ vs $T^{3/2}$ to a straight line and extrapolating to $T=0$. Fig 3.22 shows $H_{eff}(T)$ vs $T^{3/2}$. The straight line fitting yields $H_{eff}(0)$ for all the samples which are listed in Table (3.6) and plotted in Fig 3.23 as a function of Mo concentration, x . $\Delta H_{eff}(T)/H_{eff}(0)$ for all the samples are plotted as a function of $(T/T_c)^{3/2}$ in Fig 3.24(a)-(e). From these data $B_{3/2}$ values are obtained from fitting data $\Delta H_{eff}(T)/H_{eff}(0)$ vs $(T/T_c)^{3/2}$ to a straight line. Values of $B_{3/2}$ for each sample are listed in Table (3.7). Table (3.8) lists B and $B_{3/2}$ values of some of other iron-rich metallic glasses. As seen from this table $B_{3/2}$ is typically between 0.30 and 0.50 and the same is found here. In particular, $B_{3/2}$ values of $a\text{-Fe}_{68}\text{Ni}_{14-x}\text{Mo}_x\text{Si}_2\text{B}_{16}$ are similar to those of $a\text{-Fe}_{72}\text{Ni}_{10-x}\text{Mo}_x\text{Si}_2\text{B}_{16}$ [55].

The following observations are made

- (a) The $T^{3/2}$ dependence of $\Delta H_{eff}(T)/H_{eff}(0)$ is obeyed over a much larger temperature range in the metallic glasses than in crystalline solids Fe, Ni etc., [71]. This temperature dependence easily extends to $T/T_c = 0.4$ to 0.5.
- (b) Coefficient B is about two orders of magnitude larger than the coefficient C in this temperature region. This result agrees with the result on crystalline solids. However, the actual values of B and C are 2 to 10 times higher than those of crystalline materials. A comparison of the values of $B_{3/2}$ and $C_{3/2}$ also show the same trend, i.e., they are 2 to 5 times higher than those of Fe and Ni. Even this difference is clearly brought out when in some cases an amorphous sample of a given composition retains the same chemical composition as a single compound on crystallisation [72]. Higher values of $B_{3/2}$ implies that the spin waves are excited with relative ease (to crystalline **ferromagnet**) in amorphous **ferromagnets**. This also implies that the stiffness constant D is smaller in

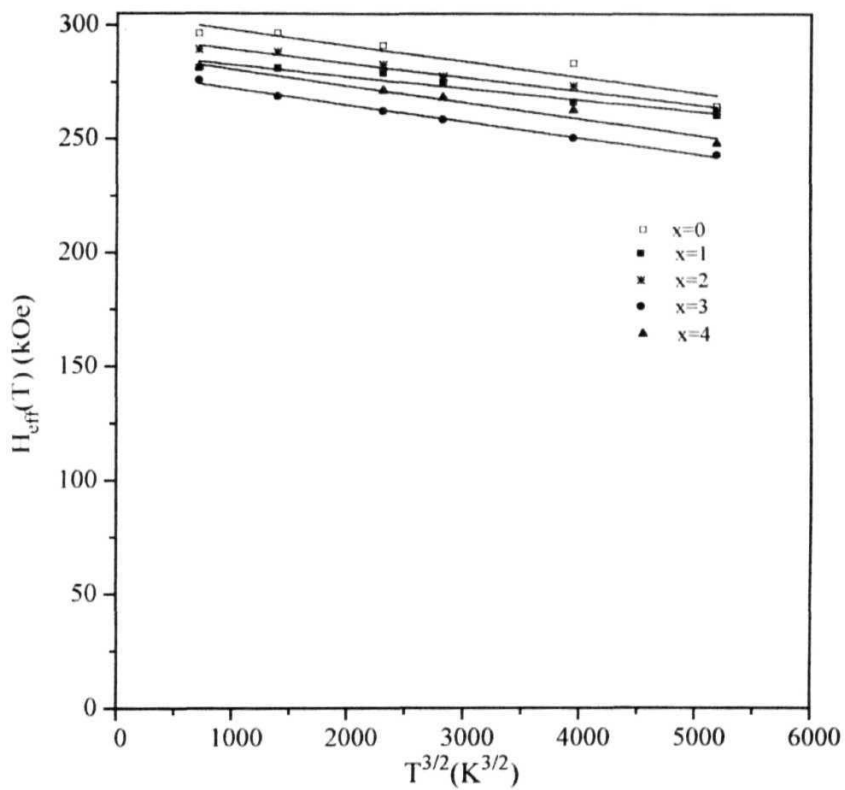


Fig 3.22 The plots of effective hyperfine field, $H_{\text{eff}}(T)$ vs $T^{3/2}$ for all the samples $\text{Fe}_{0.8}\text{Ni}_{1.4-x}\text{Mo}_x\text{Si}_2\text{B}_{16}$ ($x=0-4$) with the straight line fits

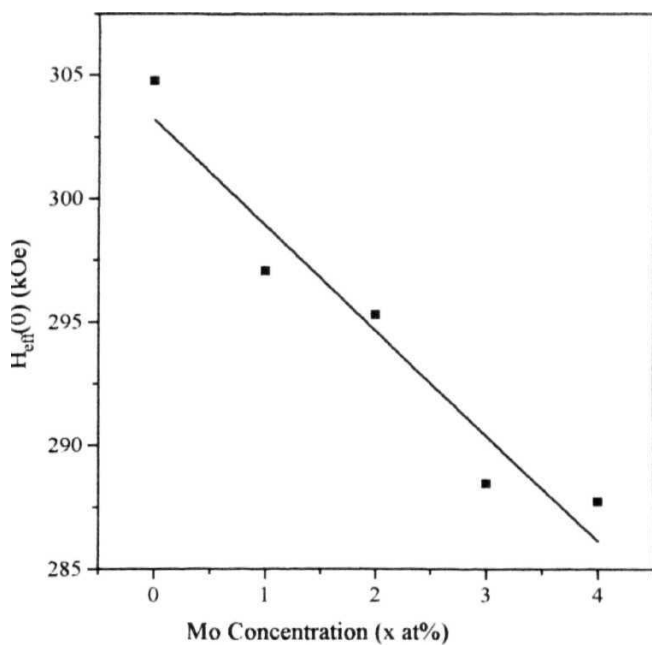


Fig 323 Saturation magnetic hyperfine field, $H_{\text{eff}}(0)$ as a function of Mo concentration, x with the fitted line

Table 3.6 The Values of Saturation hyperfine magnetic field, $H_{\text{eff}}(0)$ for different samples.

Sample (x)	$H_{\text{eff}}(0)$ (kOe)
0	305
1	297
2	295
3	288
4	287

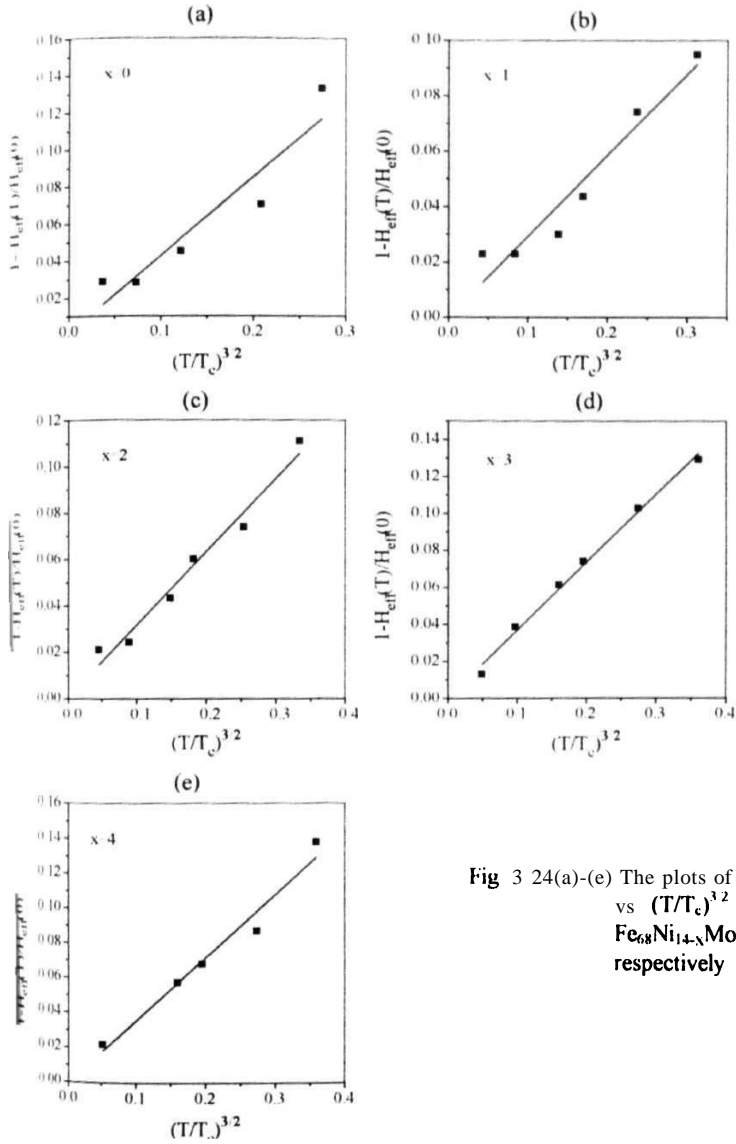


Fig 3 24(a)-(e) The plots of $\Delta H_{eff}(T)/H_{eff}(0)$ vs $(T/T_c)^{3/2}$ for the alloys $Fe_{68}Ni_{14-x}Mo_xSi_2B_{16}$ ($x=0-4$) respectively

Table 3.7 **The values of B_{32} obtained from $\Delta H_{em}(T)/H_{em}(0)$ vs $(T/T_c)^{3/2}$ plots.**

Sample (x)	B_{32}
0	0425
1	0285
2	0316
3	0.367
4	0362

Table 3.8 Sample **compositions**, Curie temperature (**T_c**), Coefficients It. **B_{32}** for amorphous ferromagnets and crystalline ferromagnets Fe and Ni.

Composition	T_c (K)	B ($10^{-6} K^{-3/2}$)	B_{32}	References
Crystalline Fe	1042	3.4 (0.2)	0 114 (0007)	68,73
Crystalline Ni	637	75 (0.2)	0 117 (0003)	66,71
Fe₇₈B₁₃Si₉	733	10	021	65
Fe₈₁B_{13.5}Si_{3.5}C₂	698	16	029	61
Fe₄₀Ni₄₀B₂₀	695	19	0 35	61
Fe₈₀B₂₀	685	22	0 40	62
Fe₈₁B_{13.5}Si_{3.5}C₂	668		030	58
Fe₇₅P₁₅C₁₀	619	23	0.36	66,71
Fe₈₀P₁₆B₁C₃	590	25	0 36	66,71
Fe₄₀Ni₄₀P₁₄B₆	537	38	047	66,71
Fe₂₀Ni₄₀P₁₄B₆Si₂	377	65	0.48	66,71
Fe₃₉Ni₃₉Mo₄Si₆B₁₂	575	34	0.47	61
Fe₇₄Co₁₀B₁₆	760	15	032	61
Fe₆₇Co₁₈B₁₄Si₁	830	19	045	61
Fe₇₂Ni₁₀B₁₆Si₂	680	16	036	55
Fe₇₂Ni₉Mo₁B₁₆Si₂	675	17	030	55
Fe₇₂Ni₈Mo₂B₁₆Si₂	650	21	034	55
Fe₇₂Ni₇Mo₃B₁₆Si₂	625	25	039	55
Fe₇₂Ni₆Mo₄B₁₆Si₂	585	33	0.47	55
Fe₆₈Ni₁₄B₁₆Si₂	711	22	0.42	Present work
Fe₆₈Ni₁₃Mo₁B₁₆Si₂	652	17	0.28	Present work
Fe₆₈Ni₁₂Mo₂B₁₆Si₂	623	20	0.31	Present work
Fe₆₈Ni₁₁Mo₃B₁₆Si₂	592	26	0.37	Present work
Fe₆₈Ni₁₀Mo₄B₁₆Si₂	594	25	0.36	Present work

amorphous **ferromagnets** than that in crystalline **ferromagnets**

Higher values of B or B_{12} in **comparison** with those of crystalline ferromagnets is most probably a consequence of the chemical **disorder**. Kaneyoshi [73] contends that while exchange fluctuations alone can describe the magnetization behaviour of rare-earth based amorphous alloys, 3d transition metal based alloys behave quite differently with temperature', in that they exhibit faster thermal demagnetization than that predicted by **Handrich's** [74] **model**. This is due to the fact that in the 3d transition metal alloys, where the moment is more easily perturbed by its environment, both the variations in moment magnitude as well as the exchange fluctuations play a decisive part in determining the ratio, $M(T)/M(0)$, hence $\Delta H_{eff}(T)/H_{eff}(0)$.

Higher values of B_{12} seems to be a characteristic feature of amorphous ferromagnets which also implies smaller value of the stiffness constant, D meaning that there is an increase in the density of states of low energy **excitations**. This is in agreement with the calculations of Montgomery [75] who has used temperature dependent double time Green functions to determine the density of spin-wave states for different values of a disorder parameter defined as $P = \langle \Delta J^2 \rangle / 3 \langle J \rangle^2$. For $P \neq 0$, a peak appears in the low energy **region**. Simpson [76] has explained this behaviour using a phenomenological agreement and found it to be due to the simultaneous effect of structural disorder, which increases the average interatomic distance and fluctuations in the exchange interactions. Some suggestions [66,72] have been made that large B values also imply a strong reduction of the range of the exchange interactions in comparison with that in pure ferromagnetic crystalline metals. However, the temperature dependence of the **Mössbauer** linewidth, $\Gamma_{1,6}$ in most cases shows that these are predominantly long range type. Therefore, this argument does not hold. Further Gubernatis and Taylor [77] have shown theoretically that for a given value of J between nearest neighbours, the density of spin waves is the same at low energies in the amorphous and in the crystalline state, therefore B and D should be in the two cases. Different values of B and D in these two cases can then only be explained by the different values of J but not by structural **disorder**. However, due to the assumption of nearest neighbour interaction only this result may be **questionable**. In the work by Bhagat et al [78] and Tarvin et al [79] on the temperature dependence of $M_s(T)$ in metglasses, it has been shown that Eqs. (3.31) and (3.32) are well obeyed

provided the effects of spin wave energy normalisation with temperature are included, i.e., the parameter B obeys the relation

$$B(T) = B(0) \left[\frac{1}{1 - aT^2} \right] \quad (333)$$

which also implies that

$$D(T) = D(0) \left[1 - b \left(\frac{T}{T_c} \right)^2 \right] \quad (334)$$

In any case, it seems that the explanation of higher values of B_{12} of **a-iron-rich metallic** glasses in comparison to those of crystalline counterparts is still waiting a rigorous theoretical **work**

3.5.6 Hyperfine Field Distribution

In glasses the lack of long-range crystalline order is responsible for a distribution of **hyperfine** interaction parameters which results in the broad and overlapping Mossbauer absorption **lines**. In addition, the observed asymmetry of the lines in the Mossbauer spectra indicates the possibility of correlations among these **parameters**. Here, we are interested in obtaining the hyperfine magnetic field distribution, $P(H)$, to observe relative changes in it as Mo is substituted in $\text{Fe}_{64}\text{Ni}_{14}\text{Si}_2\text{B}_{16}$ metallic glass.

Given the fact that Mossbauer spectra of amorphous ferromagnetic alloys consist of structureless, broad and partly overlapping lines, often with some degree of asymmetry, certain assumptions have to be made before evaluation and analysis of ME spectra. It is generally observed that the electric quadrupolar effects are negligible for amorphous ferromagnetic alloys below the magnetic ordering temperature T_c [80]. The quadrupole interaction at each site in such an alloy can be approximately described by $e^2qQ(3\cos^2\theta - 1)$, where e^2qQ is the quadrupole interaction energy and θ is the angle between the z-axis of the principal EFG tensor and the hyperfine field. The z-axis is determined by site symmetry, which varies spatially throughout the sample, whereas the magnetic hyperfine field, which is antiparallel to the magnetization axis in a ferromagnetic sample does not vary **randomly**. Hence, the values of $(3\cos^2\theta - 1)$ spatially average out to zero. In order to account for the observed asymmetry in the

ME line shape, a linear correlation between the local **isomer shift** and the local hyperfine field of the form [81]

$$\delta(H) = \delta(H_0) - \alpha(H - H_0) \quad (3.35)$$

is assumed, H_0 being the external magnetic field and α being the correlation coefficient, which implies that δ also has a distribution of values, $P(\delta)$. A similar correlation may be assumed for $T > T_c$ between the quadrupole moment and the hyperfine field, and a distribution of ΔE_Q , $P(\Delta E_Q)$ also exists. However, in analysing data to obtain $P(H)$, it is assumed that $P(\delta)$ and $P(\Delta E_Q)$ are narrow enough to be approximated with a delta function. This assumption is not strictly valid but is reasonably justified as δ and ΔE_Q are about an order of magnitude less sensitive to the changes in the chemical surroundings than hyperfine magnetic field.

Several methods exist in the literature for the evaluation of the hyperfine field distributions, $P(H)$, from the measured ME spectra. These methods fall broadly into two categories: (i) a definite shape of $P(H)$ is assumed *a priori*, e.g. a single Gaussian [82], modified Lorentzian [83] or a split-Gaussian [84] (the parameters of such functions are determined by least square fitting (LSF) procedures), (ii) no *a priori* assumption is made as regards the shape of the $P(H)$, e.g., Window method [44] in which $P(H)$ is expanded in a Fourier series, or the discrete field method proposed by Hesse and Rubartsch [85], which was later improved upon by La C  r and Dubois [86] or the method due to Vincze [87], in which $P(H)$ is approximated by a binomial distribution.

In the present work no *a priori* assumption is made as regard to the shape of the $P(H)$ curve and hence the Window's method [44] is used to analyze the Mossbauer spectra which is discussed in detail below.

The Window Method

This is a method used for the evaluation of $P(H)$, which is given by

$$P(H) = \sum_{i=1}^m a_i W_i(H) \quad (3.36)$$

where W_i are 'elementary' functions of hyperfine field distributions between $H=0$ and $H=H_{\max}$. If $W_i(H)$ is defined as

$$W_i(H) = \cos \left[\frac{i\pi(H - H_{\min})}{H_{\max} - H_{\min}} \right] - (-1)^i \quad (3.37)$$

$P(H)$ can be expanded in a Fourier (cosine) **series**,

$$P(H) = \sum_{i=1}^m a_i \left[\cos \left[\frac{i\pi(H - H_{\min})}{H_{\max} - H_{\min}} \right] - (-1)^i \right] \quad (338)$$

The distribution W_i , creates a spectrum S_i ,

$$S_i(v) = \int_0^{H_{\max}} W_i(H) \cdot L_0(H, v) dH \quad (339)$$

where v is the relative velocity between the source and the absorber and $L_0(H, v)$ is a **s sextuplet** of Lorentzian lines.

The complete spectrum is written as

$$S(v) = \sum_{i=1}^m a_i S_i(v) \quad (3.40)$$

The unknown coefficients a_i , can be calculated by a least square program, with the constraints,

$$P(H_{\max}) = 0; \quad \left(\frac{dP}{dH} \right)_{H_{\min, \max}} = 0 \quad (3.41)$$

In addition, the area under the $P(H)$ curve is normalized, i.e.,

$$\sum_{H_{\min}}^{H_{\max}} P(H) = 1 \quad (3.42)$$

All the parameters were evaluated using this method. While expanding the $P(H)$ as a cosine series (**Eq 3.38**), it is assumed that (i) the spectrum can be described by a single value of the **isomer** shift, δ (ii) the quadrupole splitting, A is negligible for $T < T_c$ and (iii) an average value of the intensity ratio, b of the component spectra, i.e., $I_{1,6}:I_{2,5}:I_{3,4}=3:b:1$, can describe the observed spectrum **adequately**. Although none of these assumptions is strictly valid for amorphous ferromagnetic systems, it has been demonstrated [88] that this method can nonetheless be used to determine $P(H)$, provided the important **Mössbauer** fitting parameters, e.g., **FWHM** of the subspectral lines, Γ intensity ratio, b and the number of terms in the Fourier expansion, N are **properly** chosen. For instance, too small a value of N can obscure some genuine details of the $P(H)$ curve whereas too large a value of N gives rise to an unphysical

structure in P(H) as a large number of terms in the Fourier **series** (Eq 3.38) **tend to fit** the statistical fluctuations in the measured **spectrum**

The optimum choice of the intrinsic parameters, b, F and N for each spectrum is based on the minimization of the χ^2 , defined by

$$\chi^2 = (m - n_p)^{-1} \sum_{i=1}^m \frac{(Y_{\text{exp}}^i - Y_{\text{cal}}^i)^2}{Y_{\text{exp}}^i} \quad (3.43)$$

where **m** and **n_p** are the number of channels and the free fitting parameters **respectively** Y_{exp}^i and Y_{cal}^i are the experimental data points and the corresponding points on the fitted curve with respect to the free fitting parameters Γ , b and a, the correlation coefficient between the **isomer** shift and hyperfine field, χ^2 as a function of b, Γ and N has been shown in Fig. 3.25. The combination of b, F and N for which χ^2 is minimum is used in the **analysis**. However, when one does this, it is observed that the value of Γ does not vary **systematically**. Therefore, we fixed the value of Γ by using the method **suggested** by Keller [88]. This was done in order to take care of broadening of the line shape with respect to that of natural iron due to the presence of distribution of the other hyperfine parameters.

P(H) vs H obtained from the Window's method of analysis of the Mossbauer spectrum of a typical iron-rich metallic glass like $\text{Fe}_{80}\text{B}_{20}$ or $\text{Fe}_{40}\text{Ni}_{40}\text{B}_{20}$ normally consists of a major peak in P(H). On either sides of the major peak oscillations in P(H) are observed, which are more prominent at lower fields. These oscillations are the artifact of the truncation of the Fourier series and one ignores these. The emphasis is normally given to the major peak showing positive P(H) **values**. The parameters of interest in P(H) vs H curve, the hyperfine field distribution curve, are **H_p**, the H value at which the maximum of major peak occurs, **FWHM** of the major peak, **AH**, the average field, **H_{av}** and the shape of the P(H) curve. By noting changes in these parameters one can infer how the substitution of Mo for Ni in $\text{a-Fe}_{68}\text{Ni}_{14}\text{Si}_2\text{B}_{16}$ is affecting magnetic properties of the host glassy **matrix**.

The distribution of hyperfine fields, P(H) vs H, of $\text{a-Fe}_{68}\text{Ni}_{14-x}\text{Mo}_x\text{Si}_2\text{B}_{16}$ (x=0,1,2,3 and 4) at different temperatures are shown in Fig. 3.26-3.30 using the Window's **method** in which N, b and F have been optimised to yield minimum χ^2

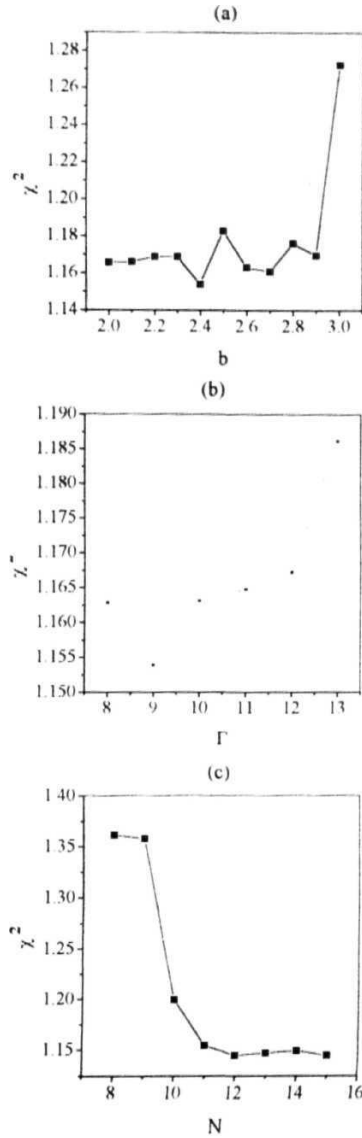


Fig 3.25(a)-(c) The parameters b , Γ and N as a function of χ^2 respectively

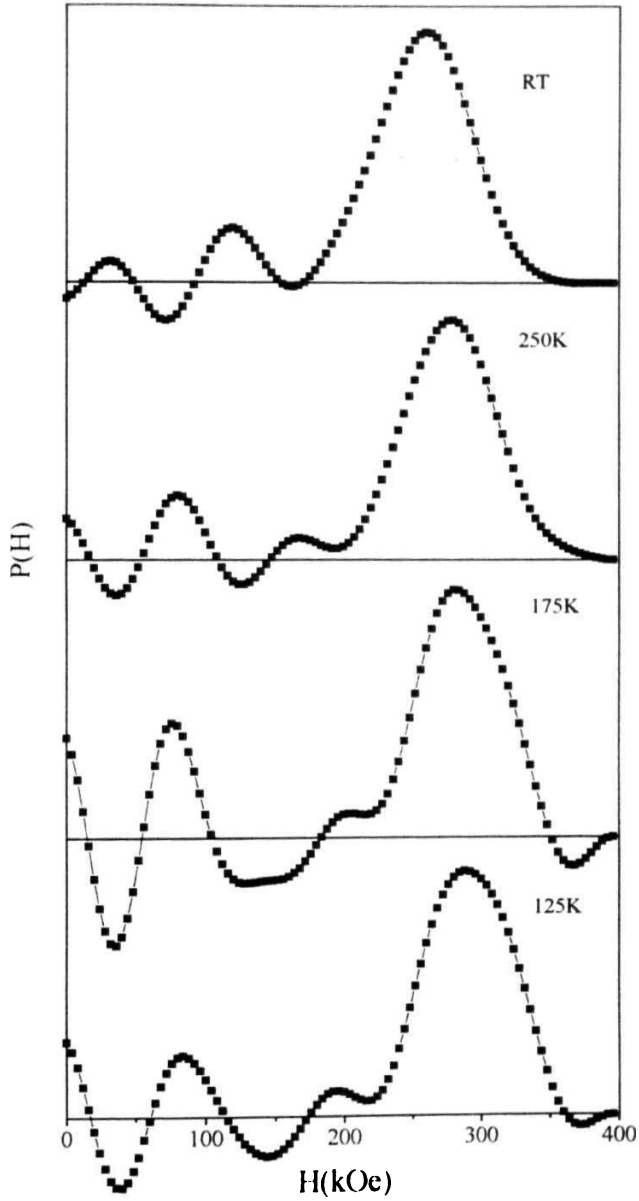


Fig. 3.26 The hyperfine field distribution curves for the sample $\text{Fe}_{68}\text{Ni}_{14-x}\text{Mo}_x\text{Si}_2\text{B}_{16}$ $x=0$ at different temperatures 125 K, 175 K, 250 K and RT.

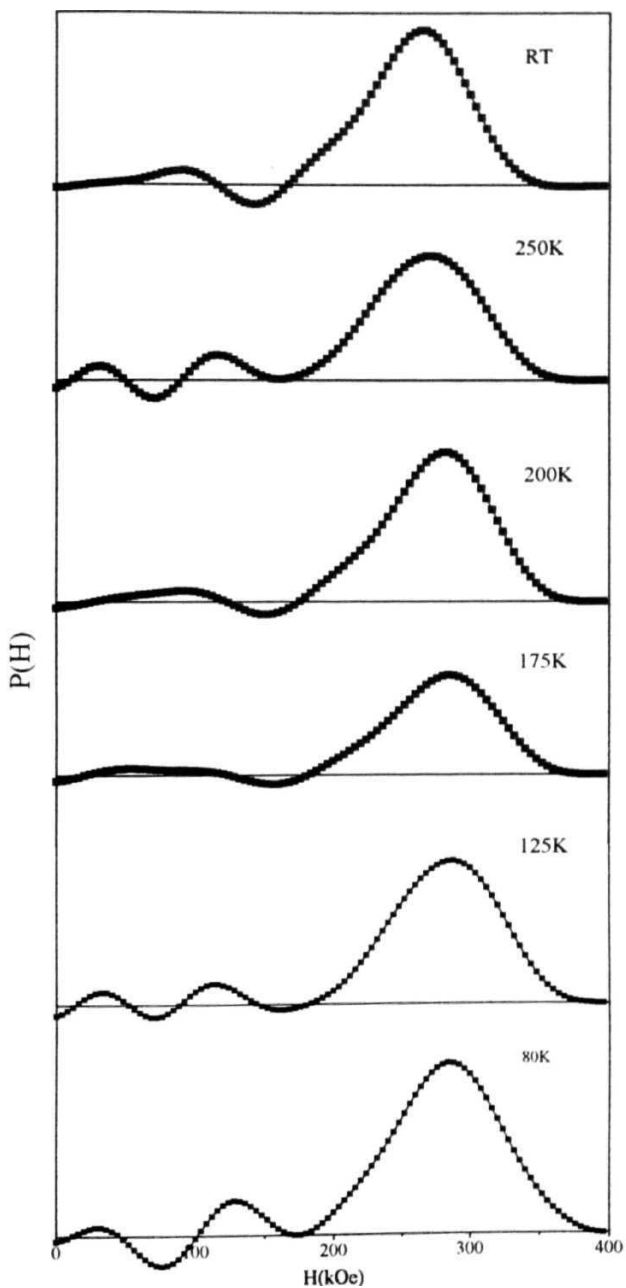


Fig. 3.27 The hyperfine field distribution curves for the sample $\text{Fe}_{68}\text{Ni}_{14-x}\text{Mo}_x\text{Si}_2\text{B}_{16}$ $x=1$ at different temperatures 80 K-RT.

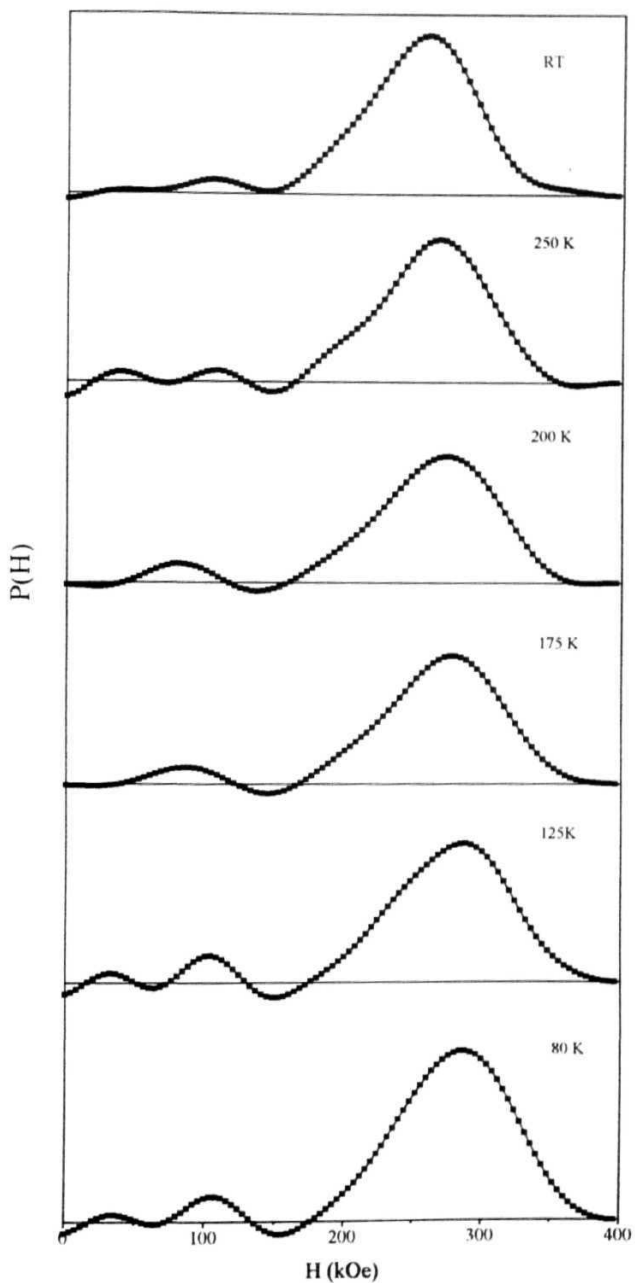


fig 3.28 The **hyperfine** field distribution curves for the sample $\text{Fe}_{68}\text{Ni}_{14-x}\text{Mo}_x\text{Si}_2\text{B}_{16}$ $x=2$ at different temperatures 80 K-RT

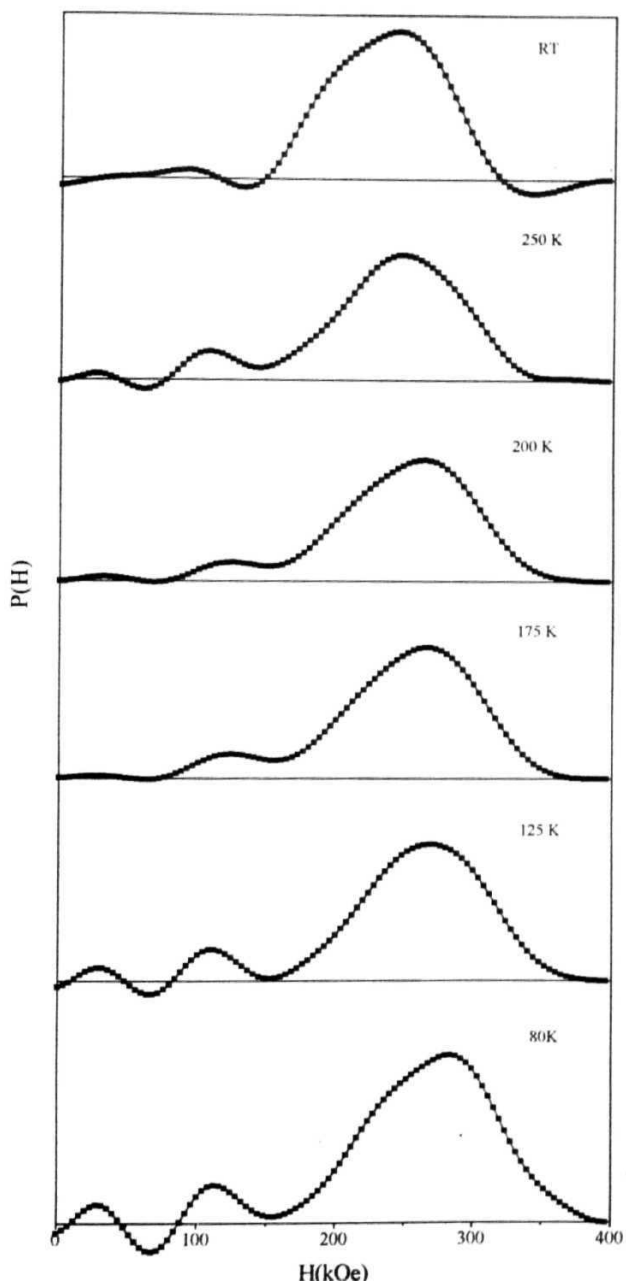


Fig 3.29 The **hyperfine** field distribution curves for the sample $\text{Fe}_{68}\text{Ni}_{14-x}\text{Mo}_x\text{Si}_2\text{B}_{16}$ $x=3$ at different temperatures 80 K-RT.

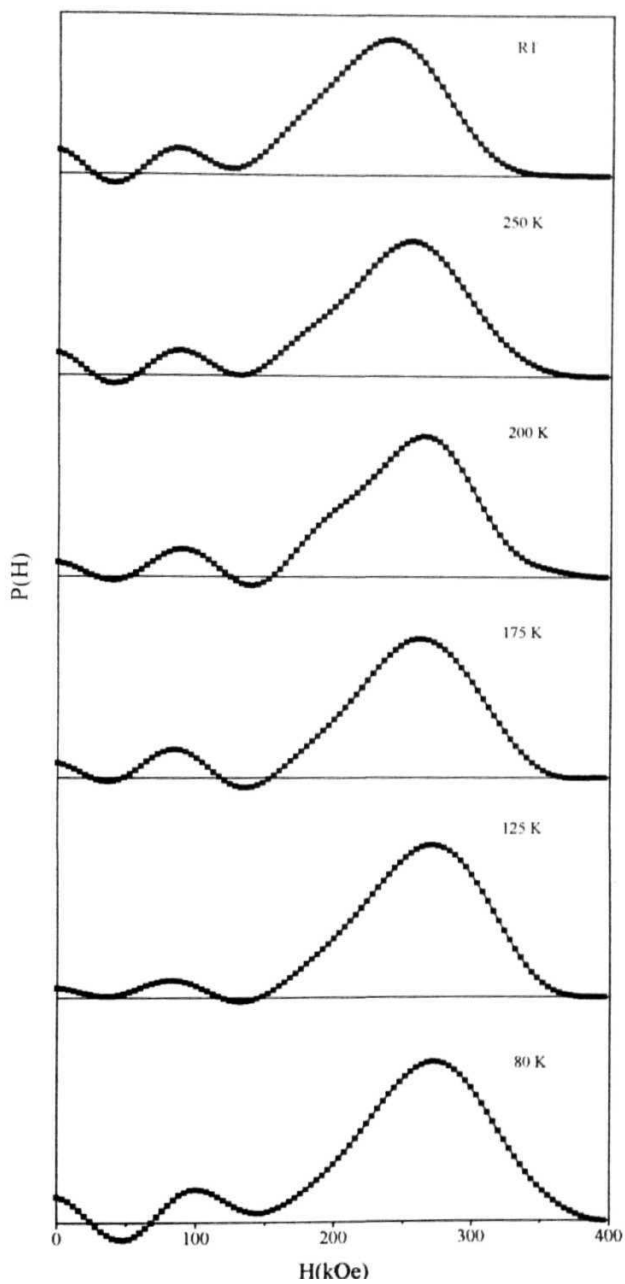


Fig. 3.30 The hyperfine field distribution curves for the sample $\text{Fe}_{68}\text{Ni}_{14-x}\text{Mo}_x\text{Si}_2\text{B}_{16}$ $x=4$ at different temperatures 80 K-RT

values as explained in the preceding paragraphs. The optimal choice chosen for the remaining parameters are $H_{\min} \approx 0$ and $H_{\max} \approx 400$ kOe, which is sufficiently high so that $P(H_{\max}) \approx 0$, a value well above that of α -Fe. All of these hyperfine field distributions exhibit a prominent peak with oscillations at lower fields due to truncation of the Fourier series as explained earlier and need to be ignored as $P(H)$ cannot be negative. χ values are between 1 and 2 but for a few cases where it is 3. However, one observes that the asymmetry is larger at RT compared to that at lower temperatures. The fit obtained between data and the calculated Mossbauer spectra are good. A typical example is shown in Fig. 3.31 for sample $x=2$ at 175 K.

Fig. 3.32 shows $P(H)$ vs H curves obtained from the Mossbauer spectra of all the samples at RT. Parameters H_p , H_{av} , AH with corresponding χ^2 values and also the values of H_{eff} for all the samples are given in Table (3.9)-Table (3.13) respectively. Fig. 3.33 shows the variation of H_p , H_{av} and H_{eff} at two temperatures (namely 80 K and 300 K) as a function of Mo concentration, x . It is observed from this figure and the Tables (3.9)-(3.13) that H_p and H_{av} show on the average a decreasing trend, as x increases as observed for $H_{eff}(RT, x)$, i.e., these parameters show an increase slightly for $x < 1$, then start decreasing for $x > 1$. Almost similar shifts (except for $x=1$) in hyperfine field distribution is observed in case of amorphous $Fe_{72}Ni_{10-x}Mo_xSi_xB_{16}$ alloys [55], $Fe_{70}Ni_{12-x}Mo_xSi_xB_{16}$ alloys [56] and of $Fe_{80-x}Mo_xB_{20}$ [39].

If one looks at the shapes of the peaks and their positions, it is seen that the peak of the position shifts towards lower field value as x increases. The shape of the curve becomes slightly asymmetric and asymmetry seems to increase with Mo concentration, x .

The asymmetry in the major peak is most probably due to overlap of another peak of smaller amplitude (probability) at lower magnetic fields with that of the main peak. This is further suggested by an increase of the FWHM of the combined peak (as shown in the figure) with Mo concentration. AH vs x is shown in Fig. 3.34. It increases at the rate of ~ 10 kOe/Mo-at% upto $x=3$ but the increase becomes less for $x=4$ sample. Similar observation of AH vs x has been reported for $Fe_{70}Ni_{12-x}Mo_xSi_xB_{16}$ [56]. One of the possible explanations of increase of AH with Mo concentration x is

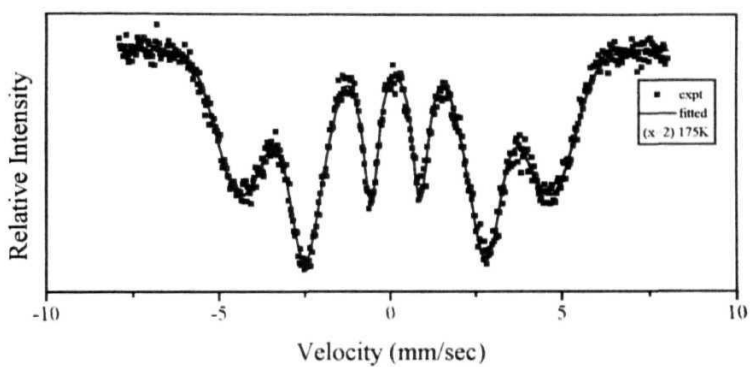


Fig. 3.31 Typical Mossbauer spectrum for the sample $\text{Fe}_{68}\text{Ni}_{14.5}\text{Mo}_x\text{Si}_2\text{B}_{16}$ x 2 at 175 K along with the fitted spectrum shown by the continuous line

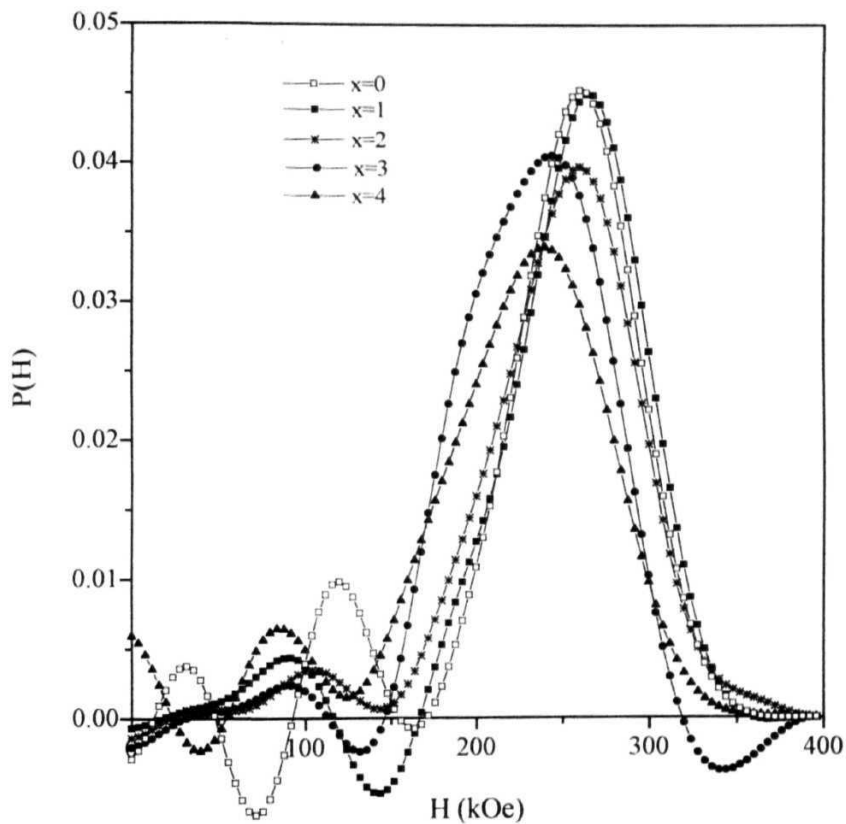


Fig. 3.32 The hyperfme field distribution curves for all the five samples $\text{Fe}_{0.8}\text{Ni}_{14-x}\text{Mo}_x\text{Si}_2\text{B}_{16}$ ($x=0-4$) at RT

Table 3.9 The values of peak field (**H_p**), average hyperfine field (**H_{av}**), fullwidth at half maximum (AH) of P(H) distribution, the corresponding **χ²** values and effective hyperfine field (**H_{eff}**) at different temperatures for the sample \ o.

Temperature (K)	H _p (kOe)	H _{av} (kOe)	AH (kOe)	χ ²	H _{eff} (T) kOe
80	306	312	68 7 5	361	296
125	291	287	81 2 5	2 70	296
175	282	278	75	2 91	291
250	284	264	81 2 5	3.17	283
300	258	262	81 2 5	1 15	264

Table 3.10 The values of peak field (**H_p**), average hyperfine field (**H_{av}**), fullwidth at half maximum (AH) of P(H) distribution, the corresponding **χ²** values and effective hyperfine field (**H_{eff}**) at different temperatures for the sample x=1.

Temperature (K)	H _p (kOe)	H _{av} (kOe)	AH (kOe)	χ ²	H _{eff} (T) kOe
80	301	286	93 7 5	1 44	290
125	292	282	93 7 5	1 31	290
175	297	279	87 5	1 13	284
200	283	276	87 5	1 42	284
250	276	263	93 7 5	1 59	275
300	267	260	81 2 5	1 45	269

Table **3.11** The values of peak field (**H_p**), average hyperfine field (**H_{av}**), fullwidth at half **maximum** (AH) of P(H) **distribution**, the corresponding χ^2 values and **effective** hyperfine field (**H_{eff}**) at different temperatures for the sample $x=2$.

Temperature (K)	(kOe)	H _{av} (kOe)	AH (kOe)	χ^2	H _{eff} (T) kOe
80	293	280	1000	1.30	289
125	292	277	1000	1.12	288
175	274	268	96.9	1.12	282
200	275	264	100.0	1.32	277
250	272	266	87.5	1.38	273
300	264	251	90.6	1.26	262

Table 3.12 The values of peak field (H_p), average hyperfine field (**H_{av}**), fullwidth at half maximum (AH) of P(H) **distribution**, the corresponding χ^2 values and effective hyperfine field (**H_{eff}**) at different temperatures for the sample $x=3$.

Temperature (K)	H _p (kOe)	H _{av} (kOe)	AH (kOe)	χ^2	H _{eff} (T) kOe
80	285	268	109.4	1.20	285
125	271	258	106.25	1.46	277
175	267	248	109.4	1.43	271
200	268	247	109.4	1.33	267
250	252	240	100.0	1.30	259
300	248	234	106.25	1.52	251

Table 3.13 The values of peak field (**H_p**), average hyperfine field (**H_{av}**), fullwidth at half maximum (ΔH) of P(H) **distribution**, the corresponding χ^2 values and effective hyperfine field (**H_{eff}**) at different temperatures for the sample x=4.

Temperature (K)	(kOe)	H _{av} (kOe)	ΔH (kOe)	χ^2	H _{eff} (T) kOe
80	275	257	109.4	1.37	281
125	276	254	109.4	1.23	278
175	269	247	103.12	1.16	271
200	267	245	103.12	1.35	268
250	260	239	103.12	1.48	263
300	244	222	109.4	1.27	248

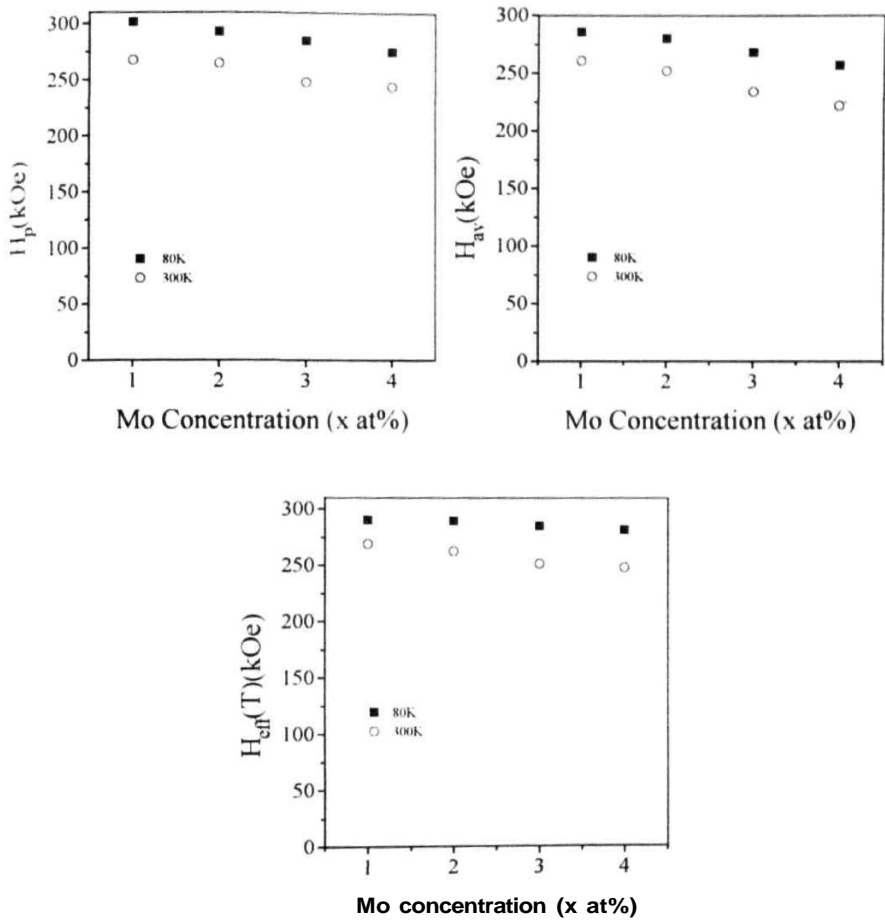


Fig 3.33 The plots of H_p , H_{av} and H_{eff} as a function of Mo concentration, x at two particular temperatures 80 K and RT

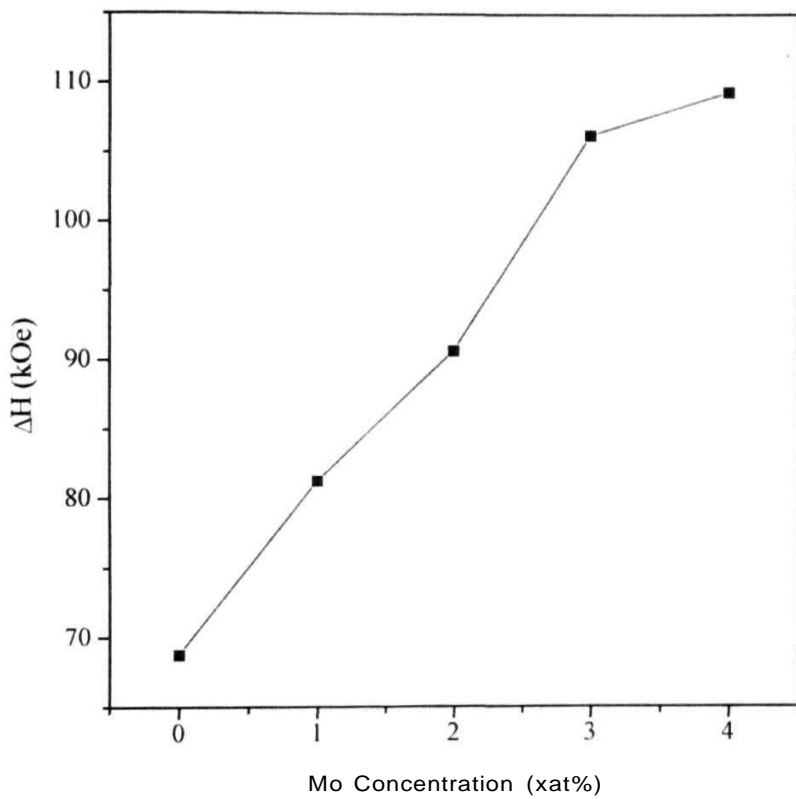


Fig 3.34 The Full width at Half Maximum (FWHM), ΔH of the peak in the $P(H)$ distribution as a function of Mo concentration, x

the probability of the increase of overlap of the smaller peak in P(H) vs H curve relatively higher intensity at lower magnetic fields. This peak **shifts** to the lower field as x **increases**. Thus the Fe atoms **find** themselves in two different environments, one of which has a higher H_p and occurs with higher probability than the other Fe-environment which has a lower H_p and occurs with relatively lower probability, i.e., the P(H) distribution is bimodal as reported earlier in Cr and Mo containing iron-rich metallic glasses [39,40,48-54]. Relatively less increase of AH for Mo concentration, 3 to 4 at% may be indicative of a limit with which the second **Fe-environment** can be different as far as the distribution of Mo around Fe atoms is concerned. It is to be noted that a clear emergence of a peak at lower fields is not there as reported earlier in Mo containing **Fe-rich** metallic glasses [89].

From the **Fig 3.35** it is evident that the values of H_p and H_{av} decrease systematically with increasing temperature. This is to be expected, as the average magnetic moment and hence the effective **hyperfine** field decreases with increasing **temperature**. The asymmetry is pronounced for the P(H) distribution at the lowest temperature measured (80 K) and maximum for x=4. The asymmetry thus, primarily **arises** due to enhanced **contribution** at low field **region**. The presence of Mo contributes to lower fields and this contribution is enhanced by increasing the Mo content, which results in more iron sites with Mo as near neighbours. Apparently due to the shifting of major peak to lower fields with increasing temperature the minor peak becomes more prominent and makes the distribution appear more asymmetric.

It is also observed that AH for a given sample does not change with temperature although some scatter is **there**. Hardly **any** change in AH values and enhanced asymmetry with increasing temperature may be attributed to different hyperfine fields exhibiting different temperature dependence [39,51,52,59]. The asymmetry particularly in the major peak may be attributed to **bimodality** of P(H) distribution. Such an asymmetry is also observed in related systems like **a-(Fe_xMo_{1-x})₇₅P₁₆B₆Al₃** [48], **a-Fe_{80-x}Mo_xB₂₀** [57], **a-Fe₇₁Mo₇B₂₀** [40], **a-Fe_{40-x/2}Ni_{40-x/2}Cr_xMo_xSi₁₀B₈** [51,90], **a-Fe₃₂Ni₃₆Cr₁₄B₆P₁₆** [52,91] and [89]. In all these cases, it is suggested that the distribution around the high field component arises due to iron with mainly Fe and Ni as near neighbours, whereas low field components originate due to iron with Mo near neighbours, thus leading to bimodality and the observed asymmetry in P(H).

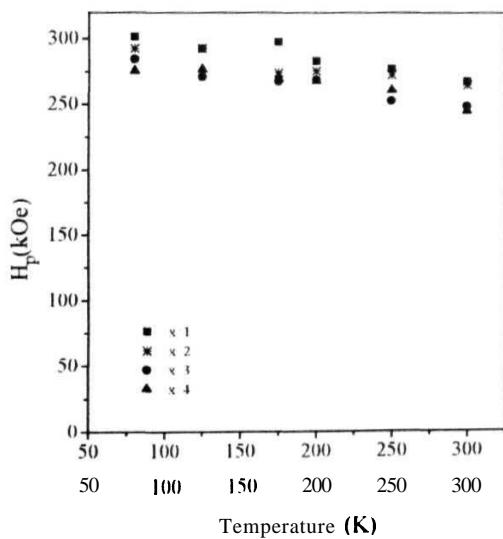
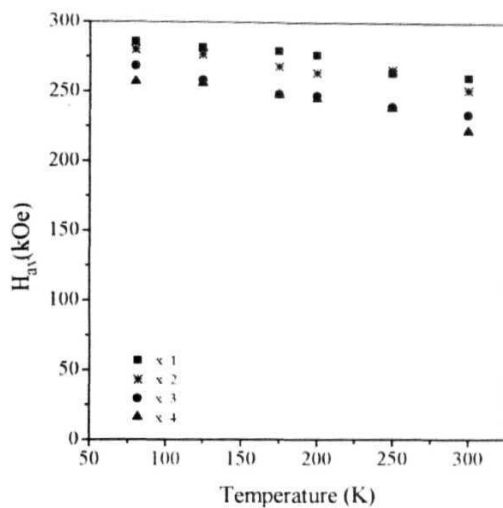


Fig. 3.35 The variation of H_p and H_{av} with temperature for the samples x 1-4

distribution

3.5.7 Bulk Magnetization Measurements

This section presents the magnetization studies done at room temperature and at low temperature in the range 10-100 K on the series of $\text{a-Fe}_{0.8}\text{Ni}_{1.4-x}\text{Mo}_x\text{Si}_3\text{B}_{16}$ ($x=0,1,2,3$ and 4) alloys

The variation of the magnetic moment with the applied field for $\text{a-Fe}_{0.8}\text{Ni}_{1.4-x}\text{Mo}_x\text{Si}_3\text{B}_{16}$ ($x=0,1,2,3$ and 4) alloys at RT are shown in Fig 3 36 This indicates that as the applied field increases the magnetic moment increases sharply up to certain field value beyond which it almost becomes constant The value of the magnetic field at which M becomes nearly independent of H is about 2000 Oe For $H > 2$ kOe, a very small slope in M vs H is observed Hence, $M_s(\text{RT})$ is calculated by extrapolating higher field M vs H data to $H = 0$ value, this value is termed as saturation magnetic moment M_s Values of M_s for different samples are listed in Table (3 14) and are plotted in Fig 3 37 as a function of Mo concentration, x Error of 7% is estimated for these values There is quite a bit of scatter, the reason being the small amount of sample being used The trend is that M_s decreases with x, however the value of M_s for $x=4$ does show some increase Repeated measurements showed the same values with the estimated error

Temperature Dependence of Magnetization

In order to check the spin wave excitations, measurements of $M(T)$ for $T < 100$ K were performed using Lakeshore equipment described earlier at Texas A&M University, USA

At low temperatures, magnetization follows the following relation

$$M(T) = M(0)(1 - BT^{3/2} - CT^{5/2}) \quad (3.44a)$$

$$[M(0) - M(T)]/M(0) = \Delta M(T)/M(0) = BT^{3/2} + CT^{5/2} \quad (3.44b)$$

Data $M(T)$ vs T ($T < 100$ K) are shown for all the samples in Fig 3 38(a)-(e) $M_s(0)$ was obtained by fitting data to Eq 3.44(a) The values of B and C obtained this way are in Table (3 15) and an extrapolation to $T=0$ gives the value of $M_s(0)$ These values of $M_s(0)$ for all the samples listed in Table (3 14) are plotted in Fig 3 39 as a function

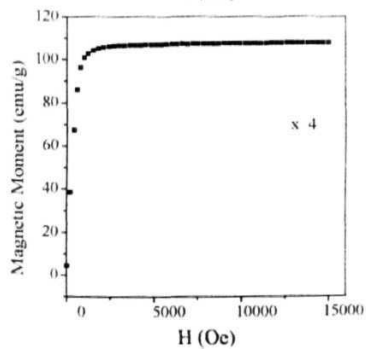
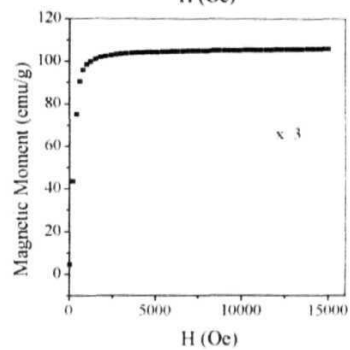
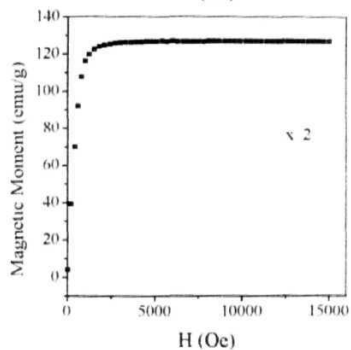
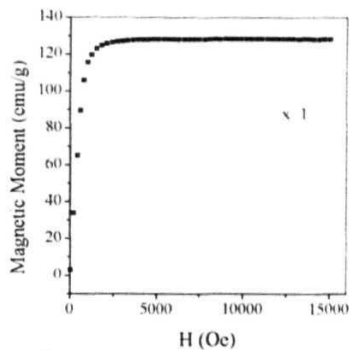
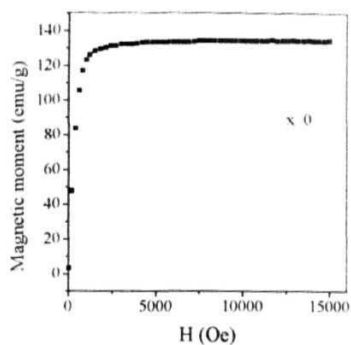


Fig 3 36 Room temperature magnetization curves
for the samples $\text{Fe}_{0.8}\text{Ni}_{1.4-x}\text{Mo}_x\text{Si}_2\text{B}_{16}$
(x= 0-4)

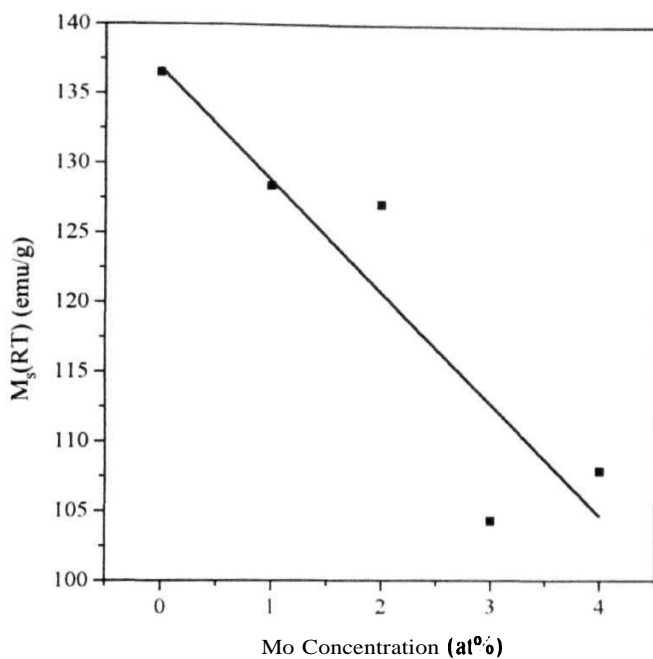


Fig. 3.37 Room temperature magnetization, $M_s(RT)$ as function of Mo concentration, x with the fitted line

Table 3.14 The values of saturation magnetization at RT, $M_s(RT)$; spontaneous magnetization, $M_s(0)$ for all the samples.

Sample (x)	$M_s(RT)$ emu/g	$M_s(0)$ emu/g
0	136.50	169.98
1	128.40	164.45
2	127.06	162.46
3	104.30	146.60
4	107.90	144.20

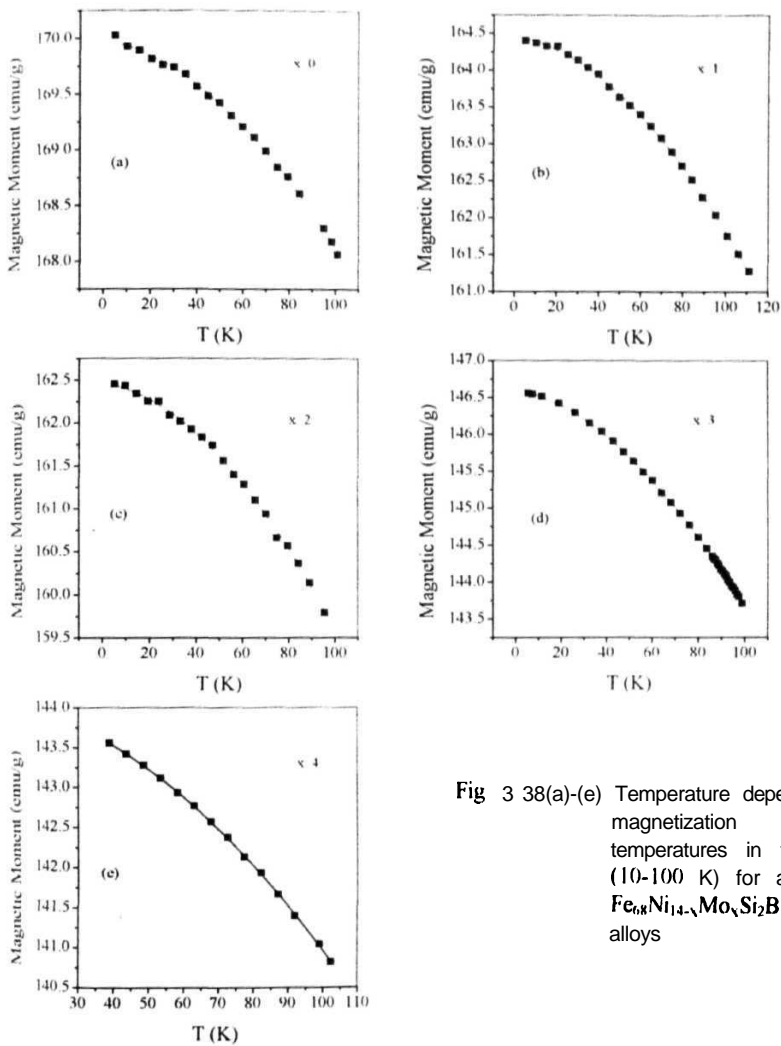


Fig 3 38(a)-(e) Temperature dependence of magnetization at low temperatures in the range (10-100 K) for amorphous $\text{Fe}_{68}\text{Ni}_{14-x}\text{Mo}_x\text{Si}_2\text{B}_{16}$ ($x=0-4$) alloys

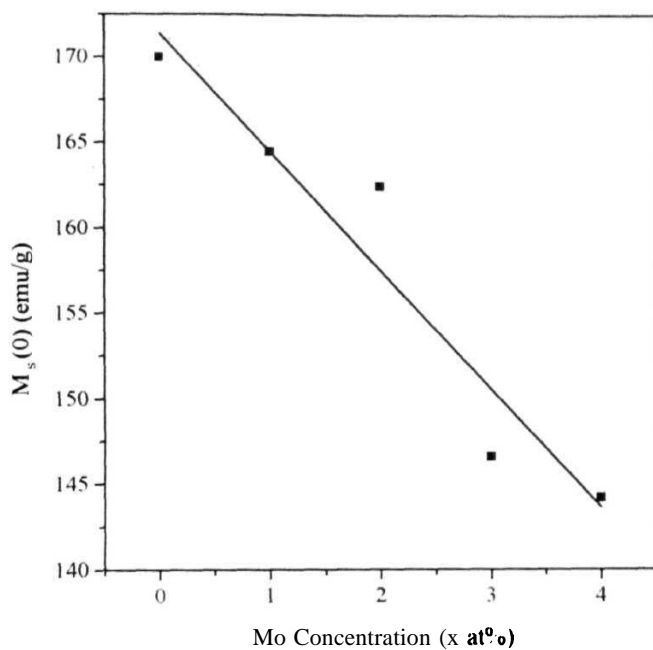


Fig 3.39 Saturation magnetization, $M_s(0)$ as function of Mo concentration, x with the fitted line

Table 3.15 The values of Spin-wave coefficients B and C obtained from magnetization data.

x	B (10^{-5}) ($K^{-3/2}$)	C (10^{-8}) ($K^{-5/2}$)
0	0.8073	28645
1	1.0713	53002
2	1.1959	5.8361
3	1.4835	5.1128
4	1.5637	6.8187

of Mo concentration, x . It is seen that the decrease of $M_s(0)$ is more systematic with x . The decrease is $\sim 7 \text{ emu/g(Mo-at\%)}$. This value of $M_s(0)$ is used to plot $M(T)/M(0)$ vs T/T_c as shown in Fig 3.40(a). Data $M(T)/M(0)$ and $H_{\text{eff}}(T)/H_{\text{eff}}(0)$ are plotted in Fig 3.40(b). Since $H_{\text{eff}} \propto M$ both data should overlap in the common temperature region. One can see from the figure that there is overlap near 100 K region. However, the average trend as shown by the line, for both data is the same. Fig 3.41 shows plots of $\Delta M/M(0)$ vs $T^{1/2}$ which clearly shows a good linearity. Values of B and $B_{1/2}$ obtained this way are listed in Table (3.16) and are plotted in Fig 3.42 as a function of Mo concentration, x . It is seen that $B_{1/2}$ increases almost linearly with a slope of 0.0292. Thus, inclusion of Mo in $\text{Fe}_{0.8}\text{Ni}_{1.4}\text{Si}_2\text{B}_{16}$ indicates that spin waves are excited with relative ease in these alloys as Mo is added, with an increase in the density of states of low energy excitations and therefore decrease of magnetization faster. For the sake of comparison, values of B and $B_{1/2}$ obtained from $\Delta H/H_{\text{eff}}(0)$ vs $T^{1/2}$ are also listed in Table (3.16). It is noted that for $x=0$, $B_{1/2}$ obtained from $\Delta M/M(0)$ vs $T^{1/2}$ data is about 1/2 of $B_{1/2}$ value obtained from $\Delta H/H_{\text{eff}}(0)$ vs $T^{1/2}$. For other samples, the difference is only about 10%. The large discrepancy between these two values of $B_{1/2}$ is baffling and we are unable to offer any explanation for it.

3.6 Summary

The Mossbauer investigations of $\text{a-Fe}_{0.8}\text{Ni}_{1.4-x}\text{Mo}_x\text{Si}_2\text{B}_{16}$ ($x=0, 1, 2, 3$ & 4) alloys have been carried out in the temperature range from RT-80 K. All the samples are ferromagnetic at room temperature. The values of saturation magnetic hyperfine field, $H_{\text{eff}}(0)$ show a decreasing trend from (305-287) kOe, with a fall of $\sim 4.3 \text{ kOe/Mo-at\%}$ and those of $H_{\text{eff}}(\text{RT})$ decrease at a rate of $\sim 5 \text{ kOe/Mo-at\%}$ which has been attributed to molybdenum acting as a magnetic diluent and/or its antiferromagnetic exchange interactions with iron.

The $P(H)$ curves obtained by Window's procedure for the recorded spectra at different temperatures show a major peak at high field and a minor peak at low field. The bimodality in the major peak arises due to the presence of Mo which can contribute to Fe-Mo antiferromagnetic exchange interactions and magnetic dilution.

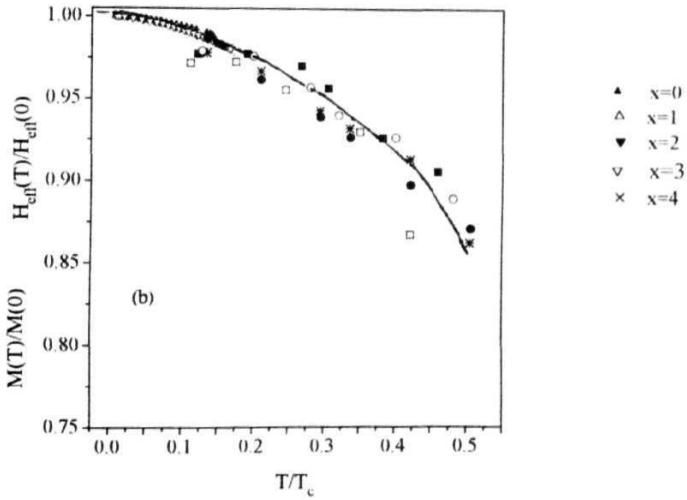
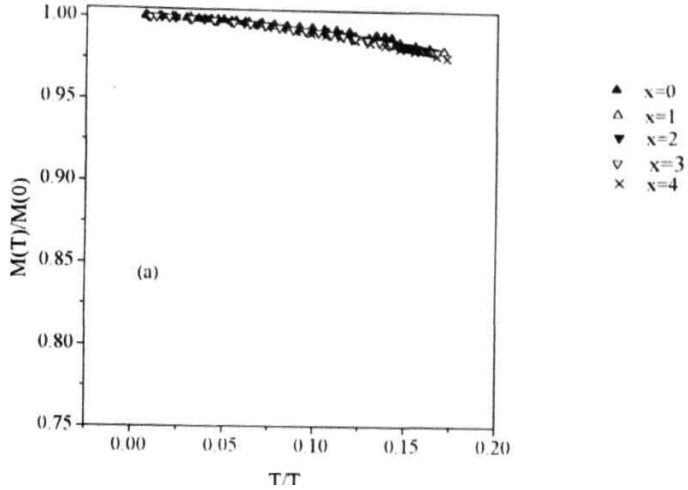


Fig 3.40(a) Reduced magnetization $M(T)/M(0)$ vs reduced temperature (T/T_c) at low temperatures in the range (10-100 K) for amorphous $\text{Fe}_{68}\text{Ni}_{14-x}\text{Mo}_x\text{Si}_2\text{B}_{16}$ ($x=0-4$) alloys.

Fig 3.40(b) Reduced magnetization $M(T)/M(0)$ vs reduced temperature (T/T_c) at low temperatures in the range (10-100 K) with reduced effective hyperfine field $H_{\text{eff}}(T)/H_{\text{eff}}(0)$ vs reduced temperature (T/T_c) in the temperature range 80 K-RT superimposed on it for amorphous $\text{Fe}_{68}\text{Ni}_{14-x}\text{Mo}_x\text{Si}_2\text{B}_{16}$ ($x=0-4$) alloys.

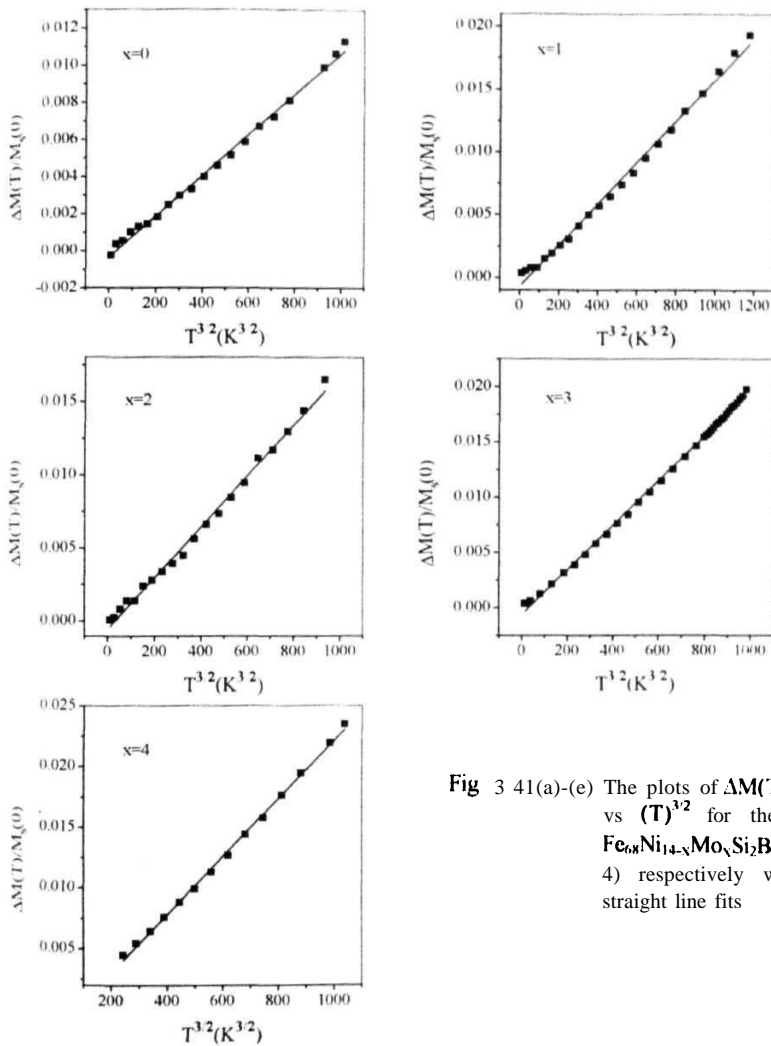


Fig 3 41(a)-(e) The plots of $\Delta M(T)/M_N(0)$ vs $(T)^{3/2}$ for the alloys $\text{Fe}_{68}\text{Ni}_{14-x}\text{Mo}_x\text{Si}_2\text{B}_{16}$ ($x=0-4$) respectively with the straight line fits

Table 3.16 The values of **B** and **B_{3/2}** obtained from **M_s(0)** and **H_{eff}(0)** values.

x	B (10 ⁻⁴)	B _{3/2}	B (10 ⁻⁴) (K ^{-3/2})	
0	1 097	0 208	2 242	0 425
1	1.649	0.275	1 714	0 285
2	1 741	0.271	2 033	0 316
3	2 014	0 290	2 551	0 368
4	2 392	0.347	2 499	0 362

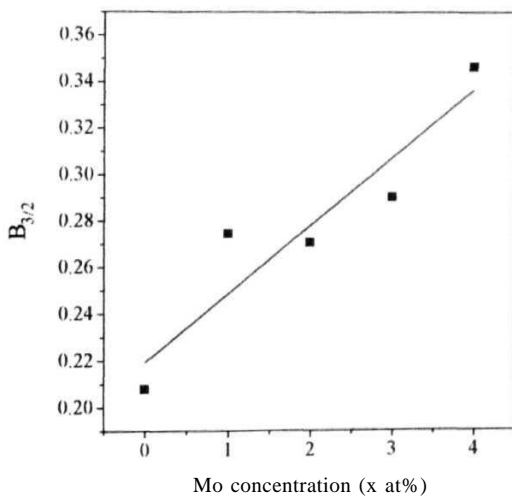
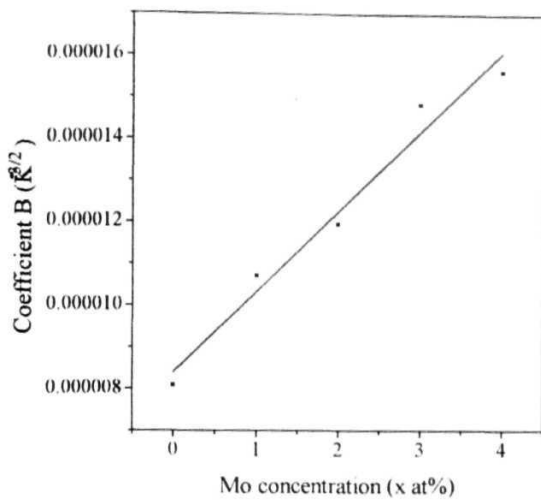


Fig 3.42 The values of spin wave coefficient B and the corresponding **B_{3/2}** as function of Mo concentration, **x**

effects contributing to the distribution in the lower field region. The $P(H)$ curves obtained for the Mossbauer spectra recorded at 80 K, indicate that the asymmetry of the major peak increases systematically as Mo content increases. Further, for all the alloys studied, the major peak shows temperature dependence and the minor peak is independent of temperature occurring at 100 kOe. The values of H_p and H_{av} decrease monotonically with increasing temperature and also with increasing Mo concentration. But the values of AH are relatively independent of temperature, especially in molybdenum rich systems indicating different hyperfine field components exhibiting different temperature dependence. These AH values increase with the increase of Mo content, at a rate of 10 kOe/Mo-at% upto $x=3$ but the increase becomes less for $x=4$.

The values of $M_s(RT)$ and $M_s(0)$ decrease with the Mo concentration and the rate of fall is ~ 8 emu/g per Mo-at% and -1 emu/g per Mo-at% respectively. Magnetization at low temperatures, well below T_c , well obeys the spin wave excitation and the values of spin wave coefficient $B_{\lambda 2}$ increases from 0.2 to 0.34 with increasing Mo content indicating that the spin waves are excited with relative ease in these alloys as Mo is added. These values of $B_{\lambda 2}$ are in agreement within 10% with those obtained from Mossbauer measurements except for $x=0$ which is 1/2 of that. This discrepancy is baffling for which an explanation is to be sought.

3.7 References

- 1 K Moorjani and J.MD Coey, "*Metallic Glasses*", Elsevier, Amsterdam (1981) Chap **VIII**, p91 and references therein
- 2 T.R. Anantharaman (ed) "*Metallic Glasses: Production, Properties and Applications*", Trans Tech Publications, Switzerland (1984)
- 3 S Steeb and H Warlimont (eds) "*Proc. of 5th Int. Conf. on Rapidly Quenched Metals*", Vol **I** and **II** North Holland, Amsterdam (1985)
- 4 A.K Bhatnagar (ed) "*Metallic and Semiconducting Glasses*", Trans Tech Publications, Switzerland (1987) (*Key Engg.Mats.* **13-15** 1987)
- 5 R. Jagannathan, *Proc. Indian Natn.Sci. Acad*, 52 (1986) 192
- 6 G Hilscher, R Hafel, K Kirchmayr, M. Muller and H -J Guntherodt, *J. Phys. F*, **11** (1981)2429.
- 7 R J Pollard, Z S Wronski and A H Morrish, *Phys. Rev. B*, **31** (1985) 7455
- 8 R A Dunlap, J E Ball and K Dini, *J. Mat. Sci. Lett.*, 4 (1985) 773
- 9 K Ganeshan, A Narayansamy, G. Konczos and T Nagarajan, *J. Magn. & Magn. Mater.*, **116** (1992) 189.
- 10 W. Zych, *Phys. Stat. Solidi (a)*, 99 (1987) K125
- 11 B Bhanuprasad, A K Bhatnagar and R Jagannathan, *Solid State Commun.*, **36** (1980) 661
- 12 B. Bhanuprasad, A K Bhatnagar and R Jagannathan, *J. Appl. Phys.*, 57 (1985) 3514
- 13 A K Bhatnagar, B Bhanuprasad, R Jagannathan and T R Anantharaman, *Solid State Commun.*, 44 (1982) 905
- 14 E E Shaisha, A A Bhagat, MR El-Kottamy and N A Eissa, *J. Mat. Sci.*, 22 (1987) 3931
- 15 F.E. Luborsky and LA Johnson, *J. Phys. (Paris) Colloq.*, **41** (1980) C8-820
- 16 D Raskin and CH. Smith, "*Amorphous Metallic Alloys*", edited by F E Luborsky, Butterworths Co., London (1983) Chap 20 and references therein
- 17 R. Hasegawa, G.E Fish and V.R.V. Ramanan, "*Proc. of 4th Int. Conf on Rapidly Quenched Metals*", Vol. **II**, edited by T Masumoto and K Suzuki, The Japan Institute of Metals, Sendai, Japan (1981) 929

- 18 F **E** Luborsky, '*Ferromagnetic Materials*', Vol I, edited by E P **Wohlfarth**, North Holland. Amsterdam (1980) Chap 6
- 19 **J Durand**, "*Glassy Metals: Magnetic, Chemical and Structural Properties*", edited by R **Hasegawa**, CRC Press, Boca, Raton **FL**, (1983) **Chap.4**
- 20 **R Jagannathan**, T.G N **Babu**, **B B Prasad**, **A K Bhatnagar** and V R V Ramanam, "*Industrial Applications of Mossbauer Effect*", edited by G **J Long** and J **G Stevens**, Plenum Press, New york, (1984) Chap 18 and references therein
- 21 J Durand,/. *de Physique - Colloques*, 41 (1980) C8-609, J Durand and P Panissod, *IEEE Trans. on Mag.*, **MAG-17** (1981) 2595
- 22 **R.L Mossbauer**, *Z. Physik*, 151 (1958) 124

N.N. Greenwood and T.C. Gibb, "*Mössbauer Spectroscopy*" Academic Press, New York, (1964).
- 24 **H. Fraunfelder**, "*The Mossbauer Effect*", Benjamin, New York (1962)
- 25 **G.K Wertheim**, "*Mossbauer Effect, Principles and Applications*", Academic Press, New York, (1964)
- 26 U. Gonser (ed), "*Mossbauer Spectroscopy -I, Topics in Appl. Phys.* ", Vol 5 (1975) and "*Mossbauer Spectroscopy - II, Topics in Current Phys.* ", Vol 25, Springer, Berlin, (1981)
- 27 **R J Gruverman**, "*Mossbauer Effect Methodology*", Vols 1-11, Plenum Press, New york, (1965-1976).
- 28 H.N. Ok and **A.H Morrish**, *Phys. Rev. B*, 22 (1980) 4215
29. **J.R. Gabriel** and **S.L Ruby**, *Nuclear Instrum. Methods*, 36 (1965) 23
- 30 **E.G.** & G PARC Model 4500 VSM Instructions Manual
- 31 S Foner, *Rev. Sci. Instr.*, 27 (1956) 548, *ibid* 30 (1959) 548
- 32 G **W Van Oosterhout**, *Appl. Sci. Res.*, B6 (1956) 101
- 33 H. Zijlstra, "*Experimental Methods in Magnetism*", Vol 2, North-Holland, Amsterdam, (1967) 116
34. **T.T Mc Guire** and P.J. Flanders, "*Magnetism and Metallurgy*", Vol 1, edited by A.E. Berkowitz and **E Kneller**, Academic press, New York, (1969) 170, L.F. Bates, "*Modern Magnetism*", Cambridge University press, London, (1963) 122.'

- 35 Lakeshore Series 7000 ac **Suceptometer/dc** Magnetometer Instructions Manual.
- 36 **A K** Bhatnagar and **N** Ravi,./. *Non-C 'ryst. Solids*, 56 (1983) 237
- 37 **A.K.** Bhatnagar, **B.B.** Prasad and **N R** **Munirathnam**, *J. Non-C 'ryst. So/ids*. **61-62** (1984) 1201
- 38 **A.K** Bhatnagar, **B B** Prasad and **R** Jagannathan, *Phys. Rev. B*, 29 (1984) **4896**
- 39 **R A** Dunlap and **G** Stronik, *C 'an. J. Phys.*. 62 (1984) **714**
- 40 **R A** Dunlap and **G** Stronik,./. *Phys. F*, 14 (1984) 3083
- 41 **A.K** Bhatnagar, *Hyper. Inter.*, **24-26** (1985) 637, **A K** Bhatnagar, **B** Bhanuprasad and **R** Jagannathan, *J. Appl. Phys.*, 57 (1985) 3514, **A K** Bhatnagar, **B.B** Prasad, **N.R.** Munirathnam, **N.** Ravi, **KV** Rao and **O V** Nielsen, "*Proc. of 5th Int. Conf. On Rapidly Quenched Metals*", Vol I edited by **S.** Steeb and **H** Warlimont, Wurzburg, Germany (1984) 1055
- 42 **L.** May, **S.J.** Druck and **M** Sellers, *U. S. Atomic Energy Comm. Rep. No. NYO* **3798-2** (1968)
- 43 **L** May, **S.R** Nassif and **M** Sellers, *U. S. Atomic Energy Comm. Rep. No. NYO* 3798-8(1970).
- 44 **B** Window,./. *Phys. F*, 4 (1971) 401
- 45 **U** Gonser, **M** Ghafari and **H G** Wagner,./. *Magn. & Magn. Mater.*, 8 (1978) 175
- 46 **P J** Schurrer and **A.H** Morrish, *Solid State (ommun.*, 28 (1978) 819
- 47 **D.C.** Price, **S.J** Campbell and **P J** Back,./. *Phys. (Paris) Colloq.*, 41 (1980) **C1-263**.
- 48 **C.L** Chien and **H S.** Chen,./. *Appl. Phys*, **50** (1979) 1574
- 49 **H.J V.** Nielsen, *J. Magn. & Magn. Mater*, 12 (1979) 187, *Solid State Commu.*, 30 (1979) 239, **M** Sostarich, **S** Dey, **M** Rosenberg, **H J V** Nielsen and **U** Gorres, "*Proc. of the 4th Int. Conf. on Rapidly Quenched Metals*", Vol II, edited by **T** Masumoto and **K** Suzuki, Japan Institute of Metals, Sendai, Japan (1982) 1109.
- 50 **L.** Novak, **L.** Potocky, **E.** **Kisdi-Koszo**, **A** Lovas and **J** **Daniel-Snado**, *Acta Phys. Slav.*, 35(1985)244.

- 51 **S Prasad, G Chandra, G Rajaram, V Srinivas, S.N. Shringi and R Krishnan, Solid State (Commun., 54 (1985) 313**
- 52 **C L Chien, Phys. Rev. B, 19 (1979) 81**
- 53 **P Allia, D Andreone, R.S Turtelli, F Vinai and G Riontino, J. Magn. & Magn. Mater., 26 (1982) 139.**
- 54 **I.W Donald, T Kemeny and H.A Davies, J. Phys. F, 11 (1981) L131.**
- 55 **T.G Narendra Babu, Ph.D. Thesis, University of Hyderabad, Hyderabad (1988); T.G.N Babu, R Jagannathan, A.K Bhatnagar and VRV Ramanan, Hyper. Int., 27 (1986) 293, 34 (1987) 499**
- 56 **N.R. Munirathnam, Ph.D. Thesis, University of Hyderabad, Hyderabad, India (1989).**
- 57 **C.L Chien and R Hasegawa, J. Appl. Phys., 49 (1978) 1721**
- 58 **N Saegusa and A.H. Morrish, Phys. Rev. B, 26 (1982) 10**
- 59 **J Balogh and I Vincze, Solid State (Commun., 25 (1978) 695**
60. **B.D Josephson, Phys. Rev. Lett., 4 (1960) 274**
- 61 **B B. Prasad, Ph.D. Thesis, University of Hyderabad, Hyderabad, India (1985)**
- 62 **C.L Chien, Phys. Rev. B, 18 (1978) 1003, F E Luborsky, J.L Walter, H.H. Leibermann and E.P Wohlfarth, J. Magn. & Magn. Mater, 15-18 (1980) 1351, C.L Chien, D Musser, E M Gyorgy, R C Sheerwood, HS Chen, F E Luborsky and J L Walter, Phys. Rev. B, 20 (1979) 283**
63. **F. Bloch, Z. Phys., 61 (1930) 206; 74 (1932) 295, S.N. Kaul, Phys. Rev. B, 24 (1981) 6550; 27 (1983) 5761**
- 64 **C. Herring and C Kittel, Phys. Rev., 81 (1951) 869**
- 65 **A K Bhatnagar and N. Ravi, Phys. Rev. B, 28 (1983) 359**
- 66 **C.L. Chien and R. Hasegawa, Phys. Rev. H, 16 (1977) 2115 and references therein**
- 67 **G. Rajaram and G Chandra, 'Proc. of Int. Conf. on the Applications of Mössbauer Effect', Jaipur, Indian National Science Academy, New Delhi, India (1982) 357**
- 68 **J J Rhyne, J.W. Lynn, F.E Luborsky and J L. Walter, J. Appl. Phys., 50**

- (1979) 1583
- 69 ML Spano and S M Bhagat,/. *Magn. rt Magn. Mater.*,**24** (1981) 143
 - 70 D G Onn,/. *Appl. Phys.*, 52 (1981) 1788
 - 71 B E Argyle, S H Charap and E W Pugh, *Phys. Rev.*, 132 (1963) 2051
 72. R Hasegawa and R Ray, *Phys. Rev. ft* 20 (1976) 211
 - 73 T Kaneyoshi, "*Metallic Glasses: Magnetic, Chemical and Structural Properties*" edited by R Hasegawa, CRC, Boca Raton, Florida, (1983) 37
 - 74 K Handrich, *Phys. Stat. Solidi*, **32** (1969) K55
 - 75 C.G Montogemery, J.I Krugler and R M Stubbs, *Phys. Rev. Lett.*, 25 (1970) 669
 - 76 A.W. Simpson and Wiss, *Z Tech. Univ. Dres.*, 3 (1974) 1020
 77. J E Gubernatis and P.L. Taylor, *Phys. Rev. B*, 9 (1974) 3828
 - 78 S M Bhagat, M.L. Spano and K V Rao,/. *Appl. Phys*, 50 (1979) 1580
 - 79 J A Tarvin, G Shirane, R.J Birgeneau and H S. Chen, *Phys. Rev. B*, 17 (1978) 241
 - 80 C.L. Chien and R Hasegawa, *Phys. Rev. B*, 16 (1977) 3024
 - 81 C.L. Chien and H S Chen,/. *Phys. (Paris) (Colloq.)*,**40** (1979) C2-118
 82. T.E sharon and C.C. Tsuei, *Solid State Commun.*,**9** (1971) 1923
 - 83 T E Sharon and C C. Tsuei, *Phys. Rev. B*, 5 (1972) 1047
 - 84 J Logan and E Sun, *J. Non-Cryst. Solids*, 20 (1976) 285
 - 85 J Hesse and A Rubartsch,/. *Phys. E*, 1 (1974) 526
 - 86 G. La Caer and J. M. Dubois, *J. Phys. E*, 12 (1979) 1083
 87. I Vincze, *Solid State Commun.*,**25** (1978) 689
 - 88 H. Keller,/. *Appl. Phys.*, 52 (1981) 5268
 89. A.K Bhatnagar, B Seshu, G.V. Sudhakar Rao and NR Munirathnam,/. *Non-Cryst. Solids*, 204 (1996) 305 and references therein.

- 90 **G Rajaram**, S Prasad, G Chandra, S N. Shringi and R Krishnan, *Phys. Lett.*,
98 A (1983) 57
- 91 **I M Tang**,/. *Magn. & A later* , 53 (1985) 23 3

Crystallisation Studies

4.1 Introduction

Metallic glasses crystallise by nucleation and growth **processes**. The driving force is the difference in free energy between the glass and the appropriate crystalline phase(s). A study of the crystallisation behaviour of $\text{Fe}_{68}\text{Ni}_{14-x}\text{Mo}_x\text{Si}_2\text{B}_{16}$ ($x=0, 1, 2, 3$ and 4) metallic glass system is presented in this **chapter**. Metallic glasses, irrespective of the method of preparation, are not in configurational equilibrium, but relax slowly through a homogeneous process towards an "ideal" **metastable** amorphous state with lower energy. Relaxation towards an ideal amorphous state is distinct from the heterogeneous process of crystallisation, which results in a metastable or stable crystalline state of the material. During crystallisation, most of the promising properties of metallic glasses e.g., the excellent magnetic behaviour or the high

hardness and strength combined with ductility and high corrosion resistance which are inherently structure sensitive **degrade**. Therefore, a study of these properties as a function of temperature can reveal details of crystallisation processes involved and provides information on the thermal stability of the system. However, controlled crystallisation of metallic glasses can be used for designing very special partially or **fully** crystallised **microstructures**, which cannot be obtained from the liquid or crystalline states. For example, partially crystallised **(Mo,Ru)₈₀B₂₀** glasses have been found to be ductile superconductors with a $T_c \sim 6 \text{ K}$ [1]. As the thermal stability against crystallisation determines their effective working limits for these glasses to be used in practical applications, an understanding of the **micromechanisms** of crystallisation can therefore be of immense value in controlling crystallisation process [1,2]. Hence for technological applications, knowledge of the process that governs the thermal stability of these materials is of considerable importance [3-7].

During the last two decades, theoretical as well as experimental studies on phase transformations in metallic glasses from glassy to crystalline state, have been extensively done by measuring changes in one or more physical properties, using different techniques such as Differential Scanning Calorimetry (DSC) or Differential Thermal Analysis (DTA) [8-19], electrical resistivity [20,21], **magnetometry**, **Mössbauer** effect [22-24] and **electron** microscopy [25,26]. To a lesser extent, positron annihilation, optical methods and photoemission or energy dispersive X-ray diffraction methods have also been employed [22,23,27,28].

DTA is the technique in which temperature difference (ΔT) between the sample and reference materials is measured as a function of temperature qualitatively and it does not give any information about the heat energy released or **absorbed**. DSC, on the otherhand provides this information quantitatively and thus change in enthalpy is measured as a function of **temperature**. DSC technique provides a rapid and precise determination of the crystallisation process and the associated kinetic parameters and as such it is a more frequently employed technique to study the crystallisation of amorphous metallic **alloys**. Amorphous to crystalline phase transition is a first order transition which occurs essentially by diffusional movements of **atoms**. Depending on concentration, **the** transition of the metastable amorphous phase into the crystalline phase can **proceed** by one of the following reactions :

- a) **Polymorphous Crystallisation** : It is the reaction in which crystallisation of an amorphous alloy takes place without any change in concentration into just a single crystalline phase e g , $\text{Fe}_{75}\text{B}_{25} \rightarrow \text{Fe}_3\text{B}$
- b) **Primary Crystallisation** : Here crystallisation of an amorphous alloy undergoes a two step crystallisation, which occurs via long range diffusion and leads to a single crystalline phase followed by a enriched amorphous phase e g , $\text{Fe}_{86}\text{B}_{14} \rightarrow \alpha\text{-Fe} + \text{amorphous (Fe-B)}$ This reaction is diffusion controlled
- c) **Eutectic crystallisation** : In such a reaction simultaneous crystallisation of two crystalline phases takes place e g , $\text{Fe}_{80}\text{B}_{20} \rightarrow \alpha\text{-Fe} + \text{Fe}_3\text{B}$ This is governed by nucleation and growth of crystals

Both polymorphous and eutectic crystallisation processes involve only short range **diffusional** atomic movement whereas primary crystallisation involves long range **diffusion**.

Using the DSC technique, one can discern whether the transformation takes place by polymorphous or primary and eutectic crystallisation processes [2] In addition, the process of nucleation and growth of crystals in highly cooled melts, which are of scientific interest, can be studied using the DSC technique [29-34] Crystallisation kinetics also may be studied **isothermally** by keeping the sample at a fixed temperature and observing the change in its enthalpy as a function of time or **non-isothermally**, by scanning the temperature of the sample at a constant heating rate [8,29, 35-37]. Isothermal method is mathematically more definitive and rigorous [38] while experimentally the non-isothermal method has been more convenient [29,37] Non-isothermal method can be performed over a wider temperature range in a shorter time period compared to the isothermal **method** In addition, because of the inherent transients associated with the experimental set up [37], many phase transitions occur too rapidly to be measured under isothermal **conditions**

Work has been reported in detail on the crystallisation behaviour of many Fe-based metallic glasses due to the addition of transition metals like Ni and Cr [39] A study of crystallisation behaviour, especially as a function of increasing amounts of **elements** that are known to contribute to the stability of amorphous alloys can therefore provide valuable **information**

Crystallisation studies on $\text{Fe}_{40}\text{Ni}_{38}\text{Mo}_4\text{B}_{18}$ (2826MB) have been done

extensively [17,40-45] which show a double stage crystallisation, the first stage of crystallisation corresponds to primary crystallisation with an **fcc** structure followed by a polymorphic reaction for the second **stage**. The reported values of crystallisation temperatures for the two peaks are 703 K and 777 K respectively and the corresponding activation energies are 2% and 334 kJ/mol. The enthalpy changes are 28 and 57 J/g **respectively**. Muralidharan et al [43] have reported the value of **Avrami** exponent, $n=0.83$, a much lower value which strongly suggests that primary crystallisation is possibly caused by the growth of quenched in nuclei existing in the glass. It has been observed that the crystallisation temperature increases as a consequence of addition of 1 at% of Mo in Fe-Ni-B alloys [46]. The substitution of transition metals from the group Cr, Mo, Nb or V for iron in the compositional family $[\text{Fe}_{100-x}\text{Mo}_x]_{83}\text{B}_{12}\text{Si}_5$ increases the thermal stability and Mo produces the largest **effect**. Crystallisation temperature increases linearly with the transition metal additions and correlates with the atomic size of the substituted solute atom [47]. Influence of Mo on the crystallisation behaviour of FeSiB glass has been reported by Liu et al [48] using DSC and TEM **techniques**. Two step crystallisation was observed, the second peak shrinks quickly as Mo is added and the temperature gap between the two peaks found to be decreased with Mo **addition**. An increase of thermal stability of these glasses containing Mo element is clear, as indicated by the increase in both crystallisation temperatures and activation energy for the first **step**. Different crystalline phases were identified and at least two **metastable** phases, $(\text{Fe},\text{Mo})_3\text{B}$ and $(\text{Fe},\text{Mo})_{23}\text{B}_6$ were present. Susie [19] has reported crystallisation data of $\text{Fe}_{0.40}\text{Ni}_{0.38}\text{Mo}_{0.04}\text{B}_{0.18}$ and $\text{Fe}_{0.70}\text{Ni}_{0.08}\text{Mo}_{0.10}\text{B}_{0.12}$ and identified the crystalline phases using X-ray **diffraction**. The alloy $(\text{Fe}_{0.99}\text{Mo}_{0.01})_{85}\text{B}_{15}$ has been studied by Maslov et al [49] and the values reported are crystallisation temperature, $T_p=684$ K, enthalpy **change**=14.37 J/g and activation **energy**=198 kJ/mol. The crystallisation of the alloy $\text{Fe}_{78}\text{Mo}_2\text{B}_{20}$ has been given [44] which has a single crystallisation step and is similar to that of FeB **alloys**. $(\text{Fe}_{0.99}\text{Mo}_{0.01})_{78}\text{Si}_5\text{B}_{13}$ metallic glass has been investigated to study various crystalline phases during crystallisation [50]. The sequence of metastable phase formation during crystallisation of this metallic glass is as follows: $\alpha\text{-Fe}(\text{Si-Mo})$ (**bcc**) $\rightarrow(\text{Fe},\text{Mo})_3\text{B}$, $(\text{Fe},\text{Mo})_{3,5}\text{B}$ and $(\text{Fe},\text{Mo})_{23}\text{B}_6$ (**fcc**) $\rightarrow\text{Fe}_2\text{B}$. Ramanan et al [45] have reported activation energies and Avrami exponents for many Mo containing **alloys**. They

conclude that presence of both Mo and Ni in small quantities in Fe-rich alloys reduces both nucleation and growth rates

In this chapter, details of investigations of the effect of addition of Molybdenum, Mo, a non-magnetic **metal**, on the crystallisation kinetics by non-isothermal method in $\text{Fe}_{68}\text{Ni}_{14-x}\text{Mo}_x\text{Si}_2\text{B}_{16}$ ($x=0,1,2,3$ and 4) using the DSC technique are **presented**. Results are analyzed and discussed using the well known Kissinger method [51]. The isothermal kinetic parameter, the **Avrami exponent**, n , is also calculated in an indirect method from the non-isothermal data and its agreement with the reported literature is discussed.

4.2 The Technique: Differential Scanning Calorimetry (DSC)

4.2.1 Introduction

Differential Scanning Calorimetry (DSC) and Differential Thermal Analysis (DTA) are very useful techniques in the study of phase transformations involving nucleation and growth of microcrystallites in general and in the study of crystallisation kinetics of amorphous solids in particular [8-19,29,31-34]. The term DSC was apparently first used by Watson et al [52]. DSC is the technique in which the difference in input energies of a sample material and a reference material is measured as a function of temperature, while the sample and reference materials are subjected to an electronically controlled temperature **program**. In the non-isothermal DSC technique the sample and the reference material are maintained isothermal to each other by proper application of electrical energy, as they are heated or cooled at a linear **rate**. DSC technique has proved to be a very sensitive tool for the investigation of thermally activated processes such as crystallisation [53-58] and relaxation phenomena in non-crystalline solids [59-63]. One of the advantages of DSC is that it allows a continuous record of the thermal evolution of the system as a function of time or **temperature**. Thus the information can be collected in a single run, not only regarding the relaxation to a more “**stable**” glassy state at temperatures lower than the glass transition **temperature** T_g , but also about the kinetics of crystallisation at higher temperatures.

The technique is highly accurate and versatile in measuring the heat effects

associated with physical or chemical changes that take place when the substance is heated at a uniform **rate**. Heat changes either exothermic or **endothermic** are caused by phase transitions - such as **fusion**, boiling, decomposition, sublimation, crystallisation etc, and are recorded as heat **flow** dH/dt in W/g (**mcal/s**) as a function of temperature under non-isothermal conditions. Whereas, in isothermal conditions, the sample and reference materials are kept at a constant temperature and the DSC thermogram is recorded as a function of **time**. Typical non-isothermal and isothermal DSC **thermograms** are shown in Figs 4 1(a) and 4 1(b). In the true **thermodynamic** sense, an endothermic peak is indicated conventionally by a peak in the upward direction (increase in enthalpy), while an exothermic peak is shown in the opposite **direction**. The DSC thermogram looks very similar to that of a **DTA** curve, except for the ordinate axis unit, which is ΔT in **DTA**. DTA has the qualitative aim of detecting phase transitions, while DSC is intended to determine the enthalpy changes quantitatively and accurately, and therefore can also be used to measure specific heat as a function of temperature. The area enclosed by the DSC profile is directly proportional to the enthalpy change [64],

$$\text{Area} = k(\Delta H)m \quad (4.1)$$

where k is a proportionality constant related to the geometry and thermal conductivity of the sample holder and is determined by calibration of the system with compounds having known heats of transitions and is independent of temperature, m is the mass of the reacting sample and ΔH is the enthalpy **change**. The DSC thermograms exhibit dependence on various factors, like sample quantity, holder cup, heating atmosphere and the nature of the sample **packing**.

4.2.2 Description of the Setup

Differential scanning **calorimetric** measurements have been done using Dupont model 910 DSC instrument, the schematic diagram of which is shown in Fig. 4 2. The cross sectional view of the DSC cell is as shown in Fig 4 3. The DSC cell contains a constantan disc by means of which heat is transferred to the sample and reference and also serves as one of the elements of the temperature measuring thermoelectric junctions. This calorimeter uses a sample cup made up of aluminum/copper or gold and an identical cup for **reference**. These two cups are made to sit on a raised platform

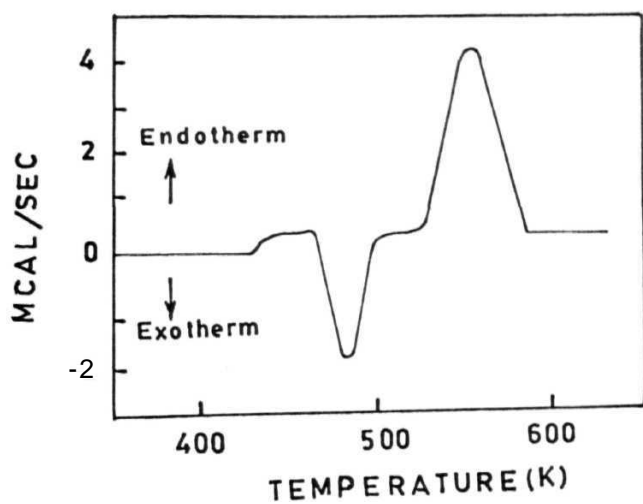


Fig. 4. l(a) A typical non-isothermal DSC curve illustrative of heat changes.

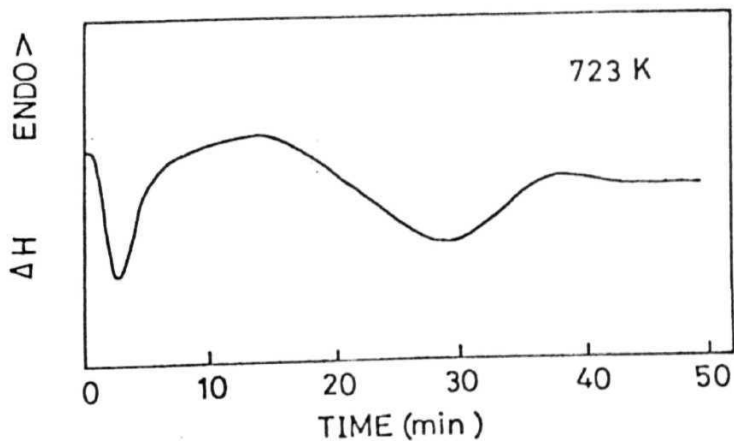


Fig. 4. l(b) A typical isotherm obtained by DSC measurement on isothermal annealing.

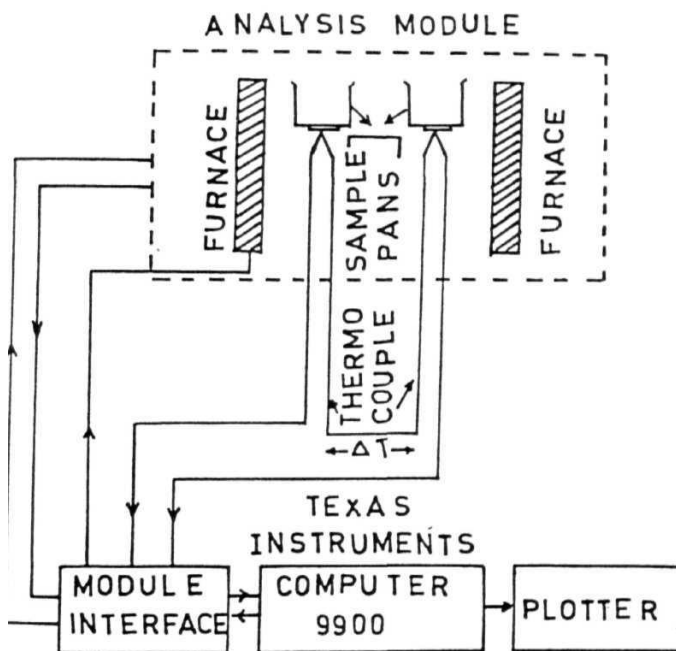


Fig. 4.2 Schematic diagram of Differential Scanning Calorimeter.

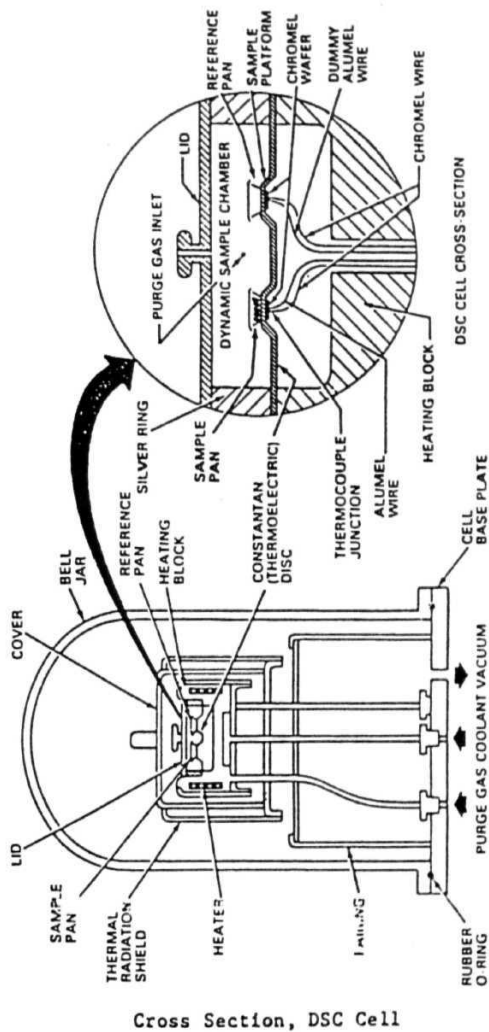


Fig. 4.3 DSC cell and its cross-section.

on the constantan **disc** Heat is transferred through the disc into the sample and **reference** The differential heat flow to the sample and reference is monitored by **chromel/constantan** thermocouples formed by the junction of the constantan disc and the **chromel** wafer which centers the downside of each platform **Chromel** and **alumel** wires are connected to the underside of the chromel wafers and the resultant **chromel/alumel** thermocouple is used to directly monitor the temperatures of the sample and reference materials Constant **calorimetric** sensitivity is maintained by electronic linearisation of the cell-calibration **coefficient** Minor complications arise mostly because the sample holders may not be strictly identical and a temperature gradient may develop across the finite thermal resistance between the sample and sample **holder** One tries to minimize these by careful selection of sample holders **etc**

The difference ΔT between the sample temperature, T_s and reference temperature, T_R is given by

$$\Delta T = (T_s - T_R) - R(C_s - C_R) \frac{dT_p}{dt} \quad (4.2)$$

where C_s and C_R are the total heat capacities of sample (and reference) plus sample holder respectively, R is the thermal resistance and $\frac{dT_p}{dt}$ is the rate at which the

programmed temperature **changes** The apparatus constant relating the area under the peak to enthalpy can be obtained by using a reference material like **Indium**, with known transition enthalpy

4.2:3 Experimental Procedure

The crystallisation studies were carried out using Dupont model **910** DSC instrument, on ribbons of amorphous $\text{Fe}_{68}\text{Ni}_{14-x}\text{Mo}_x\text{Si}_2\text{B}_{16}$ ($x=0, 1, 2, 3$ and 4) -5 mm wide and 25-30 μm thick which were prepared at Allied Signals, USA, by a single roller melt spinning technique

Both the sample and the reference chambers were heated at a programmed rate, and are maintained at same temperature The input power to the sample and the reference will be different because of the differences in the heat capacities and also due to the exothermic and endothermic transformations occurring in the sample, if any. In all the DSC measurements, **~5 mg** of the sample is placed in a copper cup and weighed

using a digital **microbalance**. The sample is then covered by a copper cover and the standard crimper press is used to crimp the cover on to the **sample**. Before doing the **calorimetric** measurements, the temperature and cell constant of the instrument are calibrated from the melting curves of 99.999% pure indium as a standard material. Pure indium ~5 mg is encapsulated (crimped) in an aluminum cup and an empty aluminum cup with cover as reference are placed on the raised platforms on the constantan **disc**. The sample is then heated from room temperature to above the melting temperature of indium with uniform scanning **rates**. The actual value of the transition temperature of indium is 156.6 °C. The unit of temperature is calibrated from the melting exotherms of pure indium. As long as there is no change in the instrument operating conditions, the temperature calibration remains **unchanged**.

Calorimetric measurements of the above mentioned amorphous alloys have been **carried** out under non-isothermal conditions i.e., samples are continuously heated from room temperature (**RT**) to the required high temperature i.e., in the temperature range RT-600 °C at different scan rates ranging from 5-40 °K/min with an interval of 5 °K/min. Continuous but a very small flow of dry and pure (99.94%) helium gas is maintained inside the DSC cell throughout the experiment to prevent oxidation **effects**.

The heat evolved is recorded as a function of temperature. **In** general metallic glasses may have one or more crystallisation peaks in their DSC **thermograms** and each peak is characterized by a peak temperature T_p , the onset and peak temperatures of crystallisation and the enthalpies are obtained using the software "Standard data analysis" [65] as pointed out in Fig. 4.4. Using these peak temperatures, the activation energies have been calculated by **Kissinger's** method [51] as described **below**. The isothermal crystallisation kinetic parameter, the **Avrami** exponent, n , using non-isothermal data was also determined using a method explained **later**.

4.3 Methodology

A survey of literature shows that the application of isothermal and non-isothermal methods for the study of phase transitions is of theoretical and experimental interest [8-19,29,37]. As already indicated in the beginning of this chapter, isothermal techniques are more definitive while non-isothermal (continuous heating) techniques have several advantages:

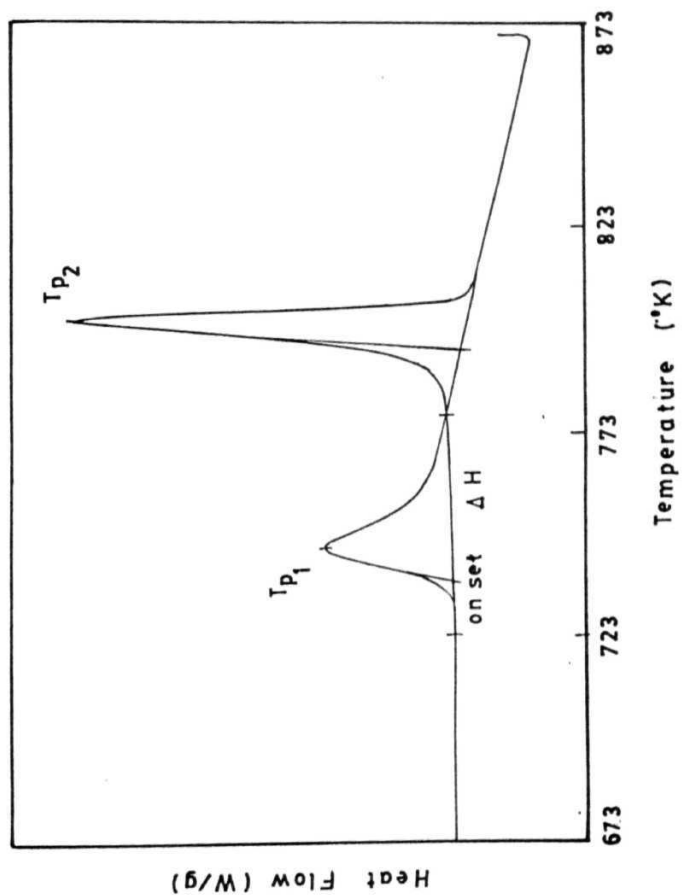


Fig. 4.4 A typical example of a non-isothermal DSC thermogram of a iron-rich metallic glass indicating the peak and onset temperatures and the entalpy.

- 1 The rapidity with which non-isothermal experiments can be performed makes them attractive
- 2 The scope to extend the temperature range for measurements beyond that accessible to isothermal experiments
- 3 Because of transients inherently associated with the experimental conditions, many phase transitions occur too rapidly to be measured under isothermal **conditions**

With all the above in mind, a definitive measurement of non-isothermal kinetics is **desirable**. Kissinger derived a kinetic model based on the rate of reaction for non-isothermal studies [51], the salient features of which are briefly described below

4.3.1 Kissinger's Method of Analysis of Non-Isothermal Transformation

In metallic glasses and particularly in crystallisation processes, it is the change in enthalpy with time or temperature variation which gives rise to **exotherms**. In the analysis of non-isothermal processes, Kissinger [51] method is used to evaluate the activation energy, E_c . It is the most popular method used in analyzing the crystallisation process by **DSC**. Originally, it was established by DTA that the temperature at which maximum deflection is observed varies with heating rate in many **reactions**. Kissinger showed that the kinetics of such reactions can be conveniently studied by systematically varying the heating rate and observing the peak temperatures. This method can be applied to all reactions, in which the dependence of the transformation rate on temperature can be separated from its dependence on the volume **fraction** transformed [66]. Kissinger demonstrated that the variation in peak temperature, (T_p), with the heating rate can be used to calculate the activation energy, E_c of the reaction, provided the other experimental conditions remain fixed. The details of **Kissinger's** method are as **follows**.

The basic equation that relates the rate of reaction to the fraction of the material decomposed, following first order reaction may be written as [67-69]

$$\left(\frac{dx}{dt}\right)_T = K_T(1-x) \quad (4.3)$$

where x is the fraction of the material decomposed, $(\frac{dx}{dt})_T$ is the rate of reaction and at absolute **temperature** T and K_1 is the magnitude of the rate constant which is given by Arrhenius equation as

$$K_T = K_0 \exp(-E_c/RT) \quad (4.4)$$

where R is the gas constant, T is the absolute temperature and K_0 is the frequency factor which is a measure of the probability that a molecule having energy E_c will participate in a reaction. E_c is the activation energy for the phase transformation and is often interpreted as the energy barrier opposing the reaction [51]. Substituting the value of K_T from Eq. (4.4) in Eq. (4.3), we get

$$(\frac{dx}{dt})_T = K_0 \exp(-E_c/RT)(1-x) \quad (4.5)$$

Eq. (4.5) holds good for any value of T , whether constant or variable, so long as x and T are measured at the same instant. When the reaction rate is maximum, i.e., corresponding to the peak maximum in the experimental situation, its derivative with respect to time is zero. The maximum value of $(\frac{dx}{dt})_T$ occurs at temperature T_p defined by [68]

$$K_0 \exp(-E_c/RT_p) = (E_c/RT_p^2) (\frac{dT}{dt}) \quad (4.6)$$

It may be easily seen from Eq. (4.6) that

$$\frac{d(\ln(\beta/T_p^2))}{d(1/T_p)} = -E_c/R$$

where $\beta = (\frac{dT}{dt})$, the heating rate. The Eq. (4.7) though derived for a first order reaction, was later shown to hold to any order of reaction [70].

The validity of the Eq. (4.7) can be tested for a given system by plotting $\ln(\beta/T_p^2)$ against $(1/T_p)$. The plot should be a straight line, the well known Kissinger plot with a slope equal to $(-E_c/R)$, and is found to be the case in many amorphous alloys [14,71-74]. This procedure has been used to calculate the values of activation energy (E_c) of all the amorphous systems reported in the present work.

4.3.2 Determination of the Avrami Exponent, n

Since crystallisation of metallic glasses is a nucleation and growth process, the overall rate of transformation will reflect the time and temperature dependence of **both** Solid state nucleation and growth transformations are usually described by the **Johnson-Mehl-Avrami (JMA)** equation [75,76]

$$\chi(t) = 1 - \exp[-b(t-t_0)^n] \quad (4.8)$$

where $\chi(t)$ is the **fraction** transformed after time t , t_0 is the incubation time, b is the rate constant and n is Avrami exponent, which need not be an integer, generally lying between 1.5 and 4 and can be **written** as

$$n = n_n + n_g \quad (4.9)$$

where n_n describes the time dependence of the nucleation rate ($0 \leq n_n \leq 1$) and n_g that of the growth rate ($1.5 \leq n_g \leq 4$). Typically n_n should be 0 for **athermal** growth of quenched in nuclei and unity for steady state nucleation, values of 1.5, 3 and 3 for n_g are expected for primary, eutectic and polymorphous growth **respectively**. These values will be reduced if the crystals show pronounced directionality of growth.

It can be shown that for various nucleation and growth mechanisms a useful picture of the crystallisation process emerges if n is partitioned as follows [20,45,77-79]:

$$n = a + bp \quad (4.10)$$

where ' a ' refers to the nucleation rate and varies from 0 (for quenched in nuclei) to 1 (for constant nucleation rate), ' b ' has the values 1, 2 or 3 and represents the dimensionality of growth of **microcrystallites**. The value of ' n ' cannot be more than 4 [80].

This picture of ' n ' is an approximate one and can only serve when the values of n are not close for different glasses so that different crystallisation mechanisms can be distinguished. However, it describes the crystallisation process well in many cases [20,77,79]. Hence the Avrami exponent, n , is an important crystallisation kinetic parameter and it gives more information about the crystallisation processes that occur through different **mechanisms**.

Marotta et al [81] classified the crystallisation mechanisms of glass into three groups in terms of the n **values**

- a) $n=1$, i.e., the crystals grow one **dimensionally from** the surface to the inside of the glass,
- b) $n=3$, i.e., each crystal grows three **dimensionally** in the **bulk**, and
- c) $1 < n < 3$, the crystals grow both from the surface and in the bulk

By taking the **JMA** Eq (4 8) [75,76] into account, the differential temperature AT at the initial part of the crystallisation is approximated as

$$\log \Delta T = \frac{-nE_c}{4.57T} + C \quad (4.11)$$

where n is the exponent, E_c is the overall kinetic energy barrier, T is the temperature and C is a constant. A plot of $\log \Delta T$ versus $(1/T)$ should yield a straight line, the slope of which gives $\frac{-nE_c}{4.57}$. On the otherhand, Thakur and Thiagarajan [82] **nave** reported an equation expressing the relationship between the exothermic peak temperature T_p and the heating rate β as

$$\log \beta = \frac{-E_c}{4.57T_p} + C' \quad (4.12)$$

where C' is a **constant**. Plotting of $\log \beta$ versus $(1/T_p)$ should yield a straight line, the slope of which is equal to $\frac{-E_c}{4.57}$. From the slopes of the lines obtained from Eqs

(4.11) and (4.12) we can determine the activation energy, E_c and the exponent, n

Using the above method for the determination of n and E_c , the parameters are calculated from the non-isothermal data and the results are **discussed**

4.4 Results

The results of the crystallisation kinetics performed on the alloys chosen for the present study, under non-isothermal conditions using DSC are presented and discussed in the light of the above mentioned **theories**

The DSC **thermograms** obtained by continuous heating of the amorphous specimens of $Fe_{68}Ni_{14-x}Mo_xSi_2B_{16}$ ($x=0,1,2,3$ and 4) in the temperature range room temperature (RT)-600 °C at different heating rates of 5, 15, 15, 20, 25, 30, 35 and 40 °K/min are shown in **Figs 4.5-4.9 respectively**. All these thermograms are

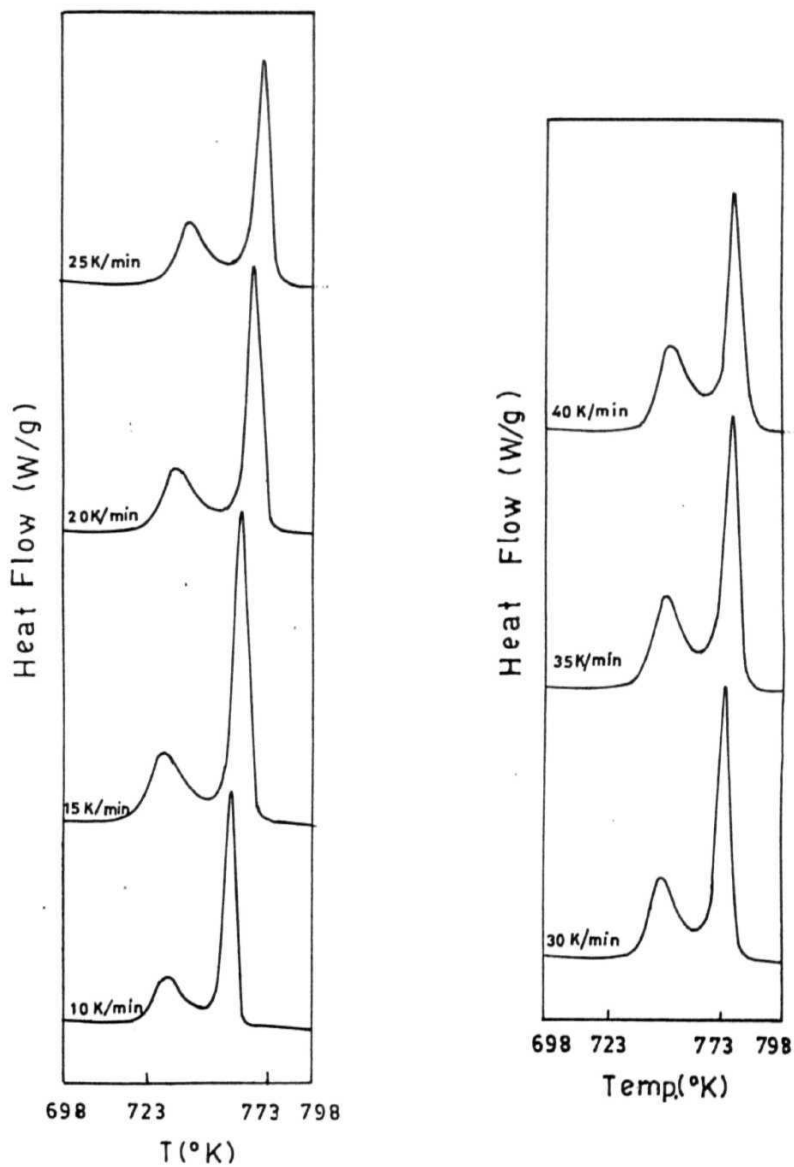
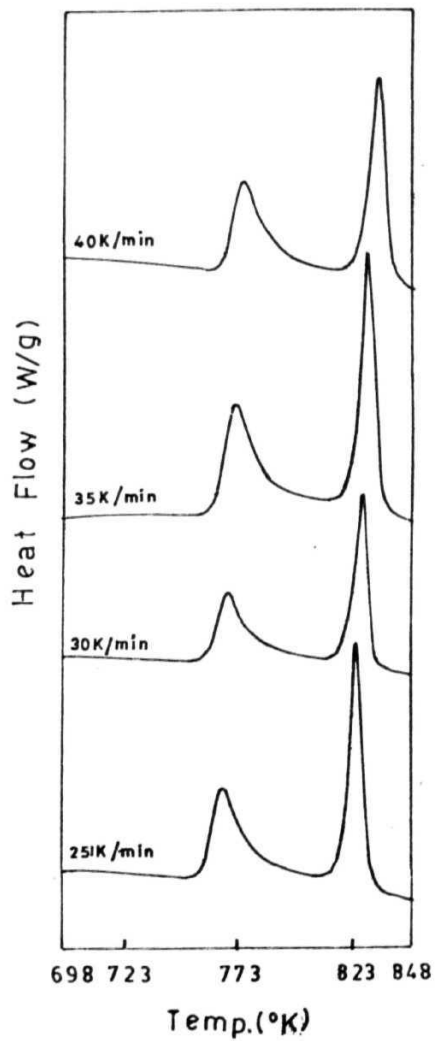
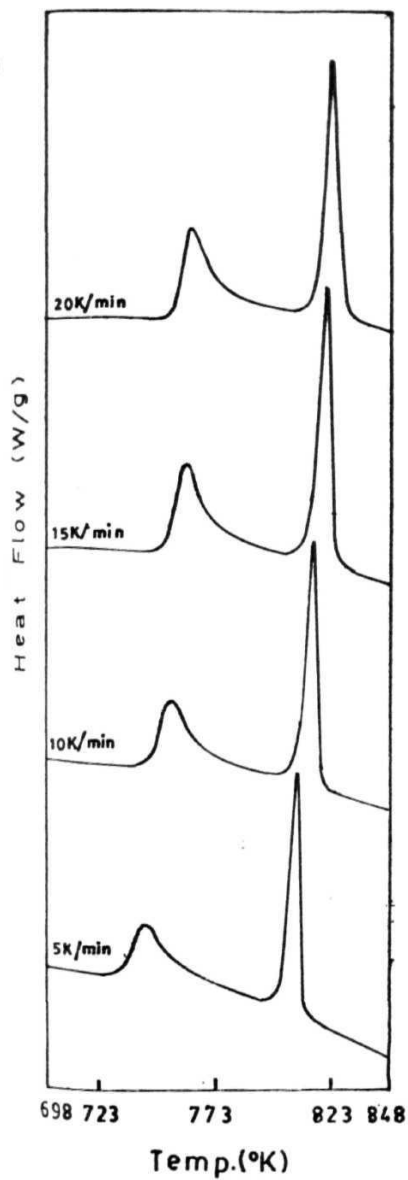


Fig. 4.5 The DSC thermograms of the sample with $x=0$ at different heating rates **5-40 K/min.**



4.6 The DSC thermograms of the sample with $x=1$ at different heating rates 5-40 K/min.

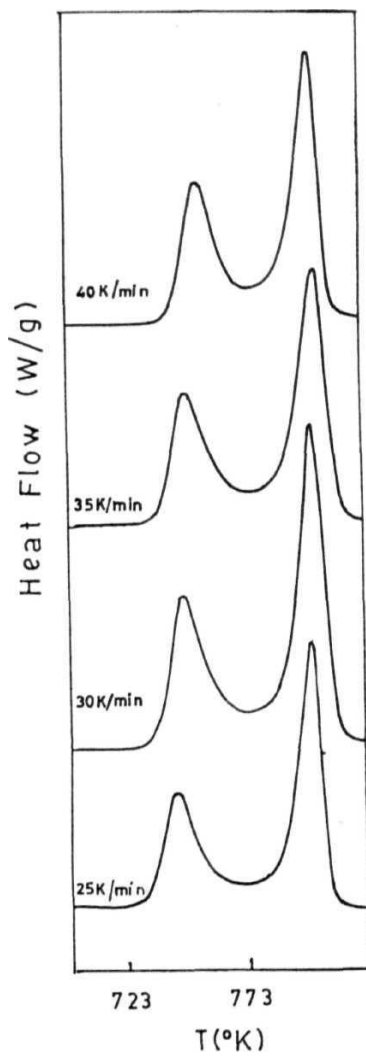
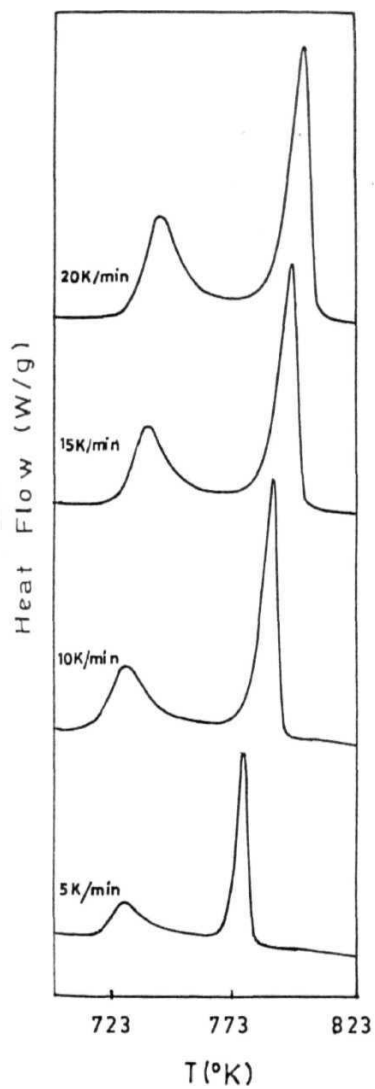


Fig. 4.7 The DSC thermograms of the sample with $x=2$ at different heating rates 5-40 K/min.

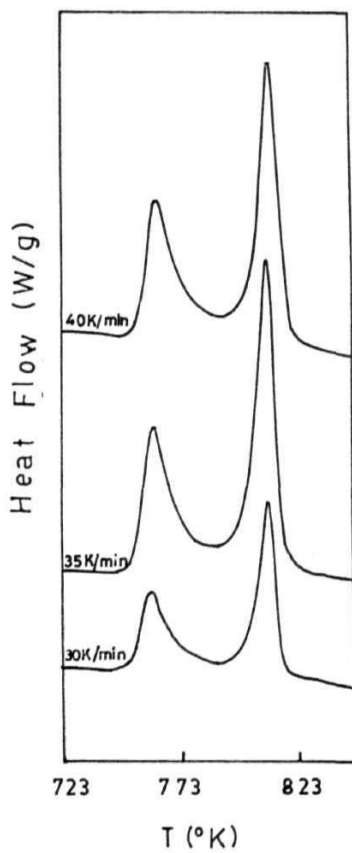
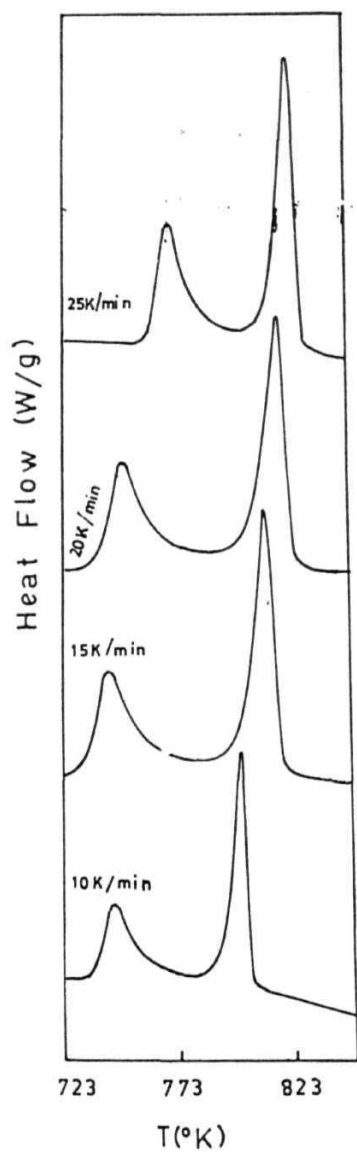


Fig. 4.8 The DSC thermograms of the sample with $x=3$ at different heating rates 5-40 K/min.

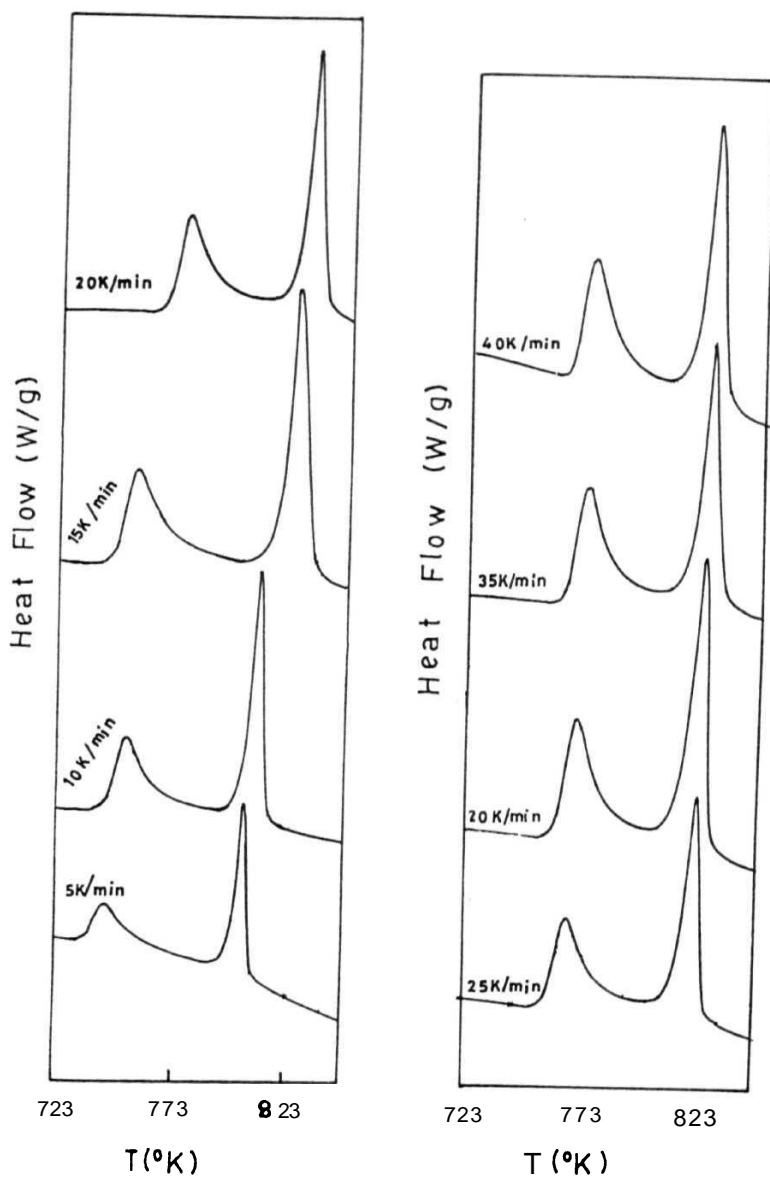


Fig. 4.9 The DSC thermograms of the sample with $x=4$ at different heating rates 5-40 K/min.

characterized by two exothermic peaks, confirming a two step crystallisation process and are well resolved irrespective of the heating **rate**. The first peak is observed to be broad while the second peak is narrower indicating the first crystallisation to be sluggish in comparison with the second one. The two peak temperatures T_{p1} and T_{p2} increase and the peaks become narrower and higher with increase of heating rate, as normally observed in many Fe-based metallic glasses [2,18,44,72,83-85]. The overall increment observed in these peak temperatures for all the samples are $\sim 20\text{-}25\text{ K}$ for the entire range of heating **rates**. However, the difference $(T_{p1}-T_{p2})$ decreases slowly as the heating rate is increased in all the samples, which is shown in **Fig 4 10(a)**

Various kinetic parameters **viz** the crystallisation peak temperatures T_{p1} and T_{p2} , the difference $(T_{p1}-T_{p2})$, the corresponding onset temperature of crystallisation and the enthalpies associated with each step of crystallisation at **different** heating rates are listed in Tables (4.1)-(4.5) for the samples $x=0$ to $x=4$ **respectively**. **Figs 4 10(b)-4 10(d)** show the parameters T_{p1} , T_{p2} and enthalpy change ΔH as a function of heating rate, p **respectively**. One can observe from these plots (b) and (c) that the peak temperatures increase with heating rates and are slightly non-linear at low heating **rates**. The slopes of these curves are nearly the same for Mo containing samples while that for the sample without Mo content ($x=0$) is higher. For the second crystallisation temperature T_{p2} , the temperature difference, ΔT between any two samples as indicated in the **Fig 4 10(c)** goes on reducing as Mo content increases which indicates that larger Mo concentration may not help any **further**. From **Fig 4 10(d)** it is evident that the change in enthalpy with respect to heating rate, β is the same for all samples except for that with $x=1$. The behaviour shows an initial rise in ΔH upto $p=20\text{ }^{\circ}\text{K/min}$ and then seems to exhibit slight oscillation behaviour which reduces as Mo concentration increases. The same parameters are shown in **Figs 4 11(a)** and **4 11(b)** as a function of Mo concentration at a particular scan rate $\beta=20\text{ }^{\circ}\text{K/min}$. The difference in peak temperatures $(T_{p1}-T_{p2})$ vs Mo concentration is shown in **Fig 4 11(c)**. **Figs. 4.12(a)-(e)** show the Kissinger plots of $\ln(\beta/T_p^2)$ vs $10^3/T_p$ for the two exothermic peaks for all the five samples respectively, where T_p is the peak temperature of the respective exotherm. **Figs. 4.13(a)** and **4.13(b)** respectively show the Kissinger plots for the first

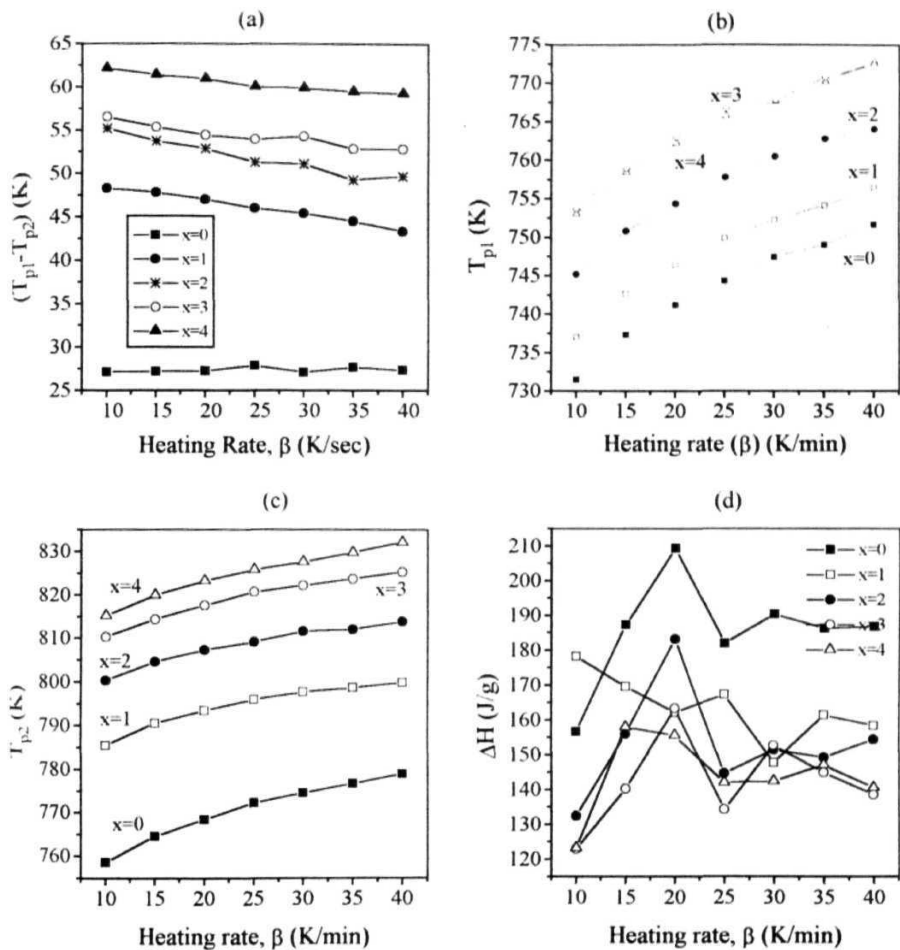


Fig. 4. 10(a)-(d) $(T_{p1} - T_{p2})$, T_{p1} , T_{p2} and ΔH as a function of heating rate, β respectively for all the samples

Table 4.1 Various crystallisation parameters for the sample x=0 at different heating rates.

Heating rate(p) °K/min	Peak <u>Temp</u> (K)		(T _{p1} -T _{p2}) (K)	Onset <u>Temp</u> (K)		Enthalpy (J/g)		Total Enthalpy AH (J/g)
	T _{p1}	T _{p2}		Peak1	Peak2	Peak1	Peak2	
5								
10	731.48	758.59	27.11	722.54	753.04	39.99	1166	156.59
15	737.34	764.55	27.21	727.23	758.69	64.04	123.2	187.24
20	741.2	768.43	27.23	731.08	762.75	72.97	136.3	209.27
25	744.39	772.28	27.89	734.3	765.89	65.52	116.4	181.92
30	747.47	774.57	27.1	737.01	768.47	70.84	119.5	190.34
35	749.02	776.69	27.67	738.75	770.01	70.41	1158	186.21
40	751.64	778.86	27.37	741.2	772.18	73.22	113.5	186.72

Table 4.2 Various crystallisation parameters for the sample |=**|** at different heating rates.

Heating rate (β) °K/min	Peak <u>Temp</u> (K)		(T _{p1} -T _{p2}) (K)	Onset <u>Temp</u> (K)		Enthalpy (J/g) (AH)		Total Enthalpy AH (J/g)
	T _{p1}	T _{p2}		Peak 1	Peak2	Peak1	Peak2	
5	727.95	77690	48 95	71744	770 88	80 86	114 1	194.26
10	737.02	785 35	48 33	727 10	77881	69 55	1087	178 25
15	742.65	790.50	47 85	732.93	78260	65 31	1042	16951
20	746.39	793.43	47 04	736.87	784.75	64.14	97 98	162.12
25	749 91	79591	46 00	740.07	786 11	6557	101 7	167.27
30	752.23	797 68	45 45	742 58	78693	58.55	89 11	147 66
35	754.11	79861	44 50	744.87	787 63	66 68	94 67	161.35
40	756 40	799 77	43.37	746 92	78837	63.33	94 99	158.32

Table 4.3 Various crystallisation parameters for the sample $\alpha=2$ at different heating rates.

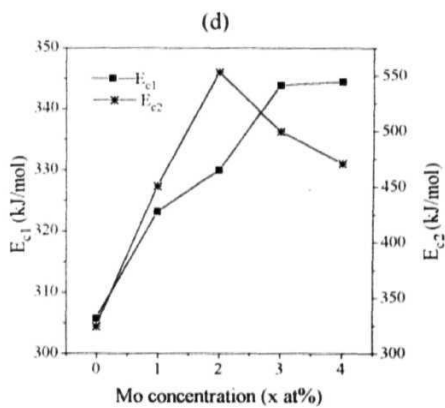
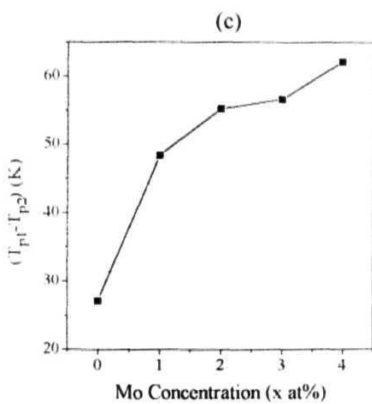
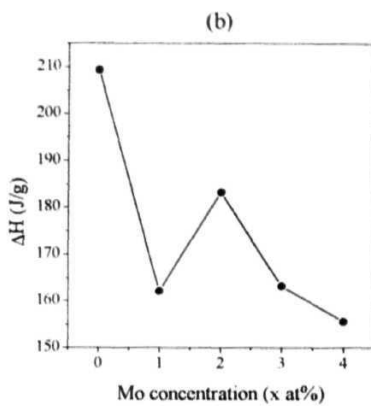
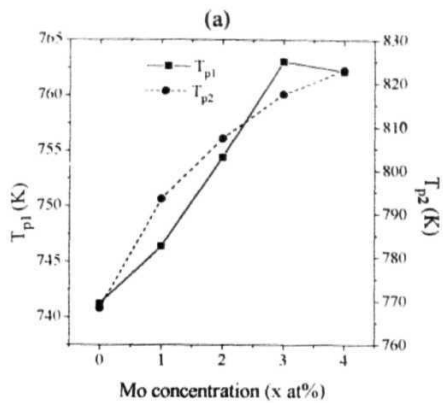
Heating rate(p) °K/min	Peak Temp. (K)		(T _{p1} -T _{p2}) (K)	Onset Temp (K)		Enthalpy (J/g)		Total Enthalpy AH(J/g)
	T _{p1}	T _{p2}		Peak 1	Peak 2	(AH) Peak1	Peak2	
5								
10	745.16	800.37	55.21	736.32	792.68	49.75	82.57	132.32
15	750.82	804.55	53.73	741.51	795.70	64.55	91.32	155.87
20	754.38	807.28	52.90	745.62	798.07	61.95	91.22	183.17
25	757.78	809.10	51.32	748.91	800.08	59.29	85.25	144.54
30	760.47	811.55	51.08	751.57	801.48	62.49	88.93	151.42
35	762.73	811.98	49.25	753.65	802.60	61.18	87.92	149.10
40	764.01	813.73	49.72	755.27	803.35	63.73	90.63	154.36

Table 4.4 Various crystallisation parameters for the sample **x=3** at different heating rates.

Heating rate (β) °K/min	Peak Temp (K)		(T _{p1} -T _{p2}) (K)	Onset Temp (K)		Enthalpy (J/g)		Total Enthalpy AH(J/g)
	T _{p1}			Peak 1	Peak2	(AM) Peak 1	Peak2	
5	74493	80299	58 06	735.91	797 26	54 50	75 14	129 64
10	75369	81021	5652	745.36	803 60	4851	7438	122 89
15	75892	814.28	5536	750.57	807 32	60 76	79.46	140.22
20	763 03	817.49	54 46	754 17	809 66	69 53	93 69	163.22
25	766 69	82063	53 94	757 68	81231	59 43	74 79	134.22
30	767.79	822.08	54.29	75955	813 31	65 91	86 65	15256
35	770.73	823 56	5283	762.28	81544	6236	8245	144.81
40	772.39	825 23	5284	763.76	816.46	60.91	77.62	138.53

Table 4.5 Various crystallisation parameters for the sample $x=4$ at different heating rates.

Heating rate (β) °K/min	Peak Temp. (K)		(T _{p1} -T _{p2}) (K)	Onset Temp (K)		Enthalpy (J/g)		Total Enthalpy AH (J/g)
	T _{p1}	T _{p2}		Peak1	Peak2	(AH) Peak1	Peak2	
5	744.65	807.58	62.93	734.09	801.89	60.87	70.82	131.69
10	753.04	815.16	62.12	743.87	809.01	55.61	67.49	123.10
15	758.44	819.82	61.38	749.12	812.87	76.72	81.27	157.99
20	762.18	823.11	60.93	753.11	815.76	74.33	81.27	155.60
25	765.69	825.71	60.02	756.52	818.43	66.96	75.01	141.97
30	767.65	827.53	59.88	758.85	820.32	66.87	75.47	142.34
35	770.20	829.64	59.44	761.23	822.15	68.60	78.40	147.00
40	772.71	831.96	59.25	763.06	823.55	66.51	73.91	140.42



4 11(aHd) (T_{p1} & T_{p2}), ΔH , ($T_{p1} - T_{p2}$) and (E_{c1} & E_{c2}) as a function of Mo concentration, x respectively

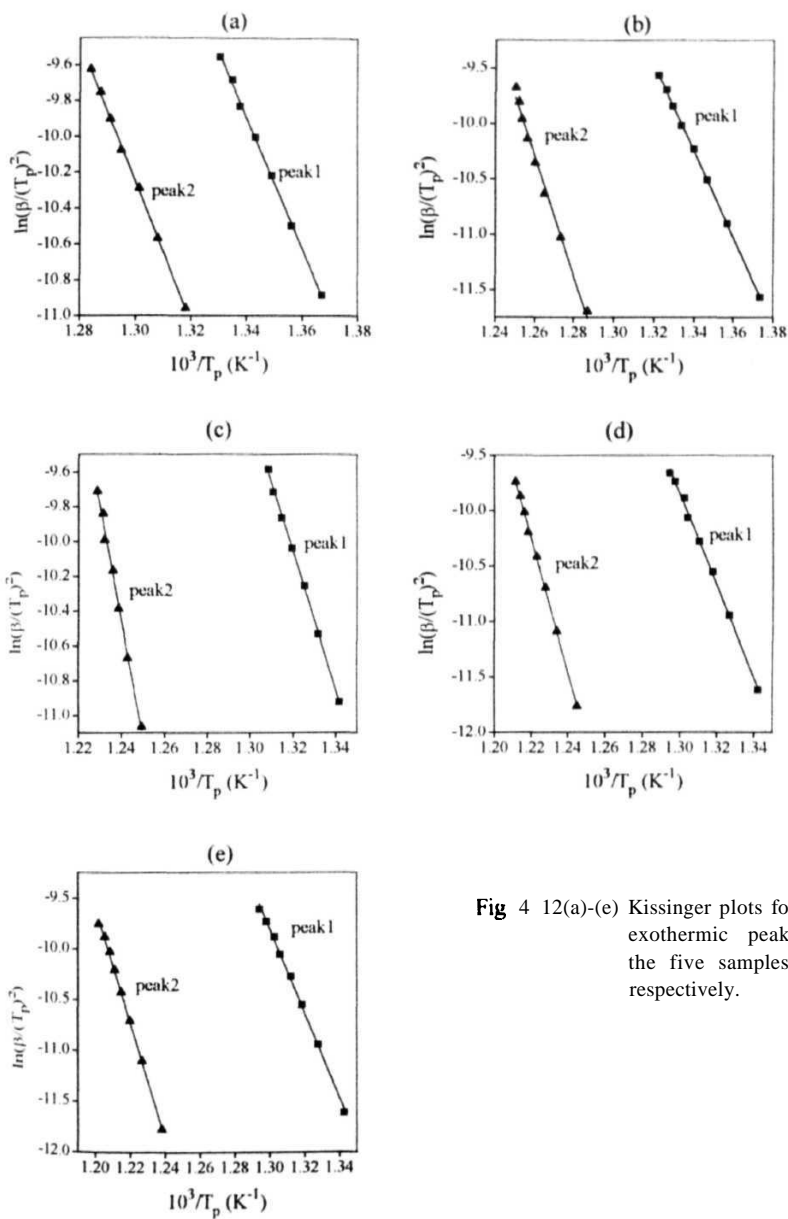


Fig 4 12(a)-(e) Kissinger plots for the two exothermic peaks of all the five samples ($x=0-4$) respectively.

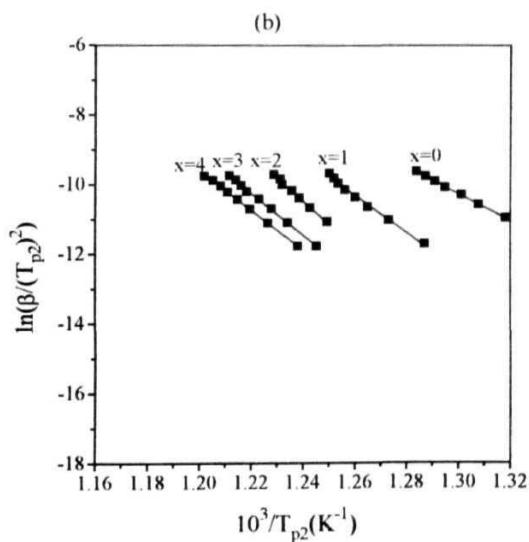
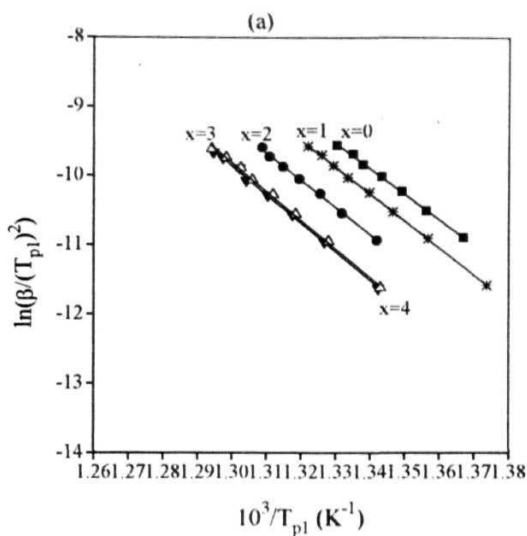


Fig 4.13(a) Kissinger plots for the first exothermic peak of all the five samples ($x=0-4$).

Fig 4.13(b) Kissinger plots for the second exothermic peak of all the five samples ($x=0-4$).

and second peaks separately for all the **samples**. All of them are fairly linear under experimental conditions, confirming that the crystallisation kinetics in these samples is of first **order**. The activation energies, E_{c1} and E_{c2} for the first and second crystallisation processes respectively for all the five samples are calculated from the slopes, $(-E_c/R)$, of the respective Kissinger plots, and the activation energies are in the range 300-350 **kJ/mol** and 320-560 **kJ/mol** for the two peaks respectively, and are listed in Table (4 **6**). These values are plotted as a **function** of Mo concentration as shown in **Fig 4 1 l(d)**. The value of E_{c2} , involved in the second step is higher than the value of E_{c1} , as evidenced by larger peak area of the second step crystallisation peak compared to that of first step.

Figs 4 14(a)-(e) show typical plots of $\log AT$ vs $10^3/T$ and **Figs 4 15(a)-(e)** show plots of $\log \beta$ vs $10^3/T_p$ at a particular heating rate for all the samples respectively, from the slopes of which the **Avrami** exponent, (n) and activation energies, (E_{c1} & E_{c2}) are calculated as described in the previous **section**. These values of E_{c1} & E_{c2} for the two peaks thus obtained are compared in Table (4.6) with those obtained from **Kissinger's** method for all the samples at a particular scan rate of 20 **"K/min**. The values of n are listed for different heating rates in Tables (4 7) and (4 8) for the first and second crystallisation steps respectively for the five **samples**.

Composition dependence of crystallisation temperatures and activation energies

Figs. 4.16(a)-(g) show the DSC curves for all the samples ($x=0,1,2,3$ and 4) for different heating rates 10-40 **"K/min respectively**. From these figures it is clear that both the peak temperatures T_{p1} , T_{p2} and their difference ($T_{p1}-T_{p2}$) increase with Mo concentration, x . The increment in these values at a particular scan rate 20 **"K/min**, as can be seen from Tables (4. 1)-(4 5) are - 20 K, ~55 K, and ~33 K respectively, from $x=0$ to $x=4$, indicating improvement of thermal stability of Mo substituted $Fe_{68}Ni_{14}Si_2B_{16}$ metallic glass.

Variation of activation energies with the Mo content is shown in **Fig 1 11(d)** from which it is clear that E_{c1} increases systematically with increased Mo content, x . Thus, the substitution of Mo for Ni in $Fe_{68}Ni_{14}Si_2B_{16}$ metallic glass enhances its thermal **stability**. However, the same behaviour is not observed for the second peak,

Table 4.6 Comparison of activation energies calculated from the two methods for all the samples.

Sample (x)	Activation Energy (kJ/mol) (Kissinger)		Activation Energy (kJ/mol) (Avrami Exponent)	
	E_{c1}	E_{c2}	E_{c1}	E_{c2}
0	305 65	324 04	317 60	336 38
1	323 16	450 56	335 08	463 03
2	329.97	553 26	342.07	565 96
3	343 87	499 40	360.02	512.32
4	344.47	470 90	35663	48395

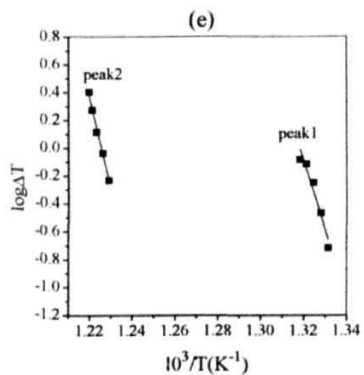
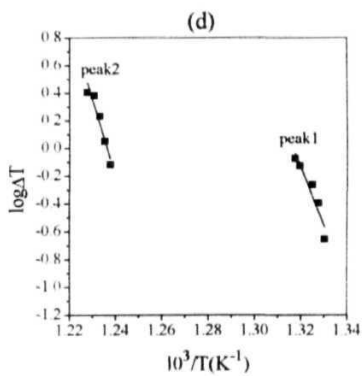
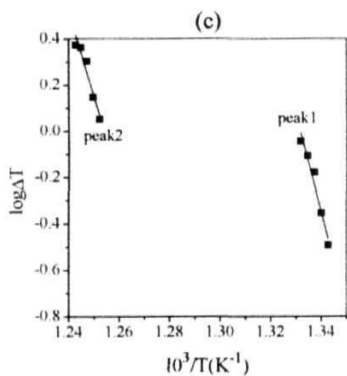
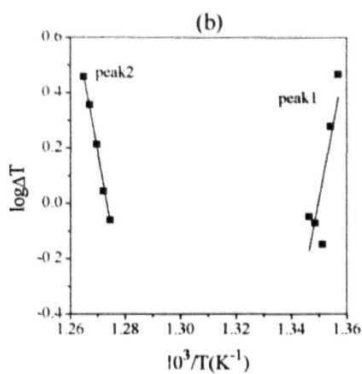
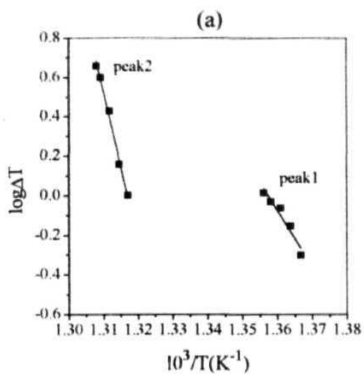


Fig 4 14(a)-(e) $\log \Delta T$ vs $10^3/T$ plots for the two exothermic peaks of all the five samples ($x=0-4$) respectively

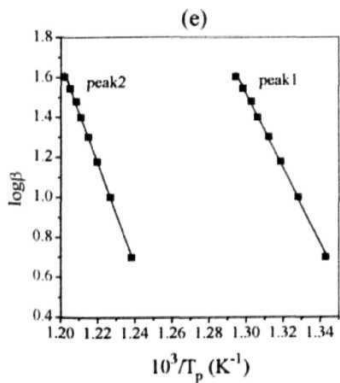
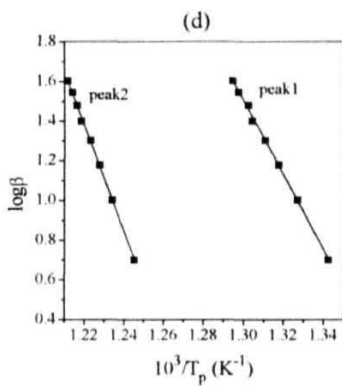
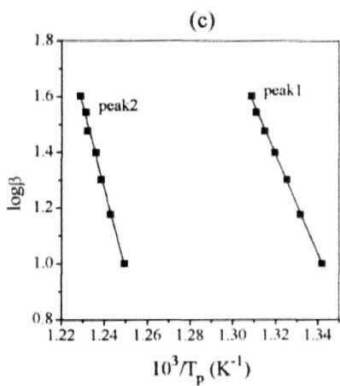
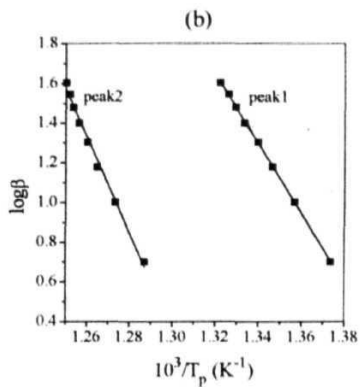
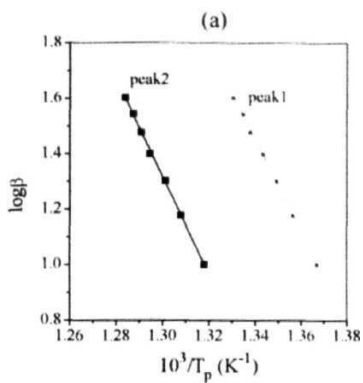


Fig 4 15(a)-(e) $\log \beta$ vs $10^3/T$ plots for the two exothermic peaks of all the five samples ($x=0-4$) respectively

Table 4.7 Values of Avrami exponent for different Mo content, x, in amorphous **Fe₆₈Ni_{14-x}Mo_xSi₂B₁₆** alloys at different heating rates for the First crystallisation peak.

Heating rate (β) °K/min	Avrami Exponent (n)				
	x = 0	x = 1	x = 2	x = 3	
5	-	2.2	-	2.0	1.5
10	3.4	1.7	2.9	2.9	2.3
15	1.7	2.2	2.5	2.2	2.6
20	2.6	2.5	3.2	2.6	3.0
25	2.1	1.6	2.5	3.6	2.8
30	1.9	1.8	2.9	3.2	2.5
35	2.5	2.6	3.2	2.8	2.8
40	2.0	1.9	3.2	2.8	2.3

Table 4.8 Values of **Avrami** exponent for different Mo content, x, in amorphous **Fe₆₈Ni_{14-x}Mo₁Si₂B₁₆** alloys at different heating rates for the second crystallisation peak.

Heating rate (β) °K/min	Avrami Exponent (n)				
	x = 0	x = 1	x = 2	x = 3	
5	-	3.4	-	3.4	3.6
10	-	2.8	2.0	2.8	3.4
15	4.2	2.3	1.2	2.0	2.6
20	4.0	1.6	1.0	2.2	2.5
25	3.8	1.7	1.8	1.0	2.5
30	3.8	1.2	1.6	1.9	2.2
35	3.4	1.7	1.4	2.1	2.3
40	3.0	1.5	1.4	1.9	2.1

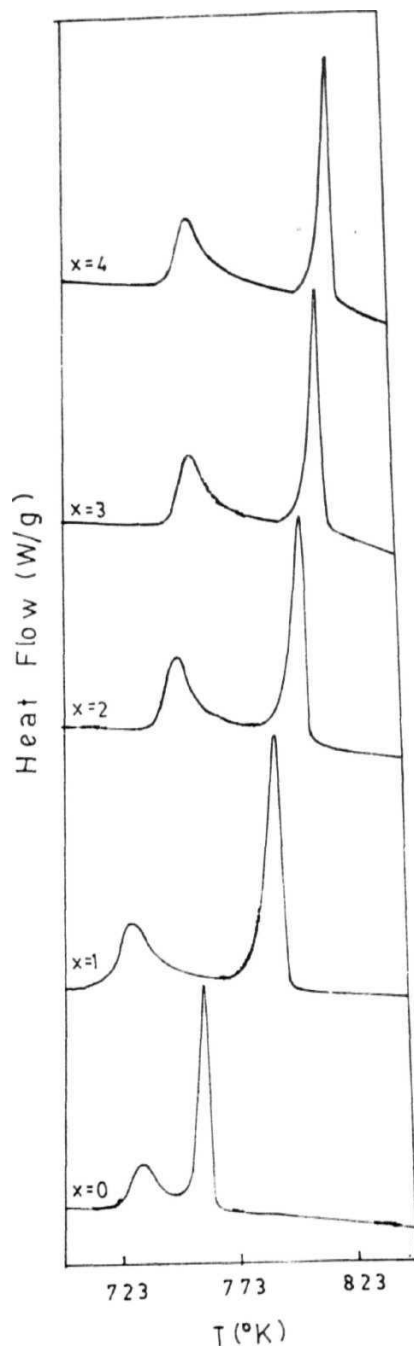


Fig. 4.16(a) The DSC thermograms of all the five samples ($x=0-4$) respectively at the heating rate of 10 K/min.

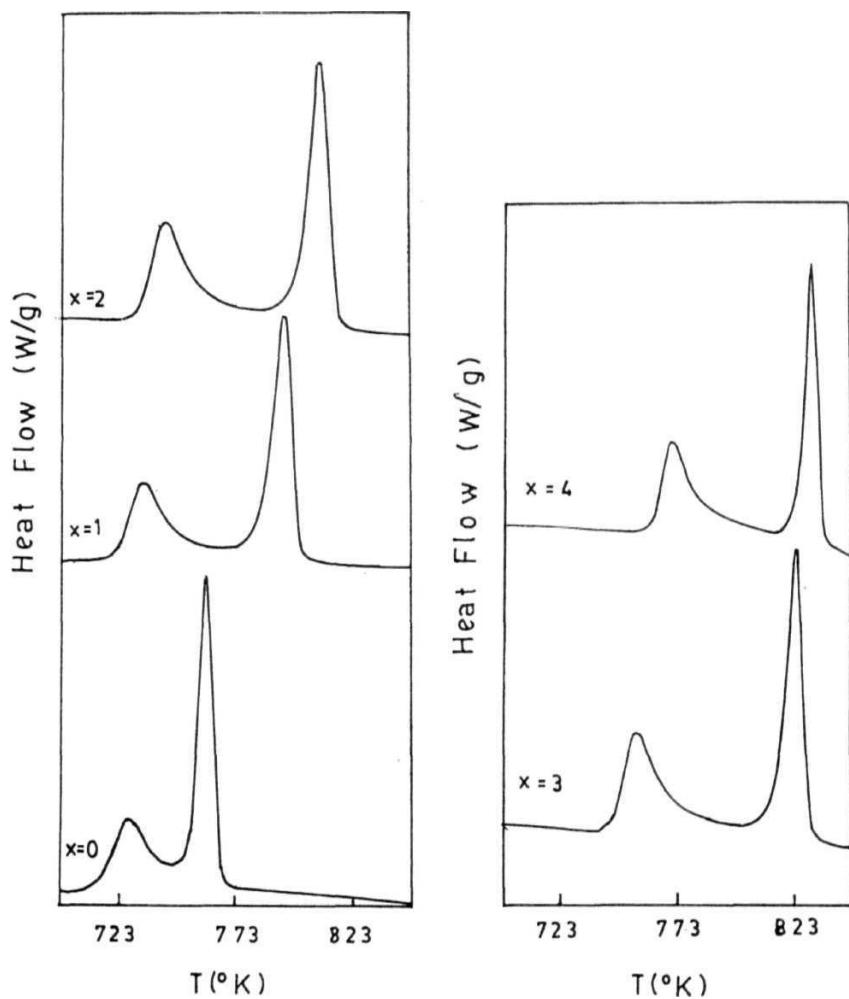


Fig. 4.16(b) The DSC **thermograms** of all the five samples ($x=0-4$) respectively at the heating rate of **15 K/min.**

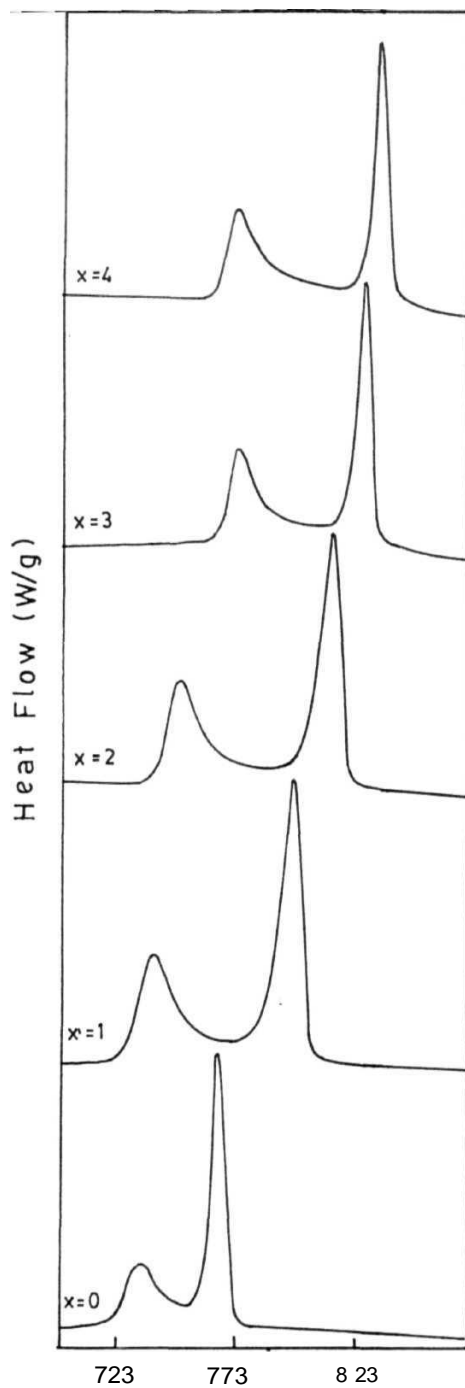


Fig. 4.16(c) The DSC thermograms of all the five samples ($x=0-4$) respectively at the heating rate of 20 K/min.

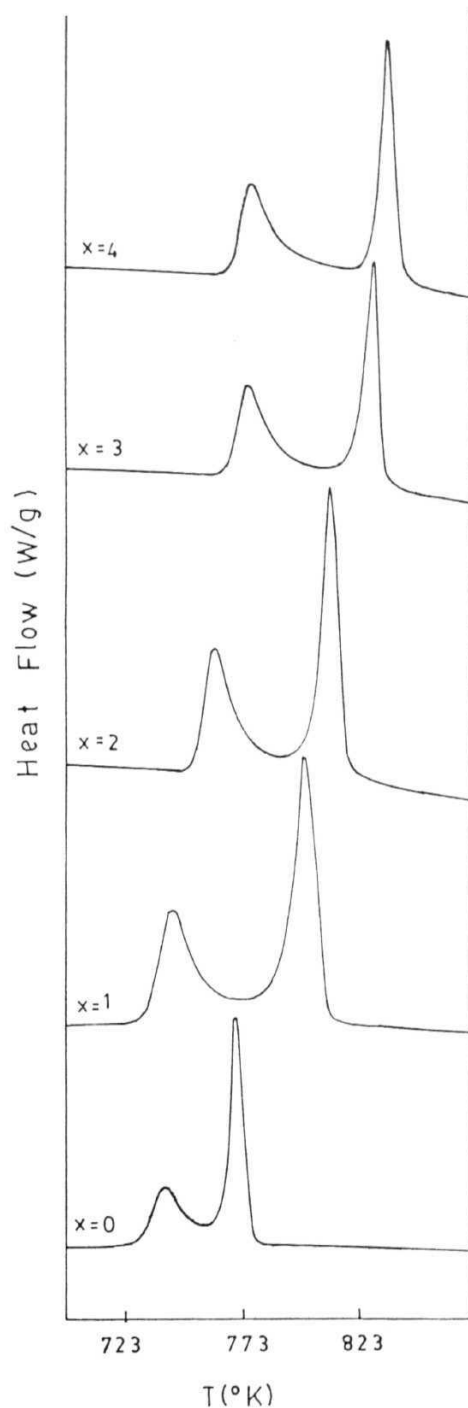


Fig. 4.16(d) The DSC thermograms of all the five samples ($x=0-4$) respectively at the heating rate of 25 K/min.

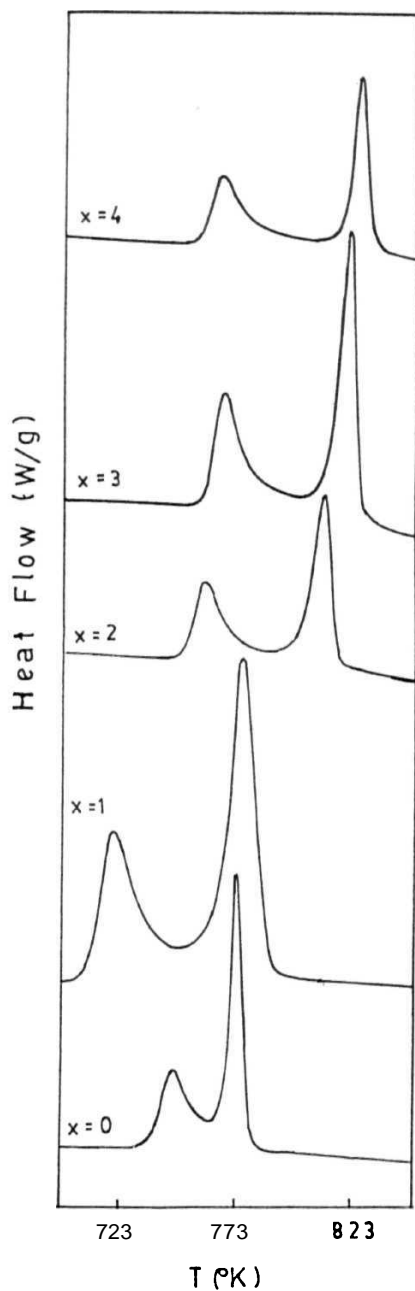


Fig. 4.16(e) The DSC thermograms of all the **five** samples (**$x=0-4$**) respectively at the heating rate of 30 K/min.

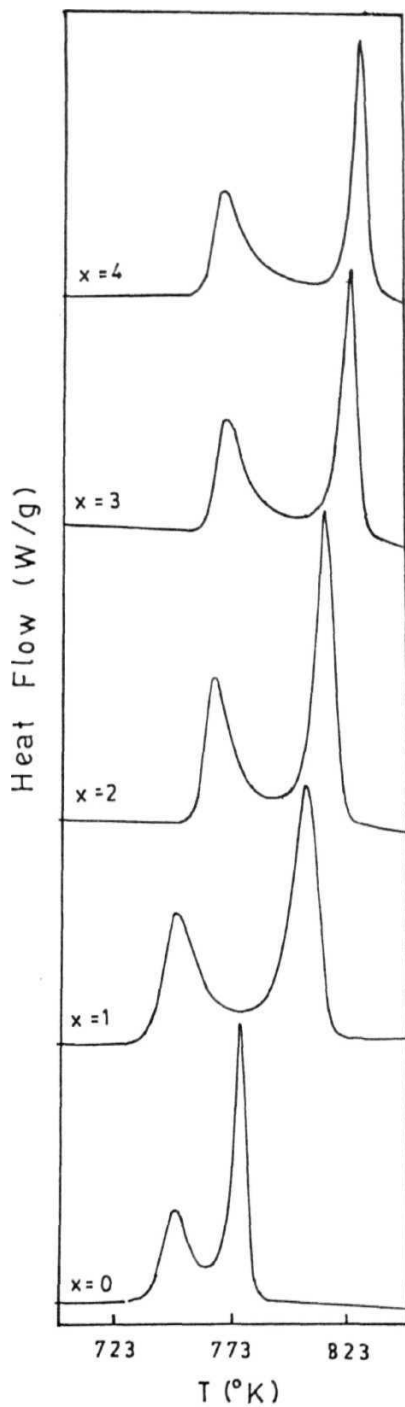


Fig. 4.16(f) The DSC thermograms of all the five samples ($x=0-4$) respectively at the heating rate of 35 K/min.

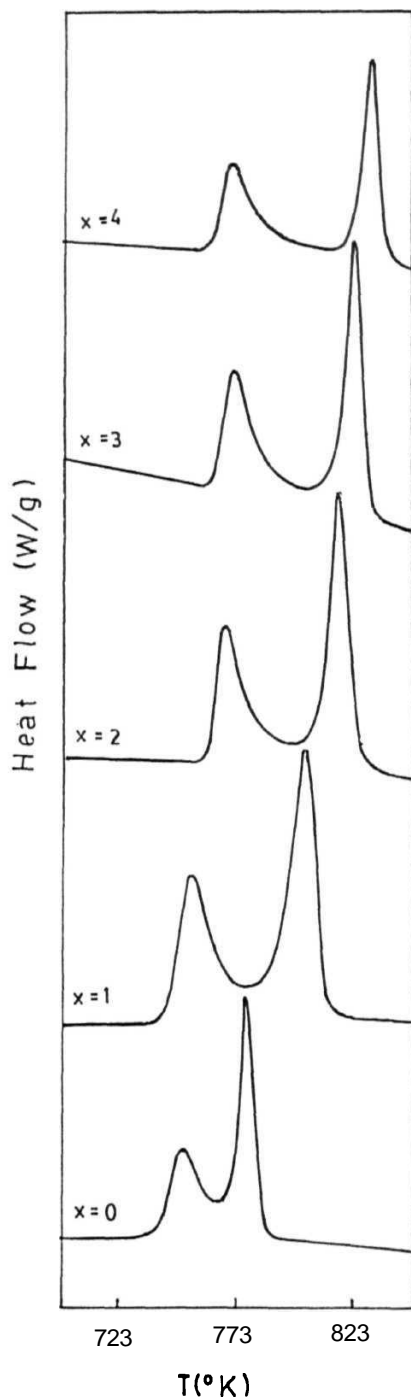


Fig. 4.16 (g) The DSC thermograms of all the five samples ($x=0-4$) respectively at the heating rate of 40 K/min.

E_{c2} first increases up to $x=2$ at% and then starts decreasing for $x>2$ at%

4.5 Discussion

The observation of the two **exotherms** in the DSC curves clearly indicates a two step crystallisation **viz.**, the primary crystallisation process resulting in the precipitation of **α -Fe**, followed by an eutectic process leading to the formation of various crystalline phases such as a-FeMo, **Fe_2B** , **Fe_2Mo** and **$Fe_{1-x}Ni_x$** alloy [1,45,86]. The two stage crystallisation observed in our studies is supported by the fact that for a variety of (Fe-Ni-Mo)B glasses a double crystallisation is observed [83,84]. Also this is a common observation made earlier in Fe-Ni-Mo-B (2826MB) glasses [44,85]. The presence of large percentage of iron atoms (**$\sim 68\%$**) in these metastable materials is responsible for these features of kinetics, which are distinctly different from systems such as **$a-Ni_{76}Si_6B_{18}$** [87] and **$a-Zr_{33}Ni_{67}$** [72] where single step polymorphous crystallisation **occurs**. Similar observation of two stage crystallisation process is made in several Fe-Ni-B, Fe-Ni-Si-B and Fe-Si-B systems by many researchers [2,18,44,72].

The first and second crystallisation processes observed in these glasses refer to primary and eutectic crystallisations respectively [88]. Temperature dependence of **Mössbauer** spectrum of similar samples also confirms the two step process, the first one being the slow precipitation of **α -iron** in the amorphous matrix followed by rapid formation of various crystallised products (a-FeMo, **Fe_2B** , **$(Fe-Mo)_2B$** , **$Fe_{1-x}Ni_x$** etc.) [86]. The broadness of the first peak in the DSC **thermograms** confirms the slow rate of the first step crystallisation, i.e., precipitation of a-Fe or **α -Fe/Mo**. This process is seen to be extending almost to the temperature at which the second and rapid eutectic crystallisation sets on. This overlap in turn depends upon the composition and the heating rate. As a matter of fact, this precipitation of a-Fe, when annealed close to but lower than the **T_{p1}** , is responsible for the better high frequency properties of these glassy alloys [89].

From Figs. 4.16(a)-4.16(g), it is clear that the values of the peak temperatures **T_{p1}** and **T_{p2}** for the two exotherms increase with the increasing Mo **content**. This shows that increase in Mo concentration results in improved thermal stability of these alloys. It has been reported by **Kemeny et al** [90] that the increase in crystallisation

temperature is related with the differences in binding energies, which influence thermal stability by changing atomic **mobility**. Mo, having a high melting point, seems to increase the strength of the chemical binding and thus can be expected to enhance the thermal stability [91]. This is supported by the results that the addition of Mo to the ternary Fe-Ni-B alloys leads to an increase in crystallisation temperatures [46,92]. Si content has a complex effect on crystallisation and causes different phases to form at higher temperatures of FeNiSiB system [93]. Alternately, the observation that can be drawn from Figs 4 16(a)-(g) is that the crystallisation temperature decreases with increasing Ni concentration. This is in good agreement with the observation reported on Fe-Ni-B alloys [94,95]. This shows that the thermal stability of Fe-Ni-B alloys decreases with increasing Ni content, which is similar to saying that addition of Mo partially for Ni improves thermal **stability**. The solid solubility of the added elements together with the metalloid concentration (Si, B) decides the type of crystallisation [40] in **2826MB**. Thermal stabilization takes place when 2% Mo ($\text{Fe}_{78}\text{Mo}_2\text{B}_{20}$) substituted to Fe in $\text{Fe}_{80}\text{B}_{20}$ for which Luborsky [96] reported a crystallisation temperature of **721 K** and an activation energy of **203 kJ/mol**, which suggests that the corresponding parameters in the present investigation are in the expected **range**. Moreover, the results are in good agreement with that of Babu [80] whose work is on a similar Fe-Ni-Mo-Si-B **system**. The system Fe-Ni-Mo-Si-B which has been developed by Hasegawa et al [89] has high frequency applications (≥ 100 kHz) comparable to or better than those of conventional crystalline materials which makes this system interesting to study for potential **applications**. The **effect** of Mo on such systems is discussed in [45]. Mo affects the crystallisation kinetics in a fashion very similar to that of **Si**. Presence of both Mo and Si in small quantities reduces both the nucleation and growth rates, an observation important to the design of technologically important metallic glasses. Similar results have been shown for $(\text{Fe}_{100-x}\text{Mo}_x)_{83}\text{B}_{12}\text{Si}_5$ [47] and $(\text{Fe}_{1-x}\text{Mo}_x)_{78}\text{Si}_9\text{B}_{13}$ [48]. Donald and Davies [97] have shown that among various refractory metals added to iron rich metallic **glasses**, Mo produces the largest effect in improving the thermal stability of these glasses. Since Mo has a high melting temperature and large size, it would reduce the atomic mobility leading to reduction in diffusion or even hopping for a given amount of thermal energy. Thus increase in crystallisation peak temperatures **T_{p1}** and **T_{p2}** with Mo concentration is quite

understandable Also, **Fig 4.1 l(c)** shows that the difference ($T_{p1}-T_{p2}$) increases with Mo content, as this makes the occurrence of the two crystallisation processes separated apart even at higher heating rates as shown in **Fig 4 16(g)**

For a given alloy, the peaks become narrower and taller with peak temperatures T_{p1} and T_{p2} shifting to higher values with the increasing heating rates as shown in **Figs 4.5-4.9** as expected and normally **observed** It also indicates that the maximum rate of crystallisation increases with heating **rates** However, the difference ($T_{p1}-T_{p2}$) decreases for all the samples except for $x=0$ as the heating rate is **increased** From the **Figs. 4 13(a) and 4 13(b)** it is clear that Kissinger plots obey well the linear relationship, from which it may be concluded that both the crystallisation steps are governed by first order **kinetics**

The activation energies for the first crystallisation process, E_{c1} increase with Mo content systematically which is shown in **Fig 4 1 l(d)** This once again establishes the fact that the content of Mo **at%** proportionally enhances the thermal **stability** The values of E_{c1} , the activation energy for the primary crystallisation are smaller than those of E_{c2} , the activation energy for the eutectic crystallisation, although not very much **different** The first crystallisation most probably is diffusion controlled Increase in E_{c1} with Mo content (**Fig 4 1 l(d)**) shows that even small concentration of Mo is effective in reducing the nucleation and growth rates of **microcrystallites** resulting in a higher crystallisation temperature and a higher activation **energy**

From **Fig 4 1 l(d)** it is seen that E_{c2} , the activation energy for the eutectic crystallisation increases with the Mo concentration upto 2 at% and then decreases for higher concentrations, and this is again in good agreement with the results obtained on a similar system [80] There are two possible explanations for this. The higher Mo concentration leads to easier formation of Mo based crystalline alloys/compounds, due to increased neighbourhood of Mo atoms to other **atoms** Hence they do not have to **migrate** to or hop longer distances to form **alloys/compounds** Hence, as Mo is increased beyond a certain limit (2 at%), relatively less thermal energy is needed for the second stage crystallisation The other possibility is that at higher concentrations some nanocrystallites are present in the amorphous matrix, **undetectable** by X-rays, which act as nucleation centers for formation of crystallized **products** One should also note

that with increase of Mo concentration, the ductility of these metallic glasses reduces, which is specially true for $x=4$ sample, and it is **very** difficult to make higher Mo concentration ($x>4$) samples although it is not impossible

In the above discussion, it should be kept in mind that the activation energies, E_{c1} and E_{c2} , consist of several contributions such as (1) activation energy for nucleation of particles (E_n), (2) activation energy for growth of particles (E_g) and (3) activation energy for diffusion of particles (E_d). The activation energy is related to these contributions through growth parameters, (Avrami exponent, n), the functional relationship of which depends upon the growth mechanism, parabolic or linear [77]. It will be of interest to extend the studies to transmission electron microscopy (TEM) to obtain further information on the individual contribution [1], which could not be done due to the unavailability of such a **facility**

The values of Avrami exponent, n for the present cases have been determined as explained in the **Sec 4.3** for each individual peak and at each scan rate and are shown in Tables (4.7) and (4.8), respectively, for all the **samples**. A survey of literature shows that n values show variations in isothermal experiments and in our case also the values of n , obtained by non-isothermal method show considerable deviations, $\approx (+0.3)$. It will, therefore, be more appropriate to refer to the range of the values **obtained**. In this method, for the first peak the values of n are found to be lying in the range $1.5 < n < 4.0$ for all the samples investigated, whereas for the second peak they are fairly close to 4 and above, for the sample $x=0$ in particular, and as low as **1.2** for the samples $x=1$ and $x=2$ (as shown in Tables (4.7) and **(4.8)**). The values are in agreement to a reasonably good extent with the values reported for similar type of alloys listed in Table **(4.9)**. Thus, it appears that the mechanism involved for the second step depends on both composition and the method through which the reaction is carried out. The wide variation in the values of n reported in the literature for apparently similar glassy metals may be due in part, to undetected surface crystallisation effects and/or multiple crystallisation processes occurring simultaneously during the **transformation**. Large values of n within the range of experimental error are indicative of complex mechanism in the crystallisation process involving simultaneous occurrence of nucleation and growth processes of different crystalline phases with nucleation rates increasing rapidly [28] and are also may be due to approximations

Table 4.9 Reported values of Effective activation energy for crystallisation **E_c** and **Avrami exponent**, n showing the effect of small additions of Ni and Mo to the FeBSi system. The estimated errors are **±0.2** eV in **E_c** and **±0.2** in n.

Composition	(eV)	n
Fe₇₅Ni₃B₂₀	2.6	2.2
Fe₇₈Ni₄B₁₆Si₂	2.6	2.3
Fe₇₈Mo₂B₂₀	3.6	3.5
Fe₇₈Mo₄B₁₆Si₂	3.6	2.2
Fe₇₆Ni₄Mo₂B₁₈	3.6	3.7
Fe₇₇Ni₂Mo₃B₁₈	4.0	3.2
Fe₇₇Ni₂Mo₃B₁₆Si₂	3.2	2.1
Fe₇₅Ni₄Mo₃B₁₆Si₂	3.7	2.0

made in **deriving** the **expressions** Low values of n can be interpreted due to **athermal** nucleation and anisotropic growth of crystals. Thus, the values of n obtained support the earlier conclusion based on activation energy that crystallisation mechanisms of the two steps are quite different

The range of n values obtained here allow us to select $b=3$ and $p=0.5$ and values of a are then either -1 or greater than unity indicating that in the present alloys the crystallisation process is effectively a three-dimensional ($b=3$) parabolic growth ($p=0.5$) with increasing nucleation rate ($a>1$)

4.6 Summary

The crystallisation kinetics of **$a\text{-Fe}_{68}\text{Ni}_{14-x}\text{Mo}_x\text{Si}_2\text{B}_{16}$** ($x=0,1,2,3$ and 4) alloys have been studied by continuous heating method. The alloys exhibit a two step crystallisation process, characterized by a primary crystallisation resulting in the precipitation of **α -iron**, followed by an eutectic process leading to the formation of various crystalline **phases**. The Kissinger method of calculation led to comparable values of activation energies E_{c1} ranging from 300-350 kJ/mol for the primary crystallisation and that of E_{c2} over a large range from 320-560 kJ/mol for the eutectic process. The lower values of E_{c1} when compared to those of E_{c2} are due to different crystallisation mechanisms involved in the two **steps**. In all the cases, both the crystallisation steps follow the Kissinger expression fairly well indicating first order **kinetics**. However, the first step shows a systematic increase in the activation energy with increasing Mo content, indicating that the Mo-at% present proportionally enhances thermal **stability**. The activation energy for the eutectic process, E_{c2} increases upto 2 Mo-at% and then starts decreasing indicating the fact that higher the Mo content, lesser is the thermal energy needed and hence lower is the activation energy in this crystallisation **step**. Also, there is a systematic increase in the peak temperatures T_{p1} and T_{p2} with increase of heating rate as well as Mo concentration, **enhancing** the thermal stability against **crystallisation**. These observations are also supported by the **Avrami** exponents determined, which are found to be in the range $1.5 \leq n \leq 4.0$ for the first step and $1.2 < n < 4.0$ or even greater than 4.0 for the second **step**. A comparison of n values for different alloys shows a compositional dependence. The

large deviation in n values for the second step of crystallisation have been attributed to complex processes with simultaneous occurrence of nucleation and growth processes of various crystalline phases **formed**. Further, primary process is very much governed by diffusion and the second step is influenced by **nucleation** and growth **processes**. The results show that Mo plays a significant role in crystallisation of these amorphous alloys, with respect to their kinetics as well as crystallisation **products**.

4.7 References

- 1 **U Köster** and **U Herald**, "*Glassy Metals I*", edited by H -J. Guntherodt and **H Beck**, Springer Verlag, (1981) Chap **10**
- 2 **M.G Scott**, *Amorphous Metallic Alloys*", edited by FE Luborsky, Butterworth & Co , London, (1983) Chap **10**
- 3 **F.E Luborsky**, "*Ferromagnetic materials*", Vol 1, edited by **E P Wohlfarth**, North-Holland, Amsterdam, (1980) Chap 6
- 4 **R W Cahn**, *Contemp. Phys.* , **21** (1980) **43**
- 5 **R W Cahn**, *J. de Phys*, 43 (1982) **C9**
6. **U Gonser**, *Atomic Energy Review suppl.no.* **1** (1981) **5**
7. **H Warlimont**, *Helv.Phys. Acta*,56 (1983) **281**
- 8 **K Masui**, **S Maruno** and **N Miyoshi**,*J. Non-Cryst. Solids*, 70 (1985) **263**
- 9 **K Masui**, **T Yamada** and **Y Hisamatsu**, *J. Metal Fin. Soc. Japan*, **31** (1981) **667**
10. **M A Marcus**,*J. Non-Cryst. Solids*, 30 (1979) **317**
- 11 **R A Dunlap**, **J E. Ball** and **K Dini**, *J. Mat. Sci. Lett.*, 4 (1985) **773**
12. **J. Cohnenero** and **J M Barandiaran**,*J. Non-Cryst. Solids*, 30 (1979) **263**
- 13 **M.R J Gibbs** and **HR Sinning**, *J. Mat. Sci.*, **20** (1985) **2517**.
14. **F.E. Luborsky** and **H.H Liebermann**, *Appl. Phys. Lett.*, 33 (1978) **233**
- 15 **K.H.J Buschow**,*J. Appl. Phys.*,52 (1981) **3319**
- 16 **J.C. Swartz**, **R Kossowsky**, **J J Haugh** and **R.F Krause**,*J. Appl.Phys.*, **52** (1981) **3324**
- 17 **F.L Cumbreira**, **H Miranda**, **A Conde**, **R Marquez** and **P Vigier**,*J. Mat. Sci.*, 17 (1982) **2677**
- 18 **M.D. Baro**, **S Surinach**, **M T Clavaguera-Mora** and **N Clavaguera**,*J. Non-Cryst. Solids*, **69** (1984) **105**
- 19 **M.V Susic**, *J. Mat. Sci. Lett.*, **5** (1986) **1251**
- 20 **T Soumura**, **S Saito**, **I Fuzimori**, **I Matsumaru** and **T Maeda**,*J. Mat. Sci. Lett.*, **5** (1986) **237**

- 21 P Duhaj, **D Barancok** and **A Ondrekha**,/. *Non-Cryst. Solids*, **21** (1976) **411**
- 22 J A Leake and **A L Greer**,/. *Non-Cryst. Solids*, **38-39** (1980) **735**
- 23 T **Kemeny**, **I Vincze** and **B Forgarrassy**, *Phys. Rev. B*, **20** (1979) **476**
- 24 **A.S. Schaafsma**, **H Snijders**, **F Vander woude**, **J M Drijver** and **S Radelaar**, *Phys. Rev. B*, **20** (1979) **4423**
- 25 **F L Cumbreira**, **M Millan**, **A Conde**, **R Marquez** and **P Vigier**,/. *Mat. Sci.*, **17** (1982) **861**
- 26 **U. Koster** and **P Weiss**,/. *Non-Cryst. Solids*, **17** (1975) **359**
- 27 **J Wolny**, **S Soltys**, **L Smardz**, **J M Dubois** and **A Calka**, *J. Non-Cryst. Solids*, **65** (1984) **409**
- 28 **W Minor**, **B Schonfeld**, **B Lebech**, **B Buras** and **W Dmowski**,/. *Mat. Sci.*, **22** (1987) **4144**
- 29 **H S Chen**,/. *Non-Cryst. Solids*, **27** (1978) **257**
- 30 **T Ozawa**, *Polymer* **12** (1971) **150**
- 31 **J. Sestak**, *Phys. Chem. Classes*, **6** (1974) **137**
- 32 **D D Thornburg** and **R.I. Johnson**, *J. Non-Cryst. Solids*, **17** (1975) **2**
- 33 **J Briggs** and **T.G Carruthers**, *Phys. Chem. Classes*, **2** (1976) **30**
- 34 **N. Claveguera**,/. *Non-Cryst. Solids*, **22** (1976) **23**
- 35 **K. Narita**, **H Fukanaga**, **J Yamasaki** and **K Hara**, *J. Magn. & Magn. Mater.*, **19** (1980) **145**
- 36 **N. Decristofaro**, **A Frielich** and **G.E Fish**, *J. Mat. Sci.*, **17** (1982) **236**
- 37 **D.W. Henderson**, *J. Non-Cryst. Solids*, **30** (1979) **301**
- 38 **D Akhtar**, *Scr. Metall.*, **20** (1986) **983**
- 39 **G V Rao**, *Ph. D. thesis*, University of Hyderabad, Hyderabad, India (1989)
- 40 **T. Nagarajan**, **U Chidambaram**, **S Asari**, **S. Srinivasan**, **V. Sridharam** and **A. Narayansamy** 'Proc. of 4th Int. Conf. on Rapidly Quenched Metals", Vol. I, edited by **T Masumoto** and **K Suzuki**, The Japan Inst of Metals, Sendai, Japan, (1981) **355**.

- 41 **S Ranganathan, J C Claus, R S Tiwari and M.V Heimendahl**, "*Proc. of Conf. on Metallic Glasses: Science and Technology*", Vol II, edited by C Hargitai, **I Bakonyi** and **T Kemeny**, Central Res Inst of Physics, Budapest, Hungary, (1980) 327
- 42 **N.R Munirathnam**, *Ph.D. thesis*, University of Hyderabad, Hyderabad, India (1989)
- 43 **R V Muralidharan and P.K.K. Nayar**, *J. Mat. Sci. Lett.*, 10 (1991) 435
- 44 **C Antonione, L Battezzati, A Lucci, G Riontno and G Venturello**, *Scr. Me tali*, 12(1978) 1011.
45. **V.R.V. Ramanan and G.E. Fish**, *J. Appl. Phys.*, 53 (1982) 2273
- 46 **L. Battezzati, C Antonione and A Cossolo**, *Z Metallkde*, 73 (1982) 185
47. **C. Piotrowski and R S Finocchiario**, *Mat. Sci. & Engg. A*, **119** (1989) 239
- 48 **X.D. Liu, J.T Wang and B.Z Ding**, *J. Mat. Sci. Lett.*, 12 (1993) 1108
- 49 **V V Maslov and D ju Paderno**, Institute of Metal Physics, NASU, Ukraine- to be published
- 50 **J M Li, M.X Quan and Z Q Hi**, *Appl. Phys. Lett.*, 16 (1996) 2356
- 51 **H.E Kissinger**, *J. Res. Natl. Bur. Stand*, 57(1956)217
- 52 **E S Watson, M J O'Neill, J Justin and N Brenner**, *Anal. Chem.*, 36 (1964) 1233.
- 53 **B G Bagley and E M Vogel**, *J. Non-Cryst. Solids*, 18 (1975) 29
- 54 **R.E Loehman and A J. Armsrong**, *J. Amer. Cer. Soc.*, 59 (1976) 527
- 55 **M.G Scott and P Ramachandra Rao**, *Mater. Sci. Engg.*, 29 (1977) 137
56. **J.J. Croat**, *J. Appl. Phys.*, 53 (1982) 6932
57. **A.L Greer**, *Acta.Met.*, 30 (1982) 171
- 58 **K.H.J Buschow**, *Acta. Met.*, 31 (1983) 155
59. **A.L Greer**, *Thermochim. Ada*, 42 (1980) 193
60. **A.L Greer**, *J. Mater. Sci.*, 17 (1982) 1117
61. **J.p. Larmagnac, J. Grenet and P Michon**, *J. Non-Cryst. Solids*, 45(1981) 157.

- 62 **R** Suzuki, K Shibue, K Osamura, **P.H** Shingu and Y Murakami, *J. Mat. Sci. Lett.*, 1(1982) **127**
- 63 RW Cahn, "*Physical Metallurgy* ". edited by R W Cahn and **P Haasen**, North-Holland, Amsterdam, Chap 28
- 64 **W.W** Wendlandt, "*Thermal Methods of Analysis*", John Wiley & sons, New York, (1973) Chap **5**
- 65 DSC Standard Data Analysis - Version 2.0, **E I** du Pont Nemours & Co., **Inc.**, Wilmington, DE **19898**
- 66 H. Yinnon and D.R. **Uhlmann**, *J. Non-Cryst. Solids*. 54 (1983) 253
- 67 **P** Murray and J White, *Trans. Brit. Ceram. Soc.*, 48 (1949) **187**
68. **P** Murray and J White, *Trans. Brit. Ceram. Soc.*, 54 (1955) **204**
- 69 **F** Vaghan, *Clay Minerals Bull.*, 2 (1955) **265**
70. **N.F** Mott and E.A. Davis (**eds.**) "*Electronic Processes in Non-crystalline Materials*", Clarendon, Oxford, (1979)
- 71 Y Q Gao and W Wang, *J. Non-Cryst. Solids*, 81 (1986) **129**
- 72 **G.K** Dey, **E.G** Baburaj and **S** Banerjee, *J. Mater. Sci.*, 21 (1986) **117**
73. **R.P** Mathur and D Akhtar, *J. Mater. Sci.*, 22 (1987) 683
- 74 **C.H** Hwang, **S** Kang, **K** Cho and **K** Kawamura, *Scr. Metall.*, 19 (1985) **1405**
- 75 W A. Johnson and **R.F** Mehl, *Trans. AIME*, **135** (1939) **416**
76. **M** Avrami, *J. Chem. Phys.*, 7(1939) 1103, 8(1940)212,9(1941) 177.
77. S. Ranganathan and **M** Von **Heimendaul**, *J. Mat. Sci.*, 16 (1981) **2401**
- 78 J.W. Christian, "*The Theory of Transportation in Metals and Alloys*" **Part-I**, Pergamon Press, New York, (1975)
79. **M** Von **Heimendhal** and **G** Kuglstatter, *J. Mat. Sci.*, 16 (1981) **2405**.
- 80 **T.G.N.** Babu, *Ph. D. Thesis*, University of Hyderabad, Hyderabad, India (1988)
- 81 Marotta, **A** Buri and **F** Branda, *Thermochim. Acta.*, 40 (1980) **397**
82. R.L. Thakur and **S** Thiagarajan, "*Glass Ceram. Res. Inst. Bull.*", 15 (1968) 67.

- 83 **B** Bhanuprasad and **A.K** Bhatnagar, *Key Engg. Mats.*, 14 (1987) 333
- 84 **B** Bhanuprasad and **A K** Bhatnagar, *Key Engg. Mats.*, 15 (1987) 579
- 85 **V.S** Raja, Kishore and **S** Ranganathan, *Bull. Mat. Sci.*, 9 (1987) 207
- 86 **T.G N** Babu, **R** Jagannathan, **A K** Bhatnagar and **V R V** Ramanan, *Hyper. Int.*, 27 (1987) 293
- 87 **T Komatsu**, **Y Tanaka**, **R** Yokota and **K** Matusita, *J. Mat. Sci.*, 22 (1987) 2185
88. **U Köster**, **U** Herald, **H S** Hillenbrand and **I** Denis, *J. Mat. Sci.*, 15 (1980) 2125
- 89 **R** Hasegawa, **G.E** Fish and **V R V** Ramanan, "*Proc. of 4th Int. Conf. on Rapidly Quenched Metals*", Vol. I, edited by **T. Masumoto** and **K** Suzuki, The Japan **Inst** of Metals, Sendai, Japan, (1981) 49
- 90 **T Kemeny**, **I** Vincze, **J** Balogh, **L** Granasy, **B** Fogarass, **F** Hajdu and **E** Svab, "*Proc. of Conf. on Metallic Glasses, Science & Technology*", Vol. II, edited by **C** Hargitai, **I** Bakony and **T. Kemeny**, Central **Res Inst** of Physics, Budapest, Hungary, (1980) 231
91. **H.S.Chen** and **B.K** Park, *Acta Metall* 21 (1973) 395.
- 92 **H Hillman** and **H.R** Hilzinger, "*Proc. of 3rd Int. Conf. on Rapidly Quenched Metals*", Vol. I, edited by **B** Cantor, The Metals Society, London, (1978) 371
- 93 **Wu-Shin Chang**, **Shiao-jung Hu**, "*Proc. of 4th Int. Conf. on Rapidly Quenched Metals*", Vol. I, edited by **T** Masumoto and **K** Suzuki, The Japan **Inst** of Metals, Sendai, Japan, (1981) 703
94. **U** Mizutani, *Ph.D. thesis*, Nagoya University, Japan
- 95 **Z. Marohnic**, **E** Babic, **J Ivkov** and **A Hamzic**, "*Proc. of 3rd Int. Conf. on Rapidly Quenched Metals*", Vol. II, edited by **B** Cantor, The Metals Society, London, (1978) 149
96. **F.E** Luborsky, *Mat. Sci. Engg.*, 28(1977) 139.
97. **I.W.Donald** and **H.A** Davies, "*Proc. of 3rd Int. Conf. on Rapidly Quenched Metals*", Vol. I, edited by **B** Cantor, The Metals Society, London (1978) 273

Corrosion Studies

5.1 Introduction

The corrosion behaviour of amorphous metallic alloys is important property to understand their chemical stability against corrosive environment, which is specially important for glasses, considered them as potential candidates for technological **applications**. Especially Fe-based metallic glasses having remarkable **soft** magnetic properties, combined with high resistivity and improved thermal stability have opened up new possibilities of their use in high frequency (>100 kHz) applications, where conventional magnetic alloys cannot be used due to excessive eddy current losses, in addition to their use in transformer cores, tape heads and magnetic shielding commercially. However, the application of these alloys for the above purposes is viable only when their chemical stability is guaranteed. It may be noted that glasses of certain compositions have far superior corrosion resistance compared to that of their

crystalline counterparts [1,2] During the last two decades a great deal of effort has been made to characterize and understand the general corrosion behaviour of metallic glasses, in particular **TM-Metalloid** metallic glasses [1,3] which are considered to have applications in power transformers While trying to improve corrosion properties of Fe-based glasses, it has been observed that an addition of elements like Cr or Mo makes these glasses relatively more corrosion resistant Extensive studies in this direction have been made on Fe-Ni and Co based alloys with various combinations of several metal and metalloid **elements** In this regard, the glass **Fe₄₀Ni₁₈Mo₄B₁₈** [4] has been reported to have better magnetic properties and thermal stability over **Fe₄₀Ni₄₀P₁₄B₆** Further it is also found that substantial reduction in Ni with simultaneous addition of Si and a heat treatment can provide excellent properties. Thus **Fe₇₅Ni₄Mo₃B₁₆Si₂** and a series of alloys **Fe_{82-x-y}Ni_xMo_yB_{18-z}Si_z** [(0<x<12), (0<y<6) and (0<z<6)] show that when optimally heat treated provide an ac work loss of just 7-8 **W/kg**, exciting power of 13-14 **VA/kg**, effective permeability of 10⁴ at 50 kHz and at an induction of 0.1 T [5] From the above literature it becomes clear that Fe-base alloys with less Ni content and no P are preferred for magnetic **applications** Fe-Ni-Mo-B-Si metallic glasses seem to have electrical and magnetic properties suitable for high frequency applications [5], therefore a systematic investigation has been carried out to study the corrosion behaviour of the **Fe₈₈Ni_{14-x}Mo_xSi₂B₁₆** (x=0,1,2,3 and 4) metallic glass system, the details of which are presented and discussed in this **chapter**

Although strong influence of metalloids on the corrosion behaviour of metallic glasses has been noted [1,3] it is still not clear as to whether such effects are results of their glassy structure or metalloid **composition** However, glasses being metastable **thermodynamically** tend to crystallise into one or more stable crystalline phases with different compositions so that it is not clear whether the superior corrosion resistance of such glasses is due to their amorphous structure or due to their chemical homogeneity. It will be generally difficult to dissociate these two aspects. The experimental results have indicated that high degree of homogeneity, both compositional and structural, confer greatly improved corrosion resistance on the glassy alloys. Also from electrochemical point of view, absence of crystalline defects such as grain boundaries, dislocations etc. in these metallic glasses results in the

absence of local electrochemical potential difference and hence minimization of the corrosion **reactions**. In addition, rapid quenching from liquid state to prepare amorphous alloys prevents solid state diffusion during quenching which generally causes segregation, precipitation and thereby reduces the localized corrosion **attack**. Thus, high corrosion resistance of metallic glasses has been attributed mainly to the chemical homogeneity of the amorphous phase coupled with the absence of crystalline defects inherent in metallic glasses and it has been **further** attributed to the high protective quality, the uniformity and the rapid formation of a passive film on the glassy **substrate**. However, composition also plays an important role in the determination of their corrosion behaviour [6,7]. Thus, **further** understanding of the relative importance of the amorphous structure and elemental composition in the corrosion resistance of amorphous metallic alloys will be **useful**.

Much interest has been centered on the effects of different alloying elements like metalloids P, B, Si, C and metals like Cr, Mo, W, Nb **etc.**, on the corrosion resistance of Fe-based metallic glasses, due to their good soft magnetic **properties**. In particular, the effects of Phosphorous, P and Molybdenum, Mo (with or without Cr) on the promotion of stable passive films have been investigated by several authors [8-12]. The corrosion resistance of these glasses exposed to H_2SO_4 and HCl environments has been the object of many investigations, as these glasses show spontaneous passivation even in such aggressive environments. Therefore, amorphous alloys are suitable model systems to probe the influence of atomic structure and composition on the electrochemical interaction of alloys with their **environment**.

It is well known that addition of P in a metallic glass enhances its corrosion resistance [6]. The addition of Ni is considered to promote the formation of a passive film in the presence of Cr, thus providing good corrosion resistance [10]. In the absence of both these elements P and Cr, the corrosion resistance of these glasses significantly decreases. Hence it is thought worthwhile to examine the corrosion behaviour of Fe based metallic glasses free from P and Cr and having low Ni content, which are generally preferred for magnetic **applications**. Also, the role of Mo being a good corrosion resistant element, has been widely investigated in crystalline alloys [13-16]. Mo is found to reduce the critical and passivation current densities in several Cr-containing alloys. On the otherhand, FeMo binary alloys (not containing Cr) do not

passivate in HCl, though a limited degree of passivation can be achieved in H_2SO_4 [13] However, if P is one of the alloying elements of the glass, the passivation resulting from Mo, is found to be enhanced in HCl even in the absence of Cr

As already much work has been reported on the effect of addition of P and Cr, in the present investigation, glasses free from P and Cr have been chosen to understand the role of Mo Also, yet another advantage in studying the influence of Mo in these systems is that, in crystalline Fe-based alloys, as the solid solubility of Mo is less, addition of Mo beyond a critical limit will introduce additional phases resulting in the destruction of homogeneous single phase nature of these alloys The latter will also influence the corrosion behaviour of the alloys in addition to Mo *per se* where as in amorphous alloys addition of alloying elements in wider range is possible, without the destruction of the homogeneous single phase

Before discussing the results of the present investigation, an attempt has been made to explain some general concepts of corrosion theory

5.2 Corrosion Principles

Corrosion is defined as the destruction or deterioration of a material due to a chemical or an electrochemical reaction with its environment Corrosion behaviour of a material is mainly determined by its structure and composition There are several ways of classifying corrosion One method divides corrosion into low-temperature and high-temperature corrosion Electrochemical corrosion reactions are conveniently divided into Dry corrosion which is mainly concerned with the oxidation of a dry metal surface and Wet corrosion in which the reactions occur in an environment which, under normal conditions, is predominantly composed of water

The importance of corrosion studies is threefold

- (i) Economic factor which is the prime motive for much of the current research in corrosion
- (ii) Improved safety in the design of the operating equipment.
- (iii) Conservation of energy and resources

A corrosion engineer applies accumulated scientific knowledge in the choice of a material which in turn depends on many factors. Fig. 5 1 shows some of the

properties that determine the choice of a structural **material**. The factors on which Corrosion resistance/behaviour depends are schematically shown in **Fig 5.2**. Thermodynamics and electrochemistry are of great importance in understanding and controlling corrosion. **Thermodynamic** studies indicate the spontaneous direction of **reaction**. Thermodynamic calculations can determine whether or not corrosion is theoretically possible [17]. Since the rate of corrosion is of primary interest for engineering applications, electrochemical theory and concepts will be considered in greater detail in the later **sections**.

5.2.1 Corrosion Rate

Corrosion behaviour of a material is quantitatively expressed in terms of corrosion **rates**. Corrosion rates have been expressed in a variety of ways in the literature, such as percent weight loss, grams per square inch per hour and milligrams per square decimeter per day (**mdd**) and this is commonly used in English and American literature. A good corrosion rate expression should involve:

- (i) Familiar units
- (ii) **Easy** calculation with minimum opportunity for error
- (iii) Ready conversion to life in years
- (iv) Penetration (rate of penetration or thinning of a structural piece)
- (v) Whole numbers without cumbersome **decimals**

The parameters, which affect the corrosion rate of a material, can be broadly classified as:

- (a) Solution chemistry (Environmental): concentration, **pH**, temperature, velocity, conductivity, presence of foreign ions, aging of the medium, exposure period, type of exposure (alternate, partial, total submersion **etc.**), bacteria, microbes **etc**
- (b) Metallurgical: **microstructure**, grain orientation, texture, alloy composition and purity, presence of defects **etc**
- (c) **Mechanical** presence of stress (applied, residual and thermal), rate of application, type of stress (tensile, compression or cyclic), strain rate, notches, application of stress before or after exposure to medium **etc**

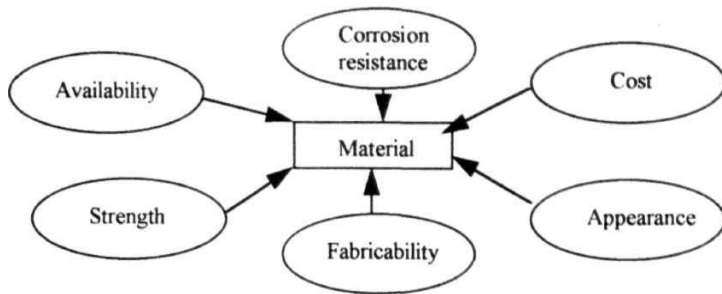


Fig 5.1 Factors affecting choice of an **engineering** material.

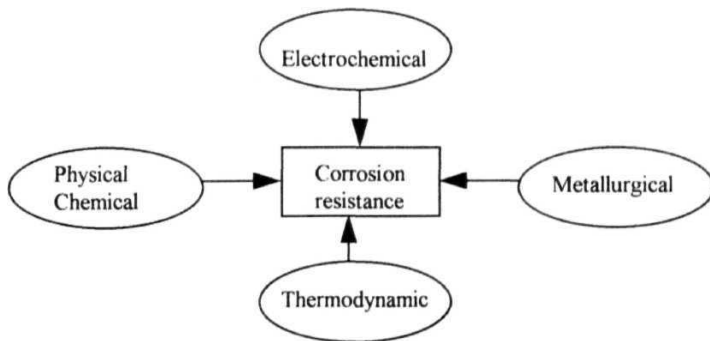


Fig 5.2 Factors affecting the corrosion resistance of a **metal**

Corrosion rates can be determined by the

- Non-electrochemical method and
- Electrochemical **method**

These are described in **Secs** 5.2 1(a) and 5.2 1(b) **below**

5.2.1 (a) Non-Electrochemical Method

Non-electrochemically, the rate of corrosion is determined by the conventional weight **loss/gain** technique [17] Using this technique, the loss of a metal due to corrosion is measured by exposing the metal specimen of known area to the corrosive environment for a particular period and finding the difference in weight before and after **exposure**

The expression 'mils per **year**' (**mpy**) is the most widely used way of expressing the corrosion rate Corrosion rate is calculated using the formula,

$$\text{Corrosion Rate (mpy)} = \frac{534W}{DAT}$$

where W = weight loss in **mg**

D = density of the specimen in **g/cm³**

A = Area of the specimen in **sq in**

T = exposure time in **hr**

Corrosion rate in mpy can also be calculated by using the **formula**

$$\text{mpy} = \frac{0.129 \times a \times i_{\text{corr}}}{n \times D}$$

where a = atomic weight

n = valence charge

i_{corr} = corrosion current density in **uA/cm²**

D = density in **g/cm³**

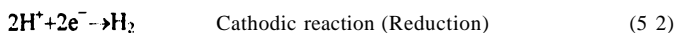
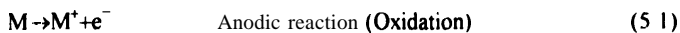
The weight loss method yields the average rate for the exposure period and is inherently inaccurate when it involves measuring small differences between initial and final weights of corroded **specimens**

The criteria for selection of the materials for construction in industries are based on corrosion rates and can be classified as:

Corrosion rate (mpy)	relative corrosion resistance of material
Less than 1	Outstanding
1-5	Excellent
5-20	Good
20-50	Fair
Greater than 50	Not suitable

5.2.1(b) Electrochemical Theory of Corrosion

The electrochemical **theory** of corrosion [17] states that corrosion proceeds by electrochemical reactions involving an anodic or oxidation reaction and a cathodic or reduction reaction, which for a given metal M in an acidic medium is given as



Eqs (5.1) and (5.2) are partial reactions and both of them must occur simultaneously and at the same rate on the metal surface, otherwise the metal would become charged which is impossible. This leads to the most basic principle of **corrosion** "During corrosion, the rate of oxidation equals the rate of **reduction**". So any reaction that can be divided into two or more partial reactions of oxidation and reduction is termed electrochemical. During corrosion, more than one oxidation and one reduction may **occur**. Since these reactions are mutually dependent, it is possible to reduce corrosion by reducing the rates of either of these **reactions**. The interpretation of corrosion processes by superimposing electrochemical partial processes was developed by Wagner and Traud [18], which is the well known 'Mixed potential theory'. The two hypotheses of this theory **are**

- I Any electrochemical reaction can be divided into two or more partial oxidation and reduction **reactions**

There can be no net accumulation of electric charge during the electrochemical **reaction**

In general the following are the commonly employed electrochemical **techniques** to measure corrosion rates.

(a) Polarisation and (b) ac Impedance Spectroscopy

The theoretical background and experimental procedures of the above methods to determine the corrosion rates are described **below**

(a) Polarisation Studies

During electrochemical corrosion the anode and cathode are not at their equilibrium potential at the surface of the **metal**. This deviation from **equilibrium** potential is called polarisation. Polarisation can be defined as the extent of potential **difference** or the displacement of electrode potential caused by net current flow to or from an electrode measured in volts, commonly known as over voltage or over potential represented by η . Polarisation is an extremely important corrosion parameter, which enables one to understand the corrosion rate processes.

There are three types of polarisation:

- 1 Activation polarisation. This refers to an electrochemical process that is controlled by the sequence of reaction taking place at the metal-electrolyte **interface**. In other words, activation polarisation is caused by a slow electrode reaction because the reaction at the electrode requires activation **energy**. Both anodic and cathodic reactions can be under activation polarisation.
- 2 Concentration **polarisation**. This is observed when the electrochemical reactions occur that are controlled by the diffusion in the electrolyte. This behaviour usually occurs when the concentration of reducible species in the environment is small e.g., corrosion in aerated salt **solutions**.
- 3 Resistance **polarisation**. This usually includes an **ohmic** potential drop through either a portion of the electrolyte surrounding the electrode or through a metal-reaction product film on the surface or both. Resistance polarisation may be written as

$$\eta_R = RI = \eta_i$$

where R = film resistance for electrode surface in ohms

I = current in amperes

γ = film resistance for 1 cm^2 area in **ohm/cm²**

i = current density in **amp/cm**

In electrochemical corrosion testing, two different approaches are **apparent**:

- 1 Control of current (i.e., corrosion rate) and
- 2 Control of potential (i.e., the oxidizing power) and measuring the resulting current

In each case the potential of an electrode in a conducting medium is changed by the **flow** of current in the electrolytic cell

The formation of the mixed potential of a corroding metal surface is illustrated in the **polarisation** diagram sometimes called Evans diagrams [19] The determination of these polarisation curves and the corrosion rate of a specimen can be done very quickly A complete curve can be determined in an hour in laboratory setup, whereas the conventional method to determine corrosion rate, i.e., by weight loss measurements takes several days or **weeks**

The schematic **Fig 5.3** illustrates some of the terminologies in a polarisation diagram, which is plotted potential vs log current density The solid lines represent the net anodic and cathodic currents for each reaction, while the dashed lines represent the forward and backward parts of each reaction The intersection of the dashed lines gives the open circuit corrosion potential, $E_{\text{corr}}(\phi_{\text{corr}})$, (when applied current density, $i_{\text{appl}}=0$) and the corrosion current density i_{corr} The intersection of the dashed lines gives the reversible potential for the reaction and its exchange current density The anodic polarisation curve is predominant at potentials more **+ve** (noble) than E_{corr} and cathodic polarisation curve is predominant at potentials more **-ve** (active) than E_{corr} β_a and β_c are the **Tafel** slopes in anodic and cathodic reactions and the intersection gives corrosion exchange current **density** The corrosion rate of the system is proportional to i_{corr} , which is determined by the intersection between the total reduction rate and the total oxidation rate Polarisation measurements have been used to

- (1) Study the effect of change of material composition or environment on corrosion rate,
- (2) Develop alloys with improved corrosion resistance,
- (3) Control quality during manufacture of a specific material of known behaviour,
- (4) Measure corrosion rate of structure which are not easily accessible like underground pipe line, tanks and large chemical plant components and

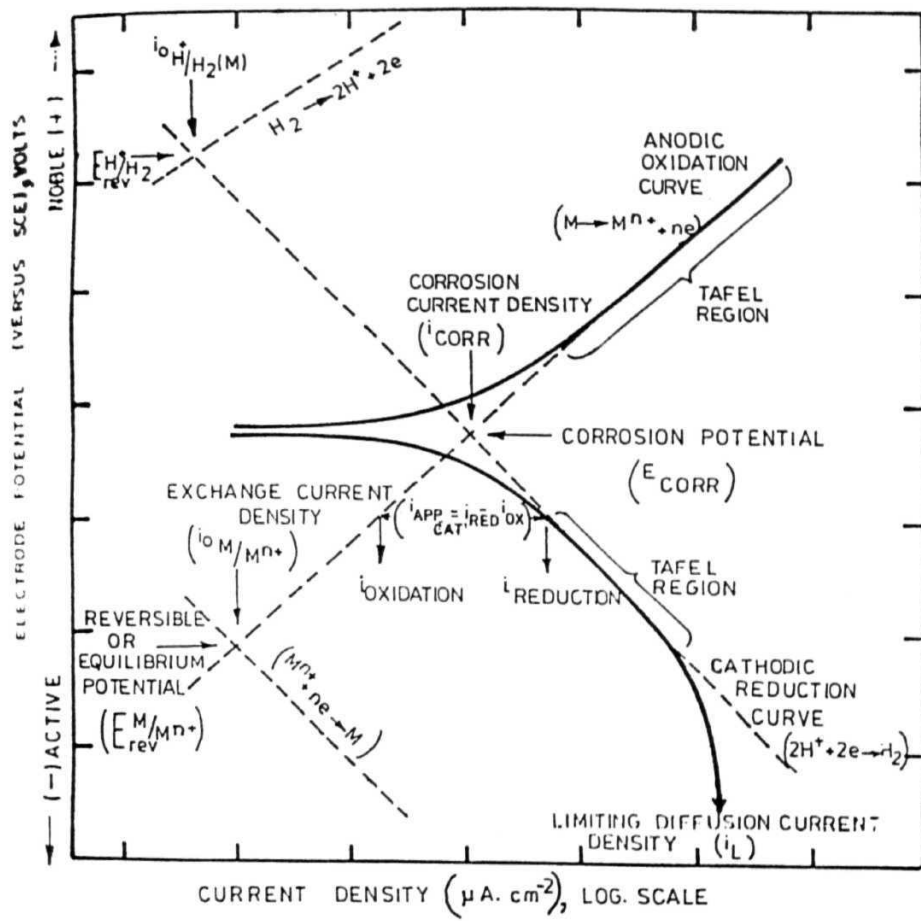


Fig. 5.3 Schematic illustration of a polarisation diagram with different terminologies.

- (S) Determine corrosion rates lesser than 0.1 mpy, which are important in pharmaceutical and food industries

The two different techniques in this are Tafel's extrapolation and Linear Polarisation methods

Tafel's extrapolation method

This method was used by Wagner and Traud [18] to verify the Mixed potential theory. A Tafel plot for a metal specimen can be obtained by polarising the specimen to about 300 mV anodically and cathodically from the corrosion potential, E_{corr} as shown in Fig 5.3. Extrapolation of the Tafel region in either cathodic or anodic polarisation curve to the corrosion potential will give corrosion current density i_{corr} , and it can be used to calculate corrosion rate.

The anodic and cathodic Tafel plots are described by the Tafel equations:

$$\eta = \beta \log(i/i_{corr}) \quad (5.3)$$

where η = over voltage, the difference between the potential of the specimen and the corrosion potential

β = Tafel constant

i_{corr} = corrosion current density in $\mu A/cm^2$

i - current density at over voltage η in $\mu A/cm^2$ or rate of oxidation or reduction in terms of current density at η .

Rearranging Eq (5.3) we get,

$$\eta = \beta (\log i - \log i_{corr}) \quad (5.4)$$

So a plot of η vs $\log i$ is a straight line with a slope β . Further, when $\eta = 0$ (E_{corr}), $\log(i/i_{corr}) = 0$ or $i = i_{corr}$

Tafel Constants, designated by β_a and β_c can be calculated for both the anodic and cathodic portion of the Tafel plot. The unit of Tafel constant is either mV/decade or V/decade. The disadvantages of Tafel plots are:

- The polarisation of test specimen by several hundred mV from the corrosion potential can disturb the system enough to distort further periodic measurements which might be made using the same specimen.
- Concentration polarisation and the IR drops can combine to reduce the linear

region to a point where extrapolation to i_{corr} is difficult

- It can sometimes happen that extrapolation of the anodic and cathodic linear **Tafel** region do not intersect at E_{corr}
- Though faster than weight loss methods, still several hours are required to obtain data for each polarisation **curve**. This may not be convenient in many cases, especially in plant **application**

Linear polarisation method

The disadvantages of the Tafel extrapolation method can be largely overcome by using the linear polarisation method, which is also known as polarisation resistance method. This method was developed during mid **1960s'** and has developed considerably [19]. The principle of this method is that within 10 **mV** more noble or more active than the corrosion potential, the applied current is a linear function of the electrode **potential**. This is shown in **Fig 5.4**. In this figure, the corrosion potential is used as an over voltage reference point and a plot of over voltage vs applied anodic and cathodic current, (i_{appl}) is shown on a linear **scale**. This plot represents the first 20 **mV** polarisation of the curve shown in **Fig 5.3**. The slope of the linear polarisation curve is related to the kinetic parameters of the system according to the following equation derived by Stern and Geary [20]

$$\frac{\Delta E}{\Delta i_{\text{appl}}} = \frac{1}{2.303 i_{\text{corr}}} \left[\frac{\beta_a \beta_c}{\beta_a + \beta_c} \right] \quad (55)$$

where ΔE is the potential shift from the corrosion potential E_{corr} , Δi_{appl} is the measured external current flowing due to this potential shift ΔE and β_a and β_c are the Tafel slopes of the anodic and cathodic reactions **respectively**

$\frac{\Delta E}{\Delta i_{\text{appl}}}$ is the slope of the linear polarisation plot and i_{corr} **is the** corrosion current

density. If the β values are known, i_{corr} , corrosion current density can be calculated using Eq. (5.5) which is a measure of the corrosion rate of the **systems**

The slope of the linear polarisation curve $\frac{\Delta E}{\Delta i_{\text{appl}}}$, is mainly controlled by i_{corr}

and is relatively insensitive to changes in β values as shown in Eq. (5.5). Therefore, it

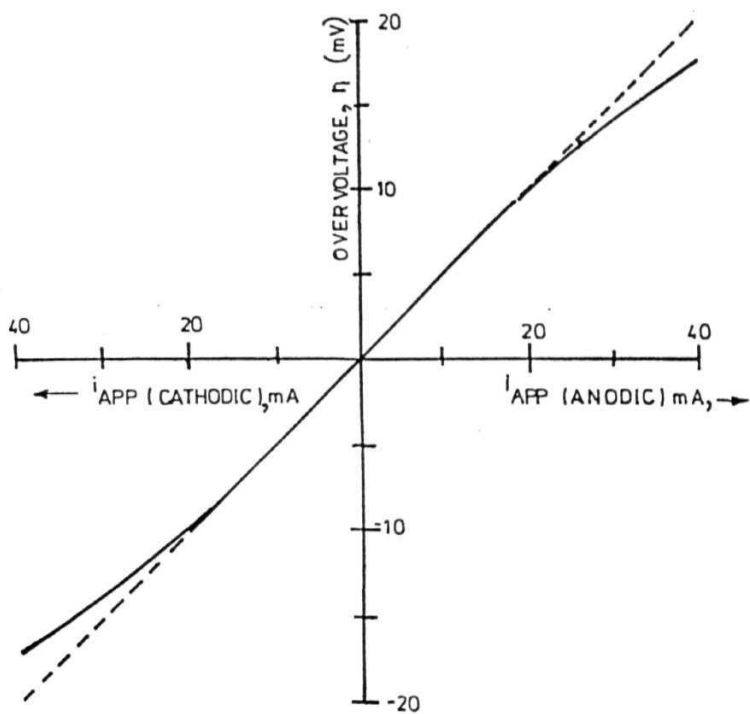


Fig. 5.4 Schematic representation of a linear polarisation diagram.

is possible to formulate reasonably accurate approximation of **Eq (5.5)**, assuming that anodic and cathodic **β** values of 0.12 V represent the average of all corrosion **systems**

Eq (5.5) may reduce to

$$\frac{\Delta E}{\Delta i_{\text{appl}}} = \frac{0.026}{i_{\text{corr}}} \quad (5.6)$$

Eq (5.6) can be used to calculate the corrosion resistance of a system without knowledge of its electrode kinetic **parameters**. Though the accuracy of this method may not be sufficient, **Eq (5.6)** provides a unique basis for the determination of relative corrosion rates rapidly.

(b) ac Impedance Spectroscopy method

Polarisation resistance method **often** gives erroneous results for systems in which the electrolyte resistance is very **high**. Impedance technique has been proved to be effective in these cases. ac impedance measurements, when applied to the study of electrochemical systems can provide a wealth of kinetic and mechanistic **information**. For this reason, the technique is becoming very popular for the study of **corrosion**.

ac impedance approach offers some distinct advantages over dc techniques:

- 1) ac impedance technique uses very small excitation amplitudes, generally in the range of 5 to 10 **mV** peak to **peak**. Excitation amplitudes of this magnitude cause only minimal perturbation of the electrochemical test system, thus reducing errors caused by the measurement technique **itself**.
- 2) Since ac impedance experiments can provide data on both electrode capacitance and charge transfer kinetics, the technique offers valuable mechanistic **information**.
- 3) Because the method does not involve a potential scan, measurements can be made in low conductivity solutions where dc techniques are subject to serious potential-control **errors**. In fact, ac impedance method can be used to determine the **uncompensated** resistance of an electrochemical **cell**.

Electrochemical systems can be examined with respect to their equivalent electrical **circuits**. A simple system could be represented by the circuit shown in **Fig 5.5**. **R_u** is the uncompensated resistance between the working electrode and the reference electrode. **R_p** is the polarization resistance at the **electrode/solution**

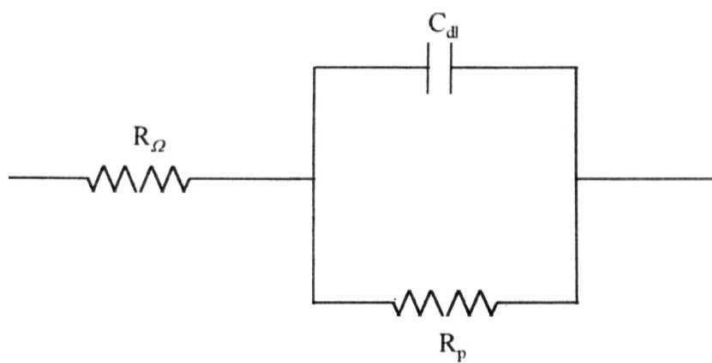


Fig 5 5 Equivalent electronic circuit for a simple electrochemical cell.

interface C_{dl} could represent the double layer capacitance at this **interface**. Knowledge of R_p permits the calculation of electrochemical reaction rates [21]. Capacitance measurements can provide information about **film** formation processes at the electrode.

The object of an ac impedance experiment may be to determine the values of the various elements in the equivalent circuit or simply to confirm that a given electrochemical system fits a particular equivalent-circuit **model**. This is done **experimentally** by studying the response of the electrochemical system to an ac excitation over a wide range of **frequencies**. The excitation can be applied as an ac voltage or an ac current. The measured response will be, respectively, an ac current or an ac voltage, **from** which the system impedance can be **calculated**. A **full** description of the electrochemical **system's** behaviour requires both in-phase and quadrature components of impedance at a number of frequencies over the desired **range**. These can be calculated from the real and imaginary components of the excitation and response waveforms using the following equation

$$Z_{TOTAL} = Z' + Z''j \quad (5.7)$$

where Z_{TOTAL} is the resultant ac impedance vector, Z' and Z'' **are** the real and imaginary parts of the impedance vector. Most electrochemical systems can be characterized by impedance data over a range of 0.001 to 10^4 Hz.

A variety of formats can be used to plot the impedance **data**. Each format offers specific advantages for revealing certain characteristics of a given test system. **Fig. 5.6** shows ac impedance profile for a simple electrochemical system in Nyquist form and that in the form of a Bode plot is shown in **Fig. 5.7** which is explained **below**.

The Nyquist plot

This form of the plot is also known as Cole-Cole plot or a complex impedance plane diagram. The imaginary component of impedance (Z'') is plotted against the real component of impedance (Z') at each excitation **frequency**. This plot could be used to compute the values of the uncompensated resistance between the working electrode and the reference electrode, R_{Ω} , the polarisation resistance at the **electrode/solution** interface, R_p , and double layer capacitance at this interface, C_{dl} .

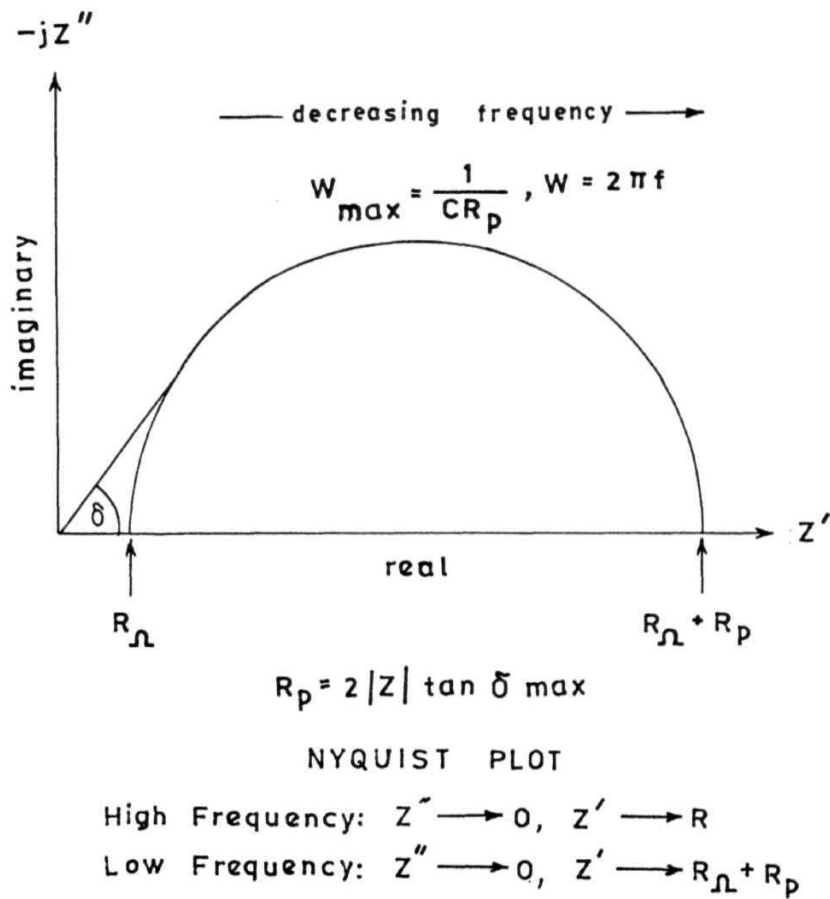


Fig. 5.6 Impedance profile for a simple electrochemical system in the form of Nyquist plot.

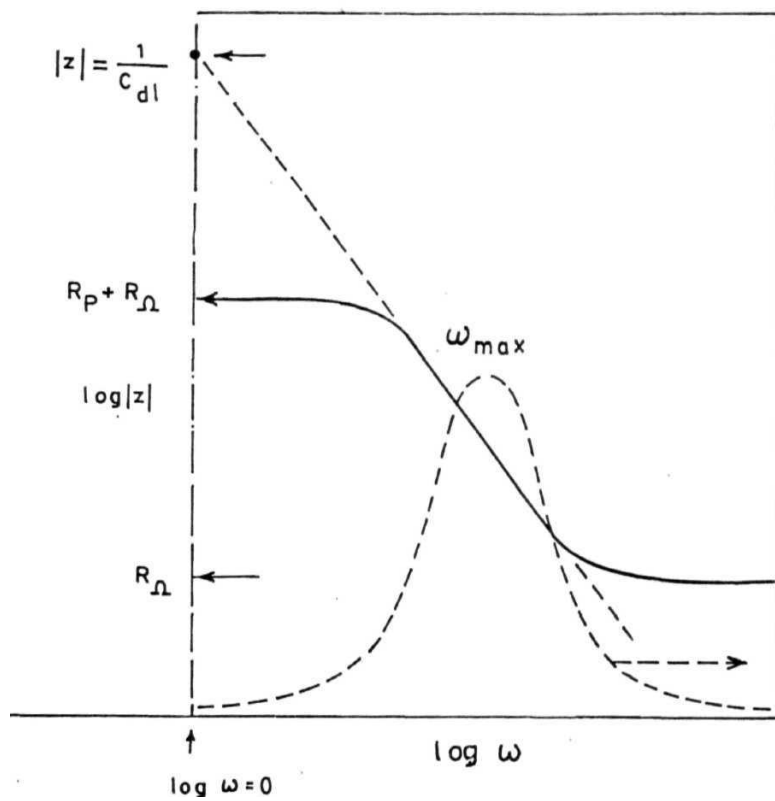


Fig. 5.7 **Impedance** profile for a simple electro-chemical system in the form of Bode plot.

Knowledge of R_p permits the calculation of electrochemical corrosion reaction **rates**

From the **Fig 5 6** it is clear that at high frequencies only the **uncompensated** resistance contributes to the real portion of impedance, while at very low frequencies the polarization resistance also contributes to this measurement. Once the excitation waveform becomes much faster than the charge-transfer rate, the polarization resistance (R_p) becomes transparent to the **technique**. An **ohmic** resistance (R_Ω) on the other hand will represent a constant impedance at all frequencies. This is consistent with the fact that R_p can also be measured by the dc technique while R_Ω **cannot**.

The Bode plot

The Bode plot is a useful alternative to the Nyquist plot to avoid longer measurement times associated with low frequency R_p determinations as this is a plot of $\log |Z|$ vs $\log \omega$. It allows a more effective extrapolation of data from higher **frequencies**. This form of the plot permits examination of the absolute impedance $|Z|$ and the phase shift θ as calculated by the following equation

$$|Z| = \sqrt{(Z')^2 + (Z'')^2} \quad \text{and} \quad \tan \theta = \frac{Z''}{Z'} \quad (58)$$

of the resultant waveform, each as a function of frequency. The $\log |Z|$ vs $\log \omega$ curve can yield values of R_p and R_Ω . At intermediate frequencies, the "break-point" of this curve should be a straight line with a slope of $-1/2$. Extrapolating this line to the $\log |Z|$ axis at $\omega = 1$ ($\log \omega = 0$) yields the value of C_{dl} from the relationship

$$Z = \frac{1}{C_{dl}} \quad (5.9)$$

5.3 Materials and Specimen Preparation

The samples in thin ribbon form of about 5 mm width prepared by single roller melt spinning technique and as received from Allied Signals, USA, were used in the present study. The two surfaces of the ribbons were not quite the **same**. One of these was shiny and another was not so shiny and is referred to as dull **surface**. X-ray diffraction patterns on both sides of these samples confirmed their amorphous nature as described earlier.

Specimen working electrodes were prepared in the following manner to study

selectively either the dull or the bright surface. 10x5 mm sample strips were taken, cleaned thoroughly with acetone and polished with alumina to remove surface oxides present, if any. These strips were soldered to a copper wire at one end to provide an electrical contact and subsequently the rough surface was fixed to a 20x5 mm Perspex disc using an epoxy **resin**. The bright side of the samples were thus exposed to the corrosive **medium**. In addition, barring an area (in the range 0.25-0.5 **cm²**), the remaining sample was insulated with the epoxy **resin**. Samples were washed in acetone, etched in **HCl**, rinsed in double distilled water and immersed in the corrosive medium, within 5 **min** of **preparation**.

Fig 5.8 shows the schematic diagram of a conventional electrochemical cell commonly used for corrosion measurements by electrochemical methods. It is a glass vessel similar to **ASTM G5 specification**. The cell consists of a 500 ml flat glass beaker with an acrylic lid on the **top**. Holes were suitably drilled to position Platinum counter electrode, specimen working electrode and a Saturated Calomel reference electrode (**SCE**). During the experiment the cell was maintained at room **temperature**. **1N H₂SO₄** and **1N HCl** acids which were the two corrosive media used, were prepared from their respective analytical reagent (**AR** grades) using distilled **water**. The corrosive medium was freely exposed to **atmosphere**.

5.4 Experimental Techniques

The measurements are usually made employing a **potentiostat**. This instrument automatically maintains the desired potential between the working and reference electrodes by passing an appropriate current between the working and counter electrodes. A basic circuit for a potentiostat is schematically shown in **Fig 5.9**. A potentiostat is a controller circuit that maintains the potential between the working and the reference electrodes equal to the value **E_{in}** shown in Fig. 5.9. If there is a small difference **E** volts, this is sensed, amplified and a current **I** flows. This process continues till the difference **AE** becomes **zero**. The direction of the current flow depends upon the sign of **ΔE**. Since the input impedance is very high, very low current flows through, and the reference electrode is not polarised. Using the potentiostat, polarisation may be accomplished either potentiostatically (in steps) or **potentiodynamically** (continuously).

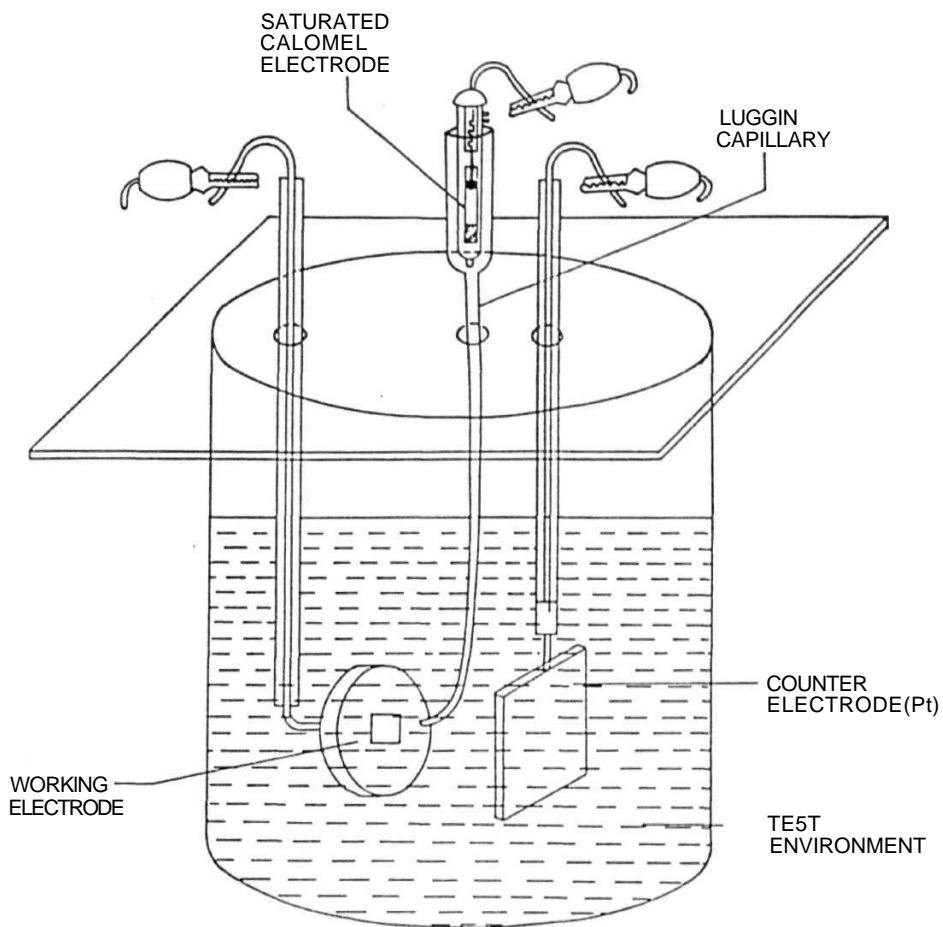


Fig. 5.8 Schematic diagram of a conventional electrochemical cell used.

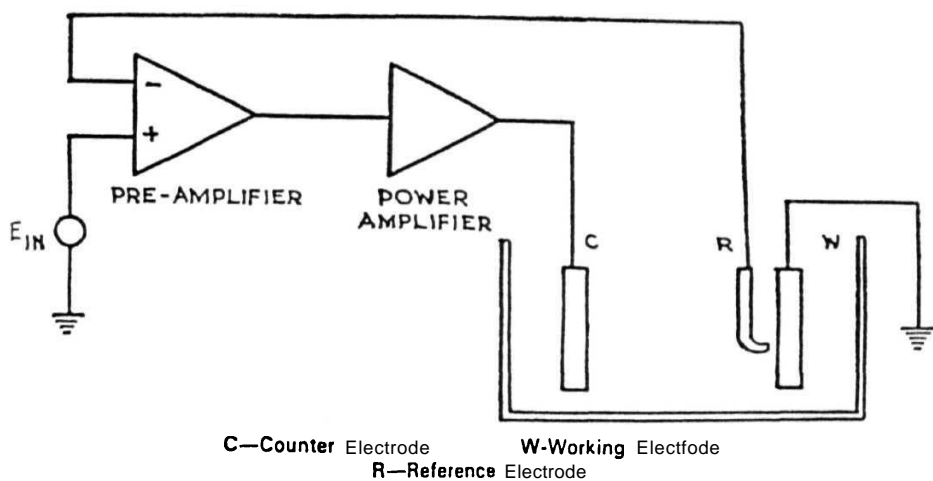


Fig. 5.9 Schematic of a basic circuit for a potentiostat.

Different models of Potentiostats are commercially available and in the present study, **potentiodynamic** polarisation measurements were carried out using an EG & G PARC potentiostat model 273 driven by **m352** software, to calculate different corrosion kinetic parameters. The electrode was cathodically polarised at 2V (SCE) for half a minute, thus facilitating the removal of surface oxides (air formed films) present, if **any**. The electrode was allowed to reach a stable corrosion potential, before potentiodynamic polarisation was carried **out**. Potentiodynamic scans were initiated in the cathodic region and then proceeded in the anodic direction at a scan rate of 1 mV/s. All the potentials were measured with respect to **SCE**. Polarisation data was plotted in the form of Evans plot i.e., potential (E) vs log current **density**.

Impedance spectra were taken by Electrochemical **Impedance** Spectroscopy (**EIS**) using a Solatron 1255 frequency response analyser, interfaced with EG & G PARC model 273 potentiostat and driven by **m388** software. Measurements were made in the frequency range 10^1 to 10^{-4} Hz with an ac excitation potential of 5 mV. **Impedance** spectra were analyzed using EQUIVCRT commercial software package supplied by Boukamp. **Impedance** spectra were plotted in the form of Nyquist plots.

5.5 Results and Discussion

Figs 5.10 and 5.11 show the polarisation behaviour of the metallic glasses under investigation, in 1N HCl and 1N H₂SO₄ solutions **respectively**. Notably the anodic curves in 1N HCl show a weak tendency for passivation, indicated by limits of passive regions a and b as shown in **Fig.5.10**, although the passive current densities exhibited by these alloys are high lying between 2.5×10^{-4} and 2.7×10^{-3} A/cm². On the contrary these alloys show an active dissolution without any revelation of passivity in H₂SO₄. Various kinetic parameters namely, corrosion potential (**E_{corr}**), corrosion current density (**i_{corr}**), anodic (**β_a**) and cathodic (**β_c**) **Tafel** slopes derived from these polarisation curves as explained earlier from **Fig 5.3** are summarized in Tables (5.1) and (5.2). Polarisation resistance, **R_p**, calculated from Stern-Geary Eq. (5.5) using the above parameters is also shown in the Tables (**5.1**) and (5.2) for both the corrosive media.

From the values of **i_{corr}** or **R_p** in Tables (5.1) and (5.2), it is clearly indicated

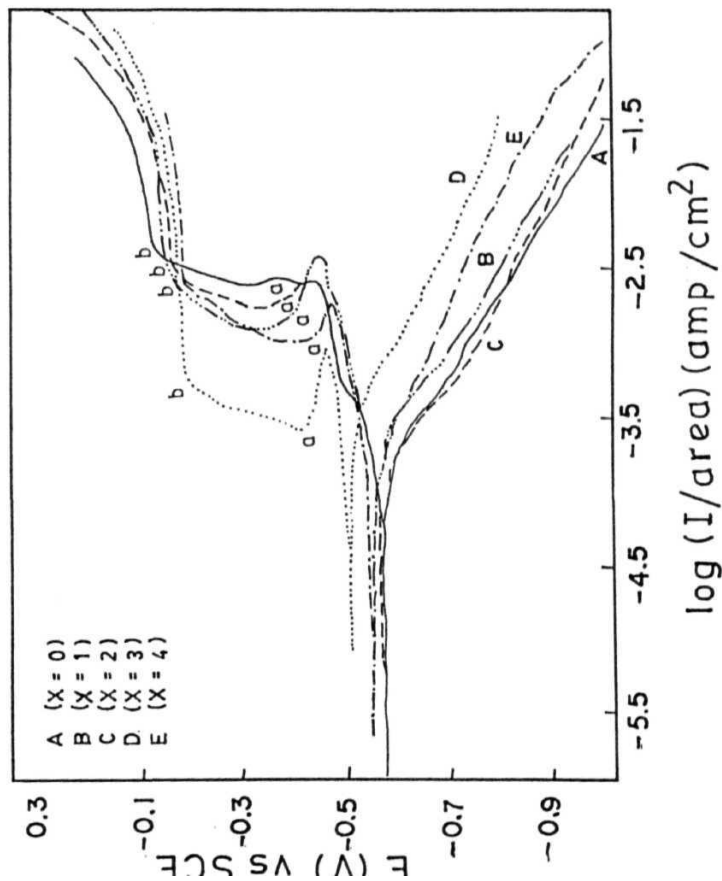


Fig. 5.10 Typical polarisation curves of $\text{Fe}_{68}\text{Ni}_{14-x}\text{Mo}_{0.8}\text{Si}_2\text{B}_{16}$ ($x=0, 1, 2, 3$ and 4) alloys in 1N HCl.

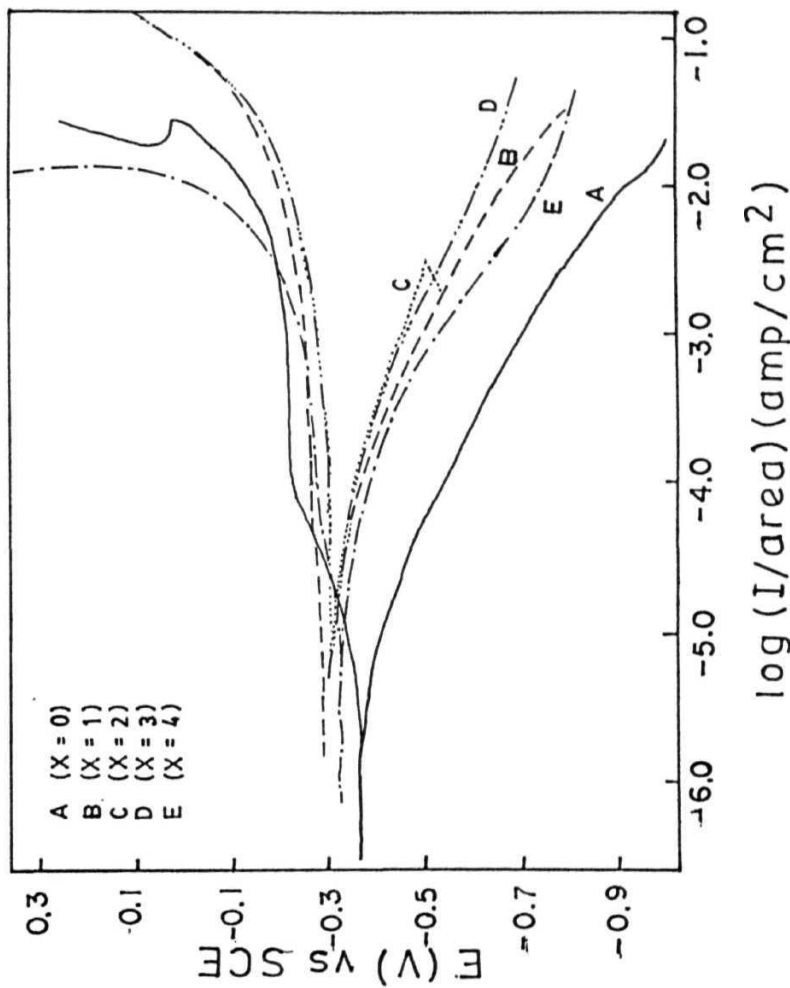


Fig. 5.11 Typical polarisation curves of $\text{Fe}_{68}\text{Ni}_{14-x}\text{Mo}_x\text{Si}_2\text{B}_{16}$ ($x=0, 1, 2, 3$ and 4) alloys in 1N H_2SO_4

Table 5.1 Kinetic parameters obtained from the polarisation curves in 1N HCl.

Sample (x)	E_{corr} mV(SCE)	i_{corr} $\mu\text{A}/\text{cm}^2$	β_a mV/decade	β_c mV/decade	R_p Ohm cm^2
0	-571	153	109	203	201
1	-540	226	71	223	103
2	-567	153	79	237	167
3	-506	271	31	154	41
4	-554	141	70	134	142

Table S.2 Kinetic parameters obtained from the polarisation curves in 1N H₂SO₄

Sample (x)	E_{corr} mV(SCE)	i_{corr} $\mu\text{A}/\text{cm}^2$	β_a mV/decade	β_c mV/decade	R_p Ohm cm^2
0	-357	13	125	176	2774
1	-290	50	25	103	154
2	-310	400	137	137	148
3	-317	200	169	169	264
4	-331	125	109	109	116

that these alloys exhibit very high corrosion rates in HCl as well as H_2SO_4 . The cathodic **Tafel** slope, β_c does not show any systematic variation though a few Mo containing alloys exhibit lower values than the base alloy without Mo. However, examination of the cathodic curves of **Figs 5 10** and **5 11** reveal that the cathodic reaction most likely the H_2 evolution has higher reaction rate with Mo addition than without Mo. This is inferred from the fact that most of the cathodic curves are shifted towards right **side**. Such a tendency is possible only when the exchange current density for the H^+/H equilibrium ($i_{0\text{H}}$) increases with Mo addition. In contrast to β_c there is a significant reduction in β_a due to Mo addition both in HCl and H_2SO_4 . These observations emphasize the fact that mere amorphous nature of the alloy is inadequate to provide resistance towards **corrosion**. The addition of Mo follows the Cr effect for improvement of corrosion resistance of Fe-P-C type of **alloys**. It is also noted that addition of Mo (≈ 5 at%) in HCl leads to a greater decrease in corrosion rate and anodic current density than the addition of an equal amount of Cr in HCl and leads to anodic passivation in 1N HCl [22,23]. The passivating capabilities of glassy metals arise when both Cr and Mo are present and addition of P increases this effect **remarkably**. Much of the work by Hashimoto, Naka, Masumoto et al [6-12,22,24] confirms these results. Also, it is known that addition of Ni is considered to promote passivation only in the presence of Cr, providing good corrosion resistance [10]. Presence of one or more passivating elements like Cr and P in the alloys is a necessary condition to extend the benefit of amorphous structure of alloys. Thus Fe-Cr-Mo-B in 6N HCl [24] $\text{Fe}_{80-x}\text{Mo}_x\text{P}_{13}\text{C}_7$ in 1N HCl [11] and $\text{Fe}_{82-x}\text{Mo}_x\text{C}_{18}$ [22] in 1N HCl have been reported to exhibit excellent corrosion **resistance**.

The present alloys fail to exhibit large corrosion resistance on two **accounts**. Firstly, the metalloids B and Si are inferior to P [61] in offering corrosion **resistance**. Secondly, unlike $\text{Fe}_{40}\text{Ni}_{38}\text{Mo}_4\text{B}_{18}$ and $\text{Fe}_{39}\text{Ni}_{39}\text{Mo}_4\text{Si}_6\text{B}_{12}$ [25] glasses, which possess good resistance to corrosion, the present alloys do not contain high Ni, which is relatively a nobler element than Fe. From the Table (5 1) there appears to be no systematic change in i_{corr} in HCl medium with the variation in x . A possible improvement in corrosion resistance due to the raise in Mo is off-set by the simultaneous reduction in Ni content of the alloy. With respect to H_2SO_4 solution a

gradual decrease in corrosion resistance occurs as x is increased from 0 to 2, which can be seen from the values of R_p given in Table (5.2). On further increasing x a steady raise in corrosion resistance is **noticed**. This indicates that at higher x values Mo has higher **beneficial** effect than Ni. **Indeed**, in a systematic study of Fe-Mo crystalline alloys, Ambrose [26] has shown that if the Mo content of Fe-Mo alloy exceeds 5 wt%, it offers good corrosion resistance, while at lower amounts Mo tends to be detrimental, agreeing with the present **trend**. Nevertheless, the effective role of Mo is decided by the complementary role played by other alloying elements. This becomes clear from the fact that in austenitic stainless steels even 2 wt% Mo brings out a significant improvement in corrosion resistance and passivity as has been shown by **AISI 304 and 316 ss** while even 5 wt% Mo brings out only a marginal change.

The electrochemical investigation of the present glassy alloys **further** enables an understanding of the role Mo plays in ferrous alloys towards passivity when Cr is not **present**. This has become possible now since homogeneous single phase nature is retained in spite of high Mo content, which would be difficult if crystalline Fe-based alloys are **chosen**. This is because in crystalline Fe based alloys the solubility of Mo is **low**. As a consequence additional phases would be formed which by itself will be a factor influencing corrosion behaviour over the intended compositional variation brought by Mo.

The passivation behaviour of these glasses is further examined using ac impedance **spectroscopy**. Impedance diagrams in the form of Nyquist plots obtained at E_{corr} in 1N HCl and 1N H_2SO_4 solutions are shown in **Fig. 5.12** and **Fig. 5.13** respectively and these exhibit two **semicircles**. As these alloys exhibit an apparent tendency to passivate in HCl their impedance behaviour were also studied at -456 mV and -200 mV (SCE) which are the limits of the passive region which are indicated by points a and b as shown in **Fig. 5.10**. The corresponding impedance profiles in the form of Nyquist plots respectively are brought out in **Fig. 5.14** and **Fig. 5.15**. In HCl barring a few cases existence of two overlapping capacitive loops are discernible in Nyquist plots obtained at E_{corr} , -456 mV and -200 mV (SCE). Nyquist plots for the glassy alloys obtained in H_2SO_4 differ from those obtained in HCl by displaying a capacitive loop followed by an inductive loop. The resistance values corresponding to first **and** second semicircles namely **R1** and **R2** are summarized in Tables (5.3) and

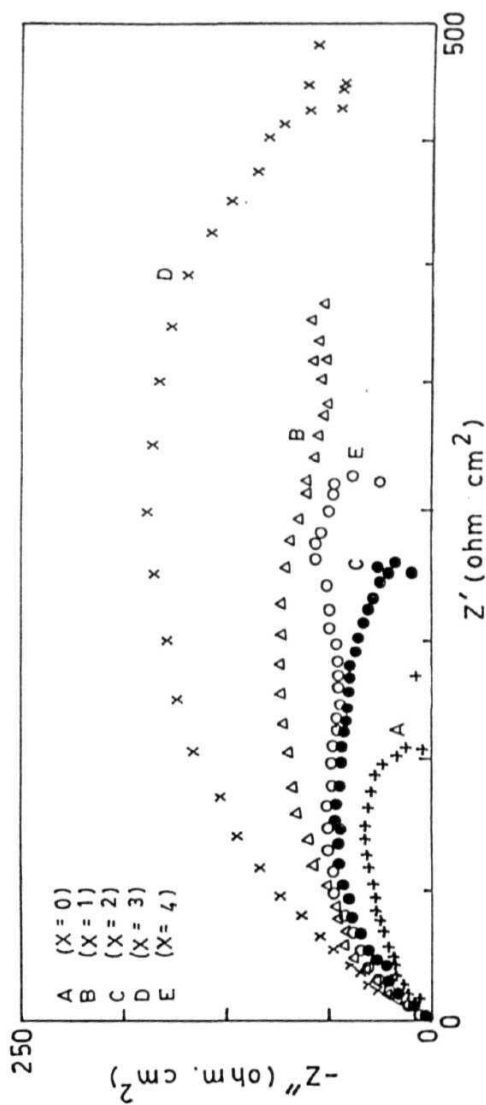


Fig. 5.12 Nyquist representation of impedance data at E_{corr} in 1N HCl.

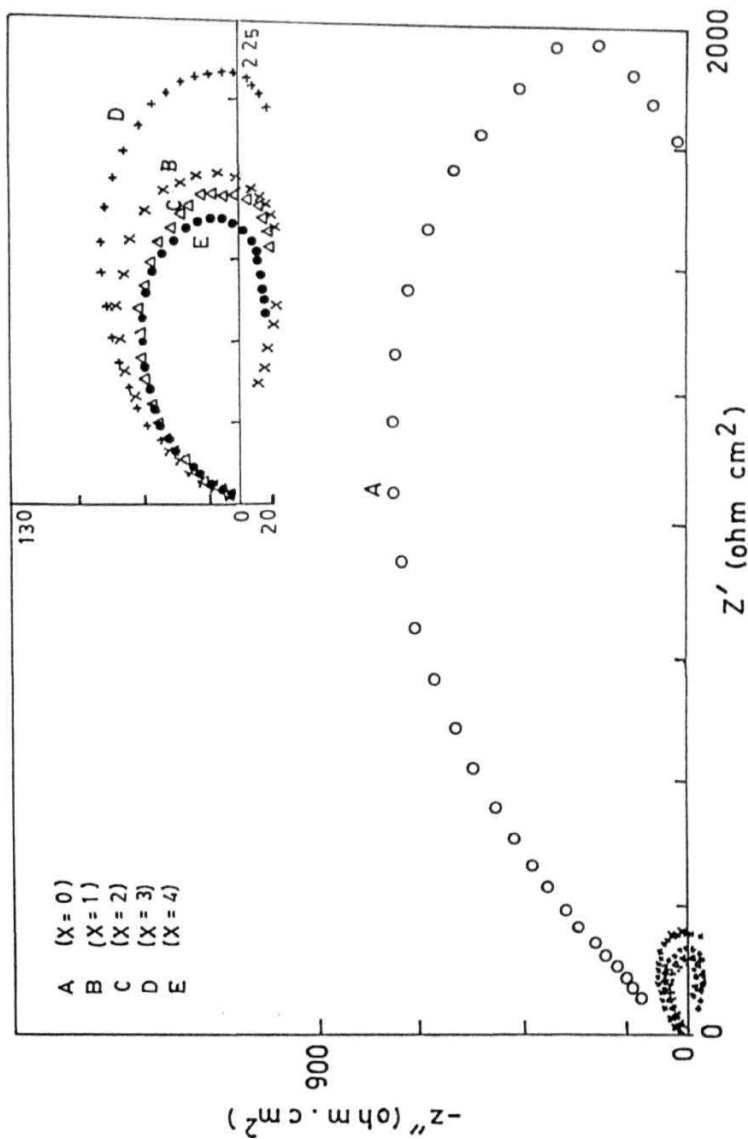


Fig. 5.13 Nyquist representation of impedance data at E_{corr} in 1N H_2SO_4 .

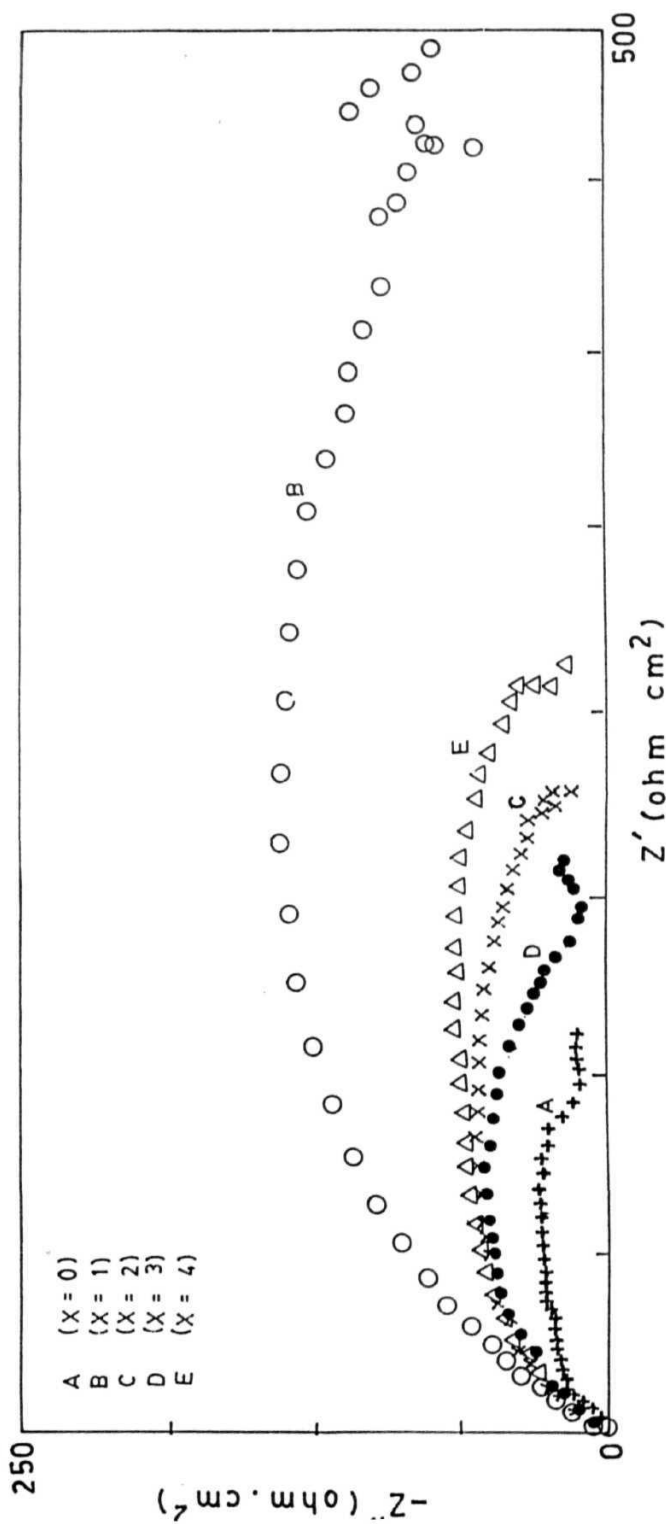


Fig. 5.14 Nyquist representation of impedance data at -456 mV (SCE) in 1N HCl.

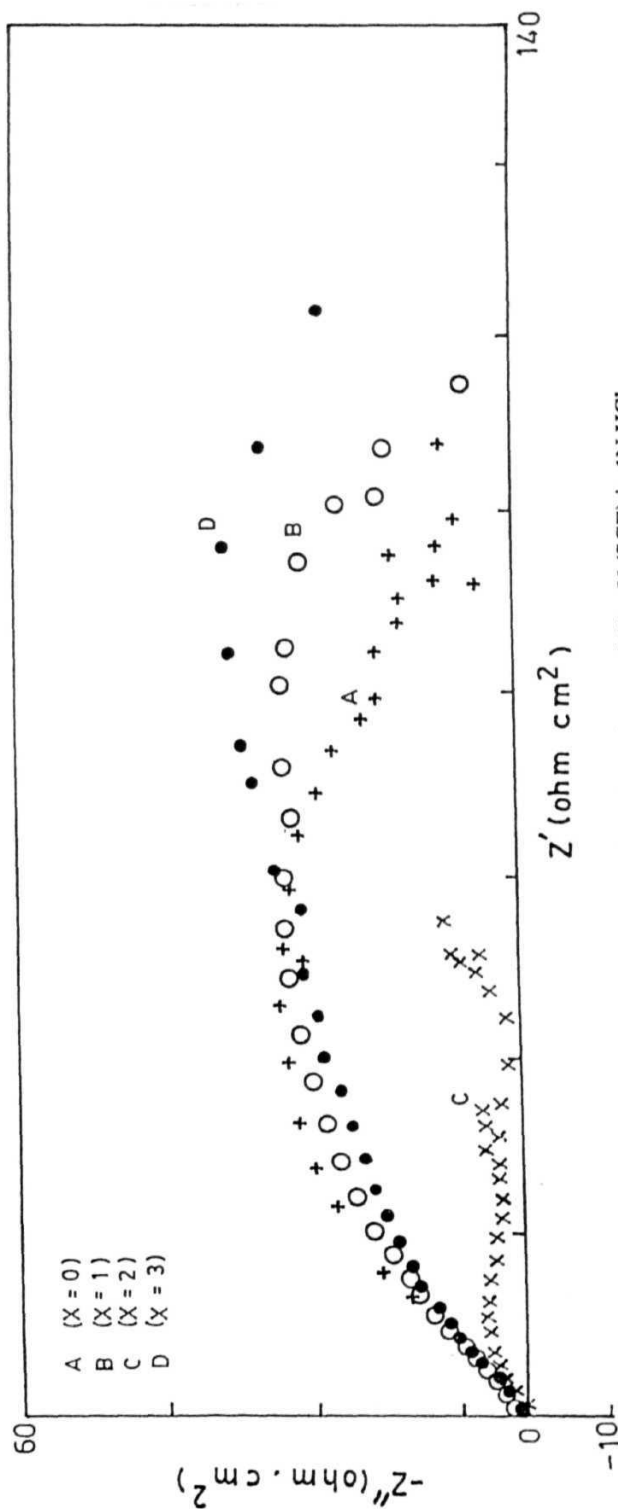


Fig. 5.15 Nyquist representation of impedance data at -200 mV (SCE) in 1N HCl.

Table 5.3 Variations in R1 and R2 values obtained from the impedance curves in 1N HCl medium.

Sample (x)	R1 Ohm. cm ²	R2 Ohm. cm ²	R _p =R1+R2 Ohm cm ²
0	101	41	141
1	325	95	420
2	195	33	228
3	485	-	485
4	184	105	289

Table 5.4 Variations in R1 and R2 values obtained from the impedance curves in 1N H₂SO₄ medium.

Sample (x)	R1 Ohm. cm ²	R2 Ohm. cm ²	R _p =R1+R2 Ohm.cm ²
0	2060	—	2060
1	145	-	145
2	148	49	197
3	212	59	271
4	92	48	140

(5 4) for **HCl** and **H₂SO₄** media **respectively** Tables (5 5) and (5 6) show the variations in **R₁** and **R₂** values obtained from the impedance spectra taken at fixed potentials of **-456 mV** and **200 mV** in **1N HCl** medium **respectively**

The appearance of high and low frequency capacitive loops has been attributed to dielectric relaxation of films and Faradaic processes, respectively, occurring on the electrode surface [27] With regards to inductive loops no definite processes can be **assigned** Literature, however, indicates that inductive loop in Nyquist representation occurs as a result of either of the following reasons namely, pitting [28] and increase in anionic defects over cationic defects [29]

The fact that the glassy alloys exhibit a high frequency capacitive loop in addition to a low frequency capacitive loop suggests that some sort of film exists on these alloys in HCl, further supporting polarisation **studies** Therefore it seems that **Cl⁻** ions promote formation of **corrosion/passive** film while **SO₄²⁻** ions do not favour such film **formation** In this context it is worthwhile to mention the well established fact that the presence of Mo in the film formed on several Mo containing stainless steels passivated in **H₂SO₄** medium only if **Cl⁻** are added to the solution [30] This suggests that **Cl⁻** differ from **SO₄²⁻** with respect to film formation Further more Ambrose [26] also proposed that Mo minimizes localized corrosion by the formation of salt film on Fe-Mo alloys This happens when the **MoO₄²⁻** concentration in the vicinity of the electrode surface is **high** The possibility of salt film formation seems to gain credence from the fact that the metallic glasses in HCl do not show any systematic variation in **R_p** value with **variation** in x value [Table (5 1)]. Even for a single composition, the values differ from one specimen to another to some **extent** This is because the nature and adherence of salt film formed on the alloy surface **will** depend more on local chemistry and surface nature than on alloy **chemistry** It is also to be noted that the resistance offered by these films at the passive potential (**200 mV**) is much lower than that obtained at **E_{corr}**

Mo seems to operate through a different mechanism to enhance passivity in **H₂SO₄** The ESCA work [30] shows that Mo enriches an alloy surface with high Ni or Cr when passivated in **H₂SO₄** The high Ni and or Cr on the surface in turn lower passive current and Mo *per se* do not contribute to **passivity** Viewed in this

Table 5.5 Variations in R1 and R2 values obtained from the impedance curves at a fixed potential of -456 mV in 1N HCl medium.

Sample (x)	R1 Ohm. cm ²	R2 Ohm. cm ²	R _p =R1+R2 Ohm cm'
0	77	40	117
1	452	-	452
2	190	37	227
3	170	-	170
4	185	83	268

Table 5.6 Variations in R1 and R2 values obtained from the impedance curves at a fixed potential of -200 mV in 1N HCl medium.

Sample (x)	R1 Ohm. cm ²	R2 Ohm. cm ²	R _p =R1+R2 Ohm cm ²
0	73	17	90
1	76	20	96
2	85	20	105
3	18	62	80
4	83	24	107

Table 5.7 Comparison of Polarisation resistance, R_p , values obtained from polarisation experiments and impedance experiments at E_{corr} in both the media.

Sample (x)	Polarisation		Impedance	
	1N HCl	1N H ₂ SO ₄	1N HCl	1N H ₂ SO ₄
0	201	2774	142	2060
1	103	154	420	145
2	67	148	228	148
3	41	264	485	212
4	12	116	289	92

perspective the present glasses fail to show high passivity because they do not have either high Ni content as in **Fe₃₉Ni₃₀Mo₄Si₆B₁₂** [25] **Cr** [24] or **P** [11] On the other hand absence of these elements results in a gradual increase in corrosion **rate** This is clear from the increase in **i_{corr}** values listed in Table (5.2) **and** the decrease in **R_p** values listed in Table (5 4) though not regularly

In the present study an attempt has been made to find out to what extent polarisation data correlate with that of impedance data using **R_p** as a parameter which is a measure of corrosion **resistance** Table (5 7) compares the **R_p** values obtained through Stern-Geary relationship with those obtained from impedance spectroscopy in both the media respectively at **E_{corr}** A good correlation seems to exist between the two data when the alloys undergo active dissolution (H₂SO₄) and not when they possess **passivity** As far as the comparison with respect to passivity is concerned, the values of **R_p** obtained from impedance curves correspond to the total contribution from the film and the charge transfer resistance The weak passivation noticed in the polarisation curve has been attributed to salt film formation as opposed to thin passive film obtained in Mo containing alloys. Thus it brings out a fact that **R_p** cannot be considered to be a factor indicating corrosion resistance of the alloy if the alloy passivates and more so if it forms salt film.

5.6 Conclusions

- 1 The present glassy alloys exhibit poor corrosion resistance both in **1N HCl** and **1N H₂SO₄ solutions**
- 2 With increase in Mo content the passivity of the alloy increases in **HCl**, though the passive current is quite high, while no such passivity is seen in **H₂SO₄**.
- 3 The mechanism of alloys' dissolution in presence of Mo in **HCl** seems to be different from that of **H₂SO₄**
- 4 A good correlation seems to exist between the polarisation resistance values obtained by impedance and polarisation techniques when the alloys undergo active dissolution and not when they possess **passivity**

5.7 References

- 1 **R B Diegle**, **N R Sorensen**, **T Tsuru** and **R M Latanision**, "*Treatise of Material Science and Technology*", vol. 23, *Corrosion : Aqueous Processes and Passive Films*", edited by **J Scully**, Academic Press, New York, (1983) **59**
- 2 **K Hashimoto** and **T Masumoto**, "*Ultra Rapid Quenching of Liquid Alloys*", "*Treatise of Material Science and Technology*", vol. 20, edited by **H. Herman**, Academic Press, New York, (1981) **291**
- 3 **K Hashimoto**, "*Amorphous Metallic Alloys*", edited by **F E Luborsky**, **Butterworth & Co** , London, (1983) **Chap 24**
- 4 **T.Egami**, **P J Flandens** and **C.D. Graham Jr.**, *AIP Conf.Proc. No.24*, edited by **C.D Graham Jr.**, **G.M. Lander** and **J J Rhyne**, (1975) **697**
- 5 **R.Hasegawa**, **G.E Fish** and **V.R.V. Ramanan**, "*Proc. of the 4th Int. Conf. on Rapidly Quenched Metals*", Vol II edited by **T. Masumoto** and **K. Suzuki**, Japan Institute of metals, Sendai, Japan, (1981) **929**
- 6 **M. Naka**, **K Hashimoto** and **T Masumoto**,/. *Non-Cryst. Solids*, 28 (1978) **403**
7. **M Naka**, **K Hashimoto** and **T Masumoto**,/. *Non-Cryst. Solids*, 31 (1979) **355**
8. **M Naka**, **K Hashimoto** **K Asami** and **T Masumoto**,/. *Physique*, 41 (1980) **862**
- 9 **K Hashimoto**, **K Asami**, **M Naka** and **T Masumoto**, *Corrsion Sci.*, 19 (1979) **857**.
- 10 **K Asami**, **K Hashimoto**, **T Masumoto** and **S Shimodaira**, *Corrosion Sci.*, 16 (1976) **71,909**.
- 11 **M. Naka**, **K Hashimoto** and **T Masumoto**,/. *Non-Cryst. Solids*, 29 (1978) **61**
- 12 **K Hashimoto**, **M Naka**, **K Asami** and **T Masumoto**, *Corrsion Sci.*, 19 (1979) **165**.
- 13 **K. Sugimoto** and **Y Sawada**, *Corrsion Sci.*, 17(1977) **425**
- 14 **M Moriya** and **M.B Ives**, *Corrsion*, 40 (1984) **62, 105**.
- 15 **W Yang**, **R Chang Ni**, **H Zhong Hua** and **A Pourbaix**, *Corrsion Sci.*, 24 (1984) **691**
- 16 **P I Marshall** and **G T. Burstein** *Corrsion Sci.*, 24 (1984) **463**
- 17 **M.G. Fontanna**, "*Corrosion Engineering*", McGraw Hill book company (1986) **Chaps 2, 9 & 10**

- 18 C Wagner and W Traud, *z. Elektrochem.*, **44**(1938) 391
- 19 S Evans and EL Koehler, *J. electrochem. Soc.*, **108** (1961) 509
- 20 M Stern and A Geary, *J. Electrochem. Soc.*, **104**(1957)56
- 21 D.D MacDonald, "*Transient Techniques in Electrochemistry*", Plenum press, New York, (1977).
- 22 M Naka, K Hashimoto, A Inoue and T Masumoto, *J. Non-Cryst. Solids*, **31** (1979) 347
- 23 M.D Archer, C.C Corke and B H Harji, *Electrochim. Acta*, **32** (1987) 13
- 24 K Asami, M. Naka, K Hashimoto and T. Masumoto, *J. Electrochem. Soc.*, **127** (1980) 2130
- 25 V.S. Raja, Kishore and S Ranganathan, *Corrosion*, **44** (1988) 263
- 26 J R. Ambrose, (*Corrosion*, **34** (1978) 27
- 27 M Seo and N Sato, *Corrosion paper no*, **138 NA CE**, New Orleans LA, (1989)
- 28 J Bessone, C Mayer, K Juttner and W.J Lorenz, *Electrochim. Acta*, **28** (1983) 171
- 29 I Epelboin, M Keddam and J (' Lestrade, *Transactions of Faraday Society*, **56** (1981) 264
- 30 R D Armstrong and K Edmondson, *Electrochim. Acta*, **18** (1973) 937

CHAPTER VI

Conclusions

Iron rich ferromagnetic metallic glass system $\text{Fe}_{68}\text{Ni}_{14-x}\text{Mo}_x\text{Si}_2\text{B}_{16}$ ($x=0,1,2,3$ and 4) has been investigated to study their electrical transport, magnetic, crystallisation and chemical properties using electrical resistivity, Mossbauer spectroscopy and magnetization using VSM and ac Lakeshore Susceptometer, Differential Scanning **Calorimetry** and Electrochemical corrosion techniques **viz** potentiodynamic polarisation and ac impedance spectroscopy **respectively**. Measurements of the different properties have been made in different temperature ranges as mentioned in each of the respective chapters.

Electrical resistivity measurements on $\text{Fe}_{68}\text{Ni}_{14-x}\text{Mo}_x\text{Si}_2\text{B}_{16}$ ($x=0,1,2$ and 3) alloys in the temperature range 10-300 K have been performed. From a comparison of our results with theoretical predictions and earlier reports, we come to the conclusion that both electron-ion potential scattering and **electron-magnon** scattering contribute to the

electrical **resistivity** ρ in the entire temperature range above T_{\min} , the structural contribution to the resistivity ρ_{str} dominates over the magnetic contribution ρ_{mag} for all the alloys studied. The $\rho_{\text{mag}}(T)$ is found to follow a quadratic temperature behaviour. All the samples showed a minimum in resistivity ρ_{\min} and the temperature (T_{\min}) at which resistivity is minimum, increases from 15 K for $x=0$ to 110 K for $x=3$. For the alloy with $x=3$ Mo at% a double minimum is observed with a very weak first minimum at around 10-15 K and the second minimum at 110 K. The resistivity ratio RR , below T_{\min} , showed similar linear behaviour with both $\ln T$ (scattering from two level states) and $-T^{1/2}$ (electron-electron or Coulomb interaction effects) though the slopes of the later are smaller and it is hard to say which one explains the resistivity behaviour well. The resistivity ratio RR above T_{\min} upto 150 K showed a quadratic temperature **dependence**. Above 100 K the temperature dependence of resistivity is slightly parabolic with a small and positive T^2 coefficient ($\sim 10^{-7}$), which gives magnetic contribution to resistivity, and it is negligibly small in our **samples**. At higher temperatures above 200 K, the temperature dependence of resistivity is found to be linear which indicates that it is purely structural contribution and the magnetic **contributions** from $T^{3/2} \sim 10^{-10}$ term is negligibly **small**. So, we can conclude that magnetic contribution from $T^{1/2}$ term can be ignored in comparison with that from T^2 term, or in other words the magnetic contribution comes from the T^2 term rather than from the $T^{3/2}$ **term**. The Debye temperature θ_D , for the alloys with $x=0-2$ are in the range 300-400 K. The Debye temperatures evaluated from these measurements are in good agreement with those of other ferromagnetic glasses and this supports the existence of magnetic contribution to resistivity in these **glasses**.

The absolute resistivity at RT, $\rho(RT)$, increase **monotonically** with increase in Mo concentration, x and the values lie in the range 95-135 $\mu\Omega\text{-cm}$ for $x=0-4$. As $\rho(RT)$ increases with increase of x from 0 to 3, the temperature coefficient of resistivity TCR at RT, $\alpha(RT)$ decreases from 2.4 to 0.4×10^{-4} and hence seems to follow Mooij **correlation**.

The **EEI** theory predicts that major contribution to resistivity arises from the diffusion channel which in turn predicts an additional term to conductivity. The diffusion

constant D which is a measure of electron-phonon interaction, is calculated for all the samples i.e., ($\sim 10^{-4}$) and the values obtained are higher than the reported values by an order of magnitude

^{57}Fe Mossbauer **spectroscopic** measurements have been carried out on $\text{Fe}_{0.8}\text{Ni}_{1.4-x}\text{Mo}_x\text{Si}_2\text{B}_{16}$ ($x=0,1,2,3$ and 4) alloys in the temperature range 80 K-RT in the transmission **geometry**. All the samples showed well resolved broad six line spectra indicating that the samples are in ferromagnetic amorphous state with random atomic arrangements and inequivalent Fe-sites. The absorption lines have large linewidths (0.5-2.0 mm/s) which are about 5-6 times larger than those of iron-foil at room **temperature**, and it is a characteristic feature observed in Mossbauer spectra of all ferromagnetic metallic **glasses**. Major broadening in these Mossbauer spectral lines is due to the magnetic **hyperfine** field distribution. Area ratios of the lines calculated from the room temperature Mossbauer spectra show that the magnetization axis is out of plane of the ribbon for $x=0$ and tilts towards the ribbon plane as x increases and it lies in the plane of the ribbon for $x=4$. The temperature dependence of the average line widths $\Gamma_{1,6}$, $\Gamma_{2,4}$ and $\Gamma_{3,4}$ shows a decreasing trend though there is quite a bit of scatter. This suggests that the long range order predominates over the short range order in alloys containing Mo. The values of **isomer** shift at RT are 0.099, 0.065, 0.081, 0.050 and 0.053 mm/s **respectively**. There seems to be a linear temperature dependence of the isomer shifts for all the samples with their slopes lying in the range $-(5-7) \times 10^{-4}$ mm/s-K, which are within the experimental error and are in good agreement with the reported theoretical **value**. One may infer from this that the coupling between the atoms in these metallic glasses is harmonic to a good **approximation**.

The values of effective magnetic hyperfine field, H_{eff} , calculated by using the line positions decrease with increase in Mo content and also with increase of temperature in the range 80 K-RT. The values of saturation magnetic hyperfine field, $H_{\text{eff}}(0)$ showed a decreasing trend from 305 to 287 kOe, with a fall of approximately 4.3 kOe/Mo-at%. The values of Curie temperature T_c also decrease with Mo content at the rate of -40 K/Mo-at% upto $x=3$ but with a slight increase for $x=4$. This decrease is attributed to Mo acting

as a magnetic diluent and/or its antiferromagnetic exchange interactions with **iron**. The values of spin wave coefficients, B_{12} are increasing with Mo content, indicating that the spin waves are excited with relative ease in these alloys, as more and more Mo is added.

The **hyperfine** field distribution $P(H)$ curves obtained by Window's method of Fourier analysis for all the spectra recorded at different temperatures showed a well defined major peak at high field side and a minor peak at low field side (~ 100 kOe) and this observation indicates that $P(H)$ has a **bimodal distribution**. This **bimodality** in the major peak arises due to the presence of Mo which can contribute to Fe-Mo antiferromagnetic exchange interactions and magnetic dilution effects contributing to the distribution in the low field **region**. With the addition of Mo, changes in internal magnetic fields occur and as a result the major peak shifts towards lower field side and becomes asymmetric. The minor peak occurring at low field (~ 100 kOe) is an artifact in the method of analysis and is independent of temperature and composition. This bimodal distribution indicates two different microscopic environments around Fe atoms, one rich in Ni atoms and the other rich in Mo **atoms**. The $P(H)$ curves obtained at 80 K indicate that the asymmetry of the major peak increases systematically with increase in Mo **concentration**. The values of H_p and H_{av} show the same trend as H_{eff} in that they decrease monotonically with increasing temperature and also with Mo **concentration**. But the values of **full** width at half maximum (FWHM), ΔH are relatively independent of temperature, especially in Mo rich systems, indicating that different hyperfine field components exhibit different temperature dependence. These ΔH values increase with increase of Mo content, at a rate of 10 kOe/Mo-at% upto $x=3$ but the increase becomes less for $x=4$.

The values of $M_s(RT)$ and $M_s(0)$ decrease with increase in Mo concentration and the rate of fall is ~ 8 emu/g per at% of Mo and ~ 7 emu/g per at% of Mo respectively. Magnetization at low temperatures, well below T_c , well obeys the spin wave excitations and the values of spin wave coefficient B_{32} increase from 0.2 to 0.34 with increasing Mo content and these values are in agreement within 10% with those obtained from **Mossbauer** measurements except for $x=0$.

The crystallisation kinetics of **a-Fe₆₈Ni_{14-x}Mo_xSi₂B₁₆** (**x=0,1,2,3** and 4) alloys have been studied by continuous heating (non-isothermal) method using **DSC**. Two crystallisation peaks are observed in all the alloys indicating a two step crystallisation process, characterized by a primary crystallisation which results in the precipitation of **α-iron**, followed by a eutectic process leading to the formation of various crystalline **phases**. There is a systematic increase in the peak temperatures **T_{p1}** and **T_{p2}** with increase in heating rate by about **~20-25K** and an increase by **~20K** and **~55K** respectively for **T_{p1}** and **T_{p2}** with increase in Mo concentration enhancing the thermal stability against **crystallisation**. The Kissinger method of calculation led to comparable values of activation energies **E_{c1}** ranging from 300-350 **kJ/mol** for the primary crystallisation and that of **E_{c2}** over a wider range from 320-560 **kJ/mol** for the eutectic **process**. The lower values of **E_{c1}** when compared to those of **E_{c2}** are due to different crystallisation mechanisms involved in the two steps. In all the cases, both the crystallisation steps follow the Kissinger expression fairly well, indicating first order **kinetics**. However, during the primary crystallisation, a systematic increase in the activation energy with increasing Mo content is observed, indicating that the Mo-at% present proportionately enhances the thermal **stability**. The activation energies for the second crystallisation step, **E_{c2}** increase up to 2 **Mo-at%** and there after **E_{c2}** starts decreasing, indicating that higher the Mo content, lesser is the thermal energy needed and hence lower is the activation energy in this crystallisation process. These observations are also supported by the **Avrami** exponents determined, which are found to be in the range **1.5 ≤ n ≤ 4.0** for the first step and **1.2 ≤ n ≤ 4.0** or even greater than 4.0 for the second step. A comparison of n values for the different alloys of the present studies shows a compositional **dependence**. The large deviation in n values for the second step crystallisation have been attributed to complex processes with simultaneous occurrence of nucleation and growth processes of various crystalline **phases formed**. The range of n values obtained here indicate that in the present alloys the crystallisation process is effectively a three dimensional parabolic growth with increasing nucleation **rate**. Further, the primary process is very much governed by diffusion and the

second step is influenced by nucleation and growth **processes**. The results show that Mo plays a significant role in improving the thermal **stability**.

The corrosion behaviour of **a-Fe₈₈Ni_{14-x}Mo_xSi₂B₁₆** ($x=0,1,2,3$ and 4) alloys has been studied using electrochemical corrosion techniques **viz.**, **potentiodynamic** polarisation and ac impedance spectroscopic techniques in two corrosive environments, **1N HCl** and **1N H₂SO₄ solutions**. In both the environments, these alloys exhibit relatively poor corrosion resistance and this may be due to the absence of strong passivators such as Cr or P. The alloys exhibit tendency for weak passivation in **1N HCl** environment, though the passive current is quite high ($\sim 2.5 \times 10^{-4}$ - 2.7×10^{-4} A/cm²) and this passivity increases with increase in Mo concentration, while no such passivity is observed in **H₂SO₄** environment and show an active dissolution without any revelation of **passivity**. The weak passivation noticed in the polarisation curves in HCl has been attributed to salt film formation as opposed to thin passive film obtained in Mo containing **alloys**. The cathodic **Tafel** slope, **P**, does not show any systematic variation though a few Mo containing alloys exhibit lower values than the base alloy without **Mo**. In contrast to this, there is a significant reduction in the anodic Tafel slope, β_a due to addition of Mo in both **1N HCl** and **1N H₂SO₄** solutions. These observations emphasize the fact that mere amorphous nature of the alloy is not sufficient to provide resistance towards **corrosion**. A possible improvement in corrosion resistance due to addition of Mo is off-set by the simultaneous reduction in the Ni content of these alloys.

Nyquist plots obtained from impedance measurements for the alloys in **H₂SO₄** differ from those obtained in HCl in that in the former plots, a capacitive loop followed by an inductive loop is displayed, while in the latter plots in HCl two overlapping capacitive loops are **observed**. Therefore it seems that **Cl⁻** ions promote formation of passive film whereas **SO₄²⁻** ions do not favour such film **formation**. Thus the mechanism of alloys' dissolution in presence of Mo in HCl seems to be different from that of **H₂SO₄**. A good correlation seems to exist between the polarisation resistance values obtained by impedance and polarisation techniques when the alloys undergo active dissolution and not when they possess **passivity**.

Suggestion for Future Work

Detailed investigations to establish the magnetic contribution to **electrical** resistivity have been suggested and these will be **useful** to confirm which theory gives better explanation of the resistivity behaviour below T_{\min} . **Investigations** of Bergmann et al (1978) and Richter et al (1979) predicted a $T^{1/2}$ power law in contrast to T^2 dependence found in our Fe-rich amorphous FM alloys. Our results are in agreement with those of Kaul et al (1986). Our experimental investigations are confined to the temperature range 10-300 K only, due to low temperature **limitations**. This can be extended from (<4.2 K) to high temperatures ($\geq T_c$). If the data is taken well below 10 K up to 4.2 K then the resistivity/conductivity behaviour well below T_{\min} can be studied more rigorously to verify the existence of the electron-electron interaction and weak localisation effects at low temperatures. Additional measurements, like magnetic field dependence of resistivity will also be **useful** to confirm which theory gives better explanation of the resistivity behaviour below T_{\min} .

Secondly, we have limited our **Mössbauer** studies to **isomer** shifts and **hyperfine** interactions only in certain limited temperature range below T_c from 80 K-RT and these studies can be extended to temperatures much above T_c and spin wave excitations and critical exponents can be **studied**. The detailed investigations can be further carried out using Handrich's model by fitting the data to an equation similar to the magnetization relation to temperature in crystalline ferromagnets, as the hyperfine fields in amorphous ferromagnets are proportional to **magnetization**.

Thirdly, the crystallisation process(es) of the metallic glasses can be clearly understood by systematic study of metallic glasses using X-ray diffraction, Transmission electron microscopy (TEM) and **DSC**. All these techniques have to be extensively used to understand the growth, nucleation, stability and crystallised **products**. These techniques need an accurate annealing and quenching of the samples prior to their **experimentation**.

Lastly, Corrosion studies in different corrosive environments can be extended by including the TEM studies of the samples there by getting more information about the

different phases formed due to the electrochemical corrosion reactions taking place in the
alloys

LIST OF PUBLICATIONS

Papers published :

- 1 Changes in resistivity behaviour of metallic glass $\text{Fe}_{70}\text{Ni}_{17}\text{B}_{16}\text{Si}_2$ due to molybdenum substitution for nickel
A K Bhatnagar, B. Seshu, K D D Rathnavaka and D G Naugle
J Appl Phys, **76** (10) (1994) 6107
- 2 Mossbauer investigation of magnetic properties of amorphous $\text{Fe}_{72-x}\text{Ni}_{10-x-y}\text{Mo}_y\text{B}_{16}\text{Si}_2$
A K Bhatnagar, B. Seshu, G V Sudhakar Rao and N R Munirathnam
J Non. Cryst Solids, **204** (1996) 305
- 3 Molybdenum induced enhancement of thermal stability of glassy $\text{Fe}_{68}\text{Ni}_{14-x}\text{Mo}_x\text{Si}_2\text{B}_{16}$ alloys
B. Seshu, A K Bhatnagar and D G Naugle
J Mat Sci. Lett, **16** (2) (1997) 165
- 4 Electrochemical Corrosion behaviour of $\text{Fe}_{68}\text{Ni}_{14-x}\text{Mo}_x\text{Si}_2\text{B}_{16}$ metallic glasses in 1N HCl and 1N H_2SO_4
B. Seshu, A Venugopal, A K Bhatnagar and V S Raja
J Mat Sci., **32** (1997) 2071.
- 5 Molybdenum dependence of electrochemical corrosion in metallic glass $\text{Fe}_{68}\text{Ni}_{14-x}\text{Mo}_x\text{Si}_2\text{B}_{16}$
B. Seshu, A Venugopal, A. K Bhatnagar and V S. Raja
J Mat. Sci & Engg A, **226-228** Supplement (1997) 318 (Proc of the 9th Int Conf on Rapidly Quenched and Metastable Materials)

Papers presented in National Conferences / Symposia :

1. Aluminium substitution in $\text{Fe}_{80}\text{P}_{13}\text{C}_7$: Resistivity study
B Anasuya, B. Seshu and A K Bhatnagar
Proceedings of the DAE Solid State Physics Symposium, **36**, held from Dec. 27th-31st, 1993 at BARC, Mumbai, India

- 2 Non-isothermal crystallisation studies of $\text{Fe}_{0.8}\text{Ni}_{1.4-x}\text{Mo}_x\text{Si}_2\text{B}_{16}$
 B. Seshu and A K Bhatnagar
 Proceedings of the DAE Solid State Physics Symposium, **38**, held from Dec 27th-31st, 1995 at I A C S, Jadavpur, Calcutta, India
- 3 Effect of Aluminium on crystallisation of glassy $\text{Fe}_{80}\text{P}_{14}\text{C}_7$
 B Anasuya, B. Seshu and A K Bhatnagar
 Proceedings of the DAE Solid State Physics Symposium, **38**, held from Dec 27th-31st, 1995 at I A C S, Jadavpur, Calcutta, India
- 4 Molybdenum induced changes in magnetic properties of amorphous $\text{Fe}_{0.8}\text{Ni}_{1.4-x}\text{Mo}_x\text{Si}_2\text{B}_{16}$ alloys
 B. Seshu and A K Bhatnagar
 Proceedings of the Symposium on Current topics in Physics of Materials held from March 27th-29th, 1997 at University of Hyderabad, Hyderabad, India

Papers presented in International Conferences :

- 1 Molybdenum dependence of electrochemical corrosion in metallic glass $\text{Fe}_{0.8}\text{Ni}_{1.4-x}\text{Mo}_x\text{Si}_2\text{B}_{16}$
 B. Seshu, A Venugopal, A K Bhatnagar and V S Raja
 Proceedings of the at Ninth international conference on Rapidly Quenched and Metastable Materials, held from August 25th-30th, 1996 at Bratislava, Slovakia
- 2 Resistivity, Mossbauer and crystallisation studies of metallic glass $\text{Fe}_{0.8}\text{Ni}_{1.4-x}\text{Mo}_x\text{Si}_2\text{B}_{16}$
 B.seshu and A K Bhatnagar
 Proceedings of the Ninth international conference on Rapidly Quenched and Metastable Materials, held from August 25th-30th, 1996 at Bratislava, Slovakia

Curriculum Vitae

Name : **BHAMIDIPATI SESHU**
Father's Name : B Subrahmanyam
Date of Birth : 10 August 1969
Place of Birth : **Kakinada**, Andhra **Pradesh**, India
Sex : Female

Educational Qualifications :

(i) M. **Sc.** in Physics (1990-1992)

Specialisation : Electronics

Passed in **1st** Division with 72.07% of Marks

Andhra University, **India**

(ii) B. **Sc.** (1986-1989)

Physics (Main), Electronics, Mathematics

Passed in 1st Division with 77.5% of Marks

Andhra University, **India**

Awards and Fellowships :

- National merit scholarship awarded for the period **1984-1989**
- Senior Research Fellow (SRF) of Council of Scientific and **Industrial** Research, **(CSIR)** India since **1995-1998** in School of Physics, University of Hyderabad, **Hyderabad**